Chair of Materials Physics

Doctoral Thesis

Micro-mechanical approach to assess the strength of nanocrystalline tungsten-copper composites

Dipl.-Ing. Klemens Silvester Schmuck

August 2024

MONTANUNIVERSITÄT LEOBEN
www.unileoben.ac.at

AFFIDAVIT

I declare on oath that I wrote this thesis independently, did not use any sources and aids other than those specified, have fully and truthfully reported the use of generative methods and models of artificial intelligence, and did not otherwise use any other unauthorized aids.

I declare that I have read, understood and complied with the "Good Scientific Practice" of the Montanuniversität Leoben.

Furthermore, I declare that the electronic and printed versions of the submitted thesis are identical in form and content.

Date 01.08.2024

Signature Author
Klemens Silvester Schmuck

Acknowledgement

I would like to express my deepest gratitude to many people in my life that helped and supported me throughout my journey to reach my goals and accomplish this thesis. I doubt I would have been able to accomplish this without them.

Foremost, I would like to thank Univ. Prof. Dr. Daniel Kiener for giving me the opportunity to get a taste of experimental work in such a diverse research field and his guidance throughout this time. Moreover, I appreciate that he gave me some academic freedom, allowing me to widen my perspective and grow. I would like to extend my sincere thanks to my Mentor Univ.-Prof. Dr. Raul Bermejo, who had always a good advice for me and helped me enhancing my research.

Special thanks to Dr. Markus Alfreider and Dr. Michael Burtscher for being patient with me and my questions, the fruitful discussions about the results and the help with all the experimental efforts, benefited the work in this thesis. They were a great support during my PhD.

I am also grateful for the fruitful discussions and helpful comments from Univ. Prof. Dr. Reinhard Pippan and Dr. Anton Hohenwarter, which helped me to interpret my observations.

Thanks should also go to Dr. Stefan Wurster for his irreplaceable optimism and the great help in urgent experimental questions.

I would also like to express my deepest appreciation to Dr. Martin Antenreiter, who helped me a lot with the image processing part and had always a good advice at hand.

Many thanks also to my office colleges Fei-Fan Cai and Eray Yüce for the delightful discussions and the interesting insights into different cultures.

Furthermore, I would also thank my PhD fellows Alexander Jelinek, Nadine Buchebner, Hannah Lichtenegger and all the others for the great time and the delightful conversations.

At last I would like to give my greats gratitude to my friends and family, without them this endeavor would not have been possible. Especially, these thanks go to Kathrin Maier, who cheered me up in case of struggles and kept smiling at me.

Abstract

The advancements in fusion reactor research and the increased trend in aerospace activity demand materials that are able to bear harsh environments. However, manufacturing of pure tungsten is challenging and costly. Hence, tungsten-based composites are frequently used. As secondary phase, copper offers an excellent ductility at the expense of strength of the composite compared to pure tungsten. Nevertheless, grain-size refining allows enhancing the material strength by retaining its ductility.

In this thesis tungsten-copper composites with 80 wt.% tungsten are investigated. To further strengthen the copper phase, it is alloyed with 10 wt.% zinc to enhance the twinning tendency. As starting point for grain refinement either a bulk tungsten-copper composite or elemental powders are used. The latter is compacted by high-pressure torsion to form green compacts. To tailor the resulting grain-size in the nanocrystalline regime by high-pressure torsion for all samples, the deformation temperature is varied between RT and 550°C. Thereby, an inverse Hall-Petch behavior is observed for the resulting grain-sizes 9 nm and 11 nm. To test the fracture behavior, micro-cantilever bending beams are fabricated from the refined samples. By varying the cantilevers cross-section, a sample size effect is examined. Below cross-sections of (10 x 10) µm^2, the fracture toughness decreases. Moreover, the fracture mechanical tests reveal a decreasing fracture toughness with increasing grain-size for the samples deformed at RT and 400°C. The 550°C samples exhibit a slightly enhanced fracture toughness. These results indicate a possible change of dominate deformation mechanisms, from grain boundary slip to dislocation based mechanism.

Furthermore, the mechanical evaluation from *in situ* acquired images provide the possibility to extract detailed fracture characteristics, such as crack length, crack tip opening displacement and -angle. The former is essential to evaluate the fracture behavior. For the extraction thereof, an image processing prototype is developed based on manually defined filter-sets, allowing for a semi-automatic evaluation. By adapting the classification process, the prototype is enhanced to incorporate the crack tip opening displacement and -angle. This routine provides a much higher fidelity in crack analysis, the performance of which is verified by manual measurements on the *in situ* images. In combination with mechanical data, the additionally evaluated fracture characteristics enable a detailed insight into fracture processes of high-performance nanocomposites for harsh environments of small-length scales.

Kurzfassung

Die Fortschritte in der Fusionsreaktorforschung und der verstärkte Trend in der Luft- und Raumfahrt erfordern Materialien, die rauen Umgebungen standhalten können. Dabei ist Wolfram häufig das Material der Wahl für Komponenten die mit dem Fusionsplasma in Kontakt stehen und für Bauteile die eine hohe Temperaturresistenz aufweisen müssen. Die Herstellung von reinem Wolfram ist jedoch schwierig und kostspielig. Daher werden häufig Verbundwerkstoffe auf Wolframbasis verwendet. Als sekundäre Phase bietet sich Kupfer, durch seine ausgezeichnete Duktilität, an. Allerdings ist die Festigkeit des Verbundwerkstoffes Wolfram-Kupfer geringer im Vergleich zu reinem Wolfram. Durch Kornfeinung lässt sich allerdings die Festigkeit des Werkstoffs unter Beibehaltung der Duktilität erhöhen.

In dieser Arbeit wurden Wolfram-Kupfer-Verbundwerkstoffe mit 80 gew.% Wolfram untersucht und durch Hochverformung die Korngröße in den nanokristallinen Bereich reduziert. Um die Kupferphase weiter zu verstärken, wurde sie mit 10 Gew.% Zink legiert, um so auch die Neigung zur Zwillingsbildung zu erhöhen. Als Ausgangsmaterial für die Kornverfeinung wurde entweder ein Komposit hergestellt durch Flüssigphasensintern oder ein verpresster Grünkörper hergestellt aus elementaren Pulvern verwendet. Für letzteres wurde ebenfalls Hochverformung zur Verdichtung angewandt. Um verschiedene Korngrößen im nanokristallinen Bereich einzustellen, wurde die Verformungstemperatur zwischen RT und 550°C variiert. Dabei wurde ein inverses Hall-Petch-Verhalten für die Korngrößen 9 nm und 11 nm beobachtet. Um das Bruchverhalten zu prüfen, wurden aus den verfeinerten Proben mikroskopisch kleine Biegebalken hergestellt. Durch Variation des Querschnitts der Balken wurde der Einfluss der Probengröße auf das Bruchverhalten analysiert. Dabei nahm unterhalb eines Querschnitts von (10 x 10) μm^2 die Bruchzähigkeit ab. Darüber hinaus zeigten die bruchmechanischen Experimente eine abnehmende Bruchzähigkeit mit zunehmender Korngröße für die bei RT und 400°C verformten Proben. Im Gegensatz dazu wies die 550°C Probe eine leichte Erhöhung der Bruchzähigkeit auf. Diese Ergebnisse deuten auf eine mögliche Änderung des vorherrschenden Verformungsmechanismus hin, von einem durch Korngrenzengleiten dominierten zu einem auf Versetzungen basierenden Mechanismus mit zunehmender Korngröße.

Neben der mechanischen Analyse bieten die *in situ* aufgenommenen Bilder die zusätzliche Möglichkeit, Bruchcharakteristiken aus den Bildern zu bestimmen, wie z. B. die Risslänge, die Verschiebung der Rissöffnung und den Rissöffnungswinkel an der Rissspitze. Dabei ist die Risslänge für die bruchmechanische Auswertung maßgeblich. Für die Extraktion dieses

Bruchcharakteristika wurde ein Protokoll entwickelt, das auf manuell definierten Filtersätzen basiert und eine halbautomatische Auswertung ermöglicht. Dieser Prototyp wurde erweitert durch die Anpassung des Klassifizierungsprozesses, um die Verschiebung der Rissöffnung und den Rissöffnungswinkel an der Rissspitze zu bestimmen. Diese Routine ermöglicht hochaufgelöste Rissanalyse mit bisher ungesehener Präzision, welche durch manuelle Messungen verifiziert wurde. In Kombination mit den mechanischen Daten erlauben die zusätzlich ausgewerteten Bruchcharakteristiken einen detaillierten Einblick in Versagensprozesse nanostrukturierter Komposite für harsche Bedingungen auf kleinen Längenskalen.

Table of Content

1 Introduction

Over the last decades a drastic growth in applications demanding materials withstanding harsh environments has emerged [1]. This originates in the continuous progress in fusion reactor research, the ongoing trend towards aerospace activity and the increasing demand by advanced technologies for materials that can operate reliably in extreme conditions. These applications necessitate materials that are able to bear high temperature loads, withstand ion as well as neutron bombardment and have a high creep-, wear and corrosion resistance. Due to the outstanding material properties of tungsten, it is frequently considered as candidate material for such applications. Although, the use of pure tungsten is limited due to the high density and poor ductility, resulting in challenges in its work-ability and performance [2]. Hence, tungsten is often composed with other elements to enhance its outstanding properties. As secondary phase, copper is frequently used, due to the in-miscibility with tungsten, allowing to retain the material properties of both elements in a composite. The combination of tungsten and copper enhances the endurance during high temperature loads due to the possible cooling from the copper transpiration [3, 4]. The interaction of the properties of both materials enables the use of tungsten-copper composites in several different high-performance applications, such as high-voltage contacts [5–7], electronic packaging [8, 9], rolling guides in steel production [10], plasma facing components [11–17], military ammunition [3, 18] and aircraft nose cones [19, 20].

Nevertheless, the high-intrinsic strength of tungsten is decreased by intermixing it with copper in a composite. Moreover, due to the low brittle-to-ductile transition temperature of tungsten of about 200°C to 400°C [21], tungsten-copper composites tend to have a low damage and fracture tolerance at RT. These properties can be improved by enhancing the materials strength and ductility, which are in general mutual exclusive [22–24]. Though, grain refinement allows to partially mitigate this exclusivity [23, 25–27]. Besides the materials strength increase, a refined microstructure benefits the wear- and arc resistance of tungsten-copper composites [28, 29]. Moreover, the refined structure is advantageous for the application in fusion reactors, as it inhibits the formation of blisters and the softening effect from helium bubbles is delayed to higher doses [22]. A simple technique to refine the grains into the ultra-fine grained and nanocrystalline regime is severe plastic deformation, in particular high-pressure torsion (HPT) [30–33], equal-channel pressing [34] or accumulative roll bonding [35, 36]. From these methods, HPT provides the highest equivalent strains, translating to the most severe grain refinement achievable by these techniques [37–39]. HPT

allows to produce nanocrystalline microstructures and tailor the grain size by adjusting the deformation parameters. Fundamental investigations regarding the microstructural evolution of various tungsten-copper composites refined by HPT are reported in literature [40, 41]. Although, a few studies analyzed the relation between microstructure and mechanical performance, literature still lacks data on the fracture mechanical data for nanocrystalline tungsten-copper composites.

However, severely deformed materials have limited strain hardening capabilities due to the reduced grain volume and the saturation of dislocation. Both inhibit the accumulation of further dislocations [42–46]. However, Zhao *et al.* [46] has reported an increase of ductility and strength for ultra-fine grained copper with 10 wt.% zinc due to promoted twinning activity. Similar findings for nanocrystalline copper produced from powder precursors are reported by Holub *et al.* [47]. This occurs as twinning is activated as additional deformation mechanism by reducing the stacking fault energy by alloying copper with zinc. Studies that utilized zinc as sintering activator for tungsten-copper composites have focused on the analysis of density, conductivity, hardness and strength [20, 48]. Yet, investigations of the fracture toughness of these composites are again scarce in literature.

The producible sample volumes by HPT are limited due to the necessary pressure [49, 50]. These small sample volumes facilitate micro mechanical testing, in particular tensile, compressive and bending tests [51]. Typically, these experiments are performed *in situ* inside electron microscopes to provide the possibility to align sample and indenter and attain visual observations. Nevertheless, tensile and compressive tests are challenging and prone to misalignment. Bending on the other hand is less sensitive to alignment errors. Additionally, the stress gradient induced by bending inhibits catastrophic failure, due to the compressive stresses behind the neutral axis. Thus, bending is primarily used to test fracture toughness at the micron- and sub-micron scale, despite the challenging evaluation [52–57]. A standard geometry for these experiments is the single edged notched cantilever bending beam, schematically illustrated in Figure 1.1 a). Figure 1.1 b) depicts an *in situ* cantilever before testing.

Fracture mechanical evaluation on the micrometer length scale frequently necessitates elastic plastic fracture mechanics (EPFM) due to size restrictions, stemming form the plastic zone ahead of the crack with respect to the specimen size. EPFM necessitates an accurate knowledge of the current crack length, which is accessible by measuring the cantilever stiffness throughout the experiment [59]. Thereby, stiffness changes are related to the crack extension, based on the assumption of an isotropic homogeneous material and straight crack front. Additionally, as mentioned above, these experiments are in general conducted in an electron microscope, allowing to acquire *in situ* images. From these images, the current crack length can be measured directly on the sample surface. Moreover, these *in situ* images provide the

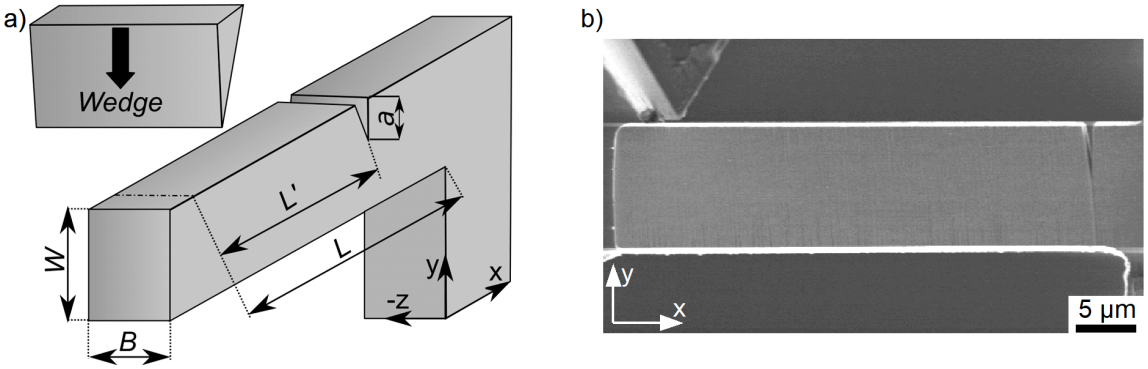

Figure 1.1: Illustration of single edge notched cantilever bending beams. a) Schematic drawing with all essential geometry variables. b) *In situ* recorded cantilever beam before testing. Adapted from [58] under the CC BY Creative Common License 4.0.

possibility to determine the purely geometrical fracture characteristics by extracting the complete crack shape, in particular crack tip opening displacement (δ) and -angle (α).

The image based evaluation of *in situ* fracture experiments faces several challenges. One of them stems from the sample mounting. A tilted sample raises the challenge to extract the crack shape and estimate fracture characteristics from images, due to visible side surfaces, schematically depicted in Figure 1.2 a). Other challenges arise form the fracture process itself. For micro-mechanical experiments, alike in macroscopic tests, different fracture types may occur, such as ductile, semi-brittle and brittle failure. From an image processing perspective, each fracture type facilitates various crack shape features, schematically illustrated in Figure 1.2 b)-d). In general brittle failure results in a thin crack, which is faint feature on the recorded *in situ* images, see Figure 1.2 b). Ductile failure exhibits extensive blunting and pore formation in front of the crack. Thereby, the material between crack tip and pores is severely teared followed by interconnecting these pores with the crack tip, leading to crack propagation, as schematically shown in Figure 1.2 c). In the case of semi-brittle failure, the combined features of ductile and brittle fracture occur with a rather thin crack tip of a few pixels. In addition, for semi-brittle failure bifurcation, crack deflection, and material bridges may occur, illustrated in Figure 1.2 d). The latter is a result of material tearing upon cracking, which leaves material behind within the crack wake making the crack tip location ambiguous. Crack deflection results in a curved crack path, while bifurcation leads to multiple crack branches causing an ill-defined crack tip. All of these features raise the challenge to localize the crack edges and extract the whole crack shape. As the transition between the fracture types is smooth, individual experiments might combine or miss out some of these crack features. Hence, standard edge-detection algorithms are insufficient to obtain the crack shape. Therefore, the measurement from *in situ* images is challenging and usually performed manually, which is a tedious time-consuming task and strongly depends on human individuality.

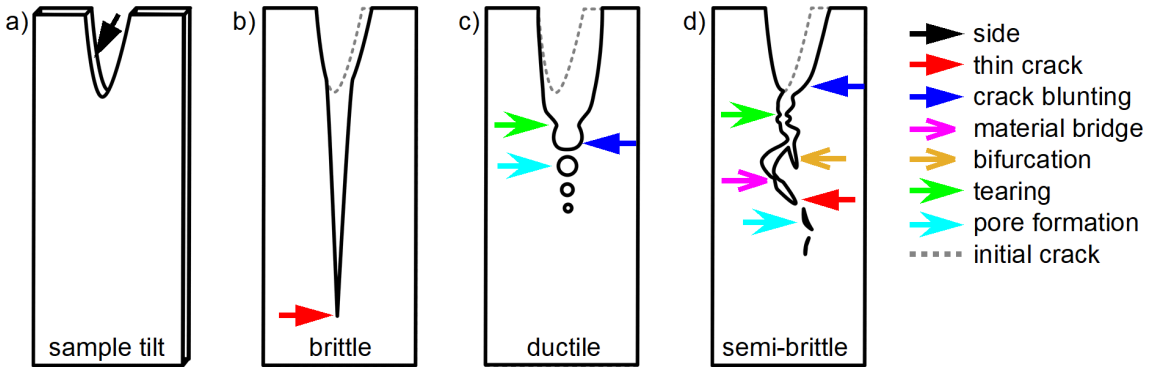

Figure 1.2: Schematic illustration of different prominent features observable from *in situ* images. a) Sample tilt leading to sample material within the crack wake. b)-d) Different fracture types with the corresponding prominent fracture features. Taken from [60] under CC BY Creative Common License 4.0.

In material science, a frequently used method to analyse images is digital image correlation (DIC) [61–70]. Thereby, consecutive images are correlated to track image changes, which are translatable in sample deformations [61, 62]. Tracking these changes allows to follow crack propagation and extract fracture characteristics [64, 71–73]. However, to detect changes, DIC necessitates self-similar structures on the sample surface and therefore requires a high image resolution. Another approach to classify images and extract image information which gained popularity in recent years is the use of convolutional neural networks (CNN) [74, 75]. Training a CNN from scratch requires a lot of computational power and a vast amount of qualitative data. However, from a single micro-mechanical fracture experiment a few hundred *in situ* images are retrieved, which represent a vast amount of data for these experiments. Though, these images are potentially self-similar, thus the amount of qualitative data is insufficient to train a CNN. Therefore, to analyze *in situ* images from fracture experiments, traditional image processing techniques have to be employed.

1.1 Objectives

The main objective in this thesis was to strengthen and enhance the fracture toughness of nanocrystalline tungsten-copper composites. High-pressure torsion is applied as a severe plastic deformation technique to refine the grains to the nanocrystalline regime to increase the composites strength. Since, lowering the grain-size below the sub-micron regime partially scarifies ductility. The optimal grain-size with respect to the composites strength, ductility and toughness had to be determined. Additionally, the ductile copper phase was alloyed with zinc to further strengthen and raise the ductility of the composite. Moreover, to enhance the comparability of the fracture toughness values in micro mechanics, the cantilever cross-section that guarantees sample size independency had to be determined. In addition

to the mechanical evaluation, the *in situ* acquired frames can be used to evaluate fracture characteristics. Therefore, the measurement is limited to only specific images and the crack length frequently. To overcome this limitation an algorithm was developed to replace the tedious manual task and facilitate a continuous evaluation of all acquired images. Beside the crack length, this algorithm should be capable to extract additional fracture characteristics, in particular crack tip opening displacement and -angle.

2 Processing of Materials

This chapter summarizes the state of the art for the fabrication methods used in this thesis. The first section introduces the investigated material composition. In the following section the technique to fabricate green compacts and produce nanocrystalline microstructures are outlined.

2.1 Tungsten-Copper Composites

The material investigated in this thesis consisted of the base elements tungsten, copper and zinc. Each element exhibits different physical properties and has its own qualities, summarized in Table 2.1. Tungsten offers the highest melting point of all metals, a low vapor pressure, high intrinsic strength and a good irradiation, arc as well as wear resistance [11–13]. This makes tungsten an ideal candidate for high performance applications. Nevertheless, toughening tungsten is challenging as alloying of tungsten is prone to form brittle inter-metallic phases. Only rare earth elements are known as alloying element for tungsten to prevent the formation of inter-metallic phases [76, 77]. Though, these elements are expensive and rare, thus the use is limited. Another possibility to enhance the properties of tungsten is to add an immiscible secondary phase. For that copper is frequently used, as it has a high ductility and is immiscible with tungsten [78]. Additionally, copper adds a high electric and thermal conductivity, making it an ideal secondary phase element for electric components in high performance application [79]. Though, the tungsten-copper composite sacrifices partially the high strength of tungsten. To mitigate this, the copper phase could be strengthened, *e.g.* by alloying. A well known element to strengthen copper is zinc to form brass, which is also a sintering activator for tungsten-copper and enhances the strength as well as density of tungsten-copper composites [3, 20, 48].

Further reinforcement of the tungsten-copper composites strength can be achieved by applying additional strengthening mechanisms, such as grain refinement and activating twinning as another deformation mechanism. The advantage of these two mechanisms is to retain the ductility while increasing the materials strength. However, within the nanocrystalline regime the ductility decreases partially with further refinement [42–44, 46, 80]. This occurs as the smaller grain size restricts dislocation motion and less dislocations can be accommodated in a grain volume [46, 80]. Twinning on the other hand provides further strain hardening capabilities. Similar to grain refinement, an ideal grain size for

extensive twinning activity exists. Below this grain size, the mechanism becomes increasingly challenging to activate [37, 81, 82]. In the case of α-brass, literature reports an ideal grain size for twinning of about 40 nm [81, 82]. In this thesis, the tungsten-copper composites were subjected to HPT, to refine the microstructure down to the nanocrystalline regime and activate the discussed strengthening mechanisms.

Table 2.1: Physical properties of the pure elements tungsten, copper and zinc at room temperature: Yield strength σ_y [76, 83], Young's modulus E [24, 76, 83, 84], theoretical density ρ [76, 83], melting temperature T_{melt} [76, 83], vapor pressure p_v at 1273 K [85] and crystal structure [76].

	σ_y [MPa]	E [GPa]	ρ [g/cm^3]	T_{melt} [K]	p_v [Pa]	crystal structure
tungsten	580	410	19.3	3700	3.7×10^{-23}	bcc
copper	69	130	8.9	1360	8.3×10^{-3}	fcc
zinc	28	115	7.1	420	2.8×10^{5}	fcc

2.2 High-Pressure Torsion Technique

Bridgman invented in 1935 the first prototype to subject disc-shaped samples to a high pressure and apply a torsional strain [86]. With this method Bridgman investigated various materials and compounds to study the polymorphic phase transformation [87]. In 1988, Valiev *et al.* introduced this method to the severe plastic deformation community and framed the method high-pressure torsion (HPT) [87, 88]. HPT quickly gained popularity as it allows to fabricated ultra-fine grained and nanocrystalline microstructures consisting of mainly high-angle grain boundaries [87, 89].

The principle of HPT is simple. The sample is placed between two anvils and subjected to a high pressure. Usually, this pressure is above the materials yield strength in the GPa-regime. To induce straining, one anvil starts to rotate while the pressure is applied, allowing a continuous deformation. Nowadays, the quasi-constrained anvil geometry is commonly used in the HPT community [49, 50], illustrated in Figure 2.1. The anvils cavities of the quasi-constrained geometry provide a central sample positioning and reduce the thickness decrease of the sample. Furthermore, the material that flows out in the gap between the anvils is confined by friction. This leads to a back pressure which induces a hydrostatic pressure inside the sample [49]. This even allows to process materials with a high strength as well as relatively brittle materials, which are otherwise impossible to refine by other severe plastic deformation techniques [49, 50, 90–92].

HPT allows to induce a high shear strain due to the continuous anvil rotation. For an ideal

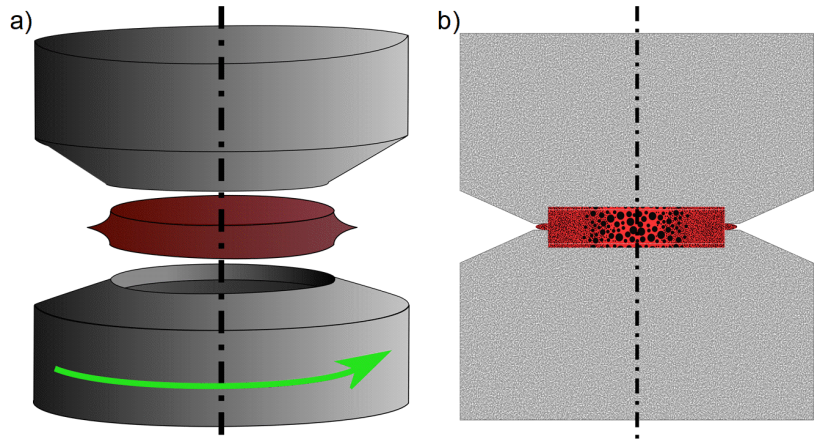

Figure 2.1: Schematic illustration of the constrained high-pressure torsion setup. a) 3D view of the anvils with the sample in between. The green arrow depicts the lower anvils rotation. b) Cross-section of the setup indicating grain-refinement gradient along the radius by the coarser structure in the sample center.

unconstrained HPT process, the shear strain (γ) can be approximated by [89],

$$\gamma = \frac{2\pi r}{t} n, \tag{2.1}$$

with the disk radius r, the applied rotations n and the disk thickness t. Due to the idealization of the HPT process, the approximation assumes a constant disk geometry. From Equation 2.1, the linear relation between γ and r is obvious, resulting in a strain gradient along the disk radius, as schematically depcited in Figure 2.1 b). Either way, to compare different severe plastic deformation techniques the equivalent strain is frequently used. To convert γ to the equivalent strain (ϵ) the von Mises criterion has been established in the HPT community [50, 93],

$$\epsilon = \frac{\gamma}{\sqrt{3}}. \tag{2.2}$$

The high achievable strains applied by HPT to a material translate into a severe grain refinement. This refinement significantly raises the materials hardness due to the Hall-Petch relation and has to be considered in the anvils selection to avoid anvil failure [26, 27]. Despite the possible infinite straining, the refinement saturates at a certain strain level, due to the equilibrium between dynamic recovering and refining processes [37]. These processes are affected by the used HPT parameters and the processed material properties [37, 94]. The latter significantly impacts the refinement process, in particular the materials melting temperature and its mechanical properties [37]. Stronger materials exhibit a more severe grain refinement. The melting temperature affects the materials strength and diffusion processes. Thus, elevated temperatures lead to a less severe refinement. This allows to tailor the grain size within the ultra-fine grained and nanocrystalline regime by adjusting the deformation temperature of the HPT process [87, 95, 96].

Furthermore, HPT provides the possibility to process powders and fabricate green compacts, similar to high iso-statistic pressing. An advantage of the HPT is the possible straining during compaction, benefiting the green compacts density. Moreover, the microstructural gradient along the radius allows to investigate various microstructures in the nanocrystalline regime on one sample. In addition, HPT enables the processing of strong and brittle materials, which is challenging otherwise. Thus, due to the necessity to process strong tungsten based composites, the HPT fabrication route was chosen for grain refinement and powder compaction. To tailor the grain-size in this thesis, the deformation temperature of the HPT process was varied from RT to 550°C.

3 Characterization

In this chapter the method to characterize the materials fracture properties are discussed. First the fracture mechanical basics are outlined, followed by the basic principles used to characterize failure and the practical application to micro-cantilever bending beams thereof. At the end image processing techniques are discussed to allow the evaluation of *in situ* acquired images from micro-mechanical fracture experiments.

3.1 Fracture Mechanics Analysis

Real components in general contain flaws of different size and shape, such as inclusions, pores and mirco-cracks. These flaws are usually the origin of failure. Thereby, the complex process of atomic bond breaking is localized in the vicinity of these flaws in a so called process zone, as depicted in Figure 3.1 a). The complex processes in this zone cannot be described by continuum mechanical models. Hence, fracture mechanical models are used to predict failure. These models assume a homogeneous isotropic material with a small processing zone compared to the sample dimensions. Fracture can be categorized in different loading configurations, referred to as modes. Mode I defines a symmetric crack opening, mode II is an in-plane shearing with respect to the crack front and mode III occurs for an out-of-plane shearing. Also combinations of these modes are possible. In this thesis mode I was used throughout all micro-mechanical bending experiments, thus, only mode I is considered throughout all further discussions. To characterize failure, different concepts evolved during the last decades, in particular based on the energy balance, stress-intensity, J-integral and crack tip opening displacement. The former was postulated by Griffith [97–99] in 1920. This concept was designed for ideally brittle and isotropic materials and establishes an energy balance between the potential and surface energy. Later, this criterion was extended to include the work dissipated by plastic deformations to facilitate its use in other material classes and smaller sample dimensions as well [51]. Though, determining the plastically dissipated energy is challenging. For the material class in this thesis, plastic deformations were observed. Consequently, the energy balance concept is impractical for this kind of failure. Hence, the more suitable concepts, the stress-intensity, J-integral and crack tip opening displacement, are discussed in more detail.

3.1.1 Stress-Intensity

The stress-intensity concept considers the stress concentration arising around a loaded crack. For simplicity, the stress-state ahead the crack is modeled in two dimensions only and is expressed in polar coordinates. Thereby, the crack tip represents the coordinate origin. For a homogeneous isotropic linear elastic material, the stress tensor σ_{ij} describes the stress-field ahead of a crack and can be expressed by [97],

$$\sigma_{ij} = \frac{K}{\sqrt{2\pi r}} f_{ij}(\theta) + \sum_{m=0}^{\infty} A_m r^{\frac{m}{2}} g_{ij}(\theta), \tag{3.1}$$

with the constant K referred to as the stress intensity factor, the dimensionless function in the leading term f_{ij} and the polar coordinates r and θ. The indexes i and j represent the tensor coordinates in x-, y- and z-direction. The higher order terms are given by the order parameter m, the amplitude A and the dimensionless function g_{ij}. In the limit of $r \to 0$, these higher order terms approach a finite value, while the leading term is asymptotic, as illustrated for the yy-component in Figure 3.1 b).

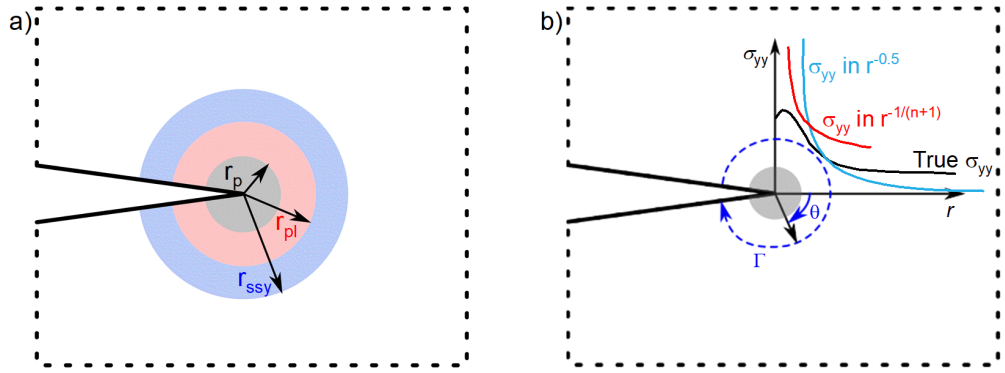

Figure 3.1: Schematic drawing of a cracked sample. a) Specific regions ahead of the crack, the processing zone r_p, the plastic zone r_{pl} and the small-scale yielding zone r_{ssy}, defining the validity of the different concepts used to characterize failure. b) True stress ahead of the crack including the stress models given by the stress-intensity concept (red) and the HRR-field (blue). The dashed blue line Γ represents the path-independent integral around the crack for the J-integral.

Therefore, the stresses in the crack vicinity are governed by the leading term and vary with $\frac{1}{\sqrt{r}}$. Hence, K can be considered as a loading parameter. The zone which is governed by the leading term of Equation 3.1 is called K-dominate zone, as illustrated by the blue shaded region in Figure 3.1 a). To ensure that this zone is large enough to govern the fracture processes, the ASTM Standard E399 defines a minimal sample geometry [100],

$$a, W - a, B \geq \frac{{K_{I,C}}^2}{\sigma_y}, \tag{3.2}$$

with the crack length a, sample height W, the ligament height $W - a$, sample thickness B, critical stress-intensity $K_{I,C}$ for mode I and the yield strength σ_y. Thereby, $K_{I,C}$ can be considered as a material parameter, defining the stress intensity a material can withstand without crack propagation, and is usually called fracture toughness. Even though dimensions of the sample adhered to the minimal requirements, the stress-intensity concept collapses inside the process zone. Moreover, realistic materials cannot withstand infinite stresses and exhibit plastic deformation above σ_y, limiting the stress ahead of the crack. Thus, in the plastic deformed zone the stress-intensity yields an incorrect stress. This gives a lower limit for the stress-intensity concept, which can be roughly approximated by plastic zone radius given the Irwin approach [97, 101],

$$r_p = \frac{1}{2\pi\alpha}\left(\frac{K_{I,C}}{\sigma_y}\right)^2, \tag{3.3}$$

where α is a constant, defining the stress state. In the case of plane stress $\alpha = 1$ while for plane strain $\alpha = 3$. The former dominates on the samples surface, while the plane strain condition governs the stress state inside the material. Usually, to characterize critical fracture parameters the sample thickness is selected so that the plane strain condition dominates failure. The samples investigated in this work were large enough to ensure that the plane strain condition governs the fracture process, unless this was studied on purpose.

3.1.2 *J*-Integral

Another commonly used concept to describe fracture is the J-integral, which is a path-independent line integral around the crack, see Figure 3.1 b). This path integral can be formulated by [97],

$$J = \int_\Gamma \left[\left(\int_0^{\varepsilon_{ij}} \sigma_{ij} d\varepsilon_{ij}\right) dy - \sigma_{ij} n_j \frac{\partial u_i}{\partial x} ds\right], \tag{3.4}$$

with the integration path Γ, the stress tensor σ_{ij}, the strain tensor ε_{ij}, the orthogonal vector with respect to the integration path n_j, the displacement vector u_i and the integration increment along the path ds. All terms of this equation are of the form $\sigma_{ij}\varepsilon_{ij}$. By considering a circular path with radius r, Equation 3.4 can be transformed into polar coordinates, resulting in a necessary singularity of $\frac{1}{r}$ for $\sigma_{ij}\varepsilon_{ij}$.This requirement is fulfilled by the stress-field outlined in the previous section with the corresponding strain field, as the strain and stress field have $\frac{1}{\sqrt{r}}$ singularity. Though, using these fields would result into a similar limitation for the J-integral as for the stress-intensity concept. However, the singularity requirement provide the possibility to chose different type of stress- and strain-fields which include hardening effects. These hardening effects result into a non-linear material behavior, which is frequently described by the Ramberg-Osgood hardening law [102]. Using this

hardening law and neglecting the linear elastic term, Hutchinson [103], Rice and Rosengren [104] were able to formulate the HRR-field, which models the stress- and strain-fields near the crack tip. The HRR-stress field is given by [97],

$$\sigma_{ij} = \sigma_y \left(\frac{EJ}{\alpha \sigma_y^2 I_N r} \right)^{\frac{1}{N+1}} \tilde{\sigma_{ij}}(N, \theta), \tag{3.5}$$

with the Young's modulus E, the constant J, the yield offset α and the hardening exponent N. The integration constant I_N and the dimensionless function $\tilde{\sigma_{ij}}$ depend on the hardening as well as on the assumed stress state.

Similarly to the stress-intensity concept, the J-integral characterizes the fracture as long as the HRR-field governs the failure process. For that the sample dimensions have to be larger than the plastic zone size. To ensure the dominance of the HRR-field, the ASTM E1820 standard defines minimal sample dimensions of [105],

$$a, W - a, B \geq 10 \frac{J_c}{\sigma_y}. \tag{3.6}$$

Although the HRR-field incorporates non-linear effects, there is also a lower validity limit for the stress-field. This limit is given by the processing zone, which is related to the crack tip opening displacement (δ) and can be approximated by 2δ.

3.1.3 Crack Tip Opening Displacement

Another fracture characterizing concept is the crack tip opening displacement (δ), which is related to the processing zone and represents a purely geometrical measure. Moreover, δ gives the capacity of a material to deform plastically, due to the direct relation to the processing zone. Shih [106] stated a frequently used method to determine δ. To measure δ, a symmetric rectangle with a 90° corner is placed at the current crack tip. The other corners of the triangle are given by the intersection between the crack flanks and triangle edges, whereby, the distance between these intersection points represent δ. An adoption of this measurement is illustrated in Figure 3.2, including the crack tip opening angle (α) measurement.

Loading of an initially sharp cracked sample leads to crack tip blunting. This is significantly influenced by the material behavior, whether it is ductile, semi-brittle or brittle. During blunting the sharp crack tip evolves to a rounded tip. For a homogeneous and elastic isotropic material blunting results in a circular shape, whereby δ is located at the initial crack tip position. The ASTM E1820 standard [105] defines the δ-measurement at the initial crack tip position throughout a fracture experiment. This definition is commonly used to

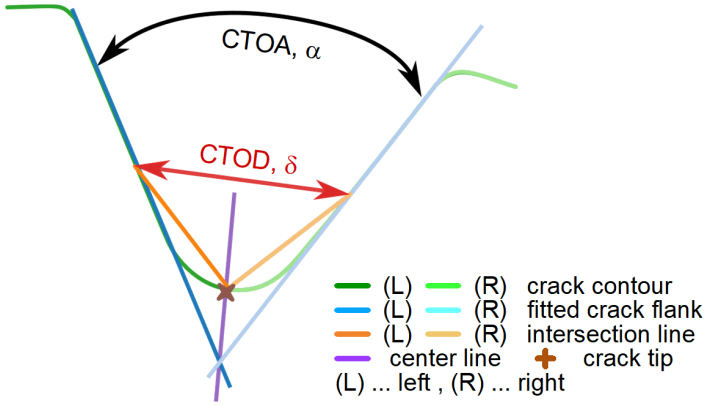

Figure 3.2: Schematic drawing of the fracture characteristic measurement: Crack tip opening displacement (δ) and -angle (α). Adopted from [60] under the CC BY Creative Common License 4.0.

measure δ from fracture experiments, due to the simpler experimental setup by using a fixed clamp at the macroscopic scale. Also the validity of δ as a material characteristic is limited and might exhibit a sample size dependency. To ensure the sample size independency of δ, the geometry of the sample has to fulfill [107],

$$a, W - a, B \geq 10\delta. \tag{3.7}$$

Despite this limitation, δ is a less restrictive measure to characterize fracture compared to the J-integral and stress-intensity concept. In the case of an isotropic material and a HRR-field dominance, δ can be transformed into the J-integral, as given by [106],

$$\delta = d\frac{J}{\sigma_y}, \tag{3.8}$$

with the Shih factor d, which depends on the assumed stress-state, hardening behavior, as well as the ratio between plasticity and elasticity of the material.

3.1.4 Practical Measurement of Fracture Characteristics

Continuous increase of device miniaturization necessitates material characterization at decreasingly smaller length scales. For this micro-mechanical testing was designed, allowing to test small sample dimensions at the micron to sub-micron scale. In general, three different loading types are frequently used at this length scale: tensile, compressive and bending. Due to the simplicity of fabrication and testing, micro-cantilever bending beams are the favored testing type [70]. In this thesis micro-cantilever bending beams were used to investigate the fracture characteristics. A representative cantilever is illustrated in Figure 1.1 b). To evaluate

these cantilevers usually elastic plastic fracture mechanics is used due to the size limitation. Moreover, due to the lack of standards for fracture experiments at the micron to sub-micron scale, the ASTM E1820 standard is frequently conducted as guideline and adopted to the requirements of micromechanics. Cantilever testing can be performed with different loading configurations, in particular static, quasi-static and dynamic loading. Whereby the former is of minor importance for fracture experiments, as it lacks the measurement of the stiffness which is used to split the area of the load-displacement curve into an elastic and plastic part. Measuring the current stiffness provides the possibility to approximate the crack length [59]. To provide stiffness data throughout the experiment, quasi-static loading was developed, which employs a simple loading scheme, consisting of several load cycles. Each cycle is divided in a loading, holding, partial unloading and holding phase, see in Figure 3.3 a). At each unloading, which should be elastic, the stiffness can be determined from the unloading slope. Nevertheless, this leads to sparse stiffness data due to the fixed number of load cycles. In the case of dynamic loading the stiffness is measured by superimposing the loading signal with a sinusoidal load of small amplitude, usually a few nm. This provides the possibility to assess the stiffness continuously throughout the experiment, as depicted in Figure 3.3 b).

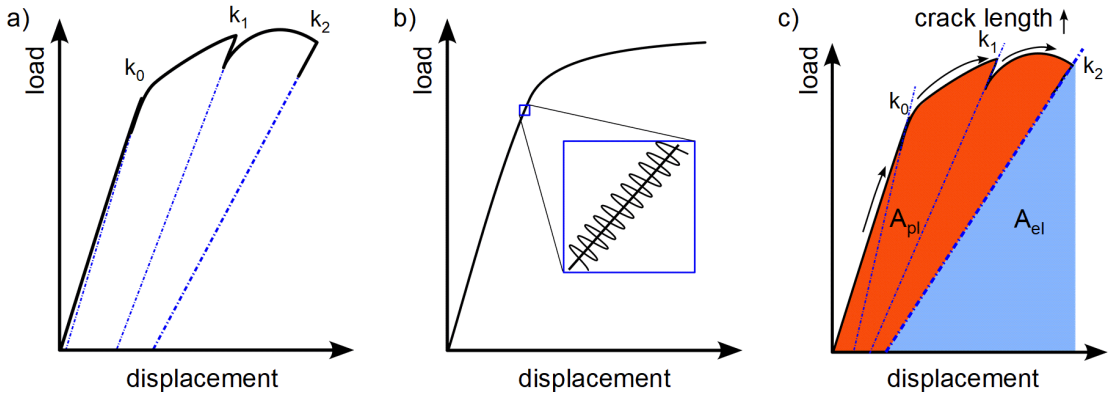

Figure 3.3: Theoretical load-displacement curves for different loading configurations used in micromechanics. a) Quasi-static loading with the stiffness measurement at each unloading step (dashed blue lines). b) Dynamic loading with continuous stiffness measurement with an inset depicting the additional sinusoidal load superimposed on the loading signal. c) Split of the load displacement curve into elastic (A_{el}) and plastic (A_{pl}) part. Taken from [108] under the CC BY Common Creative License 4.0.

For the evaluation, the recorded load-displacement curve is used. Thereby, the area below this curve represents the dissipated energy, which can be calculated by integration [105],

$$A_{tot} = \int_0^u F du, \tag{3.9}$$

with the load F and displacement u. This total area can be split in an elastic (A_{el}) and

plastic (A_{pl}) part, as illustrated in Figure 3.3 c). The split is calculated as follows [105],

$$A_{el} = \frac{F^2}{2k}, \tag{3.10}$$
$$A_{pl} = A_{tot} - A_{el}, \tag{3.11}$$

with the sample stiffness k, which is measured by either dynamic or quasi-static loading.

From A_{pl} the plastic part of the J-integral can be calculated. For that the ASTM E1820 standard defines an iterative procedure [105],

$$J_{pl,n} = (J_{pl,n-1} + \frac{\eta}{W - a_{n-1}} \frac{A_{pl,n} - A_{pl,n-1}}{B})(1 - \gamma \frac{a_n - a_{n-1}}{W - a_{n-1}}), \tag{3.12}$$

with the iteration index n and the size independent constants η and γ. These constants depend on the loading geometry. Due to the similarities between single edge bending beams and the cantilevers used in this thesis, these constants are $\eta = 1.9$ and $\gamma = 0.9$. The variables defining the cantilevers geometry are W, B and a, which are the cantilever height, -thickness and crack length, respectively. The elastic part of the J-integral is defined by the linear-elastic fracture mechanics [105],

$$J_{el} = \frac{K^2(1 - \nu^2)}{E} \tag{3.13}$$
$$K = \frac{FL}{BW^{\frac{3}{2}}} f(\frac{a}{W}) \tag{3.14}$$

with the Poisson ratio ν, the distance between crack and loading point L and the geometry factor $f(\frac{a}{W})$. The latter is determined by finite element analysis. For standard geometries the geometry factor is fitted and tabulated in literature for different $\frac{a}{W}$ ratios. The geometry factor used in this thesis was proposed by Riedl *et al.* and was designed for micro-cantilever bending beams [109, 110]. Finally, the sum over the elastic and plastic part gives the total J-integral,

$$J = J_{el} + J_{pl}. \tag{3.15}$$

In combination with the crack extension, the determined J-integral allows to construct the crack resistance curve (R-curve), an idealized representative curve is illustrated in Figure 3.4. The R-curve illustrates the materials resistance against crack growth during stable crack growth. From this curve a single J-integral value characterizing fracture can be determined. This value defines the transition from blunting to tearing regime [97], below it the load has to be increased to advance the crack, highlighted in Figure 3.4 by the gray shaded region. Above the crack growth would continue with a constant load, as illustrated in Figure 3.4. In the case that the sample fulfills all size requirements, this J-integral value represents

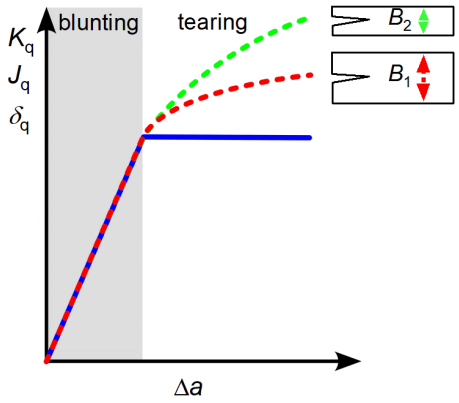

Figure 3.4: Idealized crack growth resistance curve (R-curve) for different material properties. The solid blue line illustrates the ideal brittle case, while the dashed curve represent semi-brittle or ductile failure behavior. Thereby, the green and red line depict the effect of an increasing sample size, schematically illustrated by the sample size B.

a critical material characteristic J_C, while else it is sample size dependent and referred to as conditional J_q. Decreasing the sample size blurs the transition between blunting and tearing, as with decreasing sample dimensions the tearing modulus increases [111], as illustrated by Figure 3.4. This occurs as less energy can be stored in the sample with decreasing dimensions. Thus, the energy available to advance the crack is reduced, resulting in a stabilization of crack propagation. The blurred transition from blunting to tearing complicates the extraction of fracture characteristics, especially in the case of micromechanics due to the small sample dimensions. Hence, the blunting regime is frequently determined from the *in situ* recorded images, which are correlated with the mechanical data to determine the fracture characterizing J-integral.

3.2 Image Processing

Image processing is a broad field in computer science and involves all kind of different operations applied to images. To facilitate a basic understanding for the techniques, the following section discusses the fundamental image processing techniques used in this thesis. More advanced methods are out of the scope for this thesis. To learn more about advanced methods the reader is referred to dedicated literatures [112–114]. Moreover, as image basis in this thesis, recorded *in situ* frames were used, which are a sequence of gray-scale images containing self similar image features for each experiment. In the following basic filter methods to enhance and suppress certain image features are discussed. Thereafter, classification methods are outlined.

3.2.1 Filter Methods

Image filtering plays a vital role in image processing, as it allows to suppress and enhance image features. The filters can be categorized in linear and non-linear, describing the relation between input and output. Both have a similar working principle, the filter slides over the image and applies a certain operation to a sub-area of the image. Non-linear filters are dependent on the pixels vicinity and define individual filter functions, *e.g.* median, maximum or minimum filtering. In the case of linear filtering, the weighted sum is calculated between image and the sliding filter mask. The latter is usually called kernel. This linear operation can be expressed as a convolution and is schematically illustrated in Figure 3.5 a).

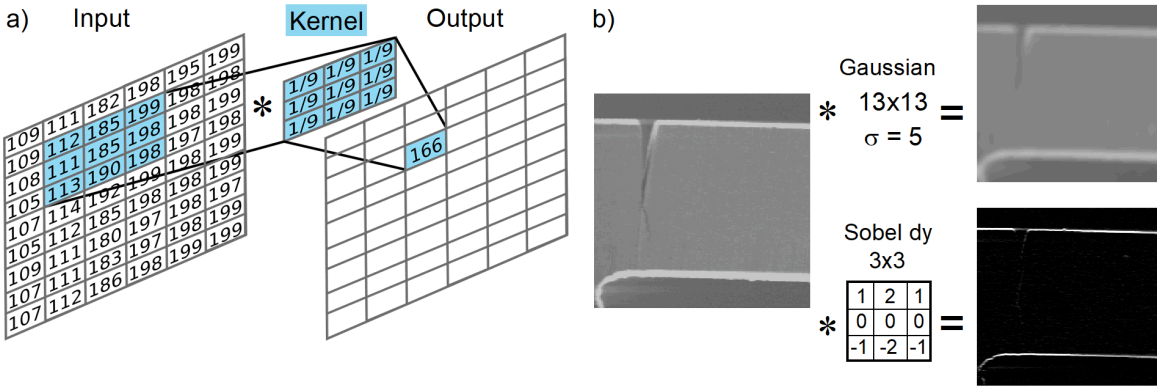

Figure 3.5: Image convolution. a) Schematic illustration of the image convolution operation. Thereby, the kernel slides over the input image and is multiplied with the respective subset, resulting into a single value in the output image. b) Application of different kernels to an *in situ* image, illustrating noise reduction by Gaussian blur and edge enhancement in y-direction by the Sobel kernel.

Mathematically, convolution is represented by a Fourier transformation of the image and kernel, multiplication in Fourier space, and back transformation of the result. Exchanging the kernel yields a different output, allowing to suppress and enhance certain image features. The former are noise reduction methods, *e.g.* Gaussian and mean filtering. Both represent a very basic level of noise reduction and remove noise at the cost of blurry edges. The application of a Gaussian kernel is illustrated in Figure 3.5 b). To enhance edges the image has to be convoluted with a derivative kernel. In a basic sense, it is the difference between the previous and the next pixel. Though, direct application of such a kernel is susceptible to image noise. A commonly used kernel to enhance edges is the Sobel operator, which is the joint application of Gaussian smoothing and a differentiation operation. Due to the joint application the Sobel operator is less susceptible to image noise, depicted in Figure 3.5 b) for the Sobel operator in y-direction.

Beside enhancing and suppressing image features, basic morphology transformations can be performed by convolution using a binary image and kernel. These basic transformations

are dilatation and erosion, which thicken and thin areas with true values, respectively. Combinations thereof allow to fill gaps and erode speckle noise from binary images. Moreover, by using an arbitrary kernel, a path can be structured according to the shape represented by the kernel.

3.2.2 Image Classification and Segmentation

Classification is defined as the labeling of image objects, whether these are single pixels or image parts. Segmentation divides an image into partitions to provide a simplified image representation for further image analysis. This is done by grouping pixels according to a certain characteristic or calculated property. The segmentation process can be categorized in traditional computer vision methods and artificial intelligence based approaches. In the following the focus will be on traditional methods, in particular Canny edge detection and an adapted histogram based method, as these were primarily used in this thesis. Once the image is segmented or classified, information can be extracted from the images for further analysis.

Canny edge detection is a popular method to extract edges from single images. As initial step the algorithm applies Gaussian filtering to suppress image noise, illustrated Figure 3.6 a). Thereafter, the edges are enhanced by a gradient based filter, *e.g.* Sobel, depicted in Figure 3.6 b). Two thresholds are applied to the resulting gradient image. Pixels with a value below both thresholds are neglected to prevent detection of spurious edges. The pixels having a value between the thresholds are considered as weak edges, while pixels above both thresholds are strong edges. If a weak edge is connected to a strong edge it is considered as an edge, otherwise it is omitted. This results in a binary image containing the edges as pixel thin paths, as shown in Figure 3.6 c), whereby the visibility of the edges was enhanced by a dilatation operation.

The histogram obtained from an image allows to segmented the image according to the pixel values. In the case of single image segmentation usually thresholds are utilized for this. To determine automatically a suitable threshold different algorithms exists, *e.g.* the Otsu [112] and the Li [115] threshold calculation techniques. Either way, the obtained image sequences allow to adapt the histogram based method to a probability based approach, allowing to classify subsequent images. Therefore, regions for each class are defined on an initial image, as shown in Figure 3.7 a). From these regions the histograms are determined and divided by the total pixel count of all regions, giving the probability for the individual classes with respect to the pixel values, depicted in Figure 3.7 b) and c). This allows to classify individual pixels and retrieve parts of the image.

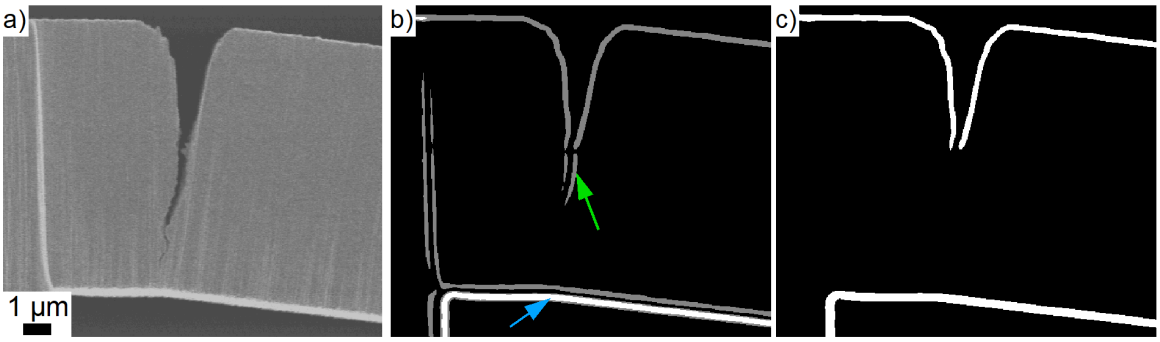

Figure 3.6: Steps of the Canny algorithm. a) Initially image smoothed by a Gaussian filtering. b) Edges obtained from the Sobel filter by calculating the absolute value from the gradients and applying the lower (weak edges, gray pixels) and upper threshold (strong edges, white pixels) marked by a green and blue arrow, respectively. c) Result from the Canny filtering operation. To enhance the visibility of the edges a dilatation operation was applied to the Canny result.

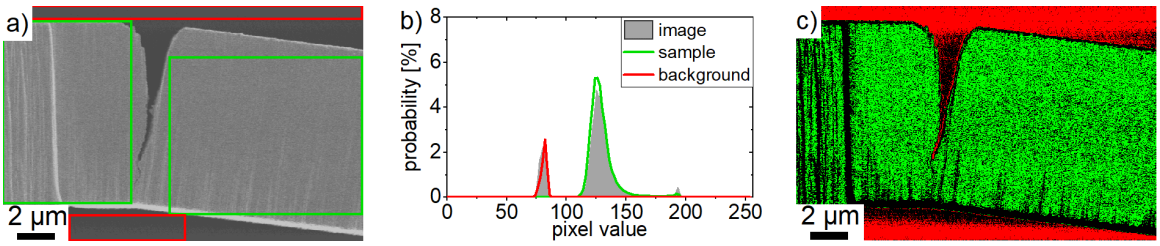

Figure 3.7: Histogram based pixel-wise classification process. a) Input image with the selected regions to calculate the histograms for each class. b) Determined histograms for each class. c) Probabilities for sample (green channel) and background (red channel) class retrieved by mapping the pixel values according to the class histograms.

4 Results and Discussion

This chapter summaries the results of this thesis, which are present in more detail in Publications A to D. First, the results of the investigated material properties are discussed. Thereafter, the highlights of the developed prototypes to extract the fracture characteristics from *in situ* acquired images are outlined.

4.1 Material Characterization

First, the influence of the deformation temperature on the resultant grain-size is discussed. Thereafter, the impact of the grain-size on the mechanical properties for the different compositions are outlined and related to the grain-size. Next, an analysis for the achieved sample density is given for the powder samples.

4.1.1 Impact of the Deformation Temperature on the Grain-Size

Adapting the HPT deformation temperature between RT and 550°C allowed to tailor the grain-size in the nanocrystalline regime. Independently from the deformation temperature, all samples exhibited a bi-modal microstructure, as visible in Figure 4.1 a) and b). These microstructures consisted of coarse tungsten grains embedded in a nanocrystalline matrix formed by tungsten and either copper or α-brass, respectively. Qualitative TEM and SEM analysis revealed an increasing matrix grain-size and an enlargement of the coarse tungsten grains with increasing temperature. To quantify the nanocrystalline matrix grain-size, TEM was used. Despite the different compositions a similar grain-size distribution was obtained for all RT samples, resulting in a mean grain-size of about 9 nm, see Figure 4.1 c). Though, at elevated temperatures, the different compositions exhibited a varying severity of grain refinement. In the case of bulk tungsten-copper samples, the deformation at 400°C lead to a grain-size increase of about 300% compared to RT. The samples fabricated from powders revealed a damped grain-size increase from RT to 400°C. Whereby the tungsten-α-brass composition exhibited the lowest grain-size enlargement, of only 22%. Thus, for this composition the deformation temperature was raised to 550°C, resulting in a grain-size increase of about 300% compared to RT, depicted in Figure 4.1 c). Besides the mean shift, the grain-size distribution significantly broadens for the samples deformed at elevated temperatures, visible by the errorbars in Figure 4.1 c). Details to the grain analysis can be

found for the bulk and powder compositions in Publication A and Publication B, respectively.

4.1.2 Effects of Grain-Size

Vickers hardness measurements along the HPT disk radius indicated higher hardness values for the powder composites. Thereby, the tungsten-α-brass composition exhibited the highest values, illustrated in Figure 4.1 c). The increased hardness values for the compositions produced from powders might occur due to possible powder degradation, *e.g.* oxides. Due to the high surface to volume ratio of powder particles, degradation thereof is hardly avoidable, despite the careful handling of the powders in argon atmosphere. These degradations may strengthen the fabricated material, leading to an increased hardness [24]. For the tungsten-α-brass composition the hardness was raised by about 12% compared to the tungsten-copper composite produced from powders. This increase can be attributed to the strengthened copper phase [116]. According to Chen [48] alloying copper with zinc to α-brass results into an approximately 30% higher hardness value for a micron sized grains. Accounting for the volume ratio of about 48% for copper and α-brass in the fabricated composites, the enhanced hardness of the tungsten-α-brass composition is in accordance with the hardness increase reported in literature. Relating the grain-sizes to the hardness indicates for the tungsten-copper compositions the commonly known Hall-Petch effect [25–27, 117]. Thereby, the grain-size increased from 9 nm at RT to 14 nm and 28 nm at 400°C for the powder and bulk fabrication route, respectively. In the case of the tungsten-α-brass composition, the grain-size exhibited a modest increase from 9 nm to 11 nm for the deformation temperatures RT to 400°C. This can be attributed to the harder α-brass phase, promoting a more pronounced refinement. In addition the grain refinement process is affected by residual elements, which lower the saturation grain-size at elevated temperatures [118]. Relating the hardness to the grain-size points to an inverse Hall-Petch, as the hardness increases with increasing grain-size, see Figure 4.1 c). In comparison literature reports the transition from normal to inverse Hall-Petch for a grain-size range of about 10 nm to 20 nm for copper and platinum [117, 119–122]. Moreover, increasing the deformation temperature to 550°C for the tungsten-α-brass compositions resulted into a grain-size of about 28 nm. This may occur as the brittle to ductile transition temperature of tungsten is about 200°C to 400°C, resulting in to a less severe grain-refinement of the tungsten grains above this temperature [21]. Furthermore, the hardness decreased between the 11 nm and 28 nm sample, indicating the normal Hall-Petch. Discussion regarding the hardness and grain-size measurements for the bulk and powder compositions can be found in Publication A and Publication B, respectively.

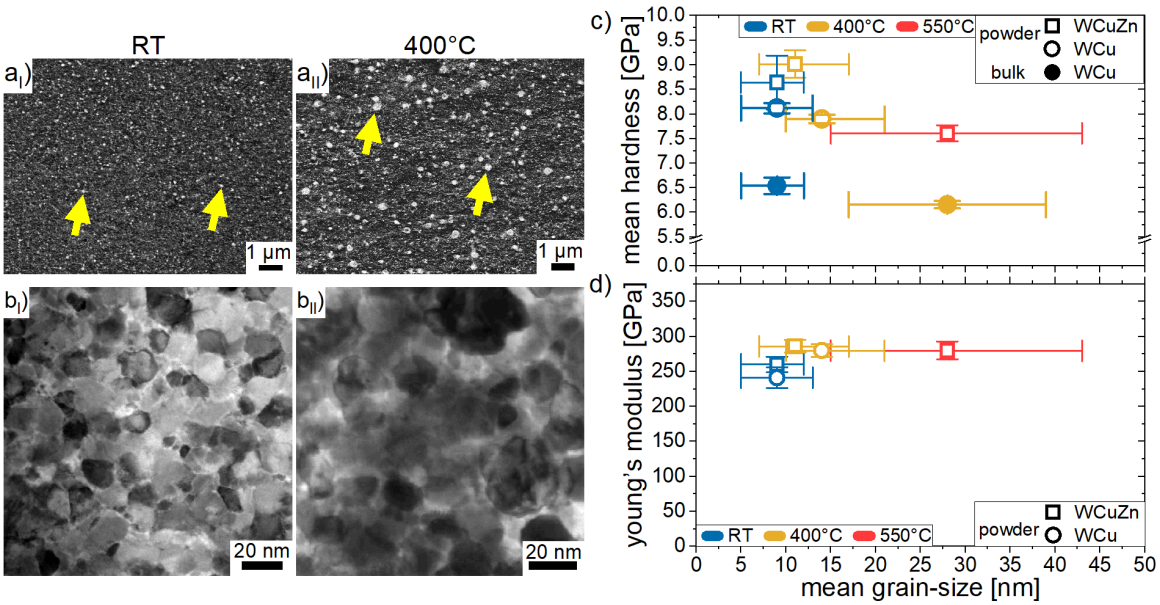

Figure 4.1: Representative micrographs of the tungsten-copper composition. a) Recorded microstructure by scanning electron microscopy illustrating the bi-modal microstructure with the yellow arrows pointing to coarse tungsten grains embedded in the nanocrystalline matrix. b) Transmission electron microscope recordings depicting the nanocrystalline matrix. c) Correlation of the hardness to the grain-size determined from the nanocrystalline matrix. d) Young's modulus measured by nanoindentation from the powder samples. Adopted from [58] under the CC BY Creative Common License 4.0.

4.1.3 Sample Density of the Powder Samples

To measure the Young's modulus, nanoindentation was performed at a HPT disk radius of about 3 mm. All Young's modulus values were within the boundaries given by the Voigt and Reuss model [123, 124]. Though, samples deformed at elevated temperature exhibited a higher Young's modulus compared to their RT counterparts, see Figure 4.1 d). This deviation can originate from multiple sources. One possibility is a variation of the material composition. As the material compositions of RT and elevated temperature were fabricated from the same powder, a possible influence from the material composition can be ruled out. Another source for a different Young's modulus can be a change in the deformation mechanism during nanoindentation, which would lead to a different pile-up, resulting in a change of the contact area [125]. This is backed by the observed inverse Hall-Petch behavior for the tungsten-α-brass composition, which arise from a change in the dominate deformation mechanism, from a dislocation based to a grain-boundary mediated mechanism [126–128]. Though, this assumption can be excluded, as SEM investigations of the nanoindentation indents revealed a similar pile-up among the different grain-sizes. A further possibility is a density variation [129, 130]. Qualitative approximation thereof based on the Young's modulus measurement revealed a density of about 90% and 99% for the RT and elevated

temperature samples, respectively. A porosity of 10% would be observable from the SEM micrographs. Nevertheless, no pores were detected from the recorded images. Possibly these pores are on the same order of magnitude as the nanocrystalline matrix and fine dispersed over the microstructure, making them undetectable by SEM. Another explanation for the decreased Young's modulus would be the raised grain boundary volume in nanocrystalline compounds [120, 131, 132]. Thereby, the RT samples with a grain-size of about 9 nm exhibit an increased grain-boundary volume compared to the other samples with a larger mean grain-size. In general, grain boundaries have a lower Young's modulus, thus the overall Young's modulus value decreases with decreasing grain-size. Either way, the reduced Young's modulus values are probably a combination resulting from a higher sample porosity and raised grain boundary volume. Publication B discusses these aspects in more detail.

4.2 Fracture Mechanical Characterization

The next section summarizes the major findings for the obtained fracture mechanical parameters, starting with the sample size effect on the J-integral (J_q), followed by a comparison between quasi-static and dynamic loading. At the end, the fracture mechanical response is characterized for the different investigated material compositions, including a compositional comparison to existing literature data.

4.2.1 Influence of Sample Size

The sample size in micro mechanics is of special concern, as for many materials, the plastic zone size is on the same order of magnitude as the sample size. To investigate a possible sample size effect, cantilevers from the bulk tungsten-copper composition with 20 wt.% copper were fabricated. For that, the cantilever cross-sections (BxW) were varied between (5x5) to (35x35) µm^2. The fracture mechanical evaluation revealed a decreasing J_q below a cantilever cross-section of (10x10) µm^2, depicted in Figure 4.2 a). To verify the fracture mechanical evaluation, δ was also measured from the *in situ* frames, exhibiting a similar trend, as illustrated in Figure 4.2 b). A similar observation was reported by Wurmshuber *et al.* [133] for a grain boundary doped tungsten alloy.Calculating the minimal sample dimension stated by the ASTM E1820 standard (Equation 3.6) with $\frac{a}{W} = 0.45$ would yield a required cross-section of about (3.5x3.5) µm^2. Though, approximating the plastic zone size by Equation 3.3 reveals that the plastic zone approaches the neutral axis for cantilevers with a cross-section below (10x10) µm^2. As a result, the evolution of the plastic zone starts to be inhibited by the compressive stresses past the neutral axis, changing the fracture behavior and decreasing J_q. Hence, in the case of bending experiments, the distance to the neutral axis should be considered as minimal size constraint.

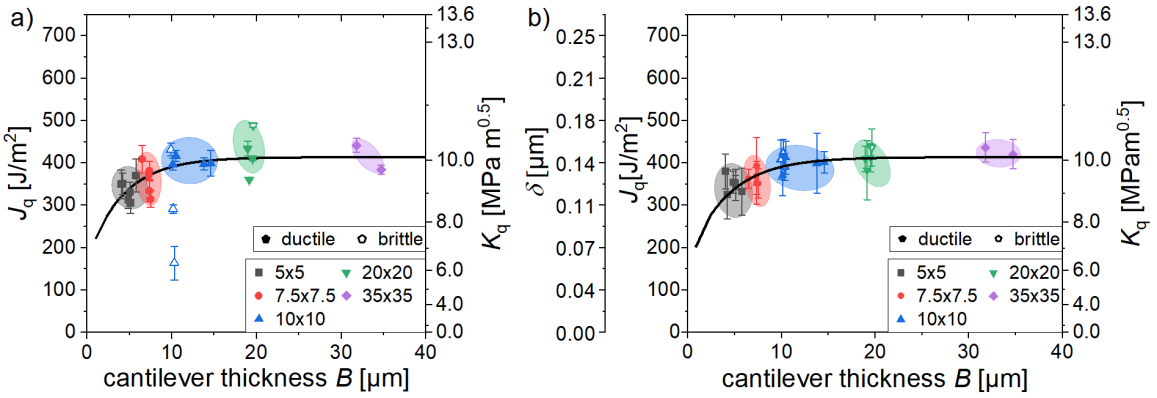

Figure 4.2: Fracture characteristics measured from differently sized cantilevers with an approximately square cross-section. a) J_q evaluated from the recorded load-displacement curves by elastic-plastic fracture mechanics. b) δ measured from the *in situ* recorded images. Taken from [108] under the CC BY Creative Common License 4.0.

Moreover, the sample size has also implications on the R-curve. In general, cantilevers can exhibit different fracture types, in particular brittle, semi-brittle and ductile, illustrated in Figure 1.2. Constructing the R-curve for brittle fracture results in a curve comparable to the ideal brittle R-curve shape, see the dashed line in Figure 4.3. For semi-brittle and ductile failure the R-curve deviates from the ideal form, as the sharp transition from blunting to tearing rounds off, especially in micro-mechanics. This makes localizing the transition point more challenging, and therefore the determination of the fracture characteristic value J_q. Moreover, decreasing the sample dimensions increases the slope in the tearing regime, visible in Figure 4.3. The slope change of the tearing modulus occurs as it is indirectly proportional to the sample size [111]. Hence, determining the transition point by fitting the tearing and blunting regime is increasingly challenging, as small deviations significantly impact the result. However, the *in situ* acquired images provide the possibility to determine the blunting and tearing regime. Correlating these images with the mechanical data allows to identify the transition point from blunting to tearing on the R-curve. This allows to assess the fracture characteristics from the R-curve. Further details about the sample size effect and the tearing slope change are given in Publication A.

4.2.2 Quasi-Static vs. Dynamic Loading

The fracture experiments conducted in this thesis utilized either quasi-static or dynamic loading. Applying these loading conditions to the same material revealed a systematic offset of the J_q between the loading conditions, depicted in Figure 4.4 a). In particular, J_q is increased for the quasi-static loading condition. This can be attributed to the sequential elastic unloading steps. During unloading, stresses within the plastic zone are relieved, leading to compressive stresses in the plastic zone and the formation of a cyclic plastic zone.

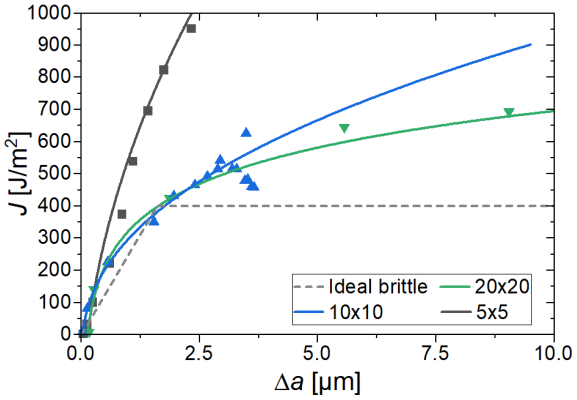

Figure 4.3: Measured crack resistance curves (R-curve) for differently sized cantilevers, including the ideal brittle curve for illustrative purpose.Adopted from [108] under the CC BY Common Creative License 4.0.

Upon reloading, these stresses effectively reduce the applied stress. Thus, the material can withstand a slightly enhanced load, impacting J_q. This is backed by the reduce J_q values for cantilevers that failed before the first unloading step, see Figure 4.4 a). Therefore, the analysis revealed a significant impact of the measurement procedure. A similar result was found by Ast *et al.* [134] for a quasi-statically loaded cantilever fabricated from a nickle-aluminum single crystal. They observed a reduced dislocation density during the partial unloadings, indicating plastic recovery. Thus for a better comparison of micro-mechanical experiments, the same setup should be used to avoid systematic errors. Thus, it would be beneficial to standardize this test method to enhance the comparability between different materials and the results obtained from various researches. The formation of the cyclic plastic zone is prevented by the dynamic loading due to the small amplitude of a few nm. Further insights into the systematic offset are given in Publication B.

4.2.3 Fracture Mechanical Response

The tungsten-copper samples fabricated from elemental powder exhibited a slightly decreasing J_q with an increasing grain-size from 9 nm to 14 nm, see Figure 4.4 b). This is counter intuitive, as larger grains are able to accommodate more dislocations and, in the case of intercrystalline failure, the fracture path would increase significantly. This decline may stem from a possible change in the deformation mechanism, which was also observed by hardness and Young's modulus measurements, as discussed above. Due to the grain-size of a few nm, grain boundary mediated deformation is plausible as a dominate deformation mechanism [126–128]. This would be negatively impacted by enlarging the grains. A similar result was found for the tungsten-α-brass composite, as by slightly increasing the grain-size from 9 nm to 11 nm, J_q declined. Thereby, the direct comparison between tungsten-copper

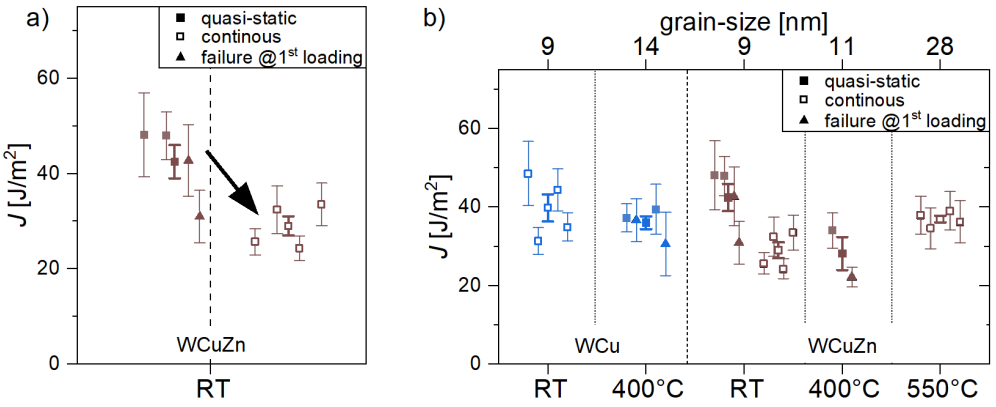

Figure 4.4: J_q determined by elastic-plastic fracture mechanics for the material compositions tungsten-copper and tungsten-α-brass produced from powders, using quasi-static and dynamic loading. a) Deviation between the quasi-static and dynamic loading condition. b) Grain-size influence on J_q for the tungsten-copper and tungsten-α-brass material composition. Adopted from [58] under the CC BY Creative Common License.

and tungsten-α-brass composition indicated a negligible impact of the zinc addition on J_q. Further, raising the grain-size up to 28 nm reversed the trend and J_q increased above the 9 nm sample, see Figure 4.4 b). Due to the grain-size the deformation mechanism of this sample tends to be governed by a dislocation based mechanism. Literature reports a deformation mechanism change for a grain-size of about 30 nm for bcc materials, such as tungsten [135]. Though, the deformation will be localized in the softer copper phase which has a fcc crystal structure. For this crystal structures, literature states a grain-size of about 10 nm for the transition from grain-boundary mediated to dislocation based deformation mechanism [126]. The grain-size exhibited by the composites investigated in this work are close to the deformation transition grain-size. Thus, a change of the deformation mechanism can be expected. This also relates to the reduced grain-boundary volume from a grain-size of 10 nm to 28 nm, as discussed above. Beside the deformation mechanism change, the grain-size of 28 nm is closer to the ideal grain-size for an extensive twinning tendency. According to literature, the ideal grain-size for twinning in α-brass is at about 40 nm [81, 82]. Hence, the enhanced J_q might be partially attributed to twinning. Though, due to the small grain-size a direct observation of twins is challenging. Detailed information to J_q variation for the powder samples can be found in Publication B.

Fracture mechanical testing of the tungsten-copper nano-composite refined from a bulk revealed a significantly increased J_q for the sample with a grain-size of 9 nm compared to the 28 nm sample, see Figure 4.2 and Figure 4.5. This enhanced J_q can be attributed to the shape developed by the coarse tungsten grains for the sample with a grain-size of 9 nm. The coarse tungsten grains formed a plate-like shape promoting a delamination-like structure, which divides the cross-section into smaller segments. These segments affect the

triaxial stress-state in front of the crack and raises J_q [136, 137]. For the 28 nm sample these coarse tungsten grains were spherical, leading to an isotropic material behavior and negligible impact on J_q. These results are discussed in greater detail in Publication A.

Comparison of the powder and bulk processing route reveals a negative impact on J_q for the powder samples. This might stem from possible degradation of the powder, as discussed above. Another possibility are the enhanced interconnections between tungsten grains for the bulk samples due to sintering, which may benefit the grain-boundary strength. In literature the fracture toughness (K_q) is frequently used to characterize failure, thus, to relate the determined J_q values to literature they were transformed into K_q. In Figure 4.5 a), K_q is related to the grain-size for the investigated material compositions. Additionally, this figure includes literature data from tungsten and tungsten-copper based composites to set the derived K_q values of this thesis in context [21, 41, 58, 90, 108, 133, 138–149]. Considering pure tungsten, a declining trend for K_q with a decreasing grain-size is observable from the coarse grained to the nanocrystalline regime. Thereby, K_q in the nanocrystalline regime was determined from sputtered tungsten [140], while all others were measured from a sintered tungsten bulk material [21, 90, 142–144, 147, 148]. Despite the declining trend in ultra-fine grained regime, a promising K_q increase was reported in literature at the transition from the ultra-fine grained to nanocrystalline regime [133]. Contrarily, for tungsten-copper composites the data is rather sparse. For these composites, K_q is increased in the coarse-grained regime and is completely lacking for ultra-fine grained microstructures, making a trend unidentifiable. Either way, in the nanocrystalline regime K_q first declines with decreasing grain-size similar as for tungsten from the coarse to ultra-fine grained regime. This trend persists to a grain-size of approximately 11 to 15 nm. Further grain refinement reverses the trend and K_q increases. This might stem from a change in deformation mechanism from a dislocation to grain boundary based mechanism [126–128]. More on this topic can be found in Publication B. Anyways, the damage tolerance of a material depends on K_q and the materials strength. Thereby, the product of both gives a possible metric for the damage tolerance [150]. For the investigated material compositions in this work, the damage tolerance is depicted in Figure 4.5 b), with the ideal material approaching the top right corner. The investigated powder compositions yielded a similar damage tolerance as pure nanocrystalline tungsten, despite the slightly enhanced K_q. The bulk samples, on the other hand, exhibited an enhanced damage tolerance compared to the powder samples and pure tungsten in the nanocrystalline regime. This difference can be attributed to the sintering of the bulk samples in a reducing atmosphere to remove volatile degradations and oxides from the composite. Moreover, to highlight the influence of copper on the damage tolerance of tungsten-copper compositions, available literature data points from pure tungsten, copper and their compositions in the nanocrystalline regime are shown in Figure 4.5 b). For the pure elements copper and tungsten in the nanocrystalline regime literature reports an almost

similar K_q, as illustrated in Figure 4.5 b). By intermixing the two elements K_q is enhanced, by retaining the strength at a higher level, benefiting the damage tolerance. More on this can be found in Publication A.

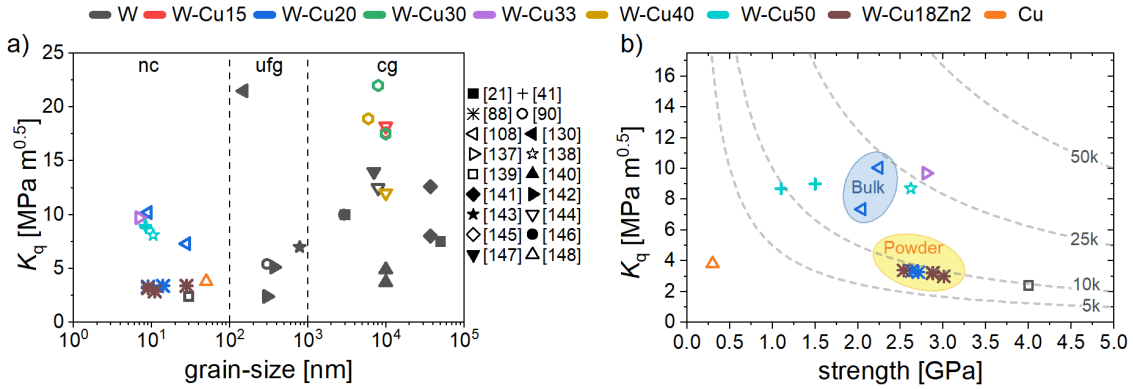

Figure 4.5: Comparison of the determined K_q values to similar composites found in literature, in particular tungsten, tungsten-copper, tungsten-α-brass and copper composites [21, 41, 58, 90, 108, 133, 138–149]. a) Relation of the grain-size to K_q across several magnitudes from nanocrystalline (nc) over ultra-fine grained (ufg) to coarse-grained (cg). b) Damage tolerance of the different compositions in the nanocrystalline regime. Adopted from [108] and [58] under the CC BY Common Creative License 4.0.

4.3 Image Processing

Beside the recorded mechanical data, the acquired *in situ* images from the fracture experiments can be used as additional high fidelity data stream to characterize failure. The images provide the possibility to measure the crack length, crack tip opening displacement (δ) and -angle (α). Though, to follow crack propagation high image acquisition rates are necessary. These rates affect the image quality, thus the acquired *in situ* images are noisy in general, as illustrated in Figure 1.1. Typically, the image acquisition rate is about 1 image/second to balance image quality and temporally resolve crack growth.

A commonly used method in material science is DIC, which tracks image changes by correlating consecutive images and translates them into sample deformations. For that a self-similar surface structure has to be observable from the recorded images. Usually, to enhance the structural recognition between frames, an artificial random pattern is applied to the surface. Nevertheless, DIC necessitates a high image resolution to detect the pattern and distinguish it from noise. Commonly used image acquisition rates for DIC are below 1 image/minute to provide detection of sub-pixel sized changes [65, 68–70]. Thus, DIC is unfeasible to capture continuous crack growth, which requires high image acquisition rates [70]. Several adapts were undertaken to enhance the acquisition rate for DIC [151], but these sacrificed the resolution of DIC, allowing to track only micron-sized changes. This

leads to the inability to determine the crack shape and -length in sufficient accuracy. Thus, DIC is inapplicable to determine fracture characteristics from *in situ* experiments performed in this thesis, as higher image acquisition rates were employed to monitor crack growth and the investigated cantilevers had an ion polished surface.

Another popular approach nowadays is CNN to classify images. The training from scratch necessitates a large amount of data to prevent the network from memorizing the training data, called over-fitting [152]. Moreover, the data should be as diverse as possible to achieve a good generalization of the classification process. However, the required amount of data can be reduced by transfer-learning using pre-trained CNN, *e.g. U-net* [153, 154] and *Segement Anything* [155, 156]. Still, this training requires thousands of different images to prevent over-fitting and to obtain reasonable results in general. *In situ* experiments yield a few hundred images, which are reasonable similar to each other, which would favor over-fitting. Hence, only a small amount of the acquired images can be considered for the training of CNN's. Additionally, a suitable loss-function is necessary, which penalizes miss-classifications. In the case of crack shape extraction, a single pixel mis-classification at the crack tip is undesirable, necessitating the design of a local loss function to solve this individual issue. Therefore, the application of CNN seems to be impractical to extract the crack shape.

To develop an algorithm allowing to extract the fracture characteristics from *in situ* acquired images, traditional image processing techniques were used in this thesis. For that a consistent magnification and crack growth direction across all acquired images was assumed. All other images that do not meet these requirements are omitted. At first a semi-automatic prototype was developed to track the crack tip throughout the experiments from *in situ* images, as representative illustrated in Figure 4.6 a). To track the crack tip, the user defines filter-sets allowing to detect the crack edges. These included suppressing of image noise, enhancing edges and detection thereof by the Canny algorithm. Additionally, the user defines the crack edge that includes the crack tip. This allows to locate this crack edge on subsequent images by calculating the Euclidean distance between the user defined crack edge and the crack edges extracted on subsequent images. The edge with the minimal distance is then the crack edge on the next image. To locate the crack tip on this edge a top-down crack growth direction is assumed for all images, defining the lowest point on the crack edge as crack tip. Moreover, to determine the crack length, the user defines an initial point on the top surface of the sample, see Figure 4.6 b). The Euclidean distance between this point and the crack tip gives the crack length. To verify the algorithms output, several frames of representative experiments were evaluated manually, revealing a good agreement between manual measurement and the results from the algorithm. Moreover, the evaluated crack lengths were in accordance with the crack lengths determined from mechanical data, by considering possible surface effects. Further information to this first prototype to extract

crack lengths from *in situ* images can be found in Publication C.

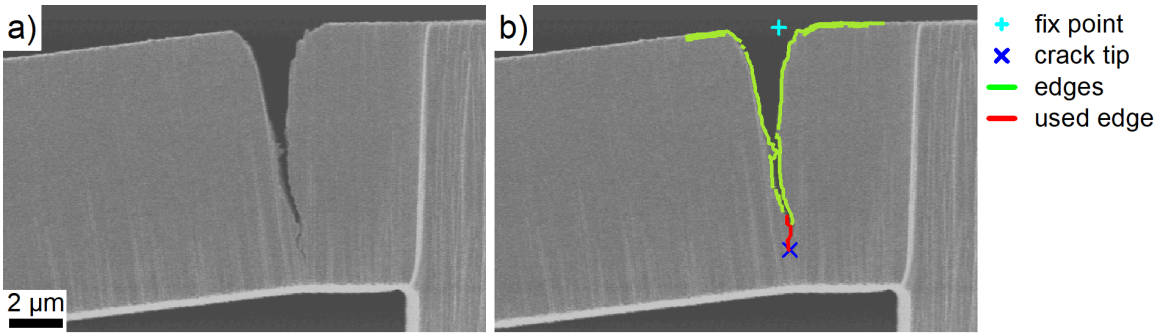

Figure 4.6: Representative *in situ* image used to track the crack tip throughout the experiment. a) Initial recorded frame. b) Detected edges by the first prototype with the crack edge used to follow crack propagation.

The prototype was further developed to extract additional fracture characteristics, such as δ and α. These characteristics necessitate the localization of both crack flanks. Despite, the possibility to extract edges, the application of the first prototype was limited, as this approach resulted into fragmented edges, highlighted in Figure 4.6 b). Moreover, to measure δ and α the crack flanks have to be separable, which is not ensured by the first prototype. Depending on the fracture type, separation of the crack flanks is rather challenging, as the pixel size limits the resolution necessary to distinguish the crack flanks and locate the crack tip. Especially, as at the crack tip, crack flanks are close to each other and frequently separated by a few pixels only, depicted Figure 4.7. Moreover, different features arise on the images during crack growth, making the crack shape extraction more challenging. These features are schematically illustrated in Figure 1.2. In Figure 4.7 these features are visualized on an *in situ* images recorded during semi-brittle failure of a representative cantilever. On the first frame the initially sharp crack is observable, which is followed by extensive blunting and pore formation, leading to material bridges. After crack initiation, the material tears and connects the pores. This leaves behind thin material obstacles within the crack path, increasing the challenge to detect the total crack shape.

To tackle the issue of discontinuous crack flanks, the classification process was further enhanced to provide two separate continuous crack flanks. This was achieved by employing a probabilistic-like pixel-wise classification procedure. For that the user defines two regions on an initial frame: One is representative for the sample and the other for the background class. These regions were used to determine a histogram, defining the probability whether a pixel belongs to sample or background class, as described in the chapter 2. In combination with the automatically calculated edge information, this enabled the algorithm to extract the complete crack shape, as illustrated by a representative *in situ* image in Figure 4.8a). These flanks are naturally jagged, thus, they are linearly fitted to obtain a single intersection

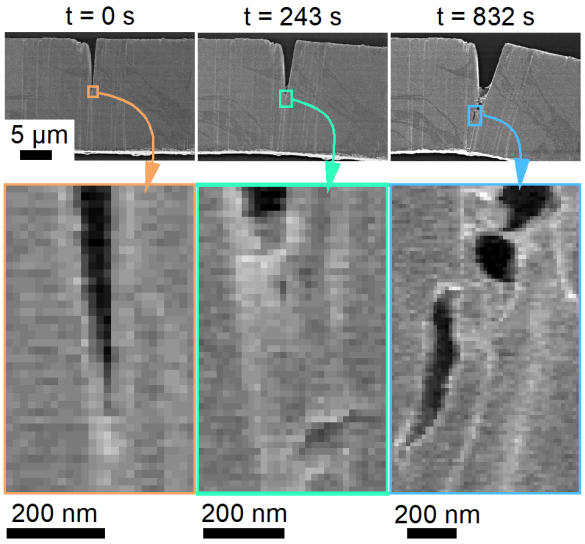

Figure 4.7: Challenges to detect the crack shape from *in situ* images.

point. The determined crack flanks and fit procedure is illustrated in Figure 4.8 b). To verify the algorithms performance several images of various experiments were evaluated manually. Thereby, the fracture behavior of these ranged from brittle over semi-brittle to ductile failure. Comparing manual and algorithmic results confirmed that they are in good agreement. Moreover, the error of manual and algorithmic measurement was on the same order of magnitude, indicating the potential of the algorithm to evaluate *in situ* experiments. Additionally, the algorithmic evaluation provides the possibility to extract the fracture characteristics of all frames in a reasonable time. Besides the additional evaluated fracture characteristics, also the necessary user-input was significantly reduced compared to the first prototype, resulting in a more automatic evaluation. Details to the more automatic algorithm and its performance can be found in Publication D.

Further, the prototype evaluates the fracture characteristics locally at the crack tip, while the ASTM E1820 standard defines them at the initial crack tip position. Within the blunting regime, the local measurement meets the ASTM E1820 definition, as depicted by Figure 4.8 c). Though, after blunting the crack begins to grow and the crack extends further into the material. As a result, the processing zone shifts with the crack tip and the direct relation between δ defined by the standard and the processing zone is diminished. However, measuring δ locally at the crack tip maintains this relation, as shown in Figure 4.8 c). Moreover, the combined extraction of crack length and fracture characteristics allows to directly construct the R-curve, as representative illustrated in Figure 4.9 for a semi-brittle fractured sample. From the R-curve, the typical shape is observable within the blunting regime. Above that, the R-curve deviates from the typical shape due to the local measurement of δ at the crack

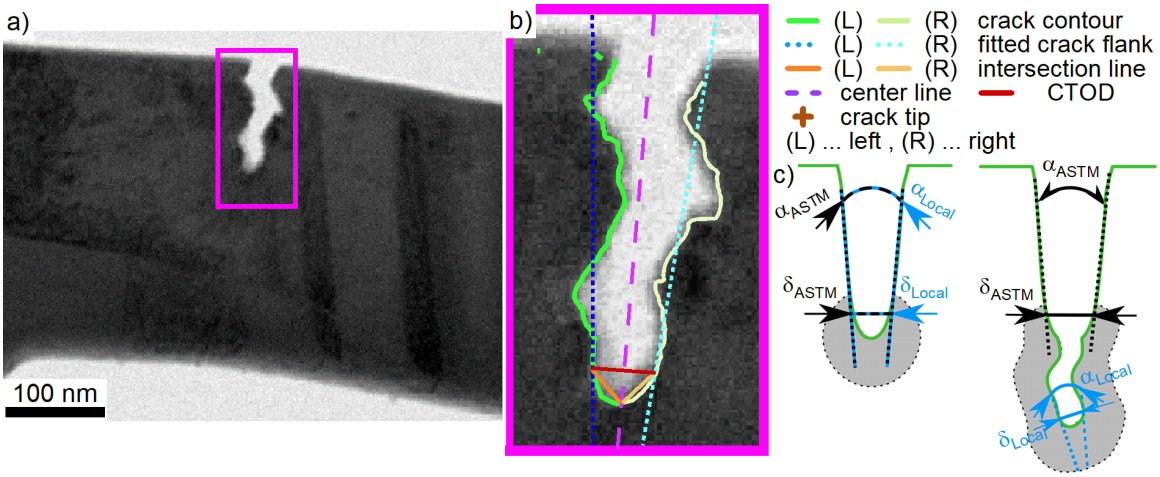

Figure 4.8: Measurement of fracture characteristics from an *in situ* image. a) Recorded *in situ* image by transmission electron microscopy. b) Detail of a) with the found continuous crack flanks, including the linear fitting lines and the measurement lines performed by the algorithm. c) Comparison between the global defined measurement by the ASTM E1820 standard and the local determination performed by the second prototype. Adopted from [60] under the CC BY Creative Common License 4.0.

tip. Though, local determination benefits the understanding of ongoing fracture processes and provides a deeper insight into fracture processes on the micron to sub-micron scale, as the relation between δ and the processing zone persists. Additionally, the local evaluation provides the possibility to directly relate the fracture characteristics to the microstructure utilizing the crack path information. Further details regarding the beneficial aspects of the local evaluation are discussed in Publication D.

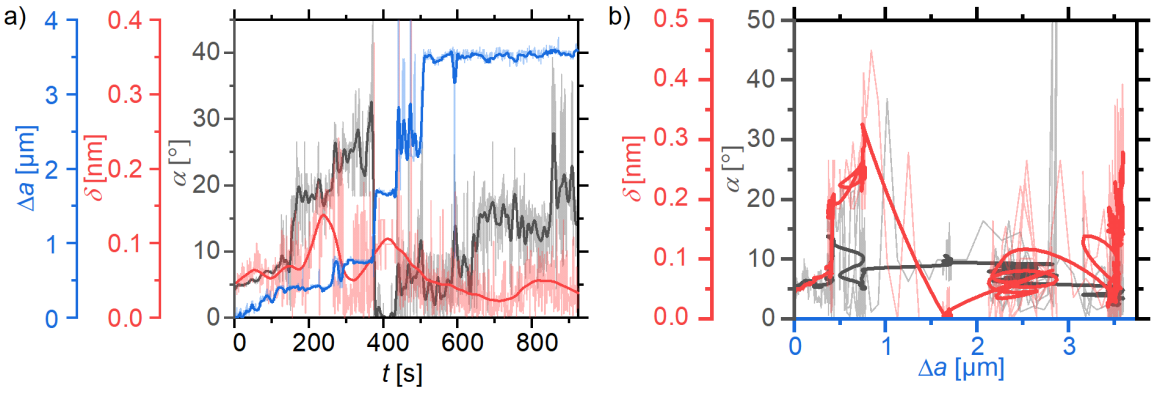

Figure 4.9: Representative evaluation of the fracture characteristics by the second prototype. a) Directly measured fracture characteristics over time. b) Crack resistance curve (R-curve) constructed from the measured fracture characteristics.

5 Summary and Conclusion

This thesis focused on the fabrication of nanocrystalline tungsten-copper and tungsten-α-brass composites with 20 wt.% of either copper or α-brass that were produced from either bulk or elemental powders.

To refine the grains down to the nanocrystalline regime, high-pressure torsion was used. Adjusting the deformation temperature between RT and 550°C allowed to tailor the grain-size within this regime. Thereby, the deformation temperature was limited by the high-pressure torsion setup, in particular the anvils strength at elevated temperature. Although the deformation was performed up to microstructural saturation, a bi-modal microstructure was obtained. This structure consisted of coarse tungsten grains with several 10 nm in size embedded in a nanocrystalline matrix. Quantifying the latter revealed a grain-size ranging from about 9 nm to 28 nm, which is below the ideal grain-size for an enhanced twinning tendency. Thereby, the grain-size of the bulk composition exhibited an enhanced deformation temperature dependency. This might be related to possible powder degradation, such as oxides or residual elements, which affect the refinement process. Moreover, the samples fabricated from elemental powders exhibited a higher hardness compared those refined from bulk. Relating the hardness to the grain-size indicated for the tungsten-copper compositions the common Hall-Petch behavior, while for the tungsten-α-brass composition the inverse behavior was observed.

In the case of the samples produced from elemental powders, the sample density was qualitatively estimated from Young's modulus measurements. These indicated an comparable sample density to traditional sintering methods above 90%. Comparison among the different deformation temperatures revealed an enhanced Young's modulus for the elevated temperatures, which partially stems from a higher density and reduced grain-boundary volume.

Moreover, to characterize the fracture behavior of the produced samples, micro-cantilever bending was employed. Different loading schemes can be applied to test micro-cantilever bending beams, in particular quasi-static and dynamic loading. Both schemes were applied to a set of cantilevers to investigate the possible influence of partial unloading steps. The evaluation revealed increased fracture toughness values for the quasi-static loading. This systematic offset might stem from the formation of a cyclic plastic zone during the partial unloading steps.

To analyze possible sample size influences on the fracture behavior and the evaluation thereof, a variation of cantilever cross-sections was fabricated from the bulk tungsten-copper samples. The fracture mechanical evaluation indicated a sample size dependency for cantilevers with a cross-section below (10x10) μm^2. A similar result was obtained from the crack tip opening displacements. This occurs as the plastic zone size approaches the neutral axis and the plastic zone formation is thus inhibited by the compressive stresses in the sample. Moreover, construction of the R-curve revealed an increasing tearing modulus with decreasing sample volume, which is related to the reduced energy storage capabilities for smaller volumes. Thus, special attention should be payed by comparing different cantilever sizes.

All tested cantilevers exhibited inter-crystalline failure. Despite this similarity, an increased fracture toughness was evaluated for the bulk tungsten-copper samples of 10 MPa$\sqrt{\text{m}}$ and 7.4 MPa$\sqrt{\text{m}}$ for the RT and 400°C sample, respectively. The enhanced fracture toughness of the RT sample can be attributed to the lamellar coarse tungsten grains present in the microstructure. In comparison all powder samples exhibited a fracture toughness of about 3 MPa$\sqrt{\text{m}}$. As for all of them similar fracture toughness values were obtained, this points to possible degradation of the powder, *e.g.* by oxides. A possibility to reduce this degradation is to sinter the composites in a reducing atmosphere. Although the fracture toughness was reduced, the material strength was raised by the powder samples, which contributes to the overall damage tolerance.

Beside the mechanical material investigations, the *in situ* acquired images were used to extract fracture characteristics. For that traditional image correlation techniques were used, instead of digital image processing and neural networks. The former was not applicable due to the necessary detectable self-similar structures on the sample surface, while the latter necessitates a vast amount of significantly different data, which were not available. An initial prototype was developed, allowing to track the crack tip and therefore measure crack growth. Comparison with manual measured and mechanical estimated crack lengths revealed a good agreement between those. This prototype was further extended to enable an automatic extraction of the crack tip opening displacement and -angle. The algorithm was tested on several fracture experiments exhibiting a fracture behavior ranging from brittle over semi-brittle to ductile. To verify the algorithms performance, it was again compared to manual measurements revealing similar results. Moreover, the fracture characteristics are evaluated locally at the crack tip by the algorithm, which provides deeper insights into the fundamental fracture and failure processes on the micro- and nano-scale.

6 Outlook

The tungsten-copper composites can be seen as a model material for immiscible bcc and fcc composites. For such systems, high-pressure torsion is a precious tool to combine these materials into a bulk form. The insights of this work can be used as a starting point for other material compositions. However, high-pressure torsion is strongly related to the material properties. Therefore, further investigations are necessary for a defined material output, e.g. the saturation grain size depends on the strength of the material, which is affected by the deformation temperature.

Fracture mechanical evaluation has shown that nanocrystalline tungsten-copper composites exhibit a lower fracture toughness compared to their coarse grained counter parts. Though, the material strength was significantly enhanced. To achieve a balance between the beneficial properties of nanocrystalline composites with respect to irradiation damage and the higher damage tolerance of coarse grained composites, ultra-fine grained composites could represent a good compromise. However, in the ultra-fine grained regime literature lacks data for fracture toughness. To fill the gap, ultra-fine grained tungsten-copper composites would be necessary, which are hardly producible by high-pressure torsion. Though, these grain-sizes might be producible by other severe plastic deformation techniques which have a less severe grain refinement. Another possibility would be a bottom-up approach, by refining powders to the ultra-fine grained regime and sinter these powders in an reducing atmosphere. Furthermore, due to the inter-crystalline fracture, the fracture toughness would benefit from grain boundary strengthening by adding doping elements during the fabrication process.

The automatic *in situ* image evaluation has great potential, although it allows only to analyze the crack visible on the sample surface. This is especially the case for complex fracture processes where mechanical evaluation is impractical. These involve heterogeneous material structures, anisotropic properties and high blunting tendency. Either way, the prototype developed in this thesis would benefit from an improved imaging and classification process. The former has a direct impact on any image base evaluation technique. Although, as the electron microscope imaging techniques have matured already, the imaging process is expected to improve less significantly. However, more sophisticated methods, such as convolutional neural networks, would enhance the classification process. These methods necessitates a vast amount of well structured training data, which is hardly available. Though, the continuous collection of *in situ* images would enable this in future.

7 Publications

The following publications are part of this thesis.

7.1 List of Publications

Publication A:
K. Schmuck, M. Burtscher, M. Alfreider, M. Wurmshuber, D. Kiener
Micro-mechanical fracture investigations on grain size tailored tungsten-copper nano-composites
JOM 76, 2302-2314, (**2024**), doi: 10.1007/s11837-023-06348-7

Publication B:
K. Schmuck, M. Burtscher, M. Alfreider, D. Kiener
Assessing the Fracture Toughness in Tungsten-Based Nanocomposites: A Micro-Mechanical Approach
Materials and Design, (**2024**), under review

Publication C:
K. Schmuck, M. Alfreider, D. Kiener
Crack length estimations for small scale fracture experiments via image processing techniques
Journal of Materials Research 37, 2848–2861, (**2022**), doi: 10.1557/s43578-022-00681-4

Publication D:
K. Schmuck, M. Antenreiter, M. Alfreider, D. Kiener
Automatic and time-resolved determination of fracture characteristics from in situ experiments
Materials and Design 243, 113038, (**2024**), doi: 10.1016/j.matdes.2024.113038

7.2 Contribution to Publications

The main concepts of the four publications listed above were prepared in collaboration with D. Kiener and M. Alfreider. For these publications, the experimental data acquisition, analysis and evaluation as well as the algorithm development were primarily performed by myself. Writing of the manuscript was mainly done by myself. All co-authors have contributed to the publications by constructive discussions and proofreading with the following exceptions:

Publication A:	The TEM analysis was performed by M. Burtscher and he helped by the evaluation of the grain-size. M. Wurmshuber and M. Alfreider performed the *in situ* fracture experiment.
Publication B	The dynamic *in situ* fracture experiments were performed by M. Alfreider and the TEM recordings were done by M. Burtscher.
Publication C	Additional experimental *in situ* videos were provided by M. Alfreider.
Publication D	A part of the algorithm was developed by M. Antenreiter. Additional experimental *in situ* videos were provided by M. Alfreider.

8 Bibliography

1. Eswarappa Prameela, S. *et al.* Materials for extreme environments. *Nature Reviews Materials* **8,** 81–88. ISSN: 20588437 (2023).
2. Ren, C. *et al.* Methods for improving ductility of tungsten - A review. *International Journal of Refractory Metals and Hard Materials* **75,** 170–183. ISSN: 22133917. https://doi.org/10.1016/j.ijrmhm.2018.04.012 (2018).
3. Dong, L. L., Ahangarkani, M., Chen, W. G. & Zhang, Y. S. Recent progress in development of tungsten-copper composites: Fabrication, modification and applications. *International Journal of Refractory Metals and Hard Materials* **75,** 30–42. ISSN: 22133917 (2018).
4. Chen, W. *et al.* Microstructure characterization of W-Cu alloy sheets produced by high temperature and high pressure deformation technique. *Materials Letters* **205,** 198–201. ISSN: 18734979. http://dx.doi.org/10.1016/j.matlet.2017.06.090 (2017).
5. Xie, H. *et al.* W–Cu/Cu composite electrodes fabricated via laser surface alloying. *Materials Characterization* **185,** 111715. ISSN: 10445803. https://doi.org/10.1016/j.matchar.2021.111715 (2022).
6. Arita, M. *et al.* Switching operation and degradation of resistive random access memory composed of tungsten oxide and copper investigated using in-situ TEM. *Scientific Reports* **5,** 1–9. ISSN: 20452322 (2015).
7. Slade, P. G. Advances in Material Development For High Power, Vacuum Interrupter Contacts. *IEEE Transactions on Components Packaging and Manufacturing Technology Part A* **17,** 96–106. ISSN: 10709886 (1994).
8. Ding, F. *et al.* Effect of microstructure refinement on surface morphology and dynamic mechanical properties of W-Cu alloys. *Materials* **14,** 1–11. ISSN: 19961944 (2021).
9. Pietranico, S., Pommier, S., Lefebvre, S. & Pattofatto, S. Thermal fatigue and failure of electronic power device substrates. *International Journal of Fatigue* **31,** 1911–1920. ISSN: 01421123. http://dx.doi.org/10.1016/j.ijfatigue.2009.03.011 (2009).
10. Chen, X. *et al.* Experimental and numerical studies on W–Cu functionally graded materials produced by explosive compaction–welding sintering. *Fusion Engineering and Design* **137,** 349–357. ISSN: 09203796. https://doi.org/10.1016/j.fusengdes.2018.10.016 (2018).

11. Zhao, M., Issa, I., Pfeifenberger, M. J., Wurmshuber, M. & Kiener, D. Tailoring ultra-strong nanocrystalline tungsten nanofoams by reverse phase dissolution. *Acta Materialia* **182,** 215–225. ISSN: 13596454. https://doi.org/10.1016/j.actamat.2019.10.030 (2020).

12. El-Atwani, O. *et al.* In-situ TEM observation of the response of ultrafine- and nanocrystalline-grained tungsten to extreme irradiation environments. *Scientific Reports* **4,** 4–10. ISSN: 20452322 (2014).

13. Rieth, M. *et al.* Recent progress in research on tungsten materials for nuclear fusion applications in Europe. *Journal of Nuclear Materials* **432,** 482–500. ISSN: 00223115 (2013).

14. Muller, A. V. *et al.* Melt infiltrated tungsten–copper composites as advanced heat sink materials for plasma facing components of future nuclear fusion devices. *Fusion Engineering and Design* **124,** 455–459. ISSN: 09203796. https://doi.org/10.1016/j.fusengdes.2017.01.042 (2017).

15. Tejado, E., Müller, A. V., You, J. H. & Pastor, J. Y. Evolution of mechanical performance with temperature of W/Cu and W/CuCrZr composites for fusion heat sink applications. *Materials Science and Engineering A* **712,** 738–746. ISSN: 09215093. https://doi.org/10.1016/j.msea.2017.12.054 (2018).

16. Tishkevich, D. I. *et al.* Isostatic Hot Pressed W–Cu Composites with Nanosized Grain Boundaries: Microstructure, Structure and Radiation Shielding Efficiency against Gamma Rays. *Nanomaterials* **12,** 1–14. ISSN: 20794991 (2022).

17. Sun, D. *et al.* Plasma facing component with built-in tungsten wires and a W-Cu functionally graded layer: A finite element assessment. *Fusion Engineering and Design* **120,** 9–14. ISSN: 09203796. http://dx.doi.org/10.1016/j.fusengdes.2017.05.006 (2017).

18. Guo, W. *et al.* Comparison of penetration performance and penetration mechanism of w-cu shaped charge liner against three kinds of target: Pure copper, carbon steel and Ti-6Al-4V alloy. *International Journal of Refractory Metals and Hard Materials* **60,** 147–153. ISSN: 22133917. http://dx.doi.org/10.1016/j.ijrmhm.2016.07.015 (2016).

19. Hou, C. *et al.* W–Cu composites with submicron- and nanostructures: progress and challenges. *NPG Asia Materials* **11.** ISSN: 18844057. http://dx.doi.org/10.1038/s41427-019-0179-x (2019).

20. Zhang, B., Yang, K., Huang, Z. & Wang, J. Recent Advances in W–Cu Composites: A Review on the Fabrication, Application, Property, Densification, and Strengthening Mechanism. *Advanced Engineering Materials* **2301204,** 1–34. ISSN: 15272648 (2023).

21. Giannattasio, A., Yao, Z., Tarleton, E. & Roberts, S. G. Brittle-ductile transitions in polycrystalline tungsten. *Philosophical Magazine* **90,** 3947–3959. ISSN: 14786435 (2010).

22. Wurmshuber, M. *et al.* Enhancing mechanical properties of ultrafine-grained tungsten for fusion applications. *International Journal of Refractory Metals and Hard Materials* **111,** 106125. ISSN: 22133917. https://doi.org/10.1016/j.ijrmhm.2023.106125 (2023).

23. Khalajhedayati, A., Pan, Z. & Rupert, T. J. Manipulating the interfacial structure of nanomaterials to achieve a unique combination of strength and ductility. *Nature Communications* **7.** ISSN: 20411723 (2016).

24. Wurmshuber, M., Doppermann, S., Wurster, S. & Kiener, D. Ultrafine-grained Tungsten by High-Pressure Torsion - Bulk precursor versus powder processing route. *IOP Conference Series: Materials Science and Engineering* **580,** 012051. ISSN: 1757899X (2019).

25. Armstrong, R. W. 60 years of hall-petch: Past to present nano-scale connections. *Materials Transactions* **55,** 2–12. ISSN: 13459678 (2014).

26. Hall, E. O. The deformation and ageing of mild steel: III Discussion of results. *Proceedings of the Physical Society. Section B* **64,** 747–753. ISSN: 03701301 (1951).

27. Petch, N. The cleavage strength of polycrystals. *Journal of Iron and Steel Research International* **174,** 25–28 (1953).

28. Zhang, Q., Liang, S. & Zhuo, L. Ultrafine-grained W–25 wt-%Cu composite with superior high-temperature characteristics. *Materials Science and Technology (United Kingdom)* **33,** 2071–2077. ISSN: 17432847 (2017).

29. Zhang, Q., Liang, S., Hou, B. & Zhuo, L. The effect of submicron-sized initial tungsten powders on microstructure and properties of infiltrated W-25 wt.% Cu alloys. *International Journal of Refractory Metals and Hard Materials* **59,** 87–92. ISSN: 22133917. http://dx.doi.org/10.1016/j.ijrmhm.2016.05.014 (2016).

30. Horita, Z., Tang, Y., Masuda, T. & Takizawa, Y. Severe Plastic Deformation under High Pressure: Upsizing Sample Dimensions. *Nippon Kinzoku Gakkaishi/Journal of the Japan Institute of Metals* **86,** 107–120. ISSN: 00214876 (2022).

31. Hohenwarter, A. Incremental high pressure torsion as a novel severe plastic deformation process: Processing features and application to copper. *Materials Science and Engineering: A* **626,** 80–85. ISSN: 09215093. http://dx.doi.org/10.1016/j.msea.2014.12.041 (2015).

32. Toth, L. S. *et al.* High pressure tube twisting for producing ultra fine grained materials: A review. *Materials Transactions* **60,** 1177–1191. ISSN: 13459678 (2019).

33. Arzaghi, M. *et al.* Microstructure, texture and mechanical properties of aluminum processed by high-pressure tube twisting. *Acta Materialia* **60,** 4393–4408. ISSN: 13596454. http://dx.doi.org/10.1016/j.actamat.2012.04.035 (2012).

34. Matsuki, K., Aida, T., Takeuchi, T., Kusui, J. & Yokoe, K. Microstructural characteristics and superplastic-like behavior in aluminum powder alloy consolidated by equal-channel angular pressing. *Acta Materialia* **48,** 2625–2632. ISSN: 13596454 (2000).

35. Hausöl, T. *et al.* Tailoring materials properties by accumulative roll bonding. *Advanced Engineering Materials* **12,** 740–746. ISSN: 14381656 (2010).

36. Ebrahimi, M. & Wang, Q. Accumulative roll-bonding of aluminum alloys and composites: An overview of properties and performance. *Journal of Materials Research and Technology* **19,** 4381–4403. ISSN: 22387854. https://doi.org/10.1016/j.jmrt.2022.06.175 (2022).

37. Zhilyaev, A. P. & Langdon, T. G. *Using high-pressure torsion for metal processing: Fundamentals and applications* 2008.

38. Edalati, K. *et al.* Severe plastic deformation for producing Superfunctional ultrafine-grained and heterostructured materials: An interdisciplinary review. *Journal of Alloys and Compounds,* 174667. ISSN: 09258388. https://doi.org/10.1016/j.jallcom.2024.174667 (2024).

39. Ni, H. *et al.* The Evolutions of Microstructure, Texture and Hardness of A1050 Deformed by HPT at the Transition Area. *Materials* **16.** ISSN: 19961944 (2023).

40. Sabirov, I. & Pippan, R. Formation of a W-25%Cu nanocomposite during high pressure torsion. *Scripta Materialia* **52,** 1293–1298. ISSN: 13596462 (2005).

41. Wurmshuber, M. *et al.* Mechanical performance of doped W–Cu nanocomposites. *Materials Science and Engineering: A* **857,** 144102. ISSN: 09215093 (2022).

42. Jia, D. *et al.* Deformation behavior and plastic instabilities of ultrafine-grained titanium. *Applied Physics Letters* **79,** 611–613. ISSN: 00036951 (2001).

43. Zhu, Y. T. & Liao, X. Retaining ductility. *Nature Materials* **3,** 351–352. ISSN: 1476-1122 (2004).

44. Budrovic, Z., Van Swygenhoven, H., Derlet, P. M., Van Petegem, S. & Schmitt, B. Plastic Deformation with Reversible Peak Broadening in Nanocrystalline Nickel. *Science* **304,** 273–276. ISSN: 00368075 (2004).

45. Zhao, Y. H., Liao, X. Z., Zhu, Y. T., Horita, Z. & Langdon, T. G. Influence of stacking fault energy on nanostructure formation under high pressure torsion. *Materials Science and Engineering A* **410-411,** 188–193. ISSN: 09215093 (2005).

46. Zhao, Y. H., Liao, X. Z., Horita, Z., Langdon, T. G. & Zhu, Y. T. Determining the optimal stacking fault energy for achieving high ductility in ultrafine-grained Cu-Zn alloys. *Materials Science and Engineering A* **493,** 123–129. ISSN: 09215093 (2008).

47. Holub, G. *Simultaneously increasing strength and ductility of nano-crystalline Cu-Zn-alloys made from powderous raw materials* diploma thesis (Montanuniversitaet Leoben, 2023), 66.

48. Chen, P., Luo, G., Li, M., Shen, Q. & Zhang, L. Effects of Zn additions on the solid-state sintering of W-Cu composites. *Materials and Design* **36,** 108–112. ISSN: 02641275. http://dx.doi.org/10.1016/j.matdes.2011.10.006 (2012).

49. Hohenwarter, A., Bachmaier, A., Gludovatz, B., Scheriau, S. & Pippan, R. Technical parameters affecting grain refinement by high pressure torsion. *Zeitschrift fuer Metallkunde/Materials Research and Advanced Techniques* **100,** 1653–1661. ISSN: 00443093 (2009).

50. Pippan, R., Scheriau, S., Hohenwarter, A. & Hafok, M. Advantages and limitations of HPT: A review. *Materials Science Forum* **584-586 PA,** 16–21. ISSN: 16629752 (2008).

51. Kiener, D. & Misra, A. Nanomechanical characterization. *MRS Bulletin* **49,** 214–223. ISSN: 08837694. https://doi.org/10.1557/s43577-023-00643-z (2024).

52. Matoy, K. *et al.* A comparative micro-cantilever study of the mechanical behavior of silicon based passivation films. *Thin Solid Films* **518,** 247–256. ISSN: 00406090. http://dx.doi.org/10.1016/j.tsf.2009.07.143 (2009).

53. Di Maio, D. & Roberts, S. G. Measuring fracture toughness of coatings using focused-ion-beam-machined microbeams. *Journal of Materials Research* **20,** 299–302. ISSN: 08842914 (2005).

54. Takashima, K. & Higo, Y. Fatigue and fracture of a Ni-P amorphous alloy thin film on the micrometer scale. *Fatigue and Fracture of Engineering Materials and Structures* **28,** 703–710. ISSN: 8756758X (2005).

55. Haiford, T. P., Rudinal, D., Takashima, K. & Higo, Y. The effect of sample preparation upon the fracture toughness of microsized TiAl. *Key Engineering Materials* **297-300 IV,** 2416–2422. ISSN: 16629795 (2005).

56. Wurster, S., Motz, C. & Pippan, R. Characterization of the fracture toughness of micro-sized tungsten single crystal notched specimens. *Philosophical Magazine* **92,** 1803–1825. ISSN: 14786435 (2012).

57. Iqbal, F., Ast, J., Göken, M. & Durst, K. In situ micro-cantilever tests to study fracture properties of NiAl single crystals. *Acta Materialia* **60,** 1193–1200. ISSN: 13596454 (2012).

58. Schmuck, K. S., Burtscher, M., Alfreider, M. & Kiener, D. Assessing the Fracture Toughness in Tungsten-Based Nanocomposites: A Micro- Mechanical Approach. *Materials & Design,* 18 (2024).

59. Alfreider, M., Kolitsch, S., Wurster, S. & Kiener, D. An analytical solution for the correct determination of crack lengths via cantilever stiffness. *Materials and Design* **194,** 9. ISSN: 18734197 (2020).

60. Schmuck, K., Antenreiter, M., Alfreider, M. & Kiener, D. Automatic and time-resolved determination of fracture characteristics from in situ experiments. *Materials and Design* **243,** 113038. ISSN: 18734197. https://doi.org/10.1016/j.matdes.2024.113038 (2024).

61. Sutton, M., Wolters, W., Peters, W., Ranson, W. & McNeill, S. Determination of displacements using an improved digital correlation method. *Image and Vision Computing* **1,** 133–139. ISSN: 02628856 (1983).

62. McNeill, S., Peters, W. & Sutton, M. Estimation of stress intensity factor by digital image correlation. *Engineering Fracture Mechanics* **28,** 101–112. ISSN: 00137944. https://linkinghub.elsevier.com/retrieve/pii/001379448790124X (Jan. 1987).

63. Roux, S., Réthoré, J. & Hild, F. Digital image correlation and fracture: An advanced technique for estimating stress intensity factors of 2D and 3D cracks. *Journal of Physics D: Applied Physics* **42.** ISSN: 00223727 (2009).

64. Thäsler, T., Holtmannspötter, J. & Gudladt, H. J. Monitoring the fatigue crack growth behavior of composite joints using in situ 2D-digital image correlation. *Journal of Adhesion* **95,** 595–613. ISSN: 15455823. https://doi.org/10.1080/00218464.2018.1562923 (2019).

65. Kammers, A. D. & Daly, S. Digital Image Correlation under Scanning Electron Microscopy: Methodology and Validation. *Experimental Mechanics* **53,** 1743–1761. ISSN: 00144851 (2013).

66. Di Gioacchino, F. & Quinta da Fonseca, J. Plastic Strain Mapping with Sub-micron Resolution Using Digital Image Correlation. *Experimental Mechanics* **53,** 743–754. ISSN: 00144851 (2013).

67. Di Gioacchino, F. & Clegg, W. J. Mapping deformation in small-scale testing. *Acta Materialia* **78,** 103–113. ISSN: 13596454. http://dx.doi.org/10.1016/j.actamat.2014.06.033 (2014).

68. Edwards, T. E. J., Di Gioacchino, F., Muñoz-Moreno, R. & Clegg, W. J. Deformation of lamellar TiAl alloys by longitudinal twinning. *Scripta Materialia* **118,** 46–50. ISSN: 13596462. http://dx.doi.org/10.1016/j.scriptamat.2016.03.004 (2016).

69. Edwards, T. E., Maeder, X., Ast, J., Berger, L. & Michler, J. Mapping pure plastic strains against locally applied stress: Revealing toughening plasticity. *Science Advances* **8,** 1–11. ISSN: 23752548 (2022).

70. Kiener, D., Wurmshuber, M., Alfreider, M., Schaffar, G. J. & Maier-Kiener, V. Recent advances in nanomechanical and in situ testing techniques: Towards extreme conditions. *Current Opinion in Solid State and Materials Science* **27,** 101108. ISSN: 13590286. https://doi.org/10.1016/j.cossms.2023.101108 (2023).

71. Chen, H. *et al.* Fracture toughness evaluation of a nuclear graphite with non-linear elastic properties by 3D imaging and inverse finite element analysis. *Engineering Fracture Mechanics* **293,** 109719. ISSN: 00137944. https://doi.org/10.1016/j.engfracmech.2023.109719 (2023).

72. Mathieu, F., Hild, F. F. & Roux, S. Identification of a crack propagation law by digital image correlation. *International Journal of Fatigue* **36,** 146–154. ISSN: 01421123. http://dx.doi.org/10.1016/j.ijfatigue.2011.08.004 (2012).

73. Strohmann, T., Starostin-Penner, D., Breitbarth, E. & Requena, G. Automatic detection of fatigue crack paths using digital image correlation and convolutional neural networks. *Fatigue and Fracture of Engineering Materials and Structures* **44,** 1336–1348. ISSN: 14602695 (2021).

74. Hossain, M. A. & Alam Sajib, M. S. Classification of Image using Convolutional Neural Network (CNN). *Global Journal of Computer Science and Technology* **19,** 13–18. ISSN: 09754350 (2019).

75. Ramprasath, M., Anand, V. M. & Hariharan, S. *Plankton image classification using convolutional neural networks* in *Proceedings of the 2015 International Conference on Image Processing, Computer Vision, and Pattern Recognition, IPCV 2015* **119** (2018), 1307–1319. ISBN: 1314-3395.

76. Lassner, E. & Schubert, W.-D. *Properties, chemistry, technology of the element, alloys, and chemical compounds* ISBN: 0306450534 (Kluwer Academic, 2005).

77. Lassner, E. & Schubert, W.-D. *Tungsten* 1455–1458. ISBN: 9781461372257 (2018).

78. Zhang, J., Huang, Y., Wang, Z. & Liu, Y. Thermodynamic mechanism for direct alloying of immiscible tungsten and copper at a critical temperature range. *Journal of Alloys and Compounds* **774,** 939–947. ISSN: 09258388. https://doi.org/10.1016/j.jallcom.2018.09.385 (2019).

79. Lunk, H. J. & Hartl, H. *Discovery, properties and applications of tungsten and its inorganic compounds* **3,** 1–37. ISBN: 0123456789. https://doi.org/10.1007/s40828-019-0088-1 (Springer International Publishing, 2019).

80. Zhao, Y. H., Liao, X. Z., Cheng, S., Ma, E. & Zhu, Y. T. Simultaneously increasing the ductility and strength of nanostructured alloys. *Advanced Materials* **18,** 2280–2283. ISSN: 09359648 (2006).

81. Zhu, Y. T., Liao, X. Z., Wu, X. L. & Narayan, J. Grain size effect on deformation twinning and detwinning. *Journal of Materials Science* **48,** 4467–4475. ISSN: 00222461 (2013).

82. Zhu, Y. T., Liao, X. Z., Srinivasan, S. G. & Lavernia, E. J. Nucleation of deformation twins in nanocrystalline face-centered-cubic metals processed by severe plastic deformation. *Journal of Applied Physics* **98.** ISSN: 00218979 (2005).

83. Cardarelli, F. *Materials Handbook* ISBN: 9783319389233 (Springer, 2018).

84. Davis, J. R. *ASM Speciality Handbook, Copper and Copper Alloys* 128. ISBN: 2001022956 (2001).

85. Schmid, M. *Vapor Pressure Calculator* 2023. `https://www2.iap.tuwien.ac.at/www/surface/vapor%7B%5C_%7Dpressure` (2024).

86. Bridgman, P. W. Effects of high shearing stress combined with high hydrostatic pressure. *Physical Review* **48,** 825–847. ISSN: 0031899X (1935).

87. Edalati, K. & Horita, Z. A review on high-pressure torsion (HPT) from 1935 to 1988. *Materials Science and Engineering: A* **652,** 325–352. ISSN: 09215093. `http://dx.doi.org/10.1016/j.msea.2015.11.074` (2016).

88. Bachmaier, A. & Pippan, R. High-pressure torsion deformation induced phase transformations and formations: New material combinations and advanced properties. *Materials Transactions* **60,** 1256–1269. ISSN: 13459678 (2019).

89. Pippan, R., Wetscher, F., Hafok, M., Vorhauer, A. & Sabirov, I. The limits of refinement by severe plastic deformation. *Advanced Engineering Materials* **8,** 1046–1056. ISSN: 14381656 (2006).

90. Faleschini, M., Kreuzer, H., Kiener, D. & Pippan, R. Fracture toughness investigations of tungsten alloys and SPD tungsten alloys. *Journal of Nuclear Materials* **367-370 A,** 800–805. ISSN: 00223115 (2007).

91. Wetscher, F., Vorhauer, A. & Pippan, R. Strain hardening during high pressure torsion deformation. *Materials Science and Engineering A* **410-411,** 213–216. ISSN: 09215093 (2005).

92. Wetscher, F., Vorhauer, A., Stock, R. & Pippan, R. Structural refinement of low alloyed steels during severe plastic deformation. *Materials Science and Engineering: A* **387-389,** 809–816. ISSN: 09215093 (2004).

93. Stüwe, H. P. Equivalent strains in severe plastic deformation. *Advanced Engineering Materials* **5,** 291–295. ISSN: 14381656 (2003).

94. Parvin, H. & Kazeminezhad, M. Limiting grain size through high-pressure torsion of different materials. *Materials Science and Technology (United Kingdom)* **36,** 245–250. ISSN: 17432847 (2020).

95. Wei, Q. *et al.* Microstructure and mechanical properties of super-strong nanocrystalline tungsten processed by high-pressure torsion. *Acta Materialia* **54,** 4079–4089. ISSN: 13596454 (2006).

96. Edalati, K., Hashiguchi, Y., Pereira, P. H. R., Horita, Z. & Langdon, T. G. Effect of temperature rise on microstructural evolution during high-pressure torsion. *Materials Science and Engineering: A* **714,** 167–171. ISSN: 09215093. `https://doi.org/10.1016/j.msea.2017.12.095` (2018).

97. Anderson, T. L. *Fracture Mechanics* 3rd ed., 630. ISBN: 9781420058215 (CRC Press, 2005).

98. Andrews, E. H. A generalized theory of fracture mechanics. *Journal of Materials Science* **9,** 887–894. ISSN: 00222461 (1974).

99. Griffith, A. A. The phenomena of rupture and flow in solids. *Philosophical Transactions* **221,** 163–198. ISSN: 00254576 (1920).

100. *ASTM Standard E399-09 Standard Test Method for Linear-Elastic Plane-Strain Fracture Toughness KIC of Metallic Materials* West Conshohocken, USA, 1997.

101. Irwin, George, R. Fracture dynamics. *Fracturing of Metals.* `https://cir.nii.ac.jp/crid/1573950400137757952.bib?lang=en` (1947).

102. Ramberg, W. & Osgood, W. R. Description of stress-strain curves by three parameters. *National Advisory Committee For Aeronautics,* Technical Note No. 902. `http://hdl.handle.net/2060/19930081614` (1943).

103. Hutchinson, J. Singular behaviour at the end of a tensile crack in a hardening material. *Journal of the Mechanics and Physics of Solids* **16,** 13–31 (1968).

104. Rice, J. R. & Rosengren, G. F. Plane strain deformation near a crack tip in a power-law hardening material. *Journal of the Mechanics and Physics of Solids* **16,** 1–12. ISSN: 00225096 (1968).

105. ASTM Standard 1820. *ASTM Book of Standards,* 1–54 (2013).

106. Shih, C. Relationship between the J-integral and the COD for stationary and extending cracks. *Journal of Mechanics and Physics of Solids* **29,** 305–326 (1981).

107. Pippan, R., Wurster, S. & Kiener, D. Fracture mechanics of micro samples: Fundamental considerations. *Materials and Design* **159,** 252–267. ISSN: 18734197. `https://doi.org/10.1016/j.matdes.2018.09.004` (2018).

108. Schmuck, K., Burtscher, M., Alfreider, M., Wurmshuber, M. & Kiener, D. Micromechanical fracture investigations on grain size tailored tungsten-copper nano- composites. *JOM.* ISSN: 1543-1851. https://doi.org/10.1007/s11837-023-06348-7 (2024).

109. Riedl, A. *et al.* A novel approach for determining fracture toughness of hard coatings on the micrometer scale. *Scripta Materialia* **67,** 708–711. ISSN: 13596462 (2012).

110. Tada, H., Paris, P. C. & Irwin, G. R. *Stress Analysis Results for Common Test Specimen Configurations* 2010.

111. Atkins, A. G., Chen, Z. & Cotterell, B. The essential work of fracture and JR curves for the double cantilever beam specimen: An examination of èlastoplastic crack propagation. *Proceedings of the Royal Society A: Mathematical, Physical and Engineering Sciences* **454,** 815–833. ISSN: 13645021 (1998).

112. Gonzalez, R. C. & Woods, R. E. *Digital Image Processing* third. ISBN: 9780131687288 (Pearson Education, 2008).

113. Qi, Y. *et al.* A Comprehensive Overview of Image Enhancement Techniques. *Archives of Computational Methods in Engineering* **29,** 583–607. ISSN: 18861784. https://doi.org/10.1007/s11831-021-09587-6 (2022).

114. Solomon, C. & Breckon, T. *Fundamentals of Digital Image Processing: A Practical Approach with Examples in Matlab* 1–328. ISBN: 9780470689776 (2011).

115. Li, C. H. & Lee, C. K. Minimum cross entropy thresholding. *Pattern Recognition* **26,** 617–625. ISSN: 00313203 (1993).

116. Feltham, P. & Copley, G. J. Yielding and work-hardening in alpha-brasses. *Acta Metallurgica* **8,** 542–550. ISSN: 00016160 (1960).

117. Nieh, T. G. & Wadsworth, J. Hall-petch relation in nanocrystalline solids. *Scripta Metallurgica et Materiala* **25,** 955–958. ISSN: 0956716X (1991).

118. Tejedor, R., Edalati, K., Benito, J. A., Horita, Z. & Cabrera, J. M. High-pressure torsion of iron with various purity levels and validation of Hall-Petch strengthening mechanism. *Materials Science and Engineering: A* **743,** 597–605. ISSN: 09215093. https://doi.org/10.1016/j.msea.2018.11.127 (2019).

119. Zhao, Z., To, S., Wang, J., Zhang, G. & Weng, Z. Materials & Design A review of micro / nanostructure effects on the machining of metallic materials. *Materials & Design* **224,** 111315. ISSN: 0264-1275. https://doi.org/10.1016/j.matdes.2022.111315 (2022).

120. Liu, J., Fan, X., Zheng, W., Singh, D. J. & Shi, Y. Nanocrystalline gold with small size : inverse Hall – Petch between mixed regime and super-soft regime. **6435** (2020).

121. Carsley, J., Ning, J., Milligan, W. W., Hackney, S. A. & Aifantis, E. C. A SIMPLE , MIXTURES-BASED MODEL FOR THE GRAIN SIZE DEPENDENCE OF STRENGTH IN NANOPHASE. *Nanostructured Materials* (1995).

122. Konstantinidis, D. A. & Aifantis, E. On the "anomalous" hardness of nanocrystalline materials. *Acta Metallurgica* **10,** 1111–1118 (1999).

123. Voigt, W. Ueber die Beziehung zwischen den beiden Elasticitätsconstanten isotroper Körper [On the relationship between the two elastic constants of an isotropic body]. *Annalen Der Physik* **274,** 573–587 (1889).

124. Reuss, A. Berechnung der Fließgrenze von Mischkristallen auf Grund der Plastizitätsbedingung für Einkristalle . *ZAMM - Journal of Applied Mathematics and Mechanics / Zeitschrift für Angewandte Mathematik und Mechanik* **9,** 49–58. ISSN: 15214001 (1929).

125. Trelewicz, J. R. & Schuh, C. A. The Hall-Petch breakdown in nanocrystalline metals: A crossover to glass-like deformation. *Acta Materialia* **55,** 5948–5958. ISSN: 13596454 (2007).

126. Cheng, S., Spencer, J. A. & Milligan, W. W. Strength and tension/compression asymmetry in nanostructured and ultrafine-grain metals. *Acta Materialia* **51,** 4505–4518. ISSN: 13596454 (2003).

127. Chandross, M. & Argibay, N. Friction of Metals: A Review of Microstructural Evolution and Nanoscale Phenomena in Shearing Contacts. *Tribology Letters* **69,** 1–27. ISSN: 15732711. https://doi.org/10.1007/s11249-021-01477-z (2021).

128. Li, J. C. M., Feng, C. R. & Rath, B. B. Emission of Dislocations from Grain Boundaries and Its Role in Nanomaterials, 1–12 (2020).

129. Suryanarayana, C. & Koch, C. C. Nanocrystalline materials – Current research and future directions. *Hyperfine Interactions* **130,** 5–44. ISSN: 03043843 (2000).

130. Meyers, M., Mishra, A. & Benson, D. Mechanical properties of nanocrystalline materials. *Progress in Materials Science* **51,** 427–556. ISSN: 00796425. https://linkinghub.elsevier.com/retrieve/pii/S0079642505000447 (May 2006).

131. Ryou, H. *et al.* Below the Hall-Petch Limit in Nanocrystalline Ceramics. *ACS Nano* **12,** 3083–3094. ISSN: 1936086X (2018).

132. Gong, J. *et al.* Nano-metric self-diffusion of Fe: effect of grain size. *RSC Advances* **7,** 9573–9578. ISSN: 20462069 (2017).

133. Wurmshuber, M., Alfreider, M., Wurster, S., Pippan, R. & Kiener, D. Small-scale fracture mechanical investigations on grain boundary doped ultrafine-grained tungsten. *Acta Materialia* **250,** 18. ISSN: 1359-6454. https://doi.org/10.1016/j.actamat.2023.118878 (2023).

134. Ast, J., Merle, B., Durst, K. & Göken, M. Fracture toughness evaluation of NiAl single crystals by microcantilevers - A new continuous J-integral method. *Journal of Materials Research* **31,** 3786–3794. ISSN: 20445326 (2016).

135. Cheng, G. M. *et al.* Grain size effect on deformation mechanisms of nanocrystalline bcc metals. *Materials Research Letters* **1,** 26–31. ISSN: 21663831 (2013).

136. Hertzberg, R., Vinici, R. & Hertzberg, J. *Deformation and fracture mechanics of engineering materials* 5th ed., 785. ISBN: 9780470527801 (Wiley, Hoboken, NJ, 1985).

137. Hohenwarter, A., Kammerhofer, C. & Pippan, R. The ductile to brittle transition of ultrafine-grained Armco iron: An experimental study. *Journal of Materials Science* **45,** 4805–4812. ISSN: 00222461 (2010).

138. Burtscher, M., Alfreider, M., Kainz, C., Schmuck, K. & Kiener, D. In situ micromechanical analysis of a nano-crystalline W-Cu composite. *Materials and Design* **220,** 110848. ISSN: 18734197. https://doi.org/10.1016/j.matdes.2022.110848 (2022).

139. Burtscher, M., Alfreider, M., Kainz, C. & Kiener, D. Deformation and failure behavior of nanocrystalline WCu. *Materials Science & Engineering A* **887,** 145760. ISSN: 0921-5093 (2023).

140. Harry, E., Rouzaud, A., Ignat, M. & Juliet, P. Mechanical properties of W and W(C) thin films: Young's modulus, fracture toughness and adhesion. *Thin Solid Films* **332,** 195–201. ISSN: 00406090 (1998).

141. Murphy, J. D. *et al.* The mechanical properties of tungsten grown by chemical vapour deposition. *Journal of Nuclear Materials* **386-388,** 583–586. ISSN: 00223115. http://dx.doi.org/10.1016/j.jnucmat.2008.12.182 (2009).

142. Margevicius, R. W., Riedle, J. & Gumbsch, P. Fracture toughness of polycrystalline tungsten under mode I and mixed mode I/II loading. *Materials Science and Engineering: A* **270,** 197–209. ISSN: 09215093 (1999).

143. Pfeifenberger, M. J., Nikolić, V., Žák, S., Hohenwarter, A. & Pippan, R. Evaluation of the intergranular crack growth resistance of ultrafine grained tungsten materials. *Acta Materialia* **176,** 330–340. ISSN: 13596454 (2019).

144. Ast, J., Göken, M. & Durst, K. Size-dependent fracture toughness of tungsten. *Acta Materialia* **138,** 198–211. ISSN: 13596454 (2017).

145. Tejado, E., Müller, A. V., You, J. H. & Pastor, J. Y. The thermo-mechanical behaviour of W-Cu metal matrix composites for fusion heat sink applications: The influence of the Cu content. *Journal of Nuclear Materials* **498,** 468–475. ISSN: 00223115. https://doi.org/10.1016/j.jnucmat.2017.08.020 (2018).

146. Tejado, E., Müller, A. V., You, J. H. & Pastor, J. Y. Mechanical behaviour of W particulate-reinforced Cu composites: Fracture toughness and R-curves. *Journal of Nuclear Materials* **571,** 0–7. ISSN: 00223115 (2022).

147. Giannattasio, A. & Roberts, S. G. Strain-rate dependence of the brittle-to-ductile transition temperature in tungsten. *Philosophical Magazine* **87,** 2589–2598. ISSN: 14786435 (2007).

148. Rupp, D., Mönig, R., Gruber, P. & Weygand, S. M. *Fracture toughness and microstructural characterization of polycrystalline rolled tungsten* in *International Journal of Refractory Metals and Hard Materials* **28** (Elsevier Ltd, 2010), 669–673. http://dx.doi.org/10.1016/j.ijrmhm.2010.05.006.

149. Keller, R. R., Phelps, J. M. & Read, D. T. Tensile and fracture behavior of free-standing copper films. *Materials Science and Engineering: A* **214,** 42–52. ISSN: 09215093 (1996).

150. Hohenwarter, A. & Pippan, R. Fracture and fracture toughness of nanopolycrystalline metals produced by severe plastic deformation. *Philosophical Transactions of the Royal Society A: Mathematical, Physical and Engineering Sciences* **373.** ISSN: 1364503X (2015).

151. Alfreider, M., Meindlhumer, M., Maier-Kiener, V., Hohenwarter, A. & Kiener, D. Extracting information from noisy data: strain mapping during dynamic in situ SEM experiments. *Journal of Materials Research* **36,** 2291–2304. ISSN: 20445326. https://doi.org/10.1557/s43578-020-00041-0 (2021).

152. Ying, X. An Overview of Overfitting and its Solutions. *Journal of Physics: Conference Series* **1168.** ISSN: 17426596 (2019).

153. Olaf, R., Philipp, F. & Thomas, B. U-Net: Convolutional Networks for Biomedical Image Segmentation. *Medical Image Computing and Computer-Assisted Intervention – MICCAI 2015. MICCAI 2015. Lecture Notes in Computer Science* **9351,** 234–241. ISSN: 16113349 (2015).

154. Siddique, N., Paheding, S., Elkin, C. P. & Devabhaktuni, V. U-net and its variants for medical image segmentation: A review of theory and applications. *IEEE Access* **9,** 82031–82057. ISSN: 21693536 (2021).

155. Kirillov, A. *et al.* Segment Anything. *Computer Vision and Pattern Recognition.* arXiv: 2304.02643. http://arxiv.org/abs/2304.02643 (2023).

156. Keckes, J. F., Jelinek, A., Kiener, D. & Alfreider, M. Neural Network Supported Microscale In Situ Deformation Tracking : A Comparative Study of Testing Geometries. *JOM.* ISSN: 1543-1851. https://doi.org/10.1007/s11837-024-06437-1 (2024).

Publication A

Micro-mechanical fracture investigations on grain size tailored tungsten-copper nano-composites

JOM 76, 2302-2314, (**2024**)
doi: 10.1007/s11837-023-06348-7

Micro-mechanical fracture investigations on grain size tailored tungsten-copper nano-composites

K. Schmuck[1,1], M. Burtscher[1], M. Alfreider[1], M. Wurmshuber[2], D. Kiener[1]
[1]Department of Material Science, Montanuniversität Leoben, Jahnstraße 12, 8700 Styria, Austria

[2]Department of Materials Science and Engineering, Friedrich-Alexander-University of Erlangen-Nürnberg, Martensstraße 5, 91058 Bavaria, Germany

Abstract

Tungsten-copper composites are used in harsh environments due to their superior material properties. This work addresses a tungsten-copper composite made of 20 wt.% copper, which was subjected to grain refinement by high-pressure torsion, whereby the deformation temperature was varied between room temperature and 400°C to tailor the grain size. Deformation was performed up to microstructural saturation, verified by hardness measurement and scanning electron microscopy. From the refined nanostructured material, micro-cantilever bending beams with cross-sections spanning from 5x5 to 35x35 µm^2 were cut to examine possible size effects and the grain size influence on the fracture behavior. Fracture experiments were performed *in situ* inside a scanning electron microscope by applying a quasi-static loading protocol with partial unloading steps. Inspection of the fracture surfaces showed that all cantilevers failed in an inter-crystalline fashion. Nevertheless, remaining coarser tungsten grains impacted the resultant fracture toughness and morphology. Cantilevers fabricated from the 400°C specimen exhibited a fracture toughness of $220\pm50\frac{J}{m^2}$. For the room temperature cantilevers, a fracture toughness of $410\pm50\frac{J}{m^2}$ was observed, which declined to $340\pm30\frac{J}{m^2}$ for cantilevers below 10x10 µm^2, confirming a size effect. The increased fracture toughness is attributed to the delamination-like structures formed in the room temperature sample.

Keywords: *in situ* testing, grain size tailoring, high-pressure torsion, micro mechanics, tungsten-copper nanocomposite

1. Introduction

Materials with outstanding properties are required for high-performance applications and harsh environments, *e.g.* plasma-facing components in fusion reactors. For that purpose,

[1]Corresponding author at: Department of Materials Physics, Montanuniversität Leoben, Leoben, Austria.
E-Mail Address: klemens.schmuck@unileoben.ac.at (K. Schmuck)

tungsten and tungsten-based materials are frequently considered as candidate materials for structural and shielding components in fusion reactors due to the superior material properties of tungsten, such as high sputter resistance, low tritium retention in fusion environments, low vapor pressure, high melting point and good intrinsic strength at elevated temperatures [1–7]. Nevertheless, the use of pure tungsten in safety-relevant applications is limited due to its low ductility and inherent brittle behavior, leading to a low overall damage tolerance [8,9]. Besides that, heat sinks used in fusion reactors to cool structural and shielding components are commonly fabricated from copper and copper-based alloys [7]. The thermal expansion coefficient between tungsten and copper differs, leading to high thermally induced stresses at their interfaces during high temperature loads. By fabricating tungsten-copper composites, the thermal stresses can be alleviated [4,10]. In addition, the secondary ductile copper phase enhances ductility of the composite, but degrades the intrinsic strength, whereby the extent depends on the material composition [11]. Strength and ductility must be enhanced to improve the damage tolerance [12,13]. A well-known method to increase strength and ductility simultaneously is grain refinement [14–16]. Coarse grained tungsten-copper composites with a copper content of 25 at.%, 51 at.% and 59 at.% have been successfully subjected to high-pressure torsion for grain refinement down to the nanocrystalline regime. For all compositions the microstructure, hardness and resulting grain size in saturation were analyzed, connecting deformation temperature with the saturated grain size [17–20]. While the structural evolution is well documented the fracture mechanical behavior was so far only investigated for the nanocrystalline tungsten-copper composition with 59 at.% copper using micro-cantilever bending experiments [20], preventing a detailed understanding of the influence of the grain size on the fracture toughness.

To contribute to this lack of knowledge, in this work a tungsten-copper composite with a copper content of only 42 at.% was subjected to high-pressure torsion at different deformation temperatures to tailor the nanocrystalline grain size. The sample disks were deformed up to the saturation regime to avoid microstructural gradients along the radius. Subsequently, micro-cantilever bending beams were fabricated from these disks to investigate the fracture toughness for different nanocrystalline grain sizes.

2. Experimental

2.1. Sample preparation

The base material was a liquid phase sintered tungsten-copper composite rod with a copper content of 42 at.% (20 wt.%) and a mean tungsten grain size of 2.5 µm (WHS Sondermetalle, Grünsfeld, Germany). From this rod with a diameter of 8 mm, three disks with a thickness of roughly 1 mm were cut.

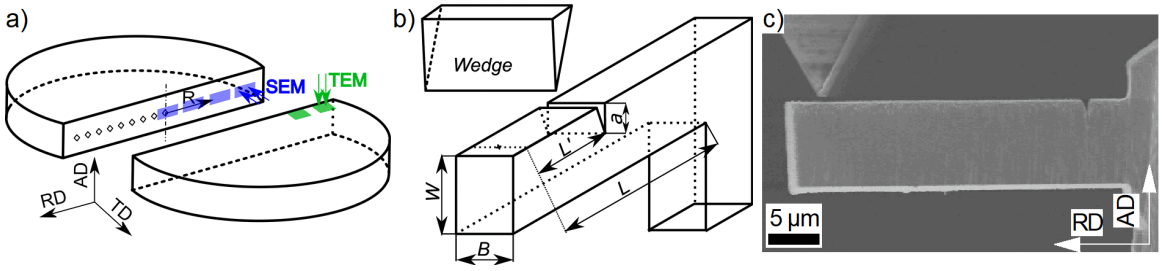

Figure 1: Sample preparation and testing. a) Compacted disk after high-pressure torsion processing. The disk is shown in halves to enhance visibility. The colors blue and green represent SEM and TEM measurements, respectively. The arrows depict the viewing direction, while the surface normal to the viewing direction was polished. The coordinate system defines the radial (RD), axial (AD) and tangential direction (TD). b) Schematic sketch of the cantilever dimensions, with WxB the cantilever cross-section, a the crack length, L' the length between indenter and crack and L the length between indenter loading point and fixation. c) Fabricated cantilever before in situ testing and relation to the HPT disk orientation.

Subsequently, the disks were subjected to high-pressure torsion (HPT, [21]) at the following deformation temperatures: room temperature (RT), 200°C and 400°C, to tailor the resultant grain size. To obtain a saturated microstructure, an equivalent strain of 160 and 680 according to Pippan *et al.* [21] was applied at a radius of 3 mm for the RT and the two elevated temperatures samples, respectively.

After HPT, the samples were cut into halves along the transversal plane with a wire saw, depicted in Fig. 1 a). One half was embedded and polished to verify the saturated and homogeneous microstructure along the radius. For quantitative verification of the saturation level, Vickers hardness measurements (HV1, Buehler Micromet 5104) were performed along the radius. The indents were placed 0.25 mm apart to each other, schematically shown by the diamond shapes in Fig. 1 a). Further, saturation and homogeneity of the microstructure were qualitatively investigated by scanning electron microscopy (SEM; Zeiss LEO type 1525) along the radius every 0.5 mm, see the exemplary blue rectangles in Fig. 1 a).

The second half disk was further cut into pieces. Along one quarter the matrix grain size was quantitatively investigated by scanning transmission electron microscopy (STEM; JEOL JEM-2200FS microscope, JEOL Ltd., Japan). To reduce preparation time, the specimen was manually ground and polished to a wedge like shape exhibiting a final thickness of about 20 µm at the wedge tip. After manual polishing, focused ion beam milling (FIB; Zeiss Auriga Laser platform, Carl Zeiss AG, Oberkochen, Germany) was used to mill thin lamellas, thereby the FIB current was subsequently reduced from 20 nA, for coarse milling, to 50 pA for polishing. The final thickness of the lamellas was about 100 nm with an area of about 2x5 µm^2 to investigate the nanocrystalline grain size, which was analyzed with image processing techniques using grain segmentation by the watershed algorithm [20,22].

The other quarter of the HPT disk was used to fabricate differently sized micro-cantilever bending beams. For that the piece was manually ground and polished to a wedge shape with a final thickness between 20 and 50 µm. To further reduce the FIB time, femtosecond laser ablation [23] within an FIB/SEM (Zeiss Auriga Laser platform, Carl Zeiss AG, Oberkochen, Germany) was performed for coarse machining and pre-cutting of the cantilevers. Final processing was done via FIB milling by subsequently reducing the FIB current from 20 nA, for coarse milling, to 500 pA, for polishing. For the RT sample, the cantilever cross-sections were varied between 5x5 and 35x35 µm^2 to investigate a possible size effect on initiation fracture toughness (J_q). For the 400°C sample, only cantilevers with cross-sections of 5x5 and 10x10 µm^2 were fabricated. The cantilever length was set to about $4\,W$ and the initial notch depth between $(0.3 - 0.4)W$. The notches were introduced by line milling from the top-view with a current of 500 pA. To reach the desired depth for the largest cantilevers 35x35 µm^2, the notch was pre-cut from the side view and finished in the top-view, respectively. The cantilever geometry and important variables are schematically illustrated in Fig. 1 b), while the *in situ* setup is shown in Fig. 1 c).

2.2. Testing setup

Fracture experiments were performed inside an SEM (DSM 982, Carl Zeiss AG, Oberkochen, Germany), which allowed to record *in situ* images at a rate of one image per second using an in-lens secondary electron detector. The imaged region was selected to the crack vicinity to enhance image resolution at the crack tip. The cantilevers were loaded with a displacement controlled micro indenter (UNAT SEM 1, ASMEC GmbH, Dresden, Germany) with a noise level of 50 µN in vacuum. Loading was performed quasi-statically with up to 15 evenly spaced sequential unloading steps [24]. Each loading/unloading step consists of the following segments: loading with a constant displacement rate of 50 nm/s, holding for 10 s, unloading with a displacement drop of 10% caped at 2 µm, and holding again for 10 s. Due to the cross-sectional variation of the cantilevers, the maximal displacement was set to 26 µm for the cross-sections of 35x35 and 20x20 µm^2, to 16 µm for the 10x10 µm^2 cantilever and to 8 µm for the cantilevers 7.5x7.5 and 5x5 µm^2, respectively.

2.3. Fracture mechanical evaluation

The fracture characteristics of the cantilevers were determined from the recorded load-displacement data, by relating stiffness changes to cross-sectional variation with respect to the crack length [25]. The cantilever stiffness was measured by linearly fitting the unloading segment for each loading cycle [24]. The first unloading stiffness in combination with the initial crack length, measured before the experiment, was used as a reference to relate stiffness

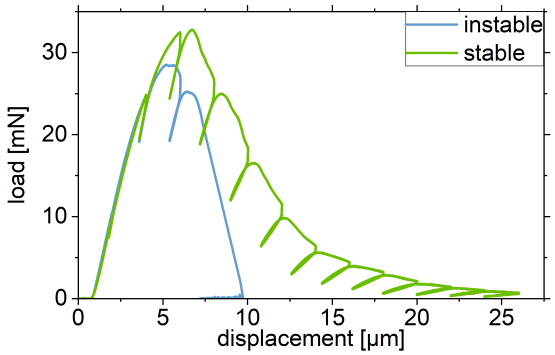

Figure 2: Representative load-displacement data recorded for stable and instable fracture, respectively, revealing in both cases a noticeable non-linearity before fracture.

changes to crack growth, according to [25]. Further, the J-integral was calculated employing elastic-plastic fracture mechanics (EPFM) following the detailed description outlined by Alfreider *et al.* [26], as all cantilevers showed noticeable non-linearity before fracture, see the representative loading curves in Fig. 2.

To compare the obtained J_q to data from literature and linear elastic fracture mechanics, the J_q values were transformed into fracture toughness (K_q) using in linear-elastic fracture mechanics according to the ASTM1820 standard [27] by:

$$K_q = \sqrt{\frac{J_q E}{(1-\nu^2)}}, \tag{1}$$

with the Young's modulus $E = 221$ GPa, measured by nano-indentation and the Poisson ratio $\nu = 0.32$ [28].

Besides the J-integral, the crack tip opening displacement (δ) is frequently used in EPFM to characterize failure processes. This can be measured from the recorded *in situ* frames, thereby for stable crack growth, the last frame before crack initiation was used, while in the case of unstable crack growth the frame before fracture was analyzed. Measurement of δ was performed manually as described by Shih *et al.* [29], where two orthogonal lines are placed on the crack tip, so that the distance between the crack tip and the intersection with the crack flanks are equal for both lines. δ is then given by the distance between the crack flank intersection points. This is exemplary shown in Fig. 3. For EPFM it has been shown that both parameters J_q and δ are linked via:

$$\delta = d_n \frac{J_q}{\sigma_y}, \tag{2}$$

with σ_y being the materials yield strength and d_n the Shih factor depending on the stress

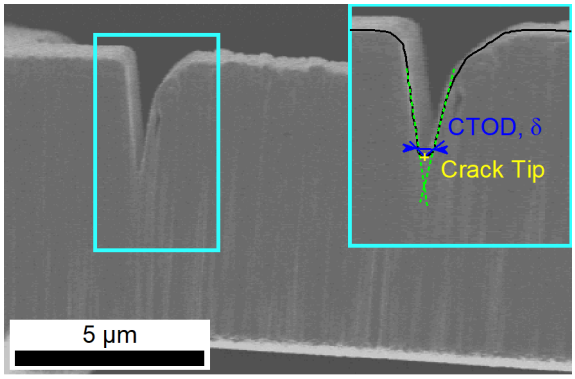

Figure 3: Manual δ measurement example on an in situ recorded micrograph. Note that the inset, marked with cyan, is distorted in x-direction for visualization reasons. The yellow cross represents the crack tip, while the green dashed lines fitted to the crack flank

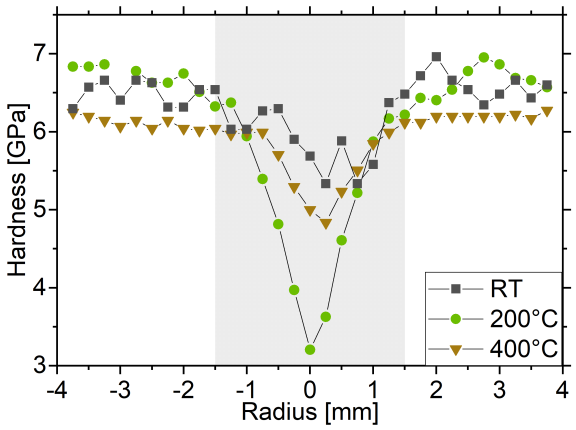

Figure 4: Vickers hardness measurement along the radius of the samples fabricated via HPT deformation at RT, 200°C and 400°C, respectively. The gray shaded area encloses the region with insufficient straining and thus unsaturated microstructure.

condition and hardening behavior of the material [29].

3. Results

3.1 Microstructural investigations

Vickers hardness measurements were performed for all specimens to verify microstructural saturation along the disk radius, as the hardness is inversely proportional to the grain size according to the Hall-Petch relation [14–16]. The hardness values measured are depicted in Fig. 4 for all samples, whereby the mean hardness values above a radius of 1.5 mm in the saturation regime are 6.8±0.2, 6.7±0.2 and 6.2±0.1 GPa for the RT, 200°C and 400°C sample, respectively.

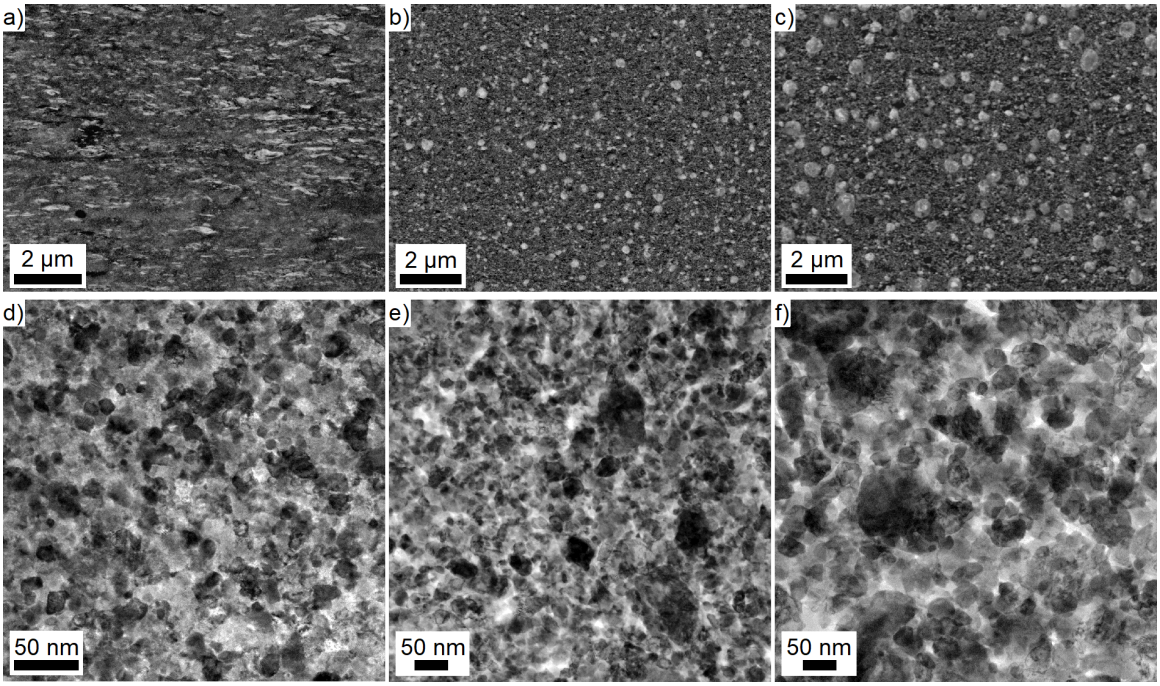

Figure 5: Obtained microstructures for the different deformation temperatures at a disk radius of 3 mm. a)-c) Backscatter electron images for deformation at a) RT, b) 200°C and 400°C. The bright spots represent coarse tungsten grains. d)-f) STEM investigations of the nanocrystalline matrix for deformation temperatures of d) RT, e) 200°C and f) 400°C.

Furthermore, the microstructure was examined by backscatter electron imaging along the radius. The microstructures at a radius of 3 mm are depicted in Fig. 5 a), b) and c) as representative microstructures above a radius of 1.5 mm for the HPT deformation temperature of RT, 200°C and 400°C, respectively. Despite the verified saturation by Vickers hardness measurements, the microstructures showed a bi-modal grain size characteristic with statistically distributed coarse tungsten grains embedded in a nanocrystalline matrix of copper and tungsten. Bright regions in the microstructure represent coarse tungsten grains, see Fig. 5 a)-c). With increasing deformation temperature, the coarse tungsten grains change their shape from an elongated flake-like, lamellar form to a spherical shape at 200°C and 400°C, compare Fig. 5 a)-c). Thereby, the median equivalent Feret diameter of the coarse tungsten grains increased from 200 to 233 nm between the RT and 400°C.

Further, the nanocrystalline matrix was investigated by STEM at a radius of about 3 mm. These investigations revealed an increasing grain size trend of the nanocrystalline matrix with rising deformation temperature, see Fig. 5 d)-f). For the specimens deformed at elevated temperatures, a few coarse tungsten grains are present in the STEM images, while for the RT specimen there are none evident. This arises from the flake-like structure in the RT specimen, which is oriented parallel to the lamella and thinner than the spherical grains observed in the elevated temperature specimens. Hence, the probability of capturing these

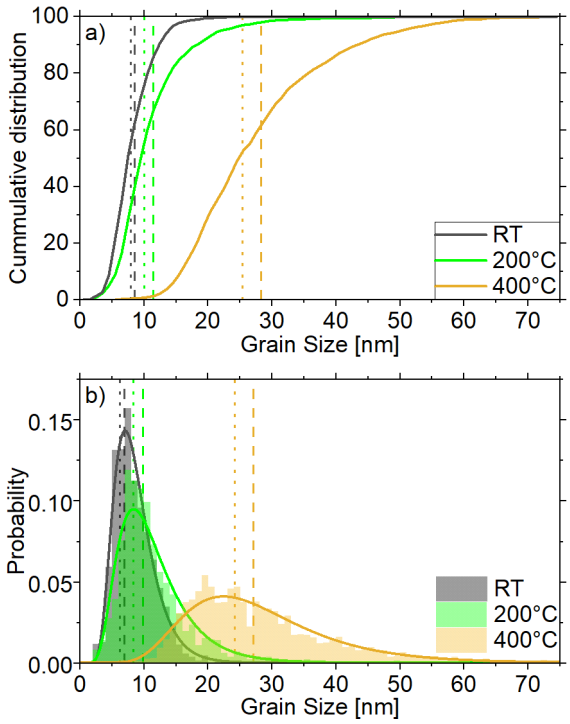

Figure 6: Matrix grain size distribution measured at a radius of 3 mm for the samples deformed at RT, 200°C and 400°C. a) Cumulative and b) probability distribution. The dashed lines represent the mean values, while the dotted ones correspond to the median values.

flake-like structures in this TEM lamella orientation is reduced. For proper statistics, at least four images were analyzed for each deformation temperature to quantify the matrix grain size. The resulting grain size distributions are depicted in Fig. 6, while the central statistical values are listed in Table 1.

Table 1: Central values of the matrix grain size distribution in nm, where p15 and p85 represent the 15% and 85% percentile

T [°C]	Mean	Median	p15	p85	Grains
RT	9	8	5	12	1658
200	11	10	6	17	1777
400	28	26	17	39	1758

3.2 Fracture mechanical testing

Notched micro-cantilever bending beams were cut to examine the fracture behavior of the RT and 400° C sample. The cantilevers were fabricated in pairs and grouped by size at a disk radius between 2 and 3.5 mm. Further, they were orientated along the radial direction, with the notch being parallel to the axial direction, see Fig. 1 a) and c) for reference.

Hence, the coarse flake-like tungsten grains evident in the RT specimen are parallel to the cantilever. For the RT specimen, the cantilever cross-section was varied between 5x5 and 35x35 µm^2 to investigate a possible sample size effect. Thereby, the initial crack length a_0 was measured for the individual cantilever sizes as: 2.4±0.5 µm ($\frac{a_0}{W} = 37 \pm 7\%$), 2.3±0.3 µm ($\frac{a_0}{W} = 31 \pm 2\%$), 3.4±0.7 µm ($\frac{a_0}{W} = 33 \pm 8\%$), 5.8±0.7 µm ($\frac{a_0}{W} = 29 \pm 4\%$), and 15.9±0.8 µm ($\frac{a_0}{W} = 46 \pm 2\%$), for the 5x5, 7.5x7.5, 10x10, 20x20 and 35x35 µm^2 cantilever, respectively. Despite the cross-sectional variation, the cantilevers from the RT sample fractured primarily by stable crack growth. Fig. 7 Ia)-If) depicts representative fracture surfaces for the different cantilever sizes of the RT sample. The subfigures Ia)-Id) and If) show failure by stable crack growth, while subfigure Ie) illustrates a fracture surface after unstable failure. Further, to investigate a grain size dependency of the fracture toughness, cantilevers with a cross-section of 5x5 and 10x10 µm^2 were fabricated from the 400°C sample. For these cantilevers, an initial crack length a_0 was determined to 2.1±0.3 µm ($\frac{a_0}{W} = 36 \pm 4\%$), and 3.8±0.4 µm ($\frac{a_0}{W} = 36 \pm 4\%$) for the 5x5 and 10x10 µm^2 cantilevers, respectively. For the 400°C sample, all cantilevers with a cross-section of 5x5 µm^2 showed stable crack growth, while all having a cross-section of 10x10 µm^2 fractured unstable. The fracture surfaces for the 400°C cantilevers are displayed in Fig. 7 IIa) and IIb).

All load-displacement curves showed noticeable non-linearity before crack initiation or catastrophic failure, see the representative Fig. 2. Hence, EPFM was used to characterize the fracture process of all cantilevers. In the case of stable crack growth, the J_q was determined before crack initiation, whereby intermediate values between two unloading steps were linearly interpolated. Thereby, the crack growth initiation was determined by visually inspecting the *in situ* frames for some crack extension, neglecting crack tip blunting. The J_q was obtained at the initiation as the transition between blunting and tearing regime becomes harder to distinguish with decreasing cantilever size, making fitting of either regime challenging, see Fig. 8. This occurs because the tearing modulus is indirect proportional to the sample size [30].

For stable crack growth, the uncertainty was approximated by $\frac{J_{n+1}-J_n}{2}$. In the case of unstable crack growth, J_q was determined at the maximum load, including the load-displacement area between the last unloading step before failure and maximum load, as schematically illustrated in Fig. 8. To validate the J_q values, the validation criterion

$$\{(W - a_0)\,; B\} > C\frac{J_q}{\sigma_y}, \tag{3}$$

is frequently used in EPFM, where C is a pre-factor ranging between 10 and 50 [24,29,31–33], whereby the ASTM1820 standard states a value of 10 [27].

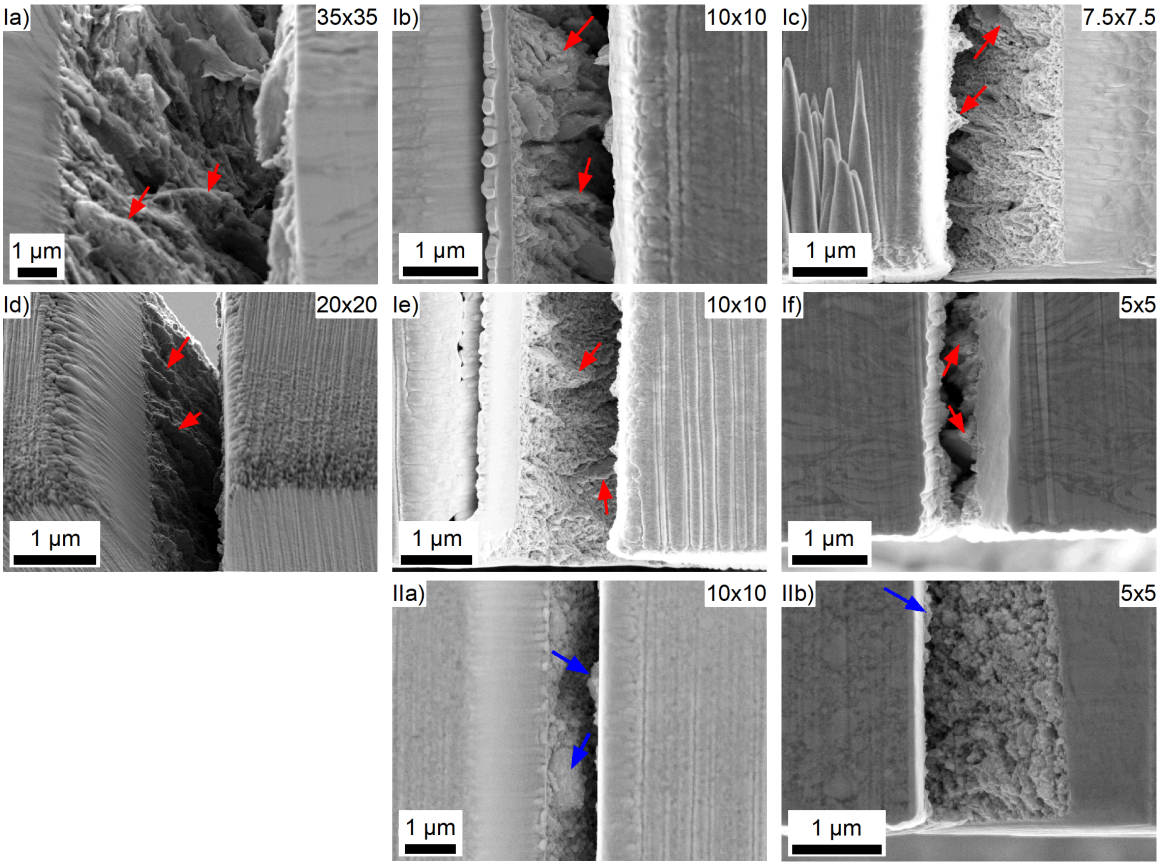

Figure 7: Post mortem fracture surfaces for the different cantilever sizes fabricated from the RT sample in Ia)-If) and the 400°C sample in IIa)-IIb). The Images Ia)-Id), If) and IIb) illustrate fracture surfaces after stable crack growth, while the surfaces shown in Ie) and IIa) represents unstable fracture. The red arrows indicate coarse tungsten grains, which form delamination-like structures for the RT sample and the blue arrows point to the spherical-shaped coarse tungsten grains in the 400°C sample.

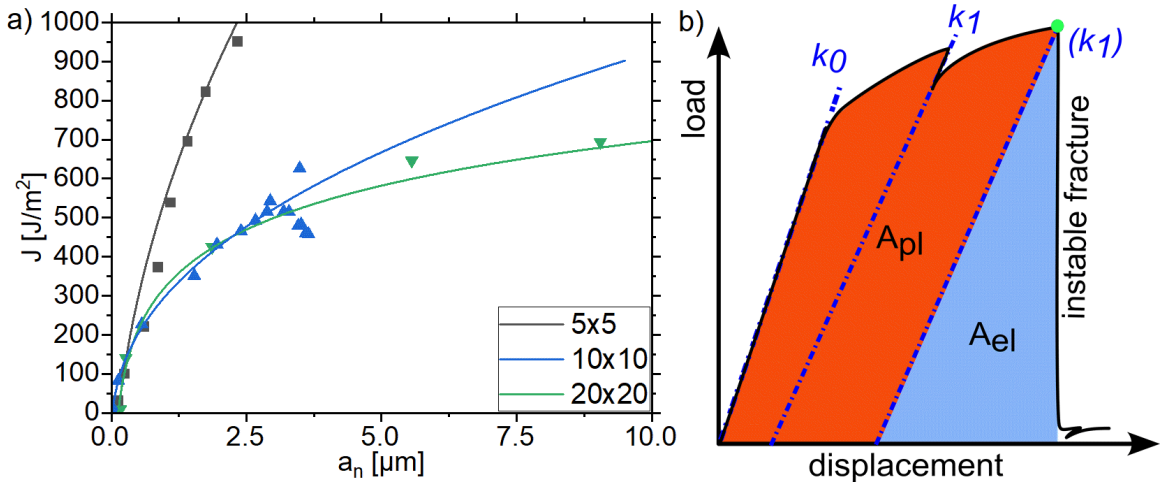

Figure 8: a) Representative R-curves fitted by a power-law fit for cantilever dimensions of 5x5, 10x10 and 20x20 µm^2, showing an increasing tearing modulus with decreasing size, rendering distinguishing between blunting and tearing part a challenging task. b) Schematic illustration for the evaluation of J_q for unstable fracture, with k_n the unloading stiffness, A_{pl} the plastic area and A_{el} the elastic area. Thereby, J_q is evaluated at the maximum load (green dot) and the area below the load-displacement curve is split into plastic and elastic area according to the last unloading stiffness (k_1).

The J_q values determined for all RT cantilevers are shown in Fig. 9 a). Thereby, the C parameter is calculated from Equation 3 by taking the minimum of the left side and solving the equation for C by assuming an equal sign. Among similar cantilever dimensions for the RT sample, median J_q values of 340±30, 370±40, 400±90, 420±50 and 410±30 $\frac{J}{m^2}$ were determined for the cantilever cross-section 5x5, 7.5x7.5, 10x10, 20x20 and 35x35 µm^2, respectively.

In addition, the δ was determined, which was challenging, as image resolution is limited due to the necessity of imaging the total cantilever height and image noise present due to the fast frame acquisition required to capture the fracture process. Thus, δ was measured several times and averaged to obtain an accurate value. For comparison, the δ values were transformed according to Equation 2 using a Shih factor of 0.78 for a non-hardening material and the plane strain condition [29]. The yield strength was approximated from the hardness measurements by $\sigma_y \approx \frac{9.810665}{3} HV$ [34] which gives 2250±60 MPa, 2330±70 MPa and 2050±30 MPa for the RT, 200°C and 400°C sample, respectively. Fig. 9 b) depicts the measured and transformed δ values for the RT sample, whereby values of 125±7, 129±6, 143±6, 146±7 and 152±3 nm were found for the cantilever cross-sections of 5x5, 7.5x7.5, 10x10, 20x20 and 35x35 µm^2, respectively. This translates to $J_{q,\delta}$ values of 360±20, 370±20, 400±20, 410±20 and 430±20 $\frac{J}{m^2}$ for these dimensions of the RT sample, respectively.

The J_q determined from mechanical data for the cantilevers fabricated from the 400°C sample are depicted in Fig. 10 a). Additionally, the J_q values of the RT cantilevers with

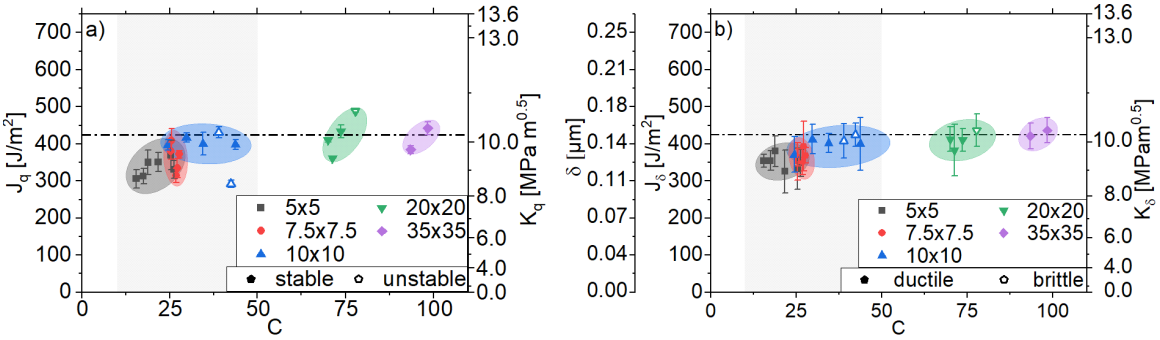

Figure 9: Characteristic fracture values depending on the pre-factor C given in Equation 3. The gray shaded area represents the minimum validity region of the J-integral for EPFM from the literature [24,27,29,31–33]. The horizontal line indicates the size-independent fracture toughness J_q obtained from the larger cantilevers. a) J_q values from the R-curve determined from the load-displacement data of RT sample. b) Measured values of the δ before crack growth initiation or failure converted into fracture toughness J_q according to Equation 2.

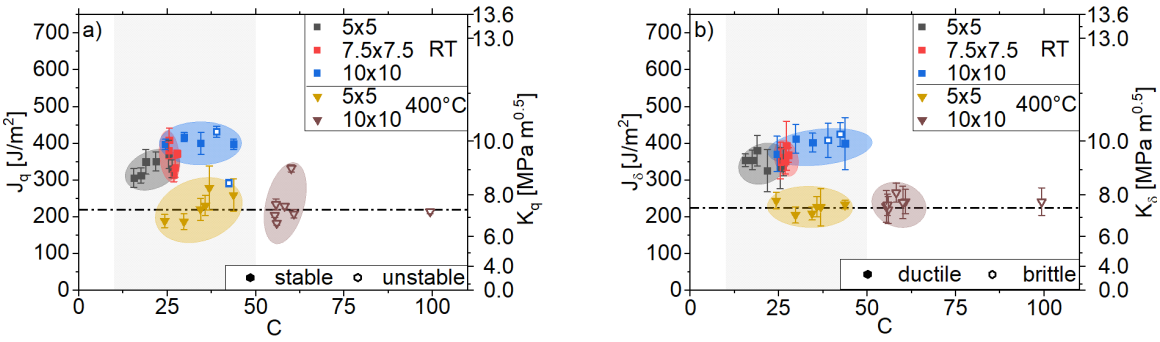

Figure 10: Comparison of the fracture characteristics between the RT and 400°C deformed samples. The fracture toughness J_q is plotted over the pre-factor C given in Equation 3, while the gray shaded region illustrates the minimum validity criterion range for the J-integral in EPFM according to literature [24,27,29,31–33]. a) Fracture toughness values J_q obtained from the R-curve, which was calculated from mechanical data. b) δ values before failure or crack growth initiation, transformed into fracture toughness values according to Equation 2.

varying cross-section are displayed for a direct comparison. Cantilevers with a cross-section of 10x10 µm^2 from the 400°C sample exhibited a J_q of 220±60 $\frac{J}{m^2}$, while cantilevers with a cross-section of 5x5 µm^2 gave 230±40 $\frac{J}{m^2}$. Further, δ values were measured from the *in situ* frames for the 400°C cantilevers and are illustrated in Fig. 10 b). Additionally, the δ data from the various RT cantilevers are included for a direct comparison. The 400°C cantilevers exhibited a δ of 90±6 and 91±6 nm, which gives a $J_{q,\delta}$ value of 230±20 and 240±20 $\frac{J}{m^2}$ for the cantilever cross-sections 5x5 and 10x10 µm^2, respectively.

4. Discussion

4.1. Microstructural investigations

The equivalent strain, introduced via HPT, depends linearly on the radius. Hence, with increasing radius more strain is introduced into the sample upon deformation, leading to an increased refinement of the microstructure. Exceeding the radius of 1.5 mm the hardness converges to a constant value, indicating microstructural saturation, see Fig. 4. Comparing the hardness among the different deformation temperatures similar values for the sample deformed at RT and 200°C are evident, while the 400°C sample shows a slightly decreased hardness, in agreement with an increased grain size, as depicted in Fig. 6. This indicates to be still within the Hall-Petch regime [35,36]. The hardness values are comparable to literature data of a bulk tungsten-copper composite with 59 at.% (33 wt.%) copper deformed at RT to the nanocrystalline regime, where a final hardness from 6 to 8 GPa was reached [19]. Nevertheless, Vickers hardness measurements examine the whole imprint volume at once, allowing to detect only mean changes within the imprint size. Hence, additional SEM investigation were performed, revealing a similar trend as the hardness values. No significant differences were observable in the microstructure above a radius of 1.5 mm, verifying microstructural saturation. Nevertheless, the observed microstructures show a bi-modal structure, consisting of statistically comparably distributed coarse tungsten grains, with an equivalent diameter of hundreds of nm, embedded into a truly nanocrystalline matrix, see Fig. 5 a)-c). This occurs as the deformation is mainly localized in the softer copper phase and the volume fraction of the nanocrystalline matrix increases during deformation, limiting the contact between large tungsten particles [18]. With increasing deformation temperature, the copper phase softens due to the related increase in homologous temperature from 0.22 to 0.35 and 0.5, respectively [37]. This leads to less grain refinement and a more spherical shape for the present coarse tungsten grains in the samples deformed at elevated temperatures, as illustrated in Fig. 5 a)-c).

From STEM images of the nanocrystalline matrix, an increasing grain size with increased deformation temperature is obvious, see Fig. 5 d)-f). The quantitative analysis of the nanocrystalline matrix by STEM, listed in Table 1, revealed a similar mean grain size of about 10 nm for the RT and 200°C samples. At the same time, the distribution slightly broadens from RT to 200°C, illustrated in Fig. 6. For the sample deformed at 400°C the mean grain size of the nanocrystalline matrix shifts to a significantly higher value of 28 nm and the grain size distribution broadens notably, see Fig. 6. Further, the 400°C sample displays only a minor overlap with the distributions of the other samples, as there are less small grains. The grain size values determined for the RT sample are in accordance with literature data from HPT refined bulk tungsten-copper composites. For these, SEM

investigations revealed a grain size range of $10 - 20$ nm when containing 25 at.% (10 wt.%) copper [17], while TEM investigations revealed a grain size range of $5 - 15$ nm for 51 at.% (26 wt.%) copper [18]. For the elevated temperatures, 200°C and 400°C, the literature states a broader grain size range of $10 - 100$ nm and $20 - 200$ nm for a tungsten-copper-25 at.% composite [17], measured by SEM. The mean grain size values determined in this study are on the lower end of the literature range [17,18]. This is not surprising, as in the present study nanocrystalline matrix was deliberately investigated by STEM, excluding the coarse tungsten grains present in the microstructure.

Besides, the HPT parameters used in this study to tailor the microstructure and grain size can be used as starting point for other material compositions. Nevertheless, there are additional investigations necessary for new material compositions, as the deformation process in HPT is related to the material properties, e.g. the saturation grain size depends on the strength of the material. Schweiger *et al.* [38] reported a detailed insight into the different aspects of HPTdeformation by using an iron-titanium-copper composite as model material. They concluded that for new multi-phase materials the interaction between the phases has to be carefully examined to achieve a homogeneous structure by HPT.

4.2. Fracture mechanical testing

Concerning the conducted miniaturized fracture experiments, all cantilevers were fabricated in the region of microstructural saturation, which was verified by hardness measurements and microstructural investigations, see Fig. 4 and Fig. 5. Nevertheless, coarse tungsten grains were still present in this region. These grains are statistically distributed and an order of magnitude smaller than the smallest cantilever size. Hence, these coarse tungsten grains are present in all cantilevers and are expected to be of minor influence on the fracture behavior with respect to the sample size. The fracture process of all cantilevers was governed by inter-crystalline failure, evident by the small feature size of the rough surface structure regardless of cantilever dimensions and deformation temperatures, see Fig. 7. For the RT cantilevers post mortem analysis of the fracture surface showed delamination-like structures, which have a similar extent as the coarse tungsten grains documented in the microstructure. This is depicted in Fig. 7 Ia) - If), where some delamination-like structures are marked by red arrows. Delaminations are known to transform the stress state at the crack front into a state with lower stress triaxiality (plane stress) by dividing the cross-section into smaller segments and improve the resulting fracture toughness of the material [39,40]. Although the RT cantilevers mainly fractured in a stable manner, a few cantilevers exhibited unstable failure. By comparing the fracture surfaces of the stable and unstable fractured samples, it is noticeable that the fracture surface of the brittle cantilevers showed a slightly reduced number of delamination-like structures, compare Fig. 7 Ib) and Ie). Thus, for the

unstable fracturing cantilevers, the stress triaxiality at the crack front is more pronounced, compared to cantilevers exhibiting a stable crack growth. In the case of the 400°C sample, all cantilevers with a cross-section of 10x10 µm^2 fractured unstable, while the cantilevers with a cross-section of 5x5 µm^2 exhibited stable crack growth, see Fig. 10. Despite the different failure behavior, both cantilever dimensions revealed a similar fracture surface, where the coarse tungsten grains are bypassed by the fracture path, see blue arrows in Fig. 7 IIa) and IIb). Fracture surface comparison of RT and 400°C shows a rougher structure for the 400°C samples, see Fig. 7 Ia)-If) and IIa)-IIb). This stems from the inter-crystalline fracture process and the increased matrix grain size, raised from 10 to 28 nm, as shown in Fig. 6. Further, the coarse tungsten grains form delamination-like structures for the RT cantilevers, thereby lowering the stress triaxiality. In contrast, for the 400°C specimens the fracture path bypassed these grains and coarse tungsten grains are pulled out from the other side, see Fig. 7 IIa) and IIb). Hence, the fracture toughness of the RT sample will be increased compared to the 400°C cantilevers, due to the reduced stress triaxiality, as depicted in Fig. 10.

The fracture toughness was quantified by EPFM, as all load-displacement curves showed noticeable non-linearity before crack growth, see Fig. 2. The RT cantilevers with cross-sections of 20x20 and 35x35 µm^2 were assessed to be above the most conservative pre-factor C in Equation 3, which ranges from 10 to 50 for size independency in literature [24,27,29,31–33]. For both cantilever dimensions a similar J_q of about 410±50 $\frac{J}{m^2}$ was evaluated, assuring samples size independence for these cross-sections due to the relative size difference, depicted in Fig. 9 a). The other cantilevers on the RT sample were dimensioned to be within the pre-factor C range of 10 to 50, resulting in cross-sectional sizes of 5x5, 7.5x7.5 and 10x10 µm^2. For these cantilevers the determined J_q showed an increased scatter, originating from a decreasing fracture load with reduced cantilever size and, therefore, deteriorating the signal to noise ratio of the load sensor, see the J_q scatter in Fig. 9 a). Additionally, the initial ligament impacts the determination of the plastic part from the J-integral [41]. The experimental ligament variations for the fabricated cantilevers are rather small and therefore a significant impact on the determined J_q values is not expected. Nevertheless, the minor variations might contribute to the scatter of the J_q values observed, see the increased scatter of the 10x10 µm^2 cantilevers. However, the resultant J_q of 400±90 $\frac{J}{m^2}$ for the cantilever cross-section of 10x10 µm^2 is similar to the value determined for the cantilevers with a cross-section of 20x20 and 35x35 µm^2. This indicates size independency for the 10x10 µm^2 cantilevers, see Fig. 9 a). Conversely the cantilever with a cross-section of 5x5 and 7.5x7.5 µm^2 exhibited a slightly decreased J_q of 340±30 and 370±40$\frac{J}{m^2}$, pointing to a distinct sample size effect, see the declining J_q values below a pre-factor $C < 30$ in Fig. 9 a). A similar pre-factor value for sample size independency was reported by Wurmshuber *et al.* [33] for micro cantilever bending beams fabricated from grain boundary doped tungsten alloys with

a grain size of about 150 nm. Although, the application field of the investigated material is above the µm regime, where the sample size effect is expected. Nevertheless, future application might apply only thin films of this material, hence, thoroughly investigations of the sample size effect is crucial.

Additionally, δ was determined from the *in situ* frames, which directly relates to the plastic zone size on the surface ahead of the crack. Therefore, the δ measurement is unaffected by the ligament variations. Cantilevers on the RT sample with a cross-section between 10x10 and 35x35 µm^2 showed a similar value of approximately 146±7 nm, illustrated in Fig. 9 b). Conversion into $J_{q,\delta}$ according to Equation 2 gives a value of 420±20 $\frac{J}{m^2}$, which is in excellent agreement with the J_q value of 410 $\frac{J}{m^2}$ obtained from mechanical data, ensuring size independence. The RT cantilevers with cross-sections of 5x5 and 7.5x7.5 µm^2 revealed a decreased δ of 125±7 and 129±6 nm. Conversion to $J_{q,\delta}$ gives values of 360±20 and 370±20 $\frac{J}{m^2}$ for these cantilevers, which are similar to J_q and exhibit the same trend of a decreasing J_q. The decline of both characteristic values signifies a sample size effect on the fracture toughness. The criteria given in Equation 3 sets limits to the minimal cantilever thickness (B) and the ligament length ($W - a_0$) for sample size independency. The former defines the dominate stress state at the crack front to be plane strain, while the ligament length in conjunction with the plastic zone size defines the valid fracture model, whether the fracture is governed by small-scale, large-scale yielding or plastic collapse [33,42]. Besides the criteria given in Equation 3, δ can be used to define a sample size independency criteria which is given by [42]:

$$W - a_0, B > 10\delta. \tag{4}$$

This criterion suggests a minimal cantilever thickness and ligament length of approximately 1.5 µm. In this case B this is fulfilled by all RT cantilevers, maintaining the plane strain condition. Therefore, the initiation parameters should be constant over the different cantilever dimensions with respect to the thickness [42]. Further, the ligament length of all RT cantilever is above the criteria given in Equation 4 and analysis of the frames recorded *in situ* showed no significant plastic deformation, excluding the occurrence of plastic collapse. Nevertheless, a decline of the toughness values is evident with decreasing size, which might stem from stress gradients due to bending. The plastic zone size was estimated by the simple Irwin model, which is given for the plane strain condition as:

$$r_p = \frac{1}{6\pi}\left(\frac{K_q}{\sigma_y}\right)^2, \tag{5}$$

with r_p as the plastic zone radius [43,44]. In combination with Equation 1 and the obtained values for J_q this gives an approximate $r_p = 1.1 \pm 0.2$ µm for the RT cantilevers. Further, due to the bending applied to the cantilever, a strain gradient forms within the ligament which gets steeper with decreasing sample dimensions. In the case of cantilevers with a cross-section of 5x5 and 7.5x7.5 µm^2 with an assumed $\frac{a_0}{W}$ ratio of 0.5, the initial ligament length is 2.5 and 3.75 µm, whereby the neutral axis is close to the ligaments halve. Thus, for these RT cantilevers the plastic zone size approaches the neutral axis. Therefore, compressive stresses may start to inhibit the plastic zone expansion. Hence, the energy dissipation from the crack tip is reduced and fracture occurs at lower J_q and δ values. Similar observations were reported by Wurmshuber *et al.* [33] for cantilevers with a cross-section of 3x3 µm^2 made from grain boundary doped tungsten alloys with a grain size of about 150 nm.

From the 400°C sample, cantilevers with a cross-section of 5x5 and 10x10 µm^2 were fabricated to reduce FIB time, as the RT cantilevers with a cross-section of 10x10 µm^2 confirmed size independency already. Fracture mechanical evaluation for the 400°C sample revealed a J_q of 230±40 and 210±60 $\frac{J}{m^2}$ for the cantilever cross-sections 5x5 and 10x10 µm^2, see Fig. 10 a). Combined with the yield strength estimated form the hardness values, this gives a pre-factor C of 66 for the 10x10 µm^2 cantilevers, which is well above the size dependency range of 10 to 50 given in literature [24,27,29,31–33]. The cantilevers with a cross-section of 5x5 µm^2 exhibit a pre-factor value of 35, which is within a similar range as the 10x10 µm^2 cantilevers fabricated from the RT sample, see Fig. 9. Despite the cross-sectional difference, the mechanical data of the 400°C cantilevers showed no size dependent trend. Nevertheless, δ was measured from *in situ* images, revealing a δ of 90±6 and 91±6 nm for the 400°C cantilevers, illustrated in Fig. 10 b). Transforming the δ into $J_{q,\delta}$ gives 230±20 and 240±20 $\frac{J}{m^2}$ for the 5x5 and 10x10 µm^2 cantilevers, which are in accordance with the J_q determined. The plane strain condition for the 400°C cantilevers was verified by Equation 4, which gives a minimal size constrain of 1.2 µm, as met by all 400°C cantilevers. Further, the plastic zone size was estimated according to Equation 5, as 0.7±0.2 µm, which fits well into a quarter of the initial ligament length of the 5x5 µm^2 cantilevers. Therefore, compressive stresses below the neutral axis do not interfere with the plastic zone. Nevertheless, the fracture behavior differs for the 400°C cantilever between 5x5 and 10x10 µm^2, as the former fractured by stable crack growth while the later exhibit unstable failure. This change in fracture behavior might originate from the fact that with decreasing size less energy is stored in the sample, stabilizing crack propagation through reduced energy release capabilities. This behavior is also reflected in the increasing tearing modulus by decreasing the sample size, see Fig. 8 and [30]. Hence, stable crack growth might occur due to the size reduction, whereby displacement controlled quasi-static loading might be further beneficial for a stable crack growth, as during unloading elastically stored energy is released and has to be reapplied during the following loading segment. Despite the size dependent crack propagation, the

crack initiation is size independent as long as Equation 4 is fulfilled [42].

Comparing the RT and 400°C sample microstructure suggests that the nanocomposite matrix grain size, increasing from 9 to 28 nm, has only a minor impact on J_q, although larger grains could potentially accumulate more dislocations. In contrast, the coarse tungsten grains present in the nanocrystalline matrix have a significant effect on J_q and $J_{q,\delta}$. In the RT samples these coarse tungsten grains form delamination-like structures, lowering the stress triaxility and leading to an anisotropic fracture behavior. From an engineering point of view, while this anisotropic characteristic could be harnessed in dedicated component design, isotropic material properties are favorable with respect to ease of material use and safety regarding unintended loading situations. For the cantilevers deformed at elevated temperatures, the spherically shaped coarse tungsten grains led to an isotropic microstructure and connected material properties. Nevertheless, cantilevers fabricated from the RT sample exhibited a high J_q and $J_{q,\delta}$ of about 410 $\frac{J}{m^2}$, while only 220 $\frac{J}{m^2}$ were obtained from the 400°C cantilevers.

To further underline the attractive properties of the present material, the metric proposed by Hohenwater *et al.* [45] for damage tolerance was used to classify the results with respect to literature data for grain refined copper, tungsten and tungsten-copper composites. This metric is given by the product of K_{IC} and the materials strength, as for damage tolerance a one-dimensional viewpoint is insufficient. A damage tolerant material has to combine a high material strength, as this defines the onset of plastification, and a high fracture toughness, which is a measure for the crack growth resistance. The iso-lines in Fig. 11 illustrate this respective damage tolerance. The investigated tungsten-copper composite showcases a noticeably increased fracture toughness compared to other nanostructured materials such as nanocrystalline copper [46], nanocrystalline magnetron sputtered tungsten [47], polycrystalline tungsten [48], and a nanocrystalline tungsten-copper composite with 50 at.% copper [49]. The latter has a comparable composition and similar grain size of 10 nm as the here investigated RT sample. Comparing the fracture toughness reveals an increased value for the present RT sample, which stems from the coarse flake-like tungsten grains, transforming the stress state. For the 400°C specimen, the coarse tungsten grains are spherical shaped and the grain size increased to 27 nm. Due to the spherical shape the coarse tungsten grains have reduced influence on the fracture toughness. Nevertheless, the 400°C specimen exhibits an increased fracture toughness compared to the tungsten-copper composite with 50 at.% copper [49] reported in literature. This fracture toughness increase can be attributed to the increased grain size. A similar trend can be deduced from the nanocrystalline [46] and ultrafine grained [50,51] copper. The tungsten-copper composite with 75 at.% [52] has similar fracture toughness level to the investigated composites, as the additional amount of copper enhanced the ductility. Though, the strength is only in

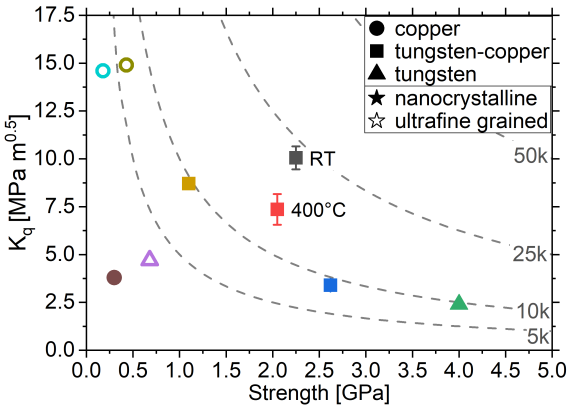

Figure 11: Relation of the investigated composite to refined material compositions, ultra-fine grained copper (cyan circle) [51], nanotwined copper (olive cricle) [50], nanocrystalline copper [46] (brown dot), nanocrystalline tungsten-copper with 75 at.% copper (orange, rectangle) [52], ultra-fine grained tungsten (unfilled purple triangle) [48], nanocrystalline tungsten-copper with 50 at.% copper (blue, rectangle) [49] and magnetron sputtered tungsten (green, triangle) [47].

the range of 1 GPa and thus well below the present material. Consequently, the damage tolerance also increased from 10.000 MPa$\sqrt{\text{m}}$, where the nanocrystalline tungsten and tungsten-copper composites reside, to 25.000 MPa$\sqrt{\text{m}}$ for the present case, see the iso-lines in Fig. 11. However, due to the observed intercrystalline fracture, the damage tolerance of the tungsten-copper composite would benefit from grain boundary strengthening, e.g. by grain boundary segregation [52]. Another possibility to enhance the damage tolerance would be to strengthen the copper phase and enable twinning as an additional deformation mechanism e.g. by alloying copper with zinc [53].

Motivated by the promising material properties of this microstructurally optimized tough nanocomposite, possibilities for transferring the achieved results to a large-scale production becomes of interest. One possibility would be to sinter bulk materials of nanocrystalline powders by liquid phase sintering or field assisted flash sintering. But processing of nanocrystalline powder is challenging due to oxidation, the necessity to remove powder agglomerates and the unwanted contamination of the powder with elements from the grinding balls or vial. Further, direct upscaling of HPT is limited to thickness of 10 mm and a diameter of ∅60 mm due to the required pressure [54]. Nevertheless, there are different severe plastic deformation methods available in literature for continuous or quasi-continuous material synthesis, *e.g.* accumulative roll bonding (ARB) [55,56], equal channel angular pressing (ECAP) [57], incremental high-pressure torsion (I-HPT) [58], continuous high-pressure torsion (C-HPT) [54] and high pressure tube twisting (HPTT) [59,60]. Though, these techniques often lack the achievable high strain that can be conveniently imposed by HPT. ARB necessitates sintered material sheets as basis and stacks material sheets to bind them by rolling. During stacking different material components like particles, fibers or foils can be incorporated to

enhance the material properties [55]. Nevertheless, ARB results in a layered structure with anisotropic material properties. For the application of C-HPT, HPTT and I-HPT a sintered base material is required, and the processing will result again in a textured microstructure [60]. However, similarly to the present results, application of an increased deformation temperature could reduce the microstructural texture for these techniques. Lastly, ECAP allows to directly consolidate powders, which produces a significant in compositional design, and produces an isotropic microstructure when following appropriate billed pressing paths. Hence, ECAP might be a promising candidate to upscale fabrication of nanocrystalline immiscible nanocomposite materials.

5. Conclusion

A bulk tungsten-copper composite was subjected to high-pressure torsion at different deformation temperatures to tailor the grain size into the nanocrystalline regime, resulting in a bi-modal microstructure despite refinement saturation. By raising the deformation temperature from room temperature to 400°C the matrix grain size was increased by a factor of three from 9 to 28 nm. Whereby coarse tungsten grains embedded in the nanocrystalline matrix changed from a flake-like shape to spherical and enlarged in size. Micro cantilever bending beams with varying size were fabricated to study a possible size effect and the impact of the matrix grain size, utilizing elastic-plastic fracture mechanical evaluation and *in situ* images from the crack initiation point. Inter-crystalline fracture governs the failure process, with features roughly corresponding to the matrix grain size. Additionally, for room temperature cantilevers, the coarse flat tungsten grains formed delamination-like structures on the fracture surface, which reduced the stress triaxiality at the crack front and therefore increased the fracture toughness. Further, the room temperature cantilevers failed mainly by stable crack growth and revealed a size dependency below a cantilever cross-section of 10x10 μm^2 as then the plastic zone size approaches the neutral axis. In the case of the 400°C cantilevers no delaminations formed on the fracture surface, as the crack path passes the spherical coarse tungsten grains. Nevertheless, the fracture behavior changed from unstable to stable with decreasing cantilever cross-section. This occurs as with reduced sample volume less energy is stored in the cantilever, as reflected in the size dependency of the tearing modulus. Despite the different fracture behavior, the determined characteristics are similar, as the criteria for size independent crack initiation values are met. The matrix grain size had only a marginal influence on the fracture characteristics, while the delamination-like structures formed by the coarse flat tungsten grains significantly increased the fracture toughness. This further allows to tailor the material transition from a tungsten shield to the copper cooling block.

Conflict of interest/Competing interests

The authors declare that they have no conflict of interest.

Availability of data and materials

The data generated during the current study are available from the corresponding author on a reasonable request.

Acknowledgments

This work was supported by European Research Council [Grant number: 771146 (TOUGHIT)]. We thank Christina Kainz for the nanoindentation measurements

References

[1] J.W. Davis, V.R. Barabash, A. Makhankov, L. Plöchl, K.T. Slattery, Assessment of tungsten for use in the ITER plasma facing components, J. Nucl. Mater. 258–263 (1998) 308–312. https://doi.org/10.1016/S0022-3115(98)00285-2.

[2] Y. Ueda, K. Tobita, Y. Katoh, PSI issues at plasma facing surfaces of blankets in fusion reactors, J. Nucl. Mater. 313–316 (2003) 32–41. https://doi.org/10.1016/S0022-3115(02)01329-6.

[3] M. Rieth, D. Armstrong, B. Dafferner, S. Heger, A. Hoffmann, M.D. Hoffmann, U. Jäntsch, C. Kübel, E. Materna-Morris, J. Reiser, M. Rohde, T. Scherer, V. Widak, H. Zimmermann, Tungsten as a Structural Divertor Material, 5th FORUM NEW Mater. PART B. 73 (211AD) 11–21. https://doi.org/10.4028/www.scientific.net/ast.73.11.

[4] D. Sun, Y. Wang, S. Huang, J. Zhao, G. Liu, J. Li, Plasma facing component with built-in tungsten wires and a W-Cu functionally graded layer: A finite element assessment, Fusion Eng. Des. 120 (2017) 9–14. https://doi.org/10.1016/j.fusengdes.2017.05.006.

[5] E. Tejado, A. V. Müller, J.H. You, J.Y. Pastor, Evolution of mechanical performance with temperature of W/Cu and W/CuCrZr composites for fusion heat sink applications, Mater. Sci. Eng. A. 712 (2018) 738–746. https://doi.org/10.1016/j.msea.2017.12.054.

[6] X. Chen, W. Sun, X. Li, X. Wang, H. Yan, K. Li, Experimental and numerical studies on W–Cu functionally graded materials produced by explosive compaction–welding sintering, Fusion Eng. Des. 137 (2018) 349–357. https://doi.org/10.1016/j.fusengdes.2018.10.016.

[7] International Atomic Energy Agency, Technical Basis for the Iter Final Design Report, Cost Review and Safety Analysis, Int. Organ. (1998).

[8] E. Gaganidze, D. Rupp, J. Aktaa, Fracture behaviour of polycrystalline tungsten, J. Nucl. Mater. 446 (2014) 240–245. https://doi.org/10.1016/j.jnucmat.2013.11.001.

[9] V. Barabash, A. Peacock, S. Fabritsiev, G. Kalinin, S. Zinkle, A. Rowcliffe, J.W. Rensman, A.A. Tavassoli, P. Marmy, P.J. Karditsas, F. Gillemot, M. Akiba, Materials challenges for ITER - Current status and future activities, J. Nucl. Mater. 367-370 A (2007) 21–32. https://doi.org/10.1016/j.jnucmat.2007.03.017.

[10] S.J. Park, Y.S. Kwon, S. Lee, J.L. Johnson, R.M. German, Thermal management application of nano tungsten-copper composite powder, Proc. World Powder Metall. Congr. Exhib. World PM 2010. 5 (2010) 2010.

[11] E. Tejado, A. V. Müller, J.H. You, J.Y. Pastor, The thermo-mechanical behaviour of W-Cu metal matrix composites for fusion heat sink applications: The influence of the Cu content, J. Nucl. Mater. 498 (2018) 468–475. https://doi.org/10.1016/j.jnucmat.2017.08.020.

[12] A. Khalajhedayati, Z. Pan, T.J. Rupert, Manipulating the interfacial structure of nanomaterials to achieve a unique combination of strength and ductility, Nat. Commun. 7 (2016). https://doi.org/10.1038/ncomms10802.

[13] M. Wurmshuber, S. Doppermann, S. Wurster, S. Jakob, M. Balooch, M. Alfreider, K. Schmuck, R. Bodlos, L. Romaner, P. Hosemann, H. Clemens, V. Maier-Kiener, D. Kiener, Enhancing mechanical properties of ultrafine-grained tungsten for fusion applications, Int. J. Refract. Met. Hard Mater. 111 (2023) 106125. https://doi.org/10.1016/j.ijrmhm.2023.106125.

[14] R.W. Armstrong, 60 years of hall-petch: Past to present nano-scale connections, Mater. Trans. 55 (2014) 2–12. https://doi.org/10.2320/matertrans.MA201302.

[15] E.O. Hall, The deformation and ageing of mild steel: III Discussion of results, Proc. Phys. Soc. Sect. B. 64 (1951) 747–753. https://doi.org/10.1088/0370-1301/64/9/303.

[16] N. Petch, The cleavage strength of polycrystals, J. Iron Steel Res. Int. 174 (1953) 25–28.

[17] I. Sabirov, R. Pippan, Formation of a W-25%Cu nanocomposite during high pressure torsion, Scr. Mater. 52 (2005) 1293–1298. https://doi.org/10.1016/j.scriptamat.2005.02.017.

[18] K.S. Kormout, R. Pippan, A. Bachmaier, Deformation-Induced Supersaturation in

Immiscible Material Systems during High-Pressure Torsion, Adv. Eng. Mater. 19 (2017) 1–19. https://doi.org/10.1002/adem.201600675.

[19] M. Burtscher, M. Zhao, J. Kappacher, A. Leitner, M. Wurmshuber, M. Pfeifenberger, V. Maier-Kiener, D. Kiener, High-temperature nanoindentation of an advanced nanocrystalline W/Cu composite, Nanomaterials. 11 (2021) 1–13. https://doi.org/10.3390/nano11112951.

[20] M. Burtscher, M. Alfreider, C. Kainz, K. Schmuck, D. Kiener, In situ micromechanical analysis of a nano-crystalline W-Cu composite, Mater. Des. 220 (2022) 110848. https://doi.org/10.1016/j.matdes.2022.110848.

[21] R. Pippan, S. Scheriau, A. Hohenwarter, M. Hafok, Advantages and limitations of HPT: A review, Mater. Sci. Forum. 584-586 PA (2008) 16–21. https://doi.org/10.4028/www.scientific.net/msf.584-586.16.

[22] R. Achanta, A. Shaji, K. Smith, A. Lucchi, P. Fua, S. Süsstrunk, Slic Superpixels Compared to State-of-the-Art Superpixels Methods, IEEE Trans. Pattern Anal. Mach. Intell. 34 (2012) 2274–2281. http://ci.nii.ac.jp/naid/110006251524/.

[23] M.J. Pfeifenberger, M. Mangang, S. Wurster, J. Reiser, A. Hohenwarter, W. Pfleging, D. Kiener, R. Pippan, The use of femtosecond laser ablation as a novel tool for rapid micro-mechanical sample preparation, Mater. Des. 121 (2017) 109–118. https://doi.org/10.1016/j.matdes.2017.02.012.

[24] S. Wurster, C. Motz, R. Pippan, Characterization of the fracture toughness of micro-sized tungsten single crystal notched specimens, Philos. Mag. 92 (2012) 1803–1825. https://doi.org/10.1080/14786435.2012.658449.

[25] M. Alfreider, S. Kolitsch, S. Wurster, D. Kiener, An analytical solution for the correct determination of crack lengths via cantilever stiffness, Mater. Des. 194 (2020) 3–7. https://doi.org/10.1016/j.matdes.2020.108914.

[26] M. Alfreider, D. Kozic, O. Kolednik, D. Kiener, In-situ elastic-plastic fracture mechanics on the microscale by means of continuous dynamical testing, Mater. Des. 148 (2018) 177–187. https://doi.org/10.1016/j.matdes.2018.03.051.

[27] ASTM Standard E1820, Standard Test Method for Measurement of Fracture Toughness, ASTM B. Stand. (2013) 1–54. https://doi.org/10.1520/E1820-13.

[28] H. Ledbetter, S.K. Datta, Elastic Constants of a Tungsten-Particle Copper-Matrix Composite, (2017). https://doi.org/10.1299/jsmea1988.34.2.

[29] C.F. Shih, M.D. German, Requirements for a one parameter characterization of crack

tip fields by the HRR singularity, Int. J. Fract. 17 (1981) 27–43. https://doi.org/10.1007/BF00043119.

[30] A.G. Atkins, Z. Chen, B. Cotterell, The essential work of fracture and JR curves for the double cantilever beam specimen: An examination of èlastoplastic crack propagation, Proc. R. Soc. A Math. Phys. Eng. Sci. 454 (1998) 815–833. https://doi.org/10.1098/rspa.1998.0187.

[31] J. Ast, M. Ghidelli, K. Durst, M. Göken, M. Sebastiani, A.M. Korsunsky, A review of experimental approaches to fracture toughness evaluation at the micro-scale, Mater. Des. 173 (2019) 107762. https://doi.org/10.1016/j.matdes.2019.107762.

[32] X.K. Zhu, J.A. Joyce, Review of fracture toughness (G, K, J, CTOD, CTOA) testing and standardization, Eng. Fract. Mech. 85 (2012) 1–46. https://doi.org/10.1016/j.engfracmech.2012.02.001.

[33] M. Wurmshuber, M. Alfreider, S. Wurster, R. Pippan, D. Kiener, Small-scale fracture mechanical investigations on grain boundary doped ultrafine-grained tungsten, Acta Mater. 250 (2022) 18. https://doi.org/10.1016/j.actamat.2023.118878.

[34] P. Zhang, S.X. Li, Z.F. Zhang, General relationship between strength and hardness, Mater. Sci. Eng. A. 529 (2011) 62–73. https://doi.org/10.1016/j.msea.2011.08.061.

[35] C.E. Carlton, P.J. Ferreira, What is behind the inverse Hall-Petch effect in nanocrystalline materials?, Acta Mater. 55 (2007) 3749–3756. https://doi.org/10.1016/j.actamat.2007.02.021.

[36] S.N. Naik, S.M. Walley, The Hall–Petch and inverse Hall–Petch relations and the hardness of nanocrystalline metals, J. Mater. Sci. 55 (2020) 2661–2681. https://doi.org/10.1007/s10853-019-04160-w.

[37] M. Spittel, T. Spittel, Part 3: Non-ferrous Alloys - Heavy Metals, Springer Materials, Berlin, 2016. https://doi.org/10.1007/978-3-642-14174-4.

[38] L. Schweiger, D. Kiener, M. Burtscher, E. Schafler, G. Mori, F. Spieckermann, J. Eckert, From unlikely pairings to functional nanocomposites: FeTi–Cu as a model system, Mater. Today Adv. 20 (2023) 100433. https://doi.org/10.1016/j.mtadv.2023.100433.

[39] R. Hertzberg, R. Vinici, J. Hertzberg, Deformation and fracture mechanics of engineering materials, 5th ed., Wiley, Hoboken, NJ, 1985.

[40] A. Hohenwarter, C. Kammerhofer, R. Pippan, The ductile to brittle transition of ultrafine-grained Armco iron: An experimental study, J. Mater. Sci. 45 (2010) 4805–4812. https://doi.org/10.1007/s10853-010-4635-9.

[41] O. Kolednik, M. Sistaninia, S. Kolitsch, J-integral testing on micro-scale cantilever beam specimens, Eng. Fract. Mech. (2023) 109636. https://doi.org/10.1016/j.engfracmech.2023.109636.

[42] R. Pippan, S. Wurster, D. Kiener, Fracture mechanics of micro samples: Fundamental considerations, Mater. Des. 159 (2018) 252–267. https://doi.org/10.1016/j.matdes.2018.09.004.

[43] T.L. Anderson, Fracture Mechanics, 3rd ed., CRC Press, Boca Raton, 2005. https://doi.org/doi.org/10.1201/9781420058215.

[44] R. Irwin, George, Fracture dynamics, Fract. Met. (1947). https://cir.nii.ac.jp/crid/1573950400137757952.bib?lang=en (accessed April 25, 2023).

[45] A. Hohenwarter, R. Pippan, Fracture and fracture toughness of nanopolycrystalline metals produced by severe plastic deformation, Philos. Trans. R. Soc. A Math. Phys. Eng. Sci. 373 (2015). https://doi.org/10.1098/rsta.2014.0366.

[46] R.R. Keller, J.M. Phelps, D.T. Read, Tensile and fracture behavior of free-standing copper films, Mater. Sci. Eng. A. 214 (1996) 42–52. https://doi.org/10.1016/0921-5093(96)10253-7.

[47] E. Harry, A. Rouzaud, P. Juliet, Y. Pauleau, M. Ignat, Failure and adhesion characterization of tungsten-carbon single layers, multilayered and graded coatings, Surf. Coatings Technol. 116–119 (1999) 172–175. https://doi.org/10.1016/S0257-8972(99)00071-7.

[48] B. Gludovatz, S. Wurster, A. Hoffmann, R. Pippan, Fracture toughness of polycrystalline tungsten alloys, 12th Int. Conf. Fract. 2009, ICF-12. 7 (2009) 5365–5372. https://doi.org/10.1016/j.ijrmhm.2010.04.007.

[49] M. Burtscher, M. Alfreider, C. Kainz, D. Kiener, Deformation and failure behavior of nanocrystalline WCu, Mater. Sci. Eng. A. 887 (2023) 145760. https://doi.org/10.1016/j.msea.2023.145760.

[50] A. Singh, L. Tang, M. Dao, L. Lu, S. Suresh, Fracture toughness and fatigue crack growth characteristics of nanotwinned copper, Acta Mater. 59 (2011) 2437–2446. https://doi.org/10.1016/j.actamat.2010.12.043.

[51] D. Rahmatabadi, M. Tayyebi, A. Sheikhi, R. Hashemi, Fracture toughness investigation of Al1050/Cu/MgAZ31ZB multi-layered composite produced by accumulative roll bonding process, Mater. Sci. Eng. A. 734 (2018) 427–436. https://doi.org/10.1016/j.msea.2018.08.017.

[52] M. Wurmshuber, M. Burtscher, S. Doppermann, R. Bodlos, D. Scheiber, L. Romaner, D. Kiener, Mechanical performance of doped W–Cu nanocomposites, Mater. Sci. Eng. A. 857 (2022) 144102. https://doi.org/10.1016/j.msea.2022.144102.

[53] Y.H. Zhao, X.Z. Liao, Y.T. Zhu, Z. Horita, T.G. Langdon, Influence of stacking fault energy on nanostructure formation under high pressure torsion, Mater. Sci. Eng. A. 410–411 (2005) 188–193. https://doi.org/10.1016/j.msea.2005.08.074.

[54] Z. Horita, Y. Tang, T. Masuda, Y. Takizawa, Severe Plastic Deformation under High Pressure: Upsizing Sample Dimensions, Nippon Kinzoku Gakkaishi/Journal Japan Inst. Met. 86 (2022) 107–120. https://doi.org/10.2320/JINSTMET.J2022009.

[55] T. Hausöl, V. Maier, C.W. Schmidt, M. Winkler, H.W. Höppel, M. Göken, Tailoring materials properties by accumulative roll bonding, Adv. Eng. Mater. 12 (2010) 740–746. https://doi.org/10.1002/adem.201000044.

[56] M. Ebrahimi, Q. Wang, Accumulative roll-bonding of aluminum alloys and composites: An overview of properties and performance, J. Mater. Res. Technol. 19 (2022) 4381–4403. https://doi.org/10.1016/j.jmrt.2022.06.175.

[57] K. Matsuki, T. Aida, T. Takeuchi, J. Kusui, K. Yokoe, Microstructural characteristics and superplastic-like behavior in aluminum powder alloy consolidated by equal-channel angular pressing, Acta Mater. 48 (2000) 2625–2632. https://doi.org/10.1016/S1359-6454(00)00061-6.

[58] A. Hohenwarter, Incremental high pressure torsion as a novel severe plastic deformation process: Processing features and application to copper, Mater. Sci. Eng. A. 626 (2015) 80–85. https://doi.org/10.1016/j.msea.2014.12.041.

[59] L.S. Toth, C. Chen, A. Pougis, M. Arzaghi, J.J. Fundenberger, R. Massion, S. Suwas, High pressure tube twisting for producing ultra fine grained materials: A review, Mater. Trans. 60 (2019) 1177–1191. https://doi.org/10.2320/matertrans.MF201910.

[60] M. Arzaghi, J.J. Fundenberger, L.S. Toth, R. Arruffat, L. Faure, B. Beausir, X. Sauvage, Microstructure, texture and mechanical properties of aluminum processed by high-pressure tube twisting, Acta Mater. 60 (2012) 4393–4408. https://doi.org/10.1016/j.actamat.2012.04.035.

Publication B

Assessing the Fracture Toughness in Tungsten-Based Nanocomposites: A Micro-Mechanical Approach

Materials and Design, (**2024**) under review (July 2024)
doi:

Assessing the Fracture Toughness in Tungsten-Based Nanocomposites: A Micro-Mechanical Approach

K. Schmuck[1 2], M. Burtscher[1], M. Alfreider[1], D. Kiener[a,1]

[a] *Corresponding author: daniel.kiener@unileoben.ac.at*

[1] *Montanuniversität Leoben, Department of Materials Science, Chair of Materials Physics, Jahnstraße 12, Leoben, 8700, Austria*

Abstract

Nanocrystalline tungsten-copper composites can favorably combine the outstanding material properties of both elements. However, the composites oftentimes lack a high damage tolerance. This work investigates tungsten-copper composites fabricated from elemental powders with 80 wt.% tungsten and either copper or α-brass containing 20 wt.% zinc, respectively. The latter was selected to enhance the twinning tendency of the secondary phase. Moreover, high-pressure torsion is used to compact the powders, strengthen the resulting composite by grain refinement, and tailor the grain-size in the nanocrystalline regime by varying the final deformation temperature between RT, 400°C and 550°C, resulting in average grain-sizes of 9 nm, 15 nm and 28 nm, respectively. Notably, hardness measurements revealed a transition from normal to inverse Hall-Petch behavior for grain-sizes below 11 nm. To examine the fracture properties, micro-cantilever bending beams with a cross-section of 10x10 µm² were fabricated from the nanocomposites. Postmortem analysis of the instable fracture surfaces revealed that inter-crystalline failure governed the fracture process. Evaluation of these experiments indicated a fracture toughness of about 3 MPa$\sqrt{m}$. The slight decrease of fracture toughness between a grain-size of 9 nm to 14 nm indicates a change in the dominant deformation mechanism, possibly from grain boundary-dominated to a dislocation based mechanism. Further grain-size increase to 28 nm reversed this trend and raised the fracture toughness to 3.4 MPa$\sqrt{m}$. Additionally, alloying the copper phase with zinc raised the composites strength and retained the composites fracture toughness, benefiting the damage tolerance.

Keywords: *tungsten-copper, tungsten-α-brass, high-pressure torsion, micro-cantilever bending, nanocrystalline microstructure*

[2]Corresponding author at: Department of Materials Physics, Montanuniversität Leoben, Leoben, Austria.
E-Mail Address: klemens.schmuck@unileoben.ac.at (K. Schmuck)

1. Introduction

Over the last decades, tungsten-copper composites have increasingly attracted the attention of researchers. As the composite allows to inherit the outstanding material properties of both elements, such as high intrinsic strength and hardness at elevated temperatures, ability to withstand high-temperature loads due to a high melting point, good electrical- and thermal conductivity, increased wear and arc erosion resistance, excellent neutron irradiation resistance, low vapor pressure and possible cooling due to transpiration of copper [1–8]. Due to these properties, tungsten-copper composites are commonly used in high-performance applications, in particular for high-voltage switches, electronic packaging, electrodes for resistance welding, aircraft nose cones and military parts [5,6,8–12]. Furthermore, tungsten-copper composites are frequently considered as material candidates for rolling guides in steel production [8] and plasma facing components in fusion reactors [2,4,13–15].

Safety relevant applications require materials that combine high damage- and fracture-tolerance. Both properties can be enhanced by simultaneously increasing the material's strength and ductility, which are naturally mutual exclusive [16–18]. This exclusivity can be mitigated by reducing the grain-size down to the ultra-fine grained and nanocrystalline regime [17,19–21]. Though, in the nanocrystalline regime the strength increase can be reversed below a certain grain-size, known as an inverse Hall-Petch behavior [22–25]. Moreover, by decreasing the grain-size the dominant deformation mechanisms in materials transforms from dislocation mediated to grain boundary governed plasticity. For this transition literature reports a grain-size of about 10 nm and 30 nm for bcc and fcc materials, respectively [26–28]. Further benefits of refined microstructures arise in applications for plasma facing components, as a finer grain-size shifts the softening effect of irradiation induced helium bubbles to higher doses and inhibits the formation of blisters [16]. Furthermore, Zhang *et al.* [29] reported an increased wear and arc resistance for refined microstructures, benefiting the application in high-voltage contacts.

Still, grain refinement sacrifices ductility due to decreasing strain hardening capabilities, as the accumulation of dislocations is restricted by either the grain-size or dislocation saturation [30–34]. The latter occurs especially for severe plastic deformation techniques due to the refinement process and respective saturation. Nevertheless, Zhao *et al.* [33] increased the ductility and strength of high-pressure torsion deformed copper by decreasing the stacking fault energy. The decrease was achieved by alloying copper with zinc, enabling the accumulation of twins as an additional deformation mechanism. To investigate the impact of stacking fault energy to promote the twinning tendency, Zhao *et al.* [34] varied the zinc content of the bulk samples between 0, 10 and 30 wt.%. They concluded that 10 wt.% zinc results in an ideal stacking fault energy, increasing the twinning tendency and enhancing the strain hardening capacities. A similar result was reported by Holub *et*

al. [35], using elemental powders as precursors. They alloyed the powders by ball milling, followed by high-pressure torsion compaction of these powders to form bulk samples. These samples were subsequently subjected to further high-pressure torsion (HPT) steps for grain refinement down to the nanocrystalline regime. Additional to the stacking fault energy, the twinning tendency depends also on the grain-size. The ideal grain-size for copper is around 40 nm [36,37].

To the best knowledge of the authors, fracture mechanical studies of nanocrystalline tungsten-copper and tungsten-α-brass composites produced from powders are lacking in the literature. Therefore, this work discusses the fracture mechanics and material parameters for these composites. For that, tungsten-copper and tungsten-α-brass composites with 80 wt.% tungsten were analyzed. A ratio of 90 wt.% copper and 10 wt.% zinc was selected for the α-brass to retrieve an ideal stacking fault energy with high twinning tendency. This enabled to study the influence of zinc on the different investigated material properties. To obtain a homogeneous microstructure within in the nanocrystalline regime, multiple HPT steps were conducted. Thereby, the temperature of the last deformation step was adjusted to tailor the grain-size. The fracture mechanical response was investigated with respect to the microstructural feature size by *in situ* micro-cantilever bending beams.

2. Experimental

2.1 Sample Preparation

Due to the lack of available bulk material with the composition of 80 wt.% tungsten, 18 wt.% copper and 2 wt.% zinc, the samples investigated in this study were fabricated from elemental powders: tungsten (2 µm, purity 99.97%, Plansee SE), copper (14-25 µm, purity 99%, Merck KGaA) and zinc (<149 µm, purity 99.9%, Alfa Aesar). The elemental powders were handled in a glove box (M. Braun LABstar Glove Box Workstation) to prevent powder degradation, *e.g.* oxidation.

The copper and zinc powders were mechanically alloyed by ball milling to produce an α-brass powder containing 90 wt.% copper and 10 wt.% zinc. Therefore, the stainless steel vials were filled with 15 g of the powder mixture and 150 g stainless steel balls with a diameter of 5 mm. Filling and removing the powder from the vials was performed inside the glove box to sustain the argon atmosphere throughout the milling process. The powders were milled in a planetary ball mill (Retsch PM400) for 1.5 h with a periodic sequence of 5 minutes milling followed by a break of equal duration to reduce a possible thermal influence during milling and to allow vial, grinding medium and powder to cool down [35].

The powders were mixed in the ratio of 80 wt.% tungsten and 20 wt.% of either pure copper

or α-brass powder to fabricate bulk samples. The powder mixtures were subjected to HPT to obtain green compacts [30]. A mini chamber, described by Wurmshuber *et al.* [18], was used to prevent oxidation during compaction. This compaction was performed at a nominal pressure of 12 GPa and a rotational speed of 1.28 rpm for a quarter of a rotation. The compaction anvils have a cavity with 8 mm diameter and 0.3 mm depth. For all further HPT processing, the cavity had a width of 8 mm diameter and 0.15 mm depth. Subsequent HPT steps were performed with a rotational speed of 1.28 rpm at a nominal pressure of 12 GPa. To homogenize the microstructure, the green compacts were subsequently subjected to HPT deformation at 200°C for 30 turns followed by 50 turns at RT. A similar two stepped process was applied by Wurmshuber *et al.* [7] to tungsten-copper compositions with a copper content of 25 wt.% and 50 wt.%, revealing the necessity of the multi-step processing for a homogenous microstructure evolution. Thereby, one turn corresponds to an equivalent strain of 72 at a radius of 3 mm [38]. Certain specimens were further deformed at 400°C for 50 turns to tailor the grain-size. Additionally, one specimen of the tungsten-α-brass composition was deformed at 550°C for 50 turns after the RT processing step to obtain an even larger grain-size.

2.2 Microstructure Characterization

The sample disks were cut into two halves with a wire saw, see Figure 1. One-half was embedded and mechanically polished to examine the microstructural saturation and homogeneity along the radius. On this specimen, the micro hardness along the radius was measured (HV1, Zwick Roell Durascan 20). The indents were placed on the center line of the disk thickness with a spacing of 0.25 mm between the indents along the radius, see Figure 1 a). Additionally, the microstructure was analyzed by scanning electron microscopy (SEM; Zeiss LEO type 1525, Oberkochen, Germany) along the radius with a step size of 0.5 mm, to obtain a qualitative insight into the microstructural homogeneity and -saturation, depicted in Figure 1 a).

The second halves of the HPT disks were used to perform nanoindentation, analyze the grain-size and characterize the fracture process. Therefore, the disk halves were cut into quarters. One quarter piece was manually ground and polished to a wedge-like shape to reduce the subsequent preparation time for lamella and cantilever cutting, illustrated in Figure 1 a). The final wedge-tip thickness (AD) was between 30 µm and 50 µm. Scanning transmission electron microscopy (STEM; JEOL JEM-2200FS microscope, JEOL Ltd.) was used to analyze the grain-size. Therefore, thin lamellas were manufactured at a disk radius of about 3 mm by focused ion beam milling (FIB; Zeiss Auriga Laser platform), see Figure 1 a). The lamellas were thinned to approximately 100 nm at a 30 kV acceleration voltage and by subsequently reducing the FIB current from 2 nA for coarse milling to 50 pA in the final

polishing step.

2.3 Mechanical Characterization

2.3.1. Nanoindentation

On the second quarter, nanoindentations (FT-NMT04, FemtoTools AG) were performed with a Berkovich tip to determine the composites Young's moduli. As mentioned above the hardness was only used to assess microstructural saturation, thus the hardness obtained from nanoindentation was neglected. For that, the sample disk quarter was ground and polished on the back and front side to obtain smooth and parallel surfaces. The final polishing step suspension had a particle size of 0.05 µm. Before measuring, the stiffness of the indentation system was calibrated on fused silica. All indents on the sample were placed at radii above 2 mm, as illustrated by the cyan triangles on the left quarter in Figure 1 a).

2.3.2. Cantilever Preparation

The cantilevers were fabricated on the quarter used for the STEM analysis and pre-cut at a radius of approximately 3 mm by femtosecond laser ablation [39] to a cantilever height of about 20 µm, as illustrated in Figure 1 a). The final shaping step of the cantilevers was performed by FIB milling. The current was subsequently reduced from 20 nA for coarse machining to 2 nA in the polishing step. The final cantilevers had a cross-section (WxB) of 10x10 µm^2 with a cantilever length (L) of about 40 µm and an initial notch depth (a) of 0.44 x W. The notch was fabricated by line milling from the top view with a current of 500 pA. Figure 1 b) illustrates schematically the final cantilever geometry with all essential geometric parameters, while Figure *1* c) depicts a final cantilever before *in situ* testing.

2.3.3. Test Setup

To test the cantilevers in a displacement controlled fashion two micro/nano indenters were used; an ASMEC indenter (UNAT SEM 1, ASMEC GmbH) mounted in a SEM (DSM 982, Carl Zeiss AG) and a FemtoTools (FT-NMT04, FemtoTools AG) situated in a SEM (SEM 1525, Carl Zeiss AG). The two different measurement systems were selected to compare the results from different loading conditions, namely partial unloading versus continuous stiffness measurement. Both indenters employed a loading rate of 50 nm/s. The ASMEC indenter had a noise level of 50 µN in vacuum. To assess the crack length for the elastic-plastic fracture mechanical evaluation, the cantilevers were loaded to a maximum displacement of 16 µm with 15 sequential unloading steps, evenly distributed along the load signal [40]. Each

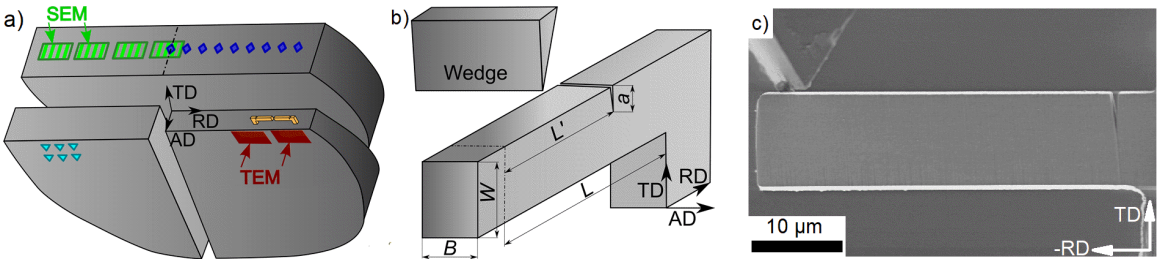

Figure 12: Sample investigation and preparation steps. a) Disk halves produced by high-pressure torsion illustrating schematically the measurement positions, Vickers hardness measurement (blue diamonds), backscatter electron imaging (green patterned squares), nanoindentation measurements (cyan triangles), micro-cantilever bending beams position (orange) and the scanning transmission electron microscopy lamella position (red rectangles). b) Schematic drawing of a cantilever with all essential geometry parameters. c) In situ cantilever before testing. To access a colored version of this graphic the reader is referred to the online version of the article

unloading step consisted of a displacement drop of 10% capped at 2 µm. Before and after each unloading, a hold segment of 10 s was employed. The FemtoTools indenter had a noise level of 100 nN in vacuum and allows superimposing the loading signal with a sinusoidal signal for quasi-continuous stiffness measurement, referred to as dynamic measurement in this work. The imposed signal had an amplitude of 2 nm and a frequency of 200 Hz. Nevertheless, the cantilevers tested by the FemtoTools were elastically pre-loaded up to 400 nm to determine the initial stiffness. After pre-loading, the cantilevers were unloaded and then loaded up to a maximum displacement of 5 µm, upon which all cantilevers exhibited unstable fracture at displacements of about 1 µm. The recording frequency of the FemtoTools indenter was set to 500 Hz. Further, in both setups, an SEM was used to record *in situ* images at a rate of one frame per second using the in-lens secondary electron detector.

2.3.4. Fracture Mechanical Evaluation

The load-displacement data of all cantilevers exhibited a perceivable non-linearity before fracture, depicted by the representative load-displacement curves in Figure 2. The inset of Figure 2 gives a detailed view of the non-linearity before failure. Hence, elastic-plastic fracture mechanics (EPFM) was used to evaluate the fracture experiments. The calculation followed the detailed description given in literature by Wurster *et al.* [40] to determine the J-integral. EPFM necessitates knowledge of the current crack length, which was obtained by associating the stiffness variations to cross-sectional changes, in particular the crack extension [41]. In the case of quasi-static loading, the cantilever stiffness was determined by linearly fitting the unloading segments of the load-displacement curves [40]. For the dynamic measurements, the stiffness was obtained directly during the experiment. Further, to convert the stiffness changes to a crack extension, the initial crack length in combination with the initial cantilever stiffness are required [41]. Therefore, the former was determined

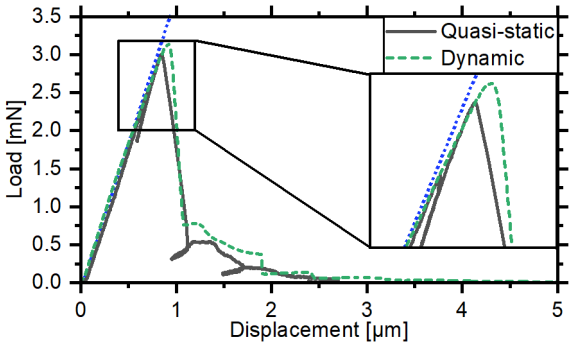

Figure 13: Representative load-displacement curves recorded from quasi-static or dynamic loading. All samples failed unstable and revealed a non-linearity before failure. The dotted blue line should guide the reader's eyes.

postmortem from the fracture surfaces, by measuring the initial crack length at least five times at equidistant locations. The initial stiffness for the quasi-static loading was obtained from the first unloading. In the case of failure before unloading, the loading stiffness was used instead. The initial stiffness for the dynamic measurements was determined by a single elastic pre-loading.

To determine J_q, the J-integral was calculated at the failure point and therefore at the maximum load. For quasi-static loading, which usually allows only evaluation at each distinct unloading, the energy dissipated between the last recorded unloading and fracture were included into the calculation, considering the last measured stiffness.

The determined J_q values were converted into the fracture toughness values (K_q), to facilitate a comparison between literature and data from linear-elastic fracture mechanics. The conversion is performed by the equation [42],

$$K_q = \sqrt{\frac{J_q E}{1-\nu^2}} \tag{1}$$

with the Young's modulus E as determined from nanoindentation data and the Poisson ratio $\nu = 0.32$ [43].

3. Result

3.1 Material Characterization

All specimens exhibited a constant micro hardness value above a radius of 1.5 mm, indicating a saturated grain-size. The mean hardness values for the tungsten-copper composition above this radius were 8.1 ± 0.1 GPa and 7.9 ± 0.1 GPa for the RT and 400°C sample, respectively.

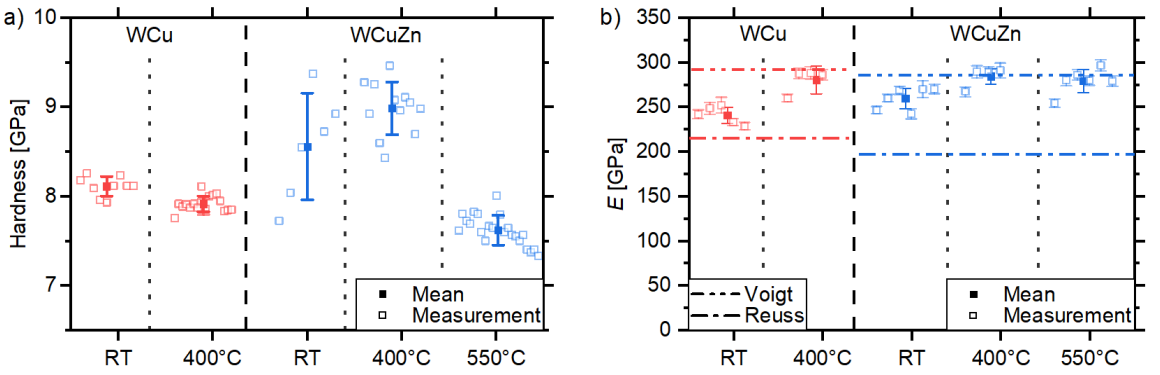

Figure 14: a) Micro Vickers hardness measurements. b) Young's modulus determined by nanoindentation for the nanostructured tungsten-copper and tungsten-α-brass composites.

For the tungsten-α-brass composites, the hardness measurement revealed a mean value of 8.6 ± 0.6 GPa, 9.0 ± 0.3 GPa and 7.6 ± 0.2 GPa for the RT, 400°C and 550°C specimen, respectively. The hardness values are depicted in Figure 3 a). Transparent data points represent individual measurements, while opaque ones illustrate the mean and standard deviation for an individual specimen.

The Young's modulus determined for the individual samples are depicted in Figure 3 b). These measurements revealed a Young's modulus of 241 ± 9 GPa and 280 ± 15 GPa for the tungsten-copper composition deformed at RT and 400°C, respectively. For the tungsten-α-brass composition a Young's modulus of 260 ± 11 GPa, 284 ± 9 GPa and 280 ± 13 GPa was measured for the RT, 400°C and 550°C samples, respectively.

The microstructure was analyzed along the HPT disk radius by SEM imaging. From the SEM images no significant microstructural changes were detected above a radius of 1.5 mm, verifying microstructural saturation and homogeneity at higher radii. Nevertheless, the obtained microstructure consisted of a bi-modal structure with coarse globular tungsten grains embedded into a nanocrystalline matrix consisting of tungsten and either copper or α-brass as second phase. Representative SEM images are illustrated in Figure 4 for the different compositions and final deformation temperatures. The bright spots in the micrographs, exemplary indicated by green arrows, represent coarse tungsten grains.

The grain-size of the nanocrystalline matrix was analyzed by STEM as depicted in Figure 5. To quantify the mean grain-size, several regions per specimen were evaluated utilizing the watershed algorithm for grain segmentation [44,45]. The grain-size distributions of the respective nanocrystalline matrixes are depicted in Figure 6 and the essential statistical values of these distributions are listed in Table 1.

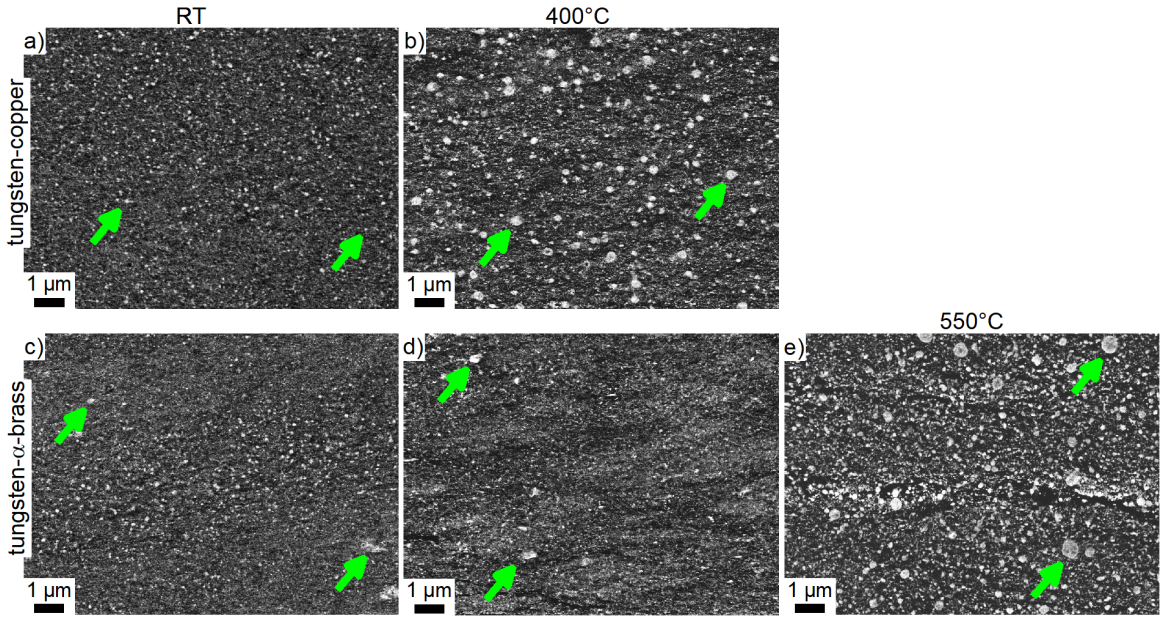

Figure 15: Representative microstructures of the tungsten-copper (a, b) and tungsten-α-brass (c-e) nanocomposites and varying deformation temperatures recorded by the backscatter electron detector above a disk radius of 1.5 mm. The green arrows indicate coarse tungsten grains.

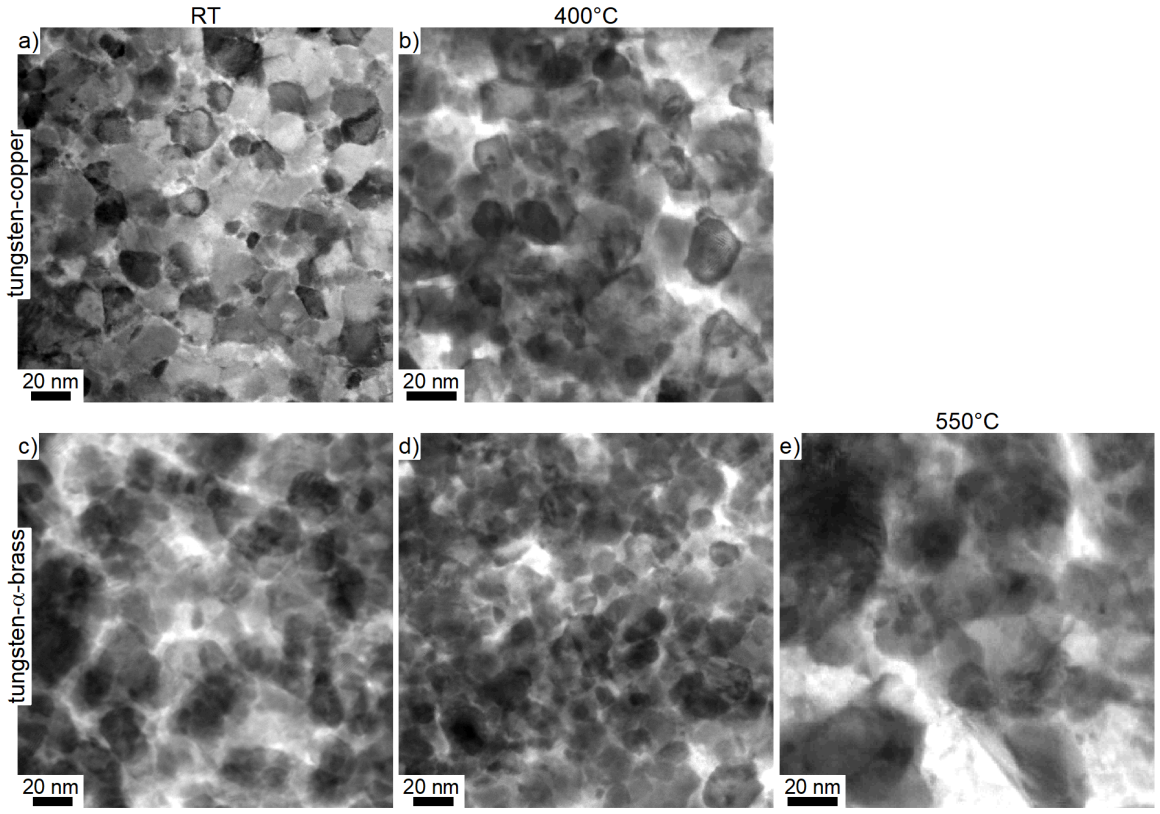

Figure 16: STEM micrographs to measure the grain-size of the nanocrystalline tungsten-copper (a, b) and tungsten-α-brass (c-e) matrix for varying final deformation temperatures, recorded by scanning transmission electron microscopy.

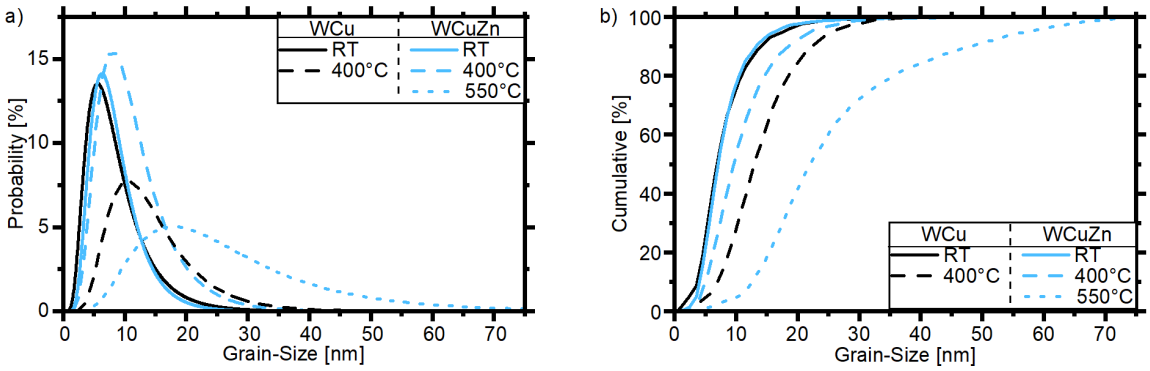

Figure 17: Grain-size distribution for the tungsten-copper (WCu) and tungsten-α-brass (WCuZn) compositions deformed at different final deformation temperatures, whereby a) depicts the probability density function (pdf) and b) the cumulative density function (cdf). For the colored version, the reader is referred to the online version of this article.

Table 2: Statistics of the grain-size distributions measured for the different sample compositions and final deformation temperatures (T). The given statistical values are: the mean with standard deviation ($\overline{d}$), the median (d_{50}), the 15$^{\text{th}}$- (d_{15}) and 85$^{\text{th}}$ percentile (d_{85}). The last column represents the evaluated grain count.

T [°C]	$\overline{d}$ [nm]	d_{50} [nm]	d_{15} [nm]	d_{85} [nm]	Grains [-]
tungsten-copper					
RT	9 ± 6	7	5	13	1693
400°C	14 ± 6	13	9	21	1892
tungsten-α-brass					
RT	9 ± 5	8	5	12	2897
400°C	11 ± 6	10	6	17	1515
550°C	28±16	23	15	43	2302

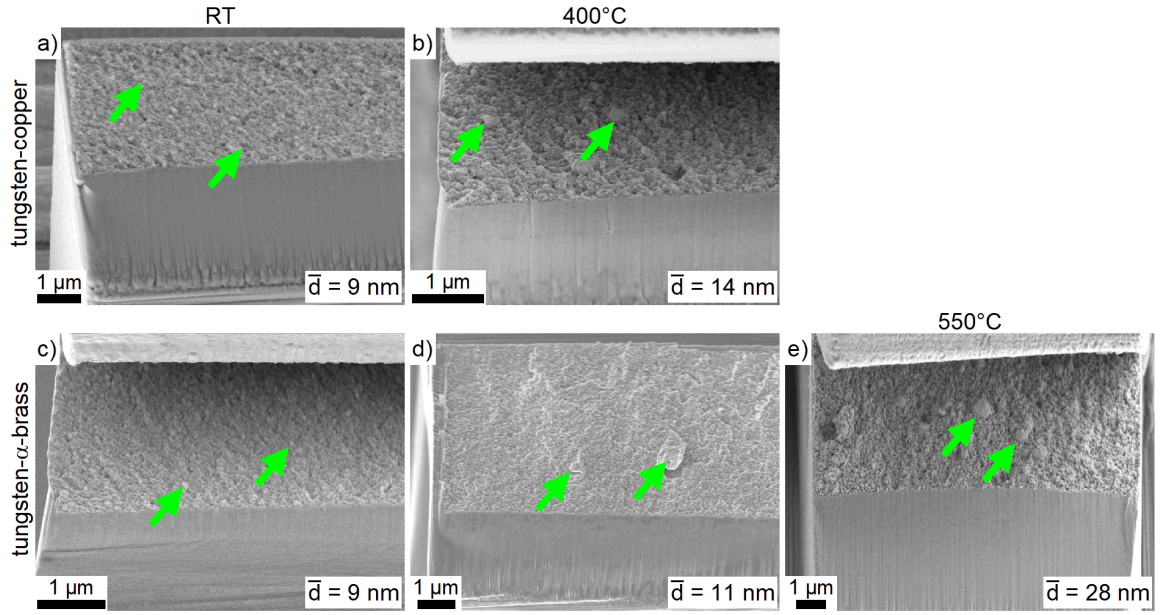

Figure 18: Postmortem analysis of the fracture surfaces for the tungsten-copper a), b) and the tungsten-α-brass c)-e) composition for the different grain-sizes. Representative coarse tungsten-grains are marked with a green arrow.

3.2 Fracture Mechanical Evaluation

All tested cantilevers failed unstable, and the respective fracture surfaces were analyzed postmortem to characterize the failure type and relate the microstructure to the fracture surface, as depicted in Figure 7. With increasing grain-size, increasingly rougher fracture surfaces are also obtained, as evident in Figure 7. The surface roughness observed from the micrographs is comparable to the grain-size present in the individual microstructures. The nanocrystalline matrix grains are unresolved due to the resolution limit of the micrographs. Nevertheless, the structure observed on the fracture surfaces is closely related to the microstructure of the sample, compare Figure 4 and Figure 7.

Furthermore, fracture surface recordings were used to determine the initial crack length. For all cantilevers, the initial crack fronts were relatively straight. Nevertheless, the initial crack fronts exhibited some variability, which was estimated by the standard deviation over multiple crack length measurements along the crack front. This resulted in a standard deviation of the crack length for individual cantilevers of 64 nm, 122 nm and 380 nm for the minimum, median and maximum deviation of the crack length, respectively. This in turn results in a relative variation of 1.4%, 2.8% and 7.3% for the minimal, median and maximal variability, respectively.

The mechanical data collected during the fracture experiments was used to calculate the fracture toughness according to EPFM. Figure 8 depicts the determined J_q values, whereby

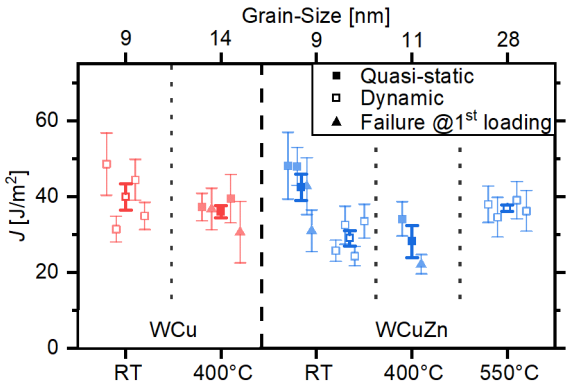

Figure 19: Fracture characteristics in terms of J-integral determined for the material composition tungsten-copper (WCu) and tungsten-α-brass (WCuZn) by testing single-edge notched bending cantilevers. For the colored version, the reader is referred to the online version of this article.

the transparency of the data points follows the same scheme as before. The measurement error of individual cantilevers was approximated by error propagation, considering the errors from material properties and geometrical measurements. Thereby, the initial crack length measurement error, estimated by the standard deviation from the postmortem initial crack length measurements, impacted the measurement error the most. For tungsten-copper, a mean J_q of 40 ± 4 $\frac{J}{m^2}$ and 36 ± 2 $\frac{J}{m^2}$ was determined for the RT and 400°C samples, respectively. To compare the quasi-static and dynamic setup, two sets of cantilevers were fabricated for the tungsten-α-brass composition deformed at RT. For both loading conditions the cantilever exhibited a similar load-displacement response and the failure occurred at a displacement of about 1 µm, see the representative loading curves in Figure 2. Though, the calculated J_q evidenced significant difference for quasi-static and dynamic loading, which were 42 ± 4 $\frac{J}{m^2}$ and 29 ± 2 $\frac{J}{m^2}$, respectively. For the tungsten-α-brass samples deformed at elevated temperatures of 400°C and 550°C, a mean J-integral value of 28 ± 4 $\frac{J}{m^2}$ and 37 ± 1 $\frac{J}{m^2}$ was determined. The estimated errors directly correlate to the single measurement scatter. This scatter is increased for the RT sample of both compositions and relates to the more significant variation of $\frac{a_0}{W}$ among the cantilevers. Further, the 400°C tungsten-α-brass sample exhibited an increased scatter as only two cantilevers were tested successfully. This was caused by the loss of cantilevers during sample transfer or invalid tests when the indenter hit some material in the background during loading.

4. Discussion

The next section outlines the possible reasons for the discrepancy between quasi-static and dynamic loading, followed by the discussion of deformation temperature impact on the microstructure. Thereafter, the two composites are compared with each other and finally set into context with literature values.

4.1 Dynamic vs. Quasi-Static Loading

Comparison between the quasi-static and dynamic measurement setup reveals an increased J_q value of about 12 $\frac{J}{m^2}$ for the quasi-statically tested cantilevers, see Figure 8. This results from the sequential unloading steps, as they share similarities with low cycle fatigue testing. During loading, the material in front of the crack deforms plastically. Throughout the partial unloading, stresses are relieved and partially inverted. This inversion leads to partial recovery of the plastic zone, but also buildup of compressive stresses and results in the formation of a cyclic plastic zone [46]. Similar findings were reported by Ast *et al.* [47]. They investigated the quasi-static loading and observed a dislocation density reduction during unloading, pointing to plastic recovery. This benefits the J_q values, as this allows to trigger slight hardening effects and enables further energy dissipation during the subsequent loading cycles [48]. Cantilevers that were loaded quasi-statically and failed before the first unloading back this assumptions, as these cantilevers exhibited lower J_q values and suggesting that no cyclic plastic zone has evolve, visible in Figure 8 by the RT tungsten-α-brass composition. Snartland *et al.* [49] reported a similar systematic offset for the fracture toughness determined by quasi-static compared to dynamic loading for single crystal α-iron. This indicates an inherent material and microstructure independent increase for the quasi-static loading condition.

4.2 Grain-Size Effects

In the case of tungsten-copper the hardness reduced from 8.2 GPa to 7.9 GPa with increasing grain-size from 9 nm to 14 nm, following the common Hall-Petch behavior. For the tungsten-α-brass composite a raised hardness from 8.6 GPa to 9 GPa was found for a slightly increasing grain-size form 9 nm to 11 nm. Further, grain-size increase reduced the hardness to 7.6 GPa. The measured hardness values are in agreement with literature data, which states 8 GPa for a nanocrystalline tungsten-copper composite with 33 wt.% copper produced by HPT [45]. Comparing the two compositions reveals a hardness increase for the tungsten-α-brass composite of about 12% for a grain-size of 9 nm. This increase can mainly be attributed to the strengthening of the copper phase, resulting in enhanced mechanical properties even at elevated temperatures [50]. Literature reports a hardness increase for alloying copper with zinc to α-brass of about 30% for a composition with micron sized grains [51]. Accounting for the volume ratio of about 48 vol.% of copper and α-brass phase the increase is in agreement with literature.

Recorded SEM micrographs evidenced a direct correlation between final deformation temperature and obtained grain-size, visible by the enlarging of coarse tungsten grains in Figure 4. Qualitative analysis of the micrographs indicates an increased deformation temperature

dependency for the tungsten-copper composition. This is identifiable by the pronounced enlargement of the coarse tungsten grains between RT and 400°C for about 35% compared to about 6% for the tungsten-copper and tungsten-α-brass composite respectively, see Figure 4. From the STEM recordings a similar trend as by SEM is observable, illustrated in Figure 5. The quantitative grain-size analysis verified this trend and revealed a direct correlation between grain-size and final deformation temperature. Increasing the deformation temperature induced a higher saturation grain-size [52], as depicted by the grain-size distribution curves in Figure 6. For the tungsten-copper composition the analysis revealed an relative mean grain-size increase of 50% by raising the deformation temperature from RT to 400°C, see Table 1. Besides the increased mean, the grain-size distribution broadens for the 400°C tungsten-copper sample, resulting in a significant amount of grains above 20 nm, shown by the black dashed distribution in Figure 6. In the case of tungsten-α-brass the mean grain-size increased only by 22% between RT and 400°C, see Table 1. This modest increase exhibited by the tungsten-α-brass composition occurs due to the harder secondary phase, which supports a pronounced grain refinement. Furthermore, residual elements contribute to a more severe grain refinement during HPT, leading to a lower saturation grain-size at elevated temperatures [53]. Either way, raising the deformation temperature for tungsten-α-brass to 550°C resulted in a grain-size increase of about 300% compared to the RT sample, tabulated in Table 1. This may occur as the brittle to ductile transition temperature of tungsten is about 200°C to 400°C, resulting in a less severe refinement of the grains by tungsten above this temperature [54]. Moreover, the distribution broadened significantly, resulting in a few grains above 50 nm, see the dotted blue distribution curve in Figure 6. Comparing the two compositions indicates an almost identical microstructure and grain-size for the samples deformed at RT. The grain-sizes obtained are in accordance with literature, which reports for HPT refined tungsten-copper samples fabricated from bulk a mean grain-size of 9 nm and 14 nm for a composition with 20 wt.% and 33 wt.% copper, respectively [55,56]. Literature states for a bulk tungsten-copper composite with 20 wt.% copper deformed by HTP at 400°C a grain-size of 28 nm. In this work 14 nm was found. This difference might stem from the use of powder precursor, which are prone to degradation, *e.g.* by oxides. These degradations may reinforce the processed material and affect the refinement process [57]. Similarly, the grain-size deviation for the investigated tungsten-α-brass composites may have a similar origin, as copper and zinc were alloyed by ball-milling.

Relating the hardness to the microstructure for the tungsten-copper composition, the hardness decrease confirms the common Hall-Petch behavior [19–21,58]. In the case of the tungsten-α-brass composition, correlating the grain-size with the hardness values evidences the transition from normal to inverse Hall-Petch characteristics. The latter occurs between samples with a grain-size of 9 nm and 11 nm. Further, by increasing the grain-size up to 28 nm the hardness decreases and indicates common Hall-Petch behavior. The grain-size for

this transition from normal to inverse Hall-Petch is debated in literature, several studies investigated this transition for copper and platinum and reported a transition for grain-sizes in the range of 10 nm to 20 nm [22–25,58].

4.3 Specimen Density

The nanoindentation measurements evidence a slight correlation between final deformation temperature and Young's modulus, see Figure 3 b). The lower and upper bound of Young's modulus can be approximated by the Reuss and Voigt model [59,60]. To approximate the bounds a Young's modulus of 410 GPa [18,61], 130 GPa [62] and 115 GPa [63] are assumed for tungsten, copper and α-brass. This gives estimated bounds of 215 GPa and 292 GPa for the tungsten-copper composition, and in the case of tungsten-α-brass 197 GPa and 286 GPa, respectively. All measured Young's moduli are within the boundaries given by the Reuss and Voigt model, see the Figure 3 b).

Moreover, literature states that Young's modulus differences of the same material can be correlated to the material's porosity [64,65] by

$$E = E_0(1 - 1.9p + 0.9p^2), \tag{2}$$

with p the porosity, E the measured Young's modulus and E_0 the Young's modulus of a fully dense sample. The material density is then given by $1 - p$. To qualitatively estimate the density of the sample, the upper bound value was used for E_0, which is 292 GPa and 286 GPa for the tungsten-copper and tungsten-α-brass composition. This gives for the former a density of approximately 91.4% and 98.4% for the RT and 400°C samples, respectively. In the case of the tungsten-α-brass composition fabricated at RT, 400°C and 550°C a density of 92.4%, 99.6 % and 99.1% was estimated. These approximated densities indicate a qualitative trend across the compositions, where increased temperature enhance the sample density. This is likely a result of the interaction between mechanical and thermal assisted compaction phenomena, similar to sintering. Moreover, adding zinc increases the achieved density slightly, which can be related to the reduced sintering temperature [66]. As the density of the tungsten-α-brass sample is even higher, this would support such an argument. In comparison, literature reports a material density of 90-95%, 98.6%, 98-99% and 99.8% for liquid sintering, activated liquid phase sintering, hot-shock consolidation and liquid sintering in combination with hot-hydrostatic extrusion, respectively [5,8]. Despite the qualitative nature of the estimated densities, the individual sample densities are comparable to conventional sintering methods.

Nevertheless, an approximate porosity of about 10% should be observable in the SEM

micrographs. Though, in the recorded micrographs no pores were observed. Possibly the pores are fine dispersed over the microstructure and therefore remain undetected. A further possibility for a decreased Young's modulus is a change in contact area, which might occur due to the transition of deformation mechanisms. Trelewicz *et al.* [67] reported for tungsten-nickel composites with a grain-size ranging between 20 nm and 3 nm a change from a homogenous, smooth to an inhomogeneous, stepped pile-up during nanoindentation. They argued that this originates in the transition from a conventional homogenous plasticity to unstable plastic flow from a grain-size of 20 nm to 3 nm. No such changes were observed from the nanoindentation imprints performed in this work. Thus, a similar deformation mechanism among all samples and a negligible impact of possible contact area variation are expected. Another possibility is the significantly raised grain boundary volume, which exhibits a reduced stiffness and affects the Young's modulus measurement [25,68,69]. To roughly estimate the grain boundary volume, the ratio between the grain surface and volume can be used. Estimating this for the tungsten-copper composition with a grain-size of 9 nm and 14 nm this yields an increase of 57%. In the case of tungsten-α-brass sample an increase of 22% can be expected. Hence, the decreased Young's modulus for the RT samples can be partially attributed to the increased grain boundary volume fraction.

4.4 Characterizing Fracture

From the fracture surfaces the two investigated material compositions are hardly differentiable, as both exhibit a similar surface structure, illustrated in Figure 7. Qualitatively, the structural feature sizes increase with increasing deformation temperature for both compositions. Relating the grain-size to the respective structural size on the fracture surfaces indicates an inter-crystalline failure for all cantilevers. An exact characterization of the fracture behavior is challenging, as the local crack path is hardly identifiable due to the relatively small grain-size. However, in the case of the tungsten-α-brass with a grain-size of 28 nm, deviation of the crack path along larger surface features is more clearly visible, see Figure 7 e). This suggests a generally high amount of inter-crystalline fracture, as is expected for these nanometer-scaled grain-sizes [70–72]. Additionally, TEM investigations were carried out near the fracture surface to analyze possible grain coarsening due to the applied deformation. From these investigations no significant grain coarsening was observed.

The fracture mechanical evaluation of the tungsten-copper compositions indicates an inverse relation between grain-size and determined J_q, as J_q is slightly reduced for a grain-size of 14 nm (400°C), visible in Figure 8. Additionally, considering the systematic offset between the quasi-static and dynamic measurement approach, this difference would increase as described above. Hence, increasing the grain-size from 9 nm to 14 nm has drawbacks for the J_q, although the fracture path length increases. Moreover, the increased density of

the 14 nm (400°C) sample has negligible impact on the fracture process compared to the fabricated notch. Thus, the J_q decrease between a grain-size of 9 nm and 14 nm points to a possible change of the deformation mechanism, from easier grain boundary mediated to dislocation-nucleation based deformation, respectively [26,73,74]. Literature reports for the transition of the deformation mechanism a grain-size of about 30 nm for bcc materials such as tungsten [27]. However, the majority of the deformation will be localized in the softer copper phase, which has an fcc crystal structure. For these literature states a transition grain-size of about 10 nm between dislocation-nucleation based and grain boundary mediated processes [26]. This is in accordance with the observed decrease of J_q in this study.

For the tungsten-α-brass composition, the grain-size increase is less pronounced from 9 nm to 11 nm by raising the deformation temperature from RT to 400°C, respectively. Though, the J_q decreased for the latter. Quasi-static testing of both grain-sizes makes the trend clearly visible, illustrated in Figure 8. This trend is similar as for the tungsten-copper composition and points to an analogous transition in deformation mechanisms. In contrast, the larger grain-size of 28 nm (550°C) reverts the trend and exhibits an average increase of 37% in J_q compared to the RT values. On one hand the larger grains increase the crack path length, allowing to dissipate more energy during crack growth. On the other hand, the grain-size 28 nm is closer to the ideal grain-size for an extensive twinning tendency. Literature reports an ideal grain-size of 40 nm to enable twinning as an additional deformation mechanism in pure copper and α-brass with 10 wt.% zinc [36,37]. Below this grain-size, twinning is increasingly challenging due to de-twinning caused by the interaction between partial dislocations and twin boundaries [75]. Despite the significant grain-size increase achieved by raising the deformation temperature, all samples exhibit a grain-size below the ideal grain-size for twinning. However, the considerable increase in grain-size by deformation at 550°C supports an argument for some additional contribution of twinning during fracture, thereby increasing J_q.

Comparison of both compositions reveals that the obtained J_q values are on the same order of magnitude. Nevertheless, the J_q values of tungsten-α-brass are slightly below the tungsten-copper results, despite the enhanced density, visible in Figure 8. A possible explanation for this is the damage introduced by focused ion beam milling of the notch. From literature, it is known that zinc and α-brass are prune to liquid metal embrittlement from gallium [76]. Hence, to rule out a possible embrittlement of the tungsten-α-brass composition during the cantilever fabrication, the penetration depth of gallium was simulated by SRIM [77]. For the simulation the Kinchin-Pease algorithm was used [78]. The acceleration voltage of the gallium ions was set to 30 keV with an incidence beam angle of 0°. This revealed a penetration depth of about 50 nm , 30 nm and 30 nm of gallium in pure zinc, α-brass and the tungsten-α-brass composition, respectively. Due to the small penetration depth, a

major impact on the J_q values from liquid metal embrittlement can be neglected. Hence, the reduced J_q might result from minor additional incorporation of impurities during the required ball milling step to alloy copper and zinc. During this step, traces of residual elements from vial and grinding balls are dissolved in the powder [79]. Nevertheless, in x-ray diffraction measurements of the α-brass powder, such elements were undetected [35]. Still, due to the resolution limit of x-ray diffraction these elements have to be considered and may impact J-integral values.

4.5 Comparing toughness to similar Material Systems

The determined J_q values were converted into conditional linear-elastic fracture toughness K_q to facilitate correlation with literature data. This results in a K_q of 3.3 ± 0.1 MPa$\sqrt{m}$ and 3.3 ± 0.2 MPa$\sqrt{m}$ for the tungsten-copper composites fabricated at RT and 400°C, respectively. For the tungsten-α-brass, the conversion yields 3.2 ± 0.1 MPa$\sqrt{m}$, 3.0 ± 0.2 MPa$\sqrt{m}$ and 3.4 ± 0.1 MPa$\sqrt{m}$ for the RT, 400°C and 550°C sample, respectively. Schmuck *et al.* [55] reports a K_q value of 7.4 MPa$\sqrt{m}$ for a nanocrystalline tungsten-copper composite with 20 wt.% copper. They used as base material bulk and performed a single HPT step to refine the grains, leading to a mean grain-size of 28 nm. For a bulk tungsten-copper composite with 50 wt.% copper deformed by HPT to a mean grain-size of 10 nm, literature reports a K_q value of 8.1 MPa$\sqrt{m}$ [80]. The investigated samples in this work exhibited lower K_q values and were produced from powders, which may impact K_q, as powder particles have a high surface to volume ratio and are therefore prone to degradation, *e.g.* oxidation. Oxygen segregation to grain boundaries is known to reduce the interface adhesion, weaken the grain boundaries and form brittle phases [81]. Although the powders were always handled in an argon atmosphere, slight degradation is challenging to avoid. In addition to oxidation, ball milling may introduce traces of residual elements from vial and grinding balls. Consequently, samples produced from powders are typically sintered in a reduction atmosphere to eliminate oxides and other potential volatile degradation. As reducing atmosphere hydrogen is frequently used for high temperature sintering. In this atmosphere in combination with high temperature zinc tends to evaporated and the zinc content will decrease significantly [82,83]. Another possibility would be sintering at low pressures to remove volatile degradation, but due to the vapor pressure of zinc and copper this is impossible in the present situation. At usual sintering temperatures of around 1250°C the vapor pressure of zinc and copper is about >10 bar and 0.012 mbar, respectively [84]. Either way, for pure nanocrystalline tungsten produced by magnetron sputtering with a grain-size of 30 nm, literature states a K_q of 2.4 MPa$\sqrt{m}$ [85,86]. A higher K_q for the compositions investigated in this work was found, indicating the potential to enhance the damage and fracture tolerance of tungsten by adding a copper as ductile phase.

Moreover, to unravel the relation between K_q and the grain-size, various literature sources were collected to identify possible trends. These points are illustrated in Figure 9 including the K_q values reported in this present study. In the case of pure polycrystalline tungsten all data points fabricated from sintered bulk samples are above the nanocrystalline regime. Their K_q declines with decreasing the grain-size from the coarse to the ultra-fine grained regime. This occurs as tungsten is prone to intercrystalline failure. Thus, the grain boundaries significantly impact the fracture process. For coarse grained materials the grain boundaries are less intrinsically stressed, allowing to accommodate more plasticity [87]. Though, on the lower end of the ultra-fine grained regime Wurmshuber *et al.* [88] reported a strong increase of the K_q to 22 MPa$\sqrt{m}$ for pure tungsten produced from elemental powders. The powder processing route allows to dope the composition to further enhance the mechanical properties of tungsten. They sintered the green compacts and subsequently refined the microstructure by HPT. However, sputtered tungsten with a nanocrystalline microstructure exhibits a low K_q of about 2.4 MPa$\sqrt{m}$ [85,86]. Beside the grain-size influence this reduced K_q can be partially attributed to the absence of sintering in the fabrication process. This assumption is backed by the lower K_q values obtained for coarse grained tungsten produced by chemical vapor deposition [89]. Sintering activates diffusion and the grain boundaries get better interconnected, thus benefiting K_q. In the case of tungsten-copper composites literature lacks data in the ultra-fine grained regime, thus a trend is hardly identifiable over the different magnitudes of grain-sizes. Nevertheless, the coarse grain-sizes exhibit a higher K_q compared to nanocrystalline microstructures. This might stem from the significantly increased amount of grain boundaries in the nanocrystalline regime, similarly as for pure tungsten between the coarse and ultra-fine grained regime. Though in the nanocrystalline regime a slightly inverse relation between fracture toughness and grain-size is observable, which might indicate a transition from dislocation to grain boundary based deformation mechanism. Moreover, tungsten-composites produced from powders without sintering revealed a decreased K_q compared to sintered samples, which points to a similar origin as stated above. Nevertheless, nanocrystalline tungsten-copper composites produced from elemental powders exhibit an enhanced K_q compared to pure sputtered tungsten in the nanocrystalline regime, indicating the potential to raise the damage and fracture tolerance by such nanocomposite design.

5. Conclusion

In this work, tungsten-copper and tungsten-α-brass nanocomposites were produced starting from elemental powders. The powders were compacted and subjected to multiple high-pressure torsion steps to refine the grains to the nanocrystalline regime. These investigations revealed a correlation between the deformation temperature and the obtained grain-size. Raising the temperature from RT to 400°C increased the mean grain-size for tungsten-

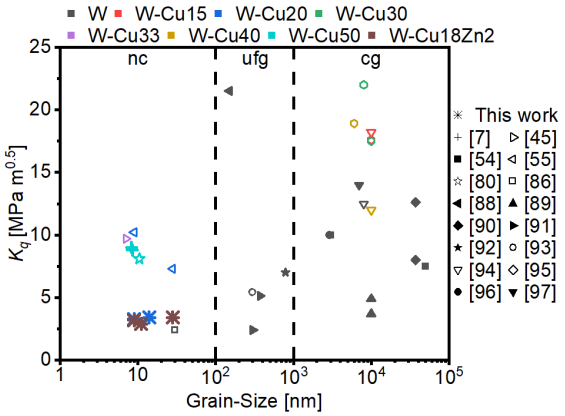

Figure 20: Comparison of the fracture toughness for various grain-sizes of polycrystalline tungsten-based composites in coarse grained (cg), ultra-fine grained (ufg) and nanocrystalline (nc) regime [7,45,54,55,80,86,88–97].

copper from 9 nm to 14 nm. In comparison, the grain-size achieved for the tungsten-α-brass composition was 9 nm, 11 nm and 28 nm for the RT, 400°C and 550°C specimens, respectively. Young's modulus measurements revealed an increase from RT to the elevated temperatures, which is likely a result of the reduced grain boundary volume. Qualitative estimation of the sample density from Young's modulus revealed a density above 90% for all samples, which is comparable to conventional sintering methods. Notched cantilever bending beams were fabricated from the deformed sample material to examine the fracture behavior. Despite the grain-size and material density increase for both compositions, the J-integral values decreased slightly from RT to 400°C, indicating a change in deformation mechanism from grain boundary mediated to dislocation-nucleation based deformation. Enlarging the grain-size lead to an increase in conditional J-integral values, which might indicate the activation of twinning in the tungsten-α-brass composition. Based on the observation in this work, the evaluated fracture performance in terms of J-integral values are on the same order of magnitude and comparable to other nanocrystalline tungsten based materials. However, the addition of zinc improved the other mechanical properties, such as Young's modulus and hardness, which translates into an overall enhanced damage tolerance for such nanocrystalline materials envisioned for use in harsh environments.

CRediT authorship contribution statement

K. Schmuck: Conceptualization, Methodology, Data Curation, Writing - Original Draft Preparation, Writing -review and editing. **M. Burtscher**: Methodology, Data Curation, Writing - review and editing. **M. Alfreider**: Methodology, Writing - review and editing. **D. Kiener**: Conceptualization, Resources, Writing - review and editing, Supervision, Project Administration, Funding Acquisition

Conflict of interest/Competing interests

The authors declare that they have no known competing financial interests or personal relationships that could have appeared to influence the work reported in this paper.

Availability of data and materials

The data generated during the current study are available from the corresponding author on a reasonable request.

Acknowledgments

This work was supported by European Research Council [Grant number: 771146 (TOUGHIT)]. The authors thank Simon Fellner to help with the TEM lift outs and Nadine Buchebner for performing the nanoindentation measurements. Also, this research was funded by the Austrian Science Fund (FWF) [P 34840-N]. For the purpose of open access, the author has applied a CC BY public copyright license to any Author Accepted Manuscript version arising from this submission.

References

[1] L. Dong, W. Chen, L. Hou, N. Deng, C. Zheng, W–Cu System: Synthesis, Modification, and Applications, Powder Metall. Met. Ceram. 56 (2017) 171–184. https://doi.org/10.1007/s11106-017-9884-6.

[2] D. Sun, Y. Wang, S. Huang, J. Zhao, G. Liu, J. Li, Plasma facing component with built-in tungsten wires and a W-Cu functionally graded layer: A finite element assessment, Fusion Eng. Des. 120 (2017) 9–14. https://doi.org/10.1016/j.fusengdes.2017.05.006.

[3] W. Chen, L. Dong, H. Zhang, J. Song, N. Deng, J. Wang, Microstructure characterization of W-Cu alloy sheets produced by high temperature and high pressure deformation technique, Mater. Lett. 205 (2017) 198–201. https://doi.org/10.1016/j.matlet.2017.06.090.

[4] E. Tejado, A. V. Müller, J.H. You, J.Y. Pastor, Evolution of mechanical performance with temperature of W/Cu and W/CuCrZr composites for fusion heat sink applications, Mater. Sci. Eng. A. 712 (2018) 738–746. https://doi.org/10.1016/j.msea.2017.12.054.

[5] L.L. Dong, M. Ahangarkani, W.G. Chen, Y.S. Zhang, Recent progress in development of tungsten-copper composites: Fabrication, modification and applications, Int. J. Refract.

Met. Hard Mater. 75 (2018) 30–42. https://doi.org/10.1016/j.ijrmhm.2018.03.014.

[6] C. Hou, X. Song, F. Tang, Y. Li, L. Cao, J. Wang, Z. Nie, W–Cu composites with submicron- and nanostructures: progress and challenges, NPG Asia Mater. 11 (2019). https://doi.org/10.1038/s41427-019-0179-x.

[7] M. Wurmshuber, M. Burtscher, S. Doppermann, R. Bodlos, D. Scheiber, L. Romaner, D. Kiener, Mechanical performance of doped W–Cu nanocomposites, Mater. Sci. Eng. A. 857 (2022) 144102. https://doi.org/10.1016/j.msea.2022.144102.

[8] B. Zhang, K. Yang, Z. Huang, J. Wang, Recent Advances in W–Cu Composites: A Review on the Fabrication, Application, Property, Densification, and Strengthening Mechanism, Adv. Eng. Mater. 2301204 (2023) 1–34. https://doi.org/10.1002/adem.202301204.

[9] W. Guo, J. Liu, Y. Xiao, S. Li, Z. Zhao, J. Cao, Comparison of penetration performance and penetration mechanism of w-cu shaped charge liner against three kinds of target: Pure copper, carbon steel and Ti-6Al-4V alloy, Int. J. Refract. Met. Hard Mater. 60 (2016) 147–153. https://doi.org/10.1016/j.ijrmhm.2016.07.015.

[10] H. Chen, F. Zheng, W. Cheng, P. Tao, C. Song, W. Shang, B. Fu, T. Deng, Low thermal expansion metal composite-based heat spreader for high temperature thermal management, Mater. Des. 208 (2021) 109897. https://doi.org/10.1016/j.matdes.2021.109897.

[11] H. Xie, W. Guan, H. Lv, H. Yang, M. Gao, Y. Fang, J. Liu, H. Wang, W–Cu/Cu composite electrodes fabricated via laser surface alloying, Mater. Charact. 185 (2022) 111715. https://doi.org/10.1016/j.matchar.2021.111715.

[12] S. Su, Y. Lu, Densified W[sbnd]Cu composite fabricated via laser additive manufacturing, Int. J. Refract. Met. Hard Mater. 87 (2020) 105122. https://doi.org/10.1016/j.ijrmhm.2019.105122.

[13] D.I. Tishkevich, T.I. Zubar, A.L. Zhaludkevich, I.U. Razanau, T.N. Vershinina, A.A. Bondaruk, E.K. Zheleznova, M. Dong, M.Y. Hanfi, M.I. Sayyed, M. V. Silibin, S. V. Trukhanov, A. V. Trukhanov, Isostatic Hot Pressed W–Cu Composites with Nanosized Grain Boundaries: Microstructure, Structure and Radiation Shielding Efficiency against Gamma Rays, Nanomaterials. 12 (2022) 1–14. https://doi.org/10.3390/nano12101642.

[14] A. V. Muller, D. Ewert, A. Galatanu, M. Milwich, R. Neu, J.Y. Pastor, U. Siefken, E. Tejado, J.H. You, Melt infiltrated tungsten–copper composites as advanced heat sink materials for plasma facing components of future nuclear fusion devices, Fusion Eng. Des. 124 (2017) 455–459. https://doi.org/10.1016/j.fusengdes.2017.01.042.

[15] X. Chen, W. Sun, X. Li, X. Wang, H. Yan, K. Li, Experimental and numerical studies

on W–Cu functionally graded materials produced by explosive compaction–welding sintering, Fusion Eng. Des. 137 (2018) 349–357. https://doi.org/10.1016/j.fusengdes.2018.10.016.

[16] M. Wurmshuber, S. Doppermann, S. Wurster, S. Jakob, M. Balooch, M. Alfreider, K. Schmuck, R. Bodlos, L. Romaner, P. Hosemann, H. Clemens, V. Maier-Kiener, D. Kiener, Enhancing mechanical properties of ultrafine-grained tungsten for fusion applications, Int. J. Refract. Met. Hard Mater. 111 (2023) 106125. https://doi.org/10.1016/j.ijrmhm.2023.106125.

[17] A. Khalajhedayati, Z. Pan, T.J. Rupert, Manipulating the interfacial structure of nanomaterials to achieve a unique combination of strength and ductility, Nat. Commun. 7 (2016). https://doi.org/10.1038/ncomms10802.

[18] M. Wurmshuber, S. Doppermann, S. Wurster, D. Kiener, Ultrafine-grained Tungsten by High-Pressure Torsion - Bulk precursor versus powder processing route, IOP Conf. Ser. Mater. Sci. Eng. 580 (2019) 012051. https://doi.org/10.1088/1757-899X/580/1/012051.

[19] R.W. Armstrong, 60 years of hall-petch: Past to present nano-scale connections, Mater. Trans. 55 (2014) 2–12. https://doi.org/10.2320/matertrans.MA201302.

[20] E.O. Hall, The deformation and ageing of mild steel: III Discussion of results, Proc. Phys. Soc. Sect. B. 64 (1951) 747–753. https://doi.org/10.1088/0370-1301/64/9/303.

[21] N. Petch, The cleavage strength of polycrystals, J. Iron Steel Res. Int. 174 (1953) 25–28.

[22] Z. Zhao, S. To, J. Wang, G. Zhang, Z. Weng, Materials & Design A review of micro / nanostructure effects on the machining of metallic materials, Mater. Des. 224 (2022) 111315. https://doi.org/10.1016/j.matdes.2022.111315.

[23] D.A. Konstantinidis, E.C. Aifantis, On the “anomalous” hardness of nanocrystalline materials, Acta Metall. 10 (1999) 1111–1118.

[24] J.E. Carsley, J. Ning, W.W. Milligan, S.A. Hackney, E.C. Aifantis, A SIMPLE, MIXTURES-BASED MODEL FOR THE GRAIN SIZE DEPENDENCE OF STRENGTH IN NANOPHASE, Nanostructured Mater. (1995).

[25] J. Liu, X. Fan, W. Zheng, D.J. Singh, Y. Shi, Nanocrystalline gold with small size : inverse Hall – Petch between mixed regime and super-soft regime, 6435 (2020). https://doi.org/10.1080/14786435.2020.1765039.

[26] S. Cheng, J.A. Spencer, W.W. Milligan, Strength and tension/compression asymmetry

in nanostructured and ultrafine-grain metals, Acta Mater. 51 (2003) 4505–4518. https://doi.org/10.1016/S1359-6454(03)00286-6.

[27] G.M. Cheng, W.W. Jian, W.Z. Xu, H. Yuan, P.C. Millett, Y.T. Zhu, Grain size effect on deformation mechanisms of nanocrystalline bcc metals, Mater. Res. Lett. 1 (2013) 26–31. https://doi.org/10.1080/21663831.2012.739580.

[28] L. Wang, Z. Zhang, X. Han, In situ experimental mechanics of nanomaterials at the atomic scale, NPG Asia Mater. 5 (2013) e40-11. https://doi.org/10.1038/am.2012.70.

[29] Q. Zhang, S. Liang, B. Hou, L. Zhuo, The effect of submicron-sized initial tungsten powders on microstructure and properties of infiltrated W-25 wt.% Cu alloys, Int. J. Refract. Met. Hard Mater. 59 (2016) 87–92. https://doi.org/10.1016/j.ijrmhm.2016.05.014.

[30] D. Jia, Y.M. Wang, K.T. Ramesh, E. Ma, Y.T. Zhu, R.Z. Valiev, Deformation behavior and plastic instabilities of ultrafine-grained titanium, Appl. Phys. Lett. 79 (2001) 611–613. https://doi.org/10.1063/1.1384000.

[31] Y.T. Zhu, X. Liao, Retaining ductility, Nat. Mater. 3 (2004) 351–352. https://doi.org/10.1038/nmat1141.

[32] Z. Budrovic, H. Van Swygenhoven, P.M. Derlet, S. Van Petegem, B. Schmitt, Plastic Deformation with Reversible Peak Broadening in Nanocrystalline Nickel, Science (80-.). 304 (2004) 273–276. https://doi.org/10.1126/science.1095071.

[33] Y.H. Zhao, X.Z. Liao, S. Cheng, E. Ma, Y.T. Zhu, Simultaneously increasing the ductility and strength of nanostructured alloys, Adv. Mater. 18 (2006) 2280–2283. https://doi.org/10.1002/adma.200600310.

[34] Y.H. Zhao, X.Z. Liao, Z. Horita, T.G. Langdon, Y.T. Zhu, Determining the optimal stacking fault energy for achieving high ductility in ultrafine-grained Cu-Zn alloys, Mater. Sci. Eng. A. 493 (2008) 123–129. https://doi.org/10.1016/j.msea.2007.11.074.

[35] G. Holub, Simultaneously increasing strength and ductility of nano-crystalline Cu-Zn-alloys made from powderous raw materials, Montanuniversitaet Leoben, 2023. https://doi.org/10.34901/MUL.PUB.2023.13.

[36] Y.T. Zhu, X.Z. Liao, S.G. Srinivasan, E.J. Lavernia, Nucleation of deformation twins in nanocrystalline face-centered-cubic metals processed by severe plastic deformation, J. Appl. Phys. 98 (2005). https://doi.org/10.1063/1.2006974.

[37] Y.T. Zhu, X.Z. Liao, X.L. Wu, J. Narayan, Grain size effect on deformation twinning and detwinning, J. Mater. Sci. 48 (2013) 4467–4475. https://doi.org/10.1007/s10853-013-7140-0.

[38] R. Pippan, S. Scheriau, A. Hohenwarter, M. Hafok, Advantages and limitations of HPT: A review, Mater. Sci. Forum. 584-586 PA (2008) 16–21. https://doi.org/10.4028/www.scientific.net/msf.584-586.16.

[39] M.J. Pfeifenberger, M. Mangang, S. Wurster, J. Reiser, A. Hohenwarter, W. Pfleging, D. Kiener, R. Pippan, The use of femtosecond laser ablation as a novel tool for rapid micro-mechanical sample preparation, Mater. Des. 121 (2017) 109–118. https://doi.org/10.1016/j.matdes.2017.02.012.

[40] S. Wurster, C. Motz, R. Pippan, Characterization of the fracture toughness of micro-sized tungsten single crystal notched specimens, Philos. Mag. 92 (2012) 1803–1825. https://doi.org/10.1080/14786435.2012.658449.

[41] M. Alfreider, S. Kolitsch, S. Wurster, D. Kiener, An analytical solution for the correct determination of crack lengths via cantilever stiffness, Mater. Des. 194 (2020) 3–7. https://doi.org/10.1016/j.matdes.2020.108914.

[42] ASTM Standard 1820, ASTM B. Stand. (2013) 1–54. https://doi.org/10.1520/E1820-13.Copyright.

[43] H. Ledbetter, S.K. Datta, Elastic Constants of a Tungsten-Particle Copper-Matrix Composite, JSME Int. J. Ser. A Solid Mech. Mater. Eng. 34 (2017). https://doi.org/10.1299/jsmea1988.34.2.

[44] R. Achanta, A. Shaji, K. Smith, A. Lucchi, P. Fua, S. Süsstrunk, Slic Superpixels Compared to State-of-the-Art Superpixels Methods, IEEE Trans. Pattern Anal. Mach. Intell. 34 (2012) 2274–2281. http://ci.nii.ac.jp/naid/110006251524/.

[45] M. Burtscher, M. Alfreider, C. Kainz, K. Schmuck, D. Kiener, In situ micromechanical analysis of a nano-crystalline W-Cu composite, Mater. Des. 220 (2022) 110848. https://doi.org/10.1016/j.matdes.2022.110848.

[46] S. Ghodrat, A.C. Riemslag, L.A.I. Kestens, Measuring plasticity with orientation contrast microscopy in aluminium 6061-T4, Metals (Basel). 7 (2017) 1–8. https://doi.org/10.3390/met7040108.

[47] J. Ast, B. Merle, K. Durst, M. Göken, Fracture toughness evaluation of NiAl single crystals by microcantilevers - A new continuous J-integral method, J. Mater. Res. 31 (2016) 3786–3794. https://doi.org/10.1557/jmr.2016.393.

[48] B.D. Snartland, A.B. Hagen, C. Thaulow, Fracture mechanical testing of single crystal notched α iron micro cantilevers, Eng. Fract. Mech. 175 (2017) 312–323. https://doi.org/10.1016/j.engfracmech.2017.01.024.

[49] B.D. Snartland, C. Thaulow, Fracture toughness testing at the microscale: The effect of the unloading compliance method, Eng. Fract. Mech. 235 (2020) 107135. https://doi.org/10.1016/j.engfracmech.2020.107135.

[50] P. Feltham, G.J. Copley, Yielding and work-hardening in alpha-brasses, Acta Metall. 8 (1960) 542–550. https://doi.org/10.1016/0001-6160(60)90108-5.

[51] P. Chen, G. Luo, M. Li, Q. Shen, L. Zhang, Effects of Zn additions on the solid-state sintering of W-Cu composites, Mater. Des. 36 (2012) 108–112. https://doi.org/10.1016/j.matdes.2011.10.006.

[52] R. Pippan, S. Scheriau, A. Taylor, M. Hafok, A. Hohenwarter, A. Bachmaier, Saturation of Fragmentation During Severe Plastic Deformation, Annu. Rev. Mater. Res. 40 (2010) 319–343. https://doi.org/10.1146/annurev-matsci-070909-104445.

[53] R. Tejedor, K. Edalati, J.A. Benito, Z. Horita, J.M. Cabrera, High-pressure torsion of iron with various purity levels and validation of Hall-Petch strengthening mechanism, Mater. Sci. Eng. A. 743 (2019) 597–605. https://doi.org/10.1016/j.msea.2018.11.127.

[54] A. Giannattasio, Z. Yao, E. Tarleton, S.G. Roberts, Brittle-ductile transitions in polycrystalline tungsten, Philos. Mag. 90 (2010) 3947–3959. https://doi.org/10.1080/14786435.2010.502145.

[55] K. Schmuck, M. Burtscher, M. Alfreider, M. Wurmshuber, D. Kiener, Micro-mechanical fracture investigations on grain size tailored tungsten-copper nano- composites, JOM. (2024). https://doi.org/10.1007/s11837-023-06348-7.

[56] M. Burtscher, M. Zhao, J. Kappacher, A. Leitner, M. Wurmshuber, M. Pfeifenberger, V. Maier-Kiener, D. Kiener, High-temperature nanoindentation of an advanced nanocrystalline W/Cu composite, Nanomaterials. 11 (2021) 1–13. https://doi.org/10.3390/nano11112951.

[57] M. Wurmshuber, S. Doppermann, S. Wurster, D. Kiener, Ultrafine-grained Tungsten by High-Pressure Torsion - Bulk precursor versus powder processing route, in: IOP Conf. Ser. Mater. Sci. Eng., 2019. https://doi.org/10.1088/1757-899X/580/1/012051.

[58] T.G. Nieh, J. Wadsworth, Hall-petch relation in nanocrystalline solids, Scr. Metall. Mater. 25 (1991) 955–958. https://doi.org/10.1016/0956-716X(91)90256-Z.

[59] A. Reuss, Berechnung der Fließgrenze von Mischkristallen auf Grund der Plastizitätsbedingung für Einkristalle ., ZAMM - J. Appl. Math. Mech. / Zeitschrift Für Angew. Math. Und Mech. 9 (1929) 49–58. https://doi.org/10.1002/zamm.19290090104.

[60] W. Voigt, Ueber die Beziehung zwischen den beiden Elasticitätsconstanten isotroper

Körper [On the relationship between the two elastic constants of an isotropic body], Ann. Phys. 274 (1889) 573–587.

[61] E. Lassner, W.-D. Schubert, Properties, chemistry, technology of the element, alloys, and chemical compounds, Kluwer Academic, 2005.

[62] F. Cardarelli, Materials Handbook, Springer, 2018. https://doi.org/10.1007/978-3-319-38925-7.

[63] J.R. Davis, ASM Speciality Handbook, Copper and Copper Alloys, 2001.

[64] M.A. Meyers, A. Mishra, D.J. Benson, Mechanical properties of nanocrystalline materials, Prog. Mater. Sci. 51 (2006) 427–556. https://doi.org/10.1016/j.pmatsci.2005.08.003.

[65] C. Suryanarayana, C.C. Koch, Nanocrystalline materials – Current research and future directions, Hyperfine Interact. 130 (2000) 5–44. https://doi.org/10.1023/A:1011026900989.

[66] P. Chen, Q. Shen, G. Luo, M. Li, L. Zhang, The mechanical properties of W-Cu composite by activated sintering, Int. J. Refract. Met. Hard Mater. 36 (2013) 220–224. https://doi.org/10.1016/j.ijrmhm.2012.09.001.

[67] J.R. Trelewicz, C.A. Schuh, The Hall-Petch breakdown in nanocrystalline metals: A crossover to glass-like deformation, Acta Mater. 55 (2007) 5948–5958. https://doi.org/10.1016/j.actamat.2007.07.020.

[68] H. Ryou, J.W. Drazin, K.J. Wahl, S.B. Qadri, E.P. Gorzkowski, B.N. Feigelson, J.A. Wollmershauser, Below the Hall-Petch Limit in Nanocrystalline Ceramics, ACS Nano. 12 (2018) 3083–3094. https://doi.org/10.1021/acsnano.7b07380.

[69] J. Gong, N. Paul, B. Nagy, M. Dolgos, L. Bottyán, P. Böni, A. Paul, Nano-metric self-diffusion of Fe: effect of grain size, RSC Adv. 7 (2017) 9573–9578. https://doi.org/10.1039/c6ra28310a.

[70] A. Hohenwarter, R. Pippan, Fracture and fracture toughness of nanopolycrystalline metals produced by severe plastic deformation, Philos. Trans. R. Soc. A Math. Phys. Eng. Sci. 373 (2015). https://doi.org/10.1098/rsta.2014.0366.

[71] R. Pippan, A. Hohenwarter, The importance of fracture toughness in ultrafine and nanocrystalline bulk materials, Mater. Res. Lett. 4 (2016) 127–136. https://doi.org/10.1080/21663831.2016.1166403.

[72] A. Pineau, A. Amine Benzerga, T. Pardoen, Failure of metals III: Fracture and fatigue of nanostructured metallic materials, Acta Mater. 107 (2016) 508–544.

https://doi.org/10.1016/j.actamat.2015.07.049.

[73] M. Chandross, N. Argibay, Friction of Metals: A Review of Microstructural Evolution and Nanoscale Phenomena in Shearing Contacts, Tribol. Lett. 69 (2021) 1–27. https://doi.org/10.1007/s11249-021-01477-z.

[74] J.C.M. Li, C.R. Feng, B.B. Rath, Emission of Dislocations from Grain Boundaries and Its Role in Nanomaterials, (2020) 1–12. https://doi.org/https://doi.org/10.3390/cryst11010041.

[75] Y. Cao, Y.B. Wang, Z.B. Chen, X.Z. Liao, M. Kawasaki, S.P. Ringer, T.G. Langdon, Y.T. Zhu, De-twinning via secondary twinning in face-centered cubic alloys, Mater. Sci. Eng. A. 578 (2013) 110–114. https://doi.org/10.1016/j.msea.2013.04.075.

[76] P.J.L. Fernandes, D.R.H. Jones, The effects of microstructure on crack initiation in liquid-metal environments, Eng. Fail. Anal. 4 (1997) 195–204. https://doi.org/10.1016/s1350-6307(97)00010-1.

[77] J.F. Ziegler, M.D. Ziegler, J.P. Biersack, SRIM - The stopping and range of ions in matter (2010), Nucl. Instruments Methods Phys. Res. Sect. B Beam Interact. with Mater. Atoms. 268 (2010) 1818–1823. https://doi.org/10.1016/j.nimb.2010.02.091.

[78] Kinchin, The displacement of atoms in solids during irradiation, Solid State Phys. 2 (1956) 307.

[79] B.T. McDermott, C.C. Koch, Preparation of beta brass by mechanical alloying of elemental copper and zinc, Scr. Metall. 20 (1986) 669–672. https://doi.org/10.1016/0036-9748(86)90487-4.

[80] M. Burtscher, M. Alfreider, C. Kainz, D. Kiener, Deformation and failure behavior of nanocrystalline WCu, Mater. Sci. Eng. A. 887 (2023) 145760. https://doi.org/10.1016/j.msea.2023.145760.

[81] R. Bodlos, D. Scheiber, J. Spitaler, L. Romaner, Modification of the Cu/W Interface Cohesion by Segregation, Metals (Basel). 13 (2023) 1–16. https://doi.org/10.3390/met13020346.

[82] J.M. Koo, H. Araki, S.B. Jung, Effect of Zn addition on mechanical properties of brass hollow spheres, Mater. Sci. Eng. A. 483–484 (2008) 254–257. https://doi.org/10.1016/j.msea.2006.01.183.

[83] I. Vishnevetsky, M. Epstein, Production of hydrogen from solar zinc in steam atmosphere, Int. J. Hydrogen Energy. 32 (2007) 2791–2802. https://doi.org/10.1016/j.ijhydene.2007.04.004.

[84] M. Schmid, Vapor Pressure Calculator, (2023). https://www2.iap.tuwien.ac.at/www/surface/vapor_pressure (accessed April 15, 2024).

[85] E. Harry, A. Rouzaud, P. Juliet, Y. Pauleau, M. Ignat, Failure and adhesion characterization of tungsten-carbon single layers, multilayered and graded coatings, Surf. Coatings Technol. 116–119 (1999) 172–175. https://doi.org/10.1016/S0257-8972(99)00071-7.

[86] E. Harry, A. Rouzaud, M. Ignat, P. Juliet, Mechanical properties of W and W(C) thin films: Young's modulus, fracture toughness and adhesion, Thin Solid Films. 332 (1998) 195–201. https://doi.org/10.1016/S0040-6090(98)01056-6.

[87] G. Dehm, J. Cairney, Implication of grain-boundary structure and chemistry on plasticity and failure, MRS Bull. 47 (2022) 800–807. https://doi.org/10.1557/s43577-022-00378-3.

[88] M. Wurmshuber, M. Alfreider, S. Wurster, R. Pippan, D. Kiener, Small-scale fracture mechanical investigations on grain boundary doped ultrafine-grained tungsten, Acta Mater. 250 (2023) 18. https://doi.org/10.1016/j.actamat.2023.118878.

[89] J.D. Murphy, A. Giannattasio, Z. Yao, C.J.D. Hetherington, P.D. Nellist, S.G. Roberts, The mechanical properties of tungsten grown by chemical vapour deposition, J. Nucl. Mater. 386–388 (2009) 583–586. https://doi.org/10.1016/j.jnucmat.2008.12.182.

[90] R.W. Margevicius, J. Riedle, P. Gumbsch, Fracture toughness of polycrystalline tungsten under mode I and mixed mode I / II loading, 270 (1999) 197–209.

[91] M.J. Pfeifenberger, V. Nikolić, S. Žák, A. Hohenwarter, R. Pippan, Evaluation of the intergranular crack growth resistance of ultrafine grained tungsten materials, Acta Mater. 176 (2019) 330–340. https://doi.org/10.1016/j.actamat.2019.06.051.

[92] J. Ast, M. Göken, K. Durst, Size-dependent fracture toughness of tungsten, Acta Mater. 138 (2017) 198–211. https://doi.org/10.1016/j.actamat.2017.07.030.

[93] M. Faleschini, H. Kreuzer, D. Kiener, R. Pippan, Fracture toughness investigations of tungsten alloys and SPD tungsten alloys, J. Nucl. Mater. 367-370 A (2007) 800–805. https://doi.org/10.1016/j.jnucmat.2007.03.079.

[94] E. Tejado, A. V. Müller, J.H. You, J.Y. Pastor, The thermo-mechanical behaviour of W-Cu metal matrix composites for fusion heat sink applications: The influence of the Cu content, J. Nucl. Mater. 498 (2018) 468–475. https://doi.org/10.1016/j.jnucmat.2017.08.020.

[95] E. Tejado, A. V. Müller, J.H. You, J.Y. Pastor, Mechanical behaviour of W particulate-

reinforced Cu composites: Fracture toughness and R-curves, J. Nucl. Mater. 571 (2022) 0–7. https://doi.org/10.1016/j.jnucmat.2022.153960.

[96] A. Giannattasio, S.G. Roberts, Strain-rate dependence of the brittle-to-ductile transition temperature in tungsten, Philos. Mag. 87 (2007) 2589–2598. https://doi.org/10.1080/14786430701253197.

[97] D. Rupp, R. Mönig, P. Gruber, S.M. Weygand, Fracture toughness and microstructural characterization of polycrystalline rolled tungsten, in: Int. J. Refract. Met. Hard Mater., Elsevier Ltd, 2010: pp. 669–673. https://doi.org/10.1016/j.ijrmhm.2010.05.006.

Publication C

Crack length estimations for small scale fracture experiments via processing techniques

Journal of Materials Research 37, 2848–2861 (**2022**)
doi:10.1557/s43578-022-00681-4

Crack length estimations for small scale fracture experiments via processing techniques

K. Schmuck[a3] M. Alfreider[a], D. Kiener[a]

[a] *Department of Materials Science, Chair of Materials Physics, Montanuniversität Leoben, Jahnstraße 12, Leoben, Austria*

Abstract

Accurate knowledge of the current crack length is crucial to evaluate fracture mechanical tests. At the sub-micron to micron scale, the crack length is directly accessible from observation during in-situ experiments in electron microscopes, or indirectly via calculation from sample stiffness. In the current work, image processing techniques were used to introduce a semi-automatic technique to measure crack lengths at the micron scale from image sequences. The technique utilizes manually defined filters and searches for contours near the previous crack tip and locates the new one according to the previous position. To demonstrate validity and capability, three micron-sized notched cantilevers were prepared for bending experiments and loaded in-situ by partial unloading. Comparison of crack lengths determined by the proposed method, manual measurement and sample stiffness revealed a reasonable agreement, while occasional deviations allow further insights into the crack behaviour. Thus, our new approach enables in-depth investigation of small-scale fracture processes.

Keywords: In-situ microcantilever testing; Crack propagation; Image processing techniques; Nanocomposite WCu;

1. Introduction

To study material behaviour at ever decreasing dimensions, small scale experiments are frequently conducted, allowing to test not only confined volumes [1–3], but also individual layers of multilayer stacks [4], hard coatings [5], individual grain boundaries [6] and/or specific interfaces [7]. Due to continuous device miniaturization and shrinking internal length scales [8,9], these miniaturized approaches were also extended to fracture experiments at the micron to submicron scale. Furthermore, performing such experiments in-situ allows gaining additional insights into fracture processes and also material behavior on small length scales [10,11].

[3]Corresponding author at: Department of Materials Physics, Montanuniversität Leoben, Leoben, Austria. *E-Mail Address:* klemens.schmuck@unileoben.ac.at (K. Schmuck)

However, the fracture mechanical evaluation relies on accurate knowledge of the crack characteristics, especially the crack length. On the macroscopic scale crack length is measured via optical observations or well-established methods such as the potential drop method [12], the partial unloading technique [13] or digital image correlation (DIC) [14]. The potential drop method is hardly applicable at the micron to sub-micron scale due to small sample dimensions. Classical DIC requires native or artificial patterns on the sample surface to track deformation or shape changes. Hence, DIC is not straight forward applicable to ion beam polished surfaces and therefore, the crack length is typically evaluated manually from captured images, which is a tedious task. Partial unloading allows to estimate the crack length at the unloading steps by measuring sample stiffness changes [15]. Inspired by the crack length measurement via partial unloading, Ast *et al.* [16] developed a method to estimate the crack length based on a continuous stiffness signal, which is obtained by superimposing a small harmonic displacement signal onto the constant displacement rate. By utilizing finite element analysis or analytical methods, sample stiffness can be converted into a crack length assuming a straight crack front [17–20].

However, it is not always possible to measure the continuous stiffness signal, e.g. on older systems or for very ductile materials which exhibit blunting only. In such cases the crack length is most often estimated manually. As this is time-consuming and dependent on human individuality, the current work proposes a new semi-automatic approach utilizing image processing techniques. We discuss the application of the image processing technique in more detail, and the derived data are compared with results from cantilever stiffness calculations and manual evaluations. Three in-situ sub-micron bending tests were performed with different specimen sizes made from a nanocrystalline W-Cu 20 wt.%. composite as an isotropic model material. This semi-brittle material represents a challenging test case to highlight the general applicability of our concept to a wide range of problems.

2. Results

Determined crack lengths from the developed algorithm were compared to manual measured crack lengths and those calculated from unloading stiffness at the individual unloading steps. At first the crack length was manually measured to avoid biased evaluation. The manual crack length measurement was independently performed several times from the top cantilever surface to the assumed crack tip. The final manual measured crack length is the mean of all measured lengths of one frame, while the minimal and maximal manually measured value is expressed by the error bars in Fig. 1a), Fig. 2a) and Fig. 3a), respectively. The gathered raw load-displacement curves are given for each sample in the supplementary.

Fig. 1a) displays determined crack lengths up to a maximum displacement of 32 µm in case

of the largest cantilever (34.3 x 31.8 µm^2). In general, the different methods to determine the crack length agree well. There are some minor differences, which will be detailed in the following to give better insight into the different methodologies. The micrograph in Fig. 1b) depicts the crack on the sample surface at the first unloading step, which was purely elastic. Among the unloading steps from position b to c, the determined crack lengths of all three techniques agree well. Obviously, starting at position c in Fig. 1a) the crack length determined from unloading stiffness deviates from measured crack lengths on the images. This might stem from crack growth inside the sample, which is not visible on any sample surface. But also from the faint crack growth in front of the algorithmically determined crack, which is an inconspicuous feature compared to the fabrication curtain of the focused ion beam (FIB), Fig. 1d) and e). The deviation of about 2.2 µm between mechanical and image-based methods remained roughly constant until the last unloading step. Algorithmically and manually measured crack lengths agree well. Small deviations arise from material bridging, -tearing and elastic crack closure due to partial unloading. These effects make manual crack evaluation rather challenging. Detailed inspection of intermediate loading frames showed that the formed material bridges were cracked already, which was not obvious to see at the manually measured individual frames.

Results obtained for the medium-sized cantilever (14.2 x 13.8 µm^2) are shown in Fig. 2a). The sample surface at the first unloading step is depicted in Fig. 2b). At the beginning, the calculated crack length from unloading stiffness revealed an unphysical crack length reduction of about 500 nm and 300 nm for the second and third unloading step, respectively. In Fig. 2a) these two points are shown as non-filled circles. This originates from a stiffness increase for the second and third unloading step compared to the first unloading step. The lower stiffness might stem from the finite system stiffness and the fact that unloading started directly after loading, resulting in a slight nonlinearity in the unloading segment due to electronic delay. As the first stiffness value is used to calculate the initial stiffness, this affects also calculated crack lengths at a later stage, which would be shifted vertically as the initial stiffness changes. However, crack lengths obtained by the image-based evaluation methods agree well until position c in Fig. 2a). At position c a small crack extension was missed by the algorithm, most likely due to contrast variations around the crack tip as depicted with a red arrow in the inset of Fig. 2c). Further, manual measurement started to scatter a lot, because for some measurements a connecting thin crack to the pore was evident, as depicted by the blue arrow in the inset of Fig. 2c). However, from position c to d in Fig. 2a) only small deviation between manually and algorithmically determined crack length occurred. These deviations stem from elastic closure during unloading due to a closed crack between pore and crack. Fig. 2d). The algorithmically determined crack length between position d and e reached a plateau early, while crack lengths manually measured and calculated from unloading stiffness showed a continuous crack growth until the last unloading step, see

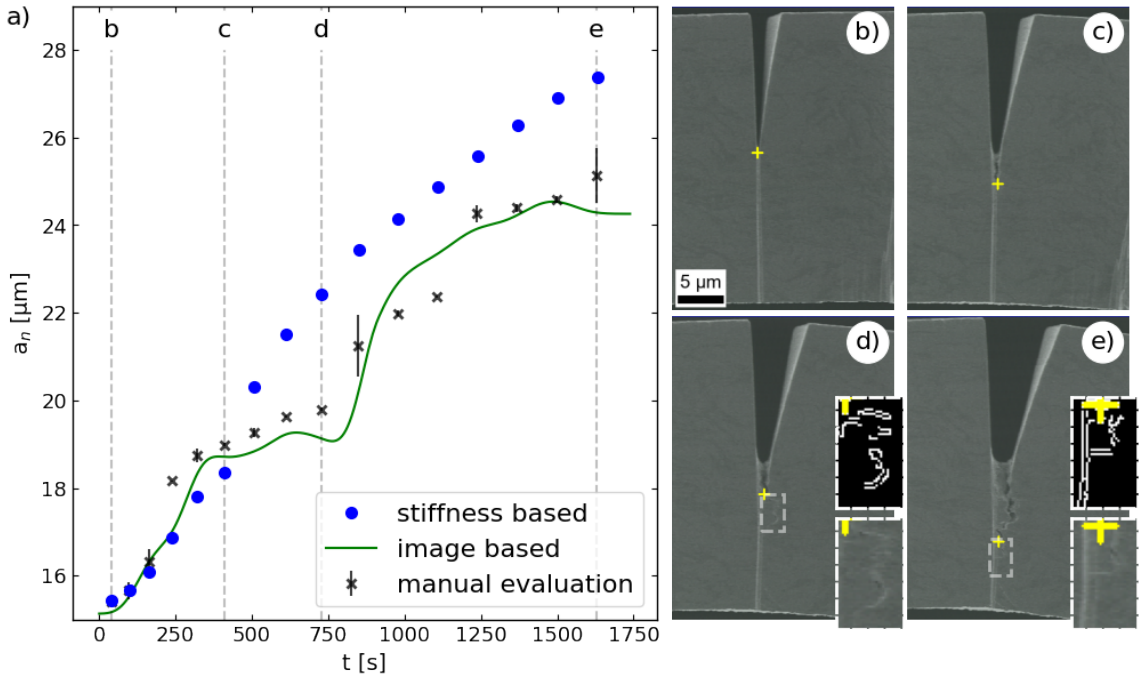

Figure 21: a) Determined crack lengths a_n for the largest cantilever with a cross-section of 34.3 x 31.4 µm^2. At each unloading step the crack length was manually measured (black crosses) and calculated from unloading stiffness (blue dots), while the algorithm determined the crack lengths of all images (solid green line). b) to e) Micrographs of the cracked sample surface at different unloading steps indicated by vertical dashed gray lines in a). The crack tip is marked with a yellow cross, whereas the zoomed insets in c) and d) show a thin crack in front of the algorithmically identified crack tip.

Fig 2a). However, at the last unloading position e in Fig. 2a) manual and algorithmically evaluated crack length agree well, which is also obvious from the corresponding micrograph, see Fig. 2e). The calculated crack length from unloading stiffness revealed a shorter crack length of about 1.2 µm compared to the image-based methods. This indicates less crack growth inside the sample. Notably, 500 nm might be explained by a too low initial stiffness.

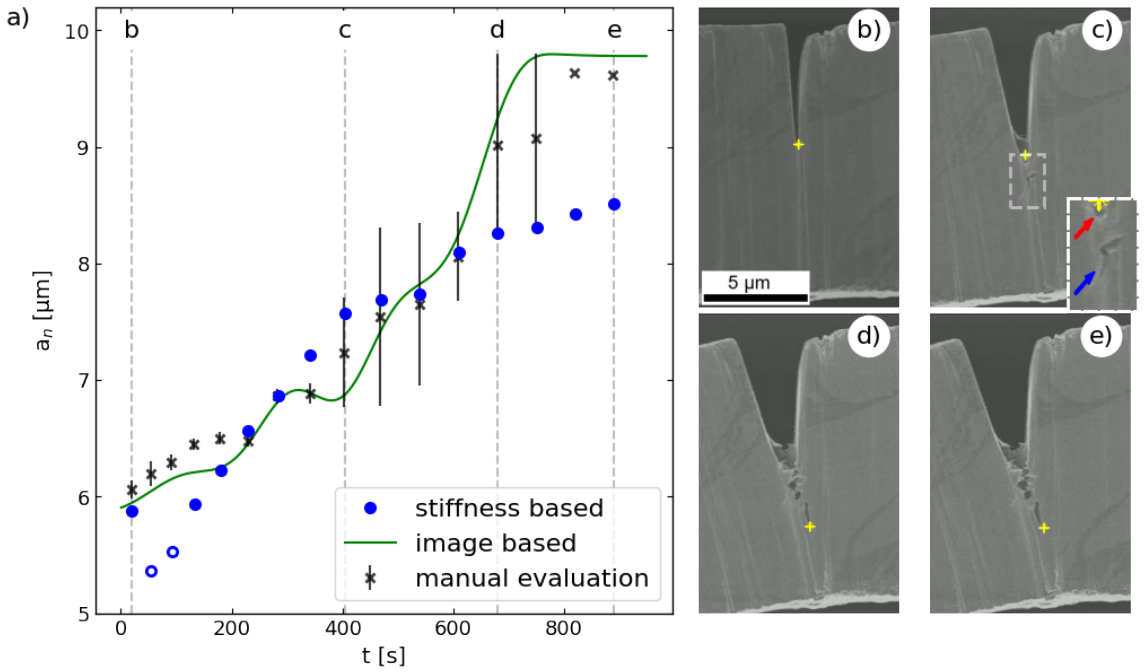

Figure 22: a) Obtained crack lengths a_n for the medium cantilever with a cross-section of 14.2 x 13.8 µm^2. At each unloading step the crack length was measured manually (black crosses) and calculated from unloading stiffness (blue dots), while on each frame the crack length was algorithmically determined (green solid line). Unphysical crack length reduction using stiffness based evaluation are shown by non-filled circles. b) to e) Micrographs of the cracked sample surface at different unloading steps indicated by vertical dashed gray lines in a). The yellow cross marks the algorithmically identified crack tip. In the inset of c) the red arrow points to a small crack extension and the blue arrow to pore formation in front of the crack.

For the smallest cantilever (6.5 x 4.3 µm2), the whole bending beam was imaged, which provides a good overview but also a lower resolution and a low contrast in the crack vicinity. However, Fig. 3b) to e) depict the selected region of interest from the captured images. Due to low contrast the algorithmic crack length determination required fine-tuning of pre-processing filters to keep the crack separated from surface effects. Also manual crack length measurement was challenging due to material bridging and tearing in addition to low contrast at the crack tip. Despite these challenges, manually a continuous crack growth was measured at each unloading step. Note that a variation of one pixel amounts to ~40 nm, which is equivalent to 1% of the total thickness. Due to the small cantilever cross section only low loads were required for bending, which resulted in a comparatively noisy signal.

Therefore, crack evaluation from mechanical data was challenging and the input data was additionally smoothed in a pre-processing step. Crack lengths calculated from unloading stiffness revealed an unphysical crack length reduction between position b and c, marked with non-filled circles in Fig. 3a). This reduction occurred because the first unloading stiffness is lower than determined stiffness values between position b and c. The reduced stiffness might stem from finite system stiffness, a non-linear unloading curve as loading is directly followed by unloading, and low loads especially at the first load cycle, see supplementary. Nevertheless, from a certain point onwards (Fig. 3c) crack lengths determined from unloading stiffness showed an overall continuous crack growth. However, the image-based methods had a roughly constant crack length difference from position b to c, see Fig. 3a). There the algorithm detected the crack tip at the bright edge, while manually the crack was located at the end of the dark region, Fig. 3b) and c). However, between position c and d manual and algorithmic measured crack lengths agree well, see Fig. 3a. Further the image-based method showed a similar crack growth rate of about 2 nm/s from position b to d in Fig. 3a). However, starting at position d to the final unloading the algorithm determined an unphysical crack length reduction from 3.3. µm to 3 µm, see Fig. 3a). This is caused by poor resolution, low contrast, contrast changes at the crack tip vicinity and material tearing. While the latter started to occur already at position c, see Fig. 3c) and increased further until the final unloading, Fig. 3d) to Fig. 3e). At the last unloading step the crack length difference between manual measurement and algorithm of about 400 nm is present, depicted in Fig. 3e).

J is illustrated over time in Fig. 4 and as classical R-curve over the determined crack extension in Fig. 5, where subfigures a), b) and c) always correspond to the largest, medium and smallest cantilever, respectively. Algorithmically the crack length was evaluated on each frame including unloading, which mathematically allows to calculate J quasi-continuously, although J is defined for static loading only. Hence, in the present case J is split into loading and unloading including re-loading, which is necessary to reach maximum displacement of the previous loading step. In Fig. 4 and Fig. 5 during loading J is depicted with a solid green line, while the unloading is plotted using a grey dashed line.

Obtained J from algorithmically and manually determined crack lengths agree well for all three specimens, Fig. 4. The evaluated J from the mechanical crack lengths showed slight deviations from t $\approx$ 500 s to t $\approx$ 850 s and at the two last unloading steps for the largest, Fig. 4a). Contrarily, for the medium and smallest specimen J of all three determined crack length sources agree despite the measured crack length scatter, as shown in Fig. 4b) and c). Further, comparing J of all three samples reveals a size effect, which can be seen in the R-curves more clearly by comparing the obtained J values and slopes in Fig. 5a) to c). Moreover, it is obvious to see, that the smallest cantilever had a clearly increased $J_{,}$ value which also stems from sample size.

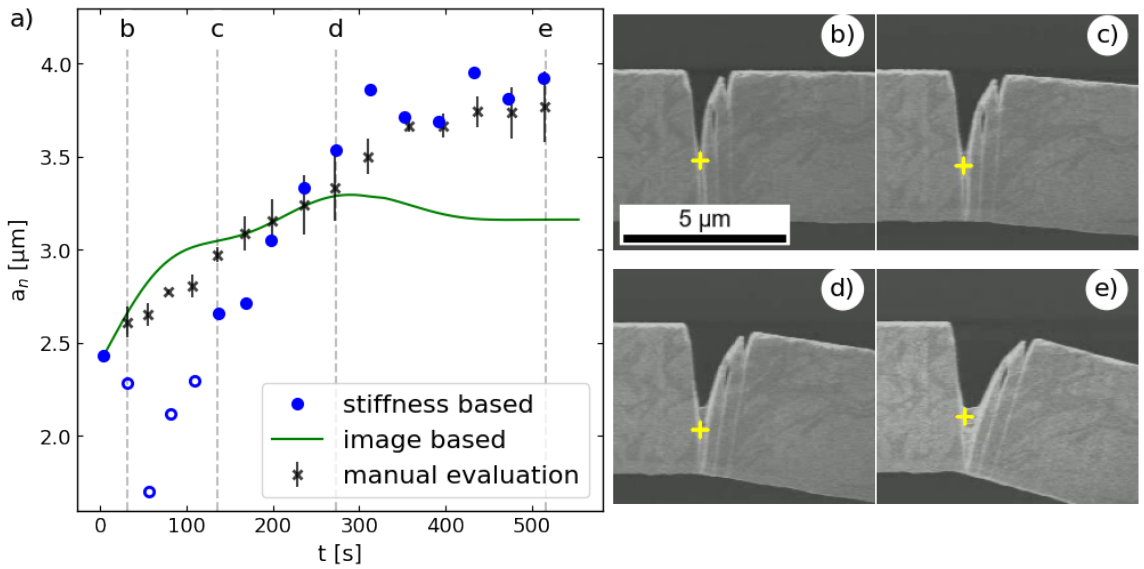

Figure 23: a) Crack lengths a_n for the smallest cantilever with a cross-section of 6.5 x 4.3 µm^2. The algorithm (solid green line) determined crack lengths on each frame, while for each unloading step the crack length was manually measured (black crosses) and calculated from unloading stiffness (blue dots). Unphysical crack lengths of the stiffness based evaluation are marked with non-filled circles. Crack lengths obtained from the algorithm were smoothed by median filtering. Vertical dashed gray lines indicate the unloading step of b)-e), which the respective micrographs show. The yellow cross marks algorithmically identified crack tips in b) to e).

Further, the standardized evaluation technique for J_{IC} is not applicable, as the sample dimensions are clearly below the crack extension criteria of 200 µm [19]. Thus, the J_q values were determined by following the description in [13], which fits the data in the blunting regime and shifts the fitting line for the half crack tip opening displacement (CTOD). Therefore, for evaluation of J the blunting regime was estimated by manual inspection of the frames, which can be hardly visualized. In Fig. 4 the dotted vertical gray line indicates the end of blunting during the experiment. In this region the R-curve values with a positive crack extension were linearly fitted. The CTOD was similar measured as described in [21] by inscribing a circle at the crack tip and measuring the diameter, which was done for each specimen on the last frame before evident crack extension occurred. As the frames have a limited resolution the circle was inscribed several times and the mean, as well as the standard deviation, was calculated, resulting in (190 ± 60) nm, (50 ± 10) nm, and (100 ± 40) nm for the large, medium and small sized cantilever, respectively. The fitted line in the blunting regime was then shifted by half of the CTOD, depicted in Fig. 5. The J_q values were determined by intersecting the blunting line with the J-integral points and the closest point was used. In case of no intersection no J_q value was obtained. All determined J_q values are listed in Table 1. The uncertainty of J_{IC} is obtained by shifting the blunting line by the CTOD uncertainty.

Table 3: Evaluated J_q values in J/m^2 for the different methods by intersecting the blunting line with the R-curve. Missing values occurred as the blunting line not always intersect with the linearly interpolated J-integral values.

Sample/J_q	Stiffness	Manual	Algorithm
Large	360 ± 50	260 ± 20	-
Medium	-	640 ± 10	590 ± 20
Small	590 ± 30	-	-

For a straightforward comparison with literature and linear elastic fracture mechanics data, the J_{IC} values were converted to K_{IC} values according to ASTM 1820 [19], S[table-format=3.0(2),separate-uncertainty]

$$K_{IC} = \sqrt{\frac{J_{IC}E}{(1-\nu^2)}}, \tag{1}$$

with the Young's modulus $E = 221$ GPa and the Poisons ratio $\nu = 0.32$.

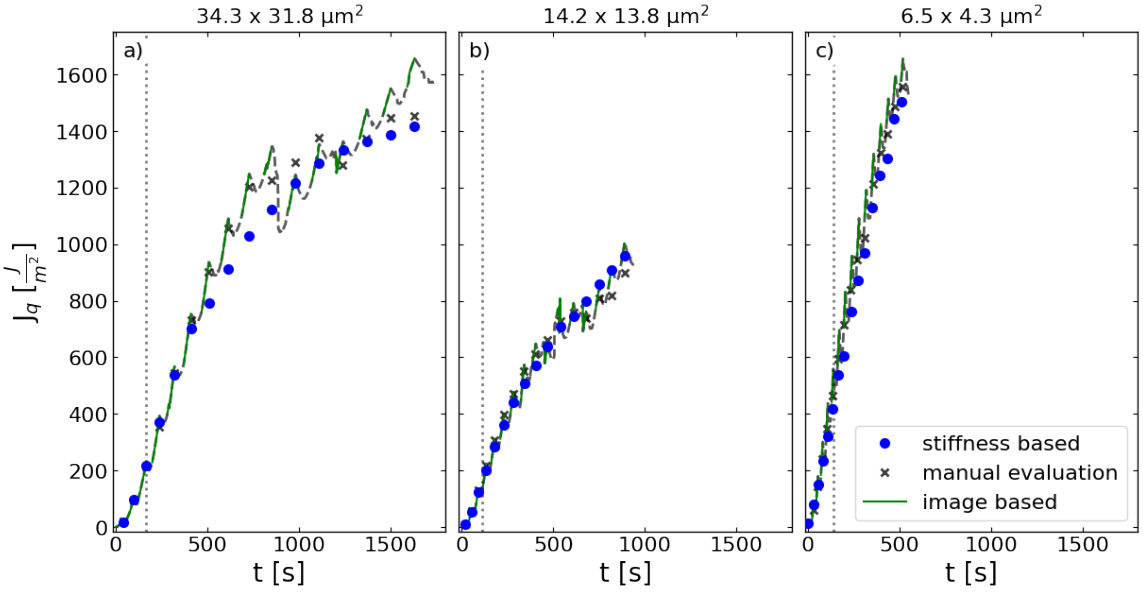

Figure 24: Calculated J-integral for the differently determined crack lengths and specimens, where a) represents the largest, b) the medium and c) the smallest cantilever. Blue dots are evaluated from stiffness based evaluations, black crosses rely on manual crack length measurements and the green solid as well as grey dashed line are determined from algorithmically estimated crack lengths. Note that the gray dashed line represents unloading and re-loading values. Up to the vertical gray dotted line the crack showed crack tip blunting.

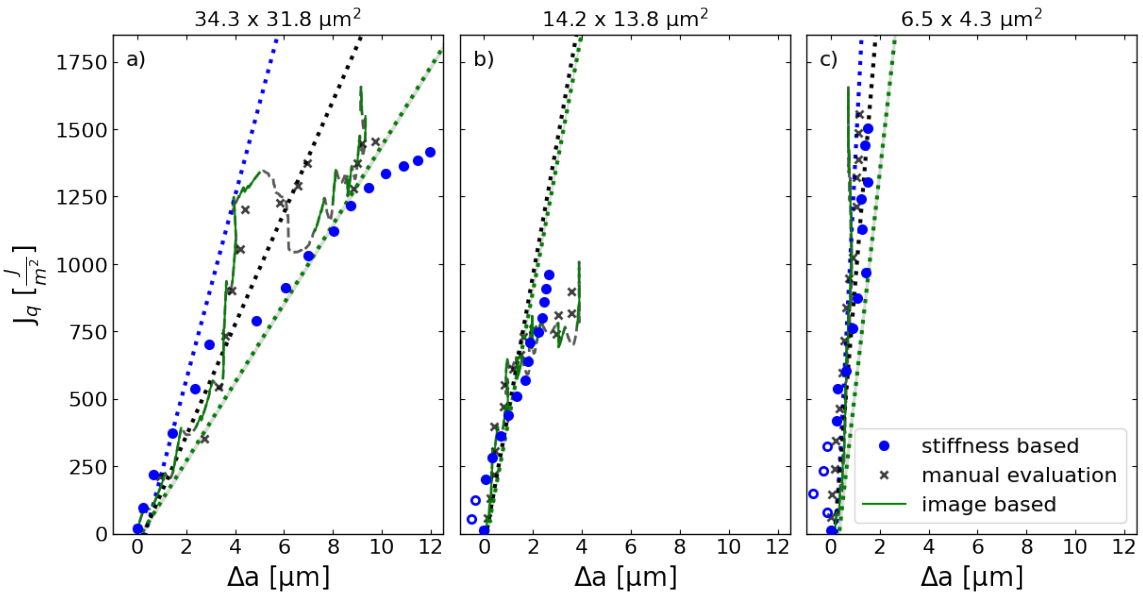

Figure 25: R-curve behavior of all three specimens calculated from the differently determined crack lengths, where a) represents the largest, b) the medium and c) the smallest cantilever. Blue dots are evaluated from the stiffness based calculation, black crosses rely on manual crack length measurements, and the green solid as well as grey dashed line are determined from the algorithmically estimated crack length. Unphysical crack lengths of the stiffness based evaluation are marked with non-filled circles. Note that the gray dashed line represents unloading steps and re-loading. The dotted straight lines represent the fitted shifted blunting lines for each method with the same color code.

3. Discussion

All three specimens exhibited a semi-brittle fracture behaviour during bending experiments, as evidenced by pore formation in front of the crack, material bridging and crack bifurcation, as commonly known for semi-brittle fracture processes [22–25]. Thus, some residual bridges between crack flanks remained, which are desired to increase material toughness, but from the automated crack detection point of view this behaviour gives rise to challenges due to lower local contrast especially at the crack vicinity, see Fig. 1c) to e), Fig. 2c) to e) and Fig. 3c) to e). Further, material bridging, tearing and pore formation complicate crack detection, as the continuous crack flank might be fragmented into multiple features, refer to Fig. 7e). For these frames also manual evaluation was challenging and showed low reproducible due to semi-brittle fracture behavior and the low contrast at the crack tip vicinity. However, image-based crack detection is much simpler for rather brittle fracture behaviour, such as the fracture of fully lamellar intermetallic TiAl alloys, to which the algorithm was already successfully applied [26].

Besides the already mentioned challenges the curtain feature introduced by FIB milling below the crack tip affected the quality of the algorithmic results to extract the crack edges

and may cause erroneous crack detection. However, fine-tuning of the pre-processing filters was capable to alleviate this for all samples. Furthermore, stochastic jumps occurred during algorithmic evaluation between frames due to the aforementioned material bridging and tearing. Thus, median filtering was applied to algorithmically determined crack lengths.

Furthermore, image resolution affects the quality of algorithmic crack flank detections, as lower resolution limits detection of smaller features. Additionally, it is obvious that reduced sample size decreases feature dimensions, and consequently detection errors of a few pixels will result in larger crack length deviations. Although the largest cantilever has the lowest image resolution, deviations of a few pixels are negligible compared to the total crack length. For the smallest cantilever a variation of a single pixel (40 nm) represents a change of 1% of the cantilever height.

Despite challenges mentioned above, manual and algorithmic crack length evaluation agree well for the large and medium sized cantilever, where only slight deviations occur. However, the image-based evaluation methods had an increased deviation for a few frames, see Fig. 1a) and Fig. 2a). But especially for these frames manual measurement scattered a lot, indicating that the exact crack tip position was not obvious. Thus, the algorithmic determined crack lengths were within the manual measurement uncertainty, Fig. 1a) and Fig. 2a). The image-based evaluated crack lengths for the smallest cantilever differ over the whole experiment due to low resolution and limited contrast at the crack tip, Fig. 3a).

Natively, evaluation of each method of this work revealed benefits and drawbacks.

Image-based methods capture only the surface part of the three-dimensional crack front. Even for an ideal crack the crack front bends up towards the surface due to the transition from plane strain inside the sample to plane stress on the surface, schematically shown in Fig. 6.

For isotropic materials Shih [27], established a relation between J-integral and CTOD, which allows to qualitatively estimate the crack length difference between plane strain and plane stress condition by assuming a circular crack tip and relating the CTOD to crack extension

$$\delta = d_n \frac{E}{\sigma_y}, \tag{2}$$

with δ_c the CTOD, $d_{n,\ c}$ the Shih factor for specific Ramberg-Osgood hardening exponent, E the Young's module and σ_y, the yield strength. The Young's module and yield strength are the same for both conditions, while the CTOD and the Ramberg-Osgood hardening exponent differ. Thus, the CTOD related to the Shih factor has to be similar for plane strain and plane stress,

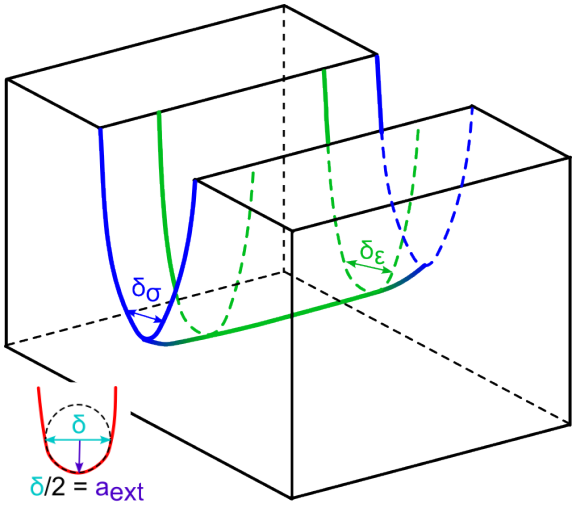

Figure 26: Crack front at blunting, in blue the region where plane stress prevails and in green the plane strain dominated area. A cross-section trough the crack is shown in red in the lower left corner, which depicts an ideal blunted crack with δ as CTOD and a_n as crack extension.

$$\frac{\delta_{plane\ strain}}{\delta_{plane\ stress}} = \frac{d_{plane\ strain}}{d_{plane\ stress}}, \tag{3}$$

The hardening factor of the material was unknown, but the ratio between the Shih factors for different hardening showed almost no variation for this material. Hence, the ratio was approximated averaging over the Ramberg-Osgood hardening exponents from 2 to 15 [28], revealing a ratio between plane strain and stress of 1.49 $\pm$ 0.03. This translates into a longer crack length for the plane strain condition at blunting of 290 nm, 75 nm and 150 nm for the large, medium and small sized cantilever, respectively. This is negligible compared to the obtained crack lengths. In this model the crack length difference persists between plane strain and stress after blunting and during crack propagation.

However, in reality the crack front shape is rather jagged and shows hardly any symmetry [29], due microstructural influences and local strain accumulations. The crack length determined from unloading stiffness gives the average over the whole crack front. Hence, the stiffness based crack length captures also crack growth inside the sample, but only allows evaluations at discrete unloading steps in this case. Nonetheless, crack growth inside the sample was noticeable for the largest cantilever starting at position c in Fig. 1a). There the image-based methods missed a possible thin crack, which started to form at position c and steadily grew until the final unloading step. For the medium sized cantilever surface crack growth has started between position c and d in Fig. 2. For this specimen it is also obvious that a well-defined reference stiffness is crucial. Therefore, it is necessary that the load-displacement curve segment during the first unloading segment is straight, which can

be achieved by starting unloading form a steady state by adding a hold segment between loading and unloading. However, image-based methods measure the crack length bias free from the captured frames. Notably manual crack length evaluations are very laborious and user-dependent, while algorithmic crack length determination from images allows to evaluate the crack length of all images in a reasonable time and is less user-dependent, although it still depends on pre-filtering. Evaluation of all available images of a miniaturized in-situ experiment provides a higher resolution of individual crack length values compared to the used stiffness based approach. Additionally, the crack length of more complicated fracture processes taking place for example in heterogeneous structures, which have different Young's moduli for each layer, are accessible by image-based methods, while evaluation from mechanical data alone is considerably more challenging due to the necessity of individual simulations. Further, image-based evaluation allows to determine fracture characteristics during loading, which are inaccessible by mechanical data from stiffness based loading, such as crack tip blunting at interfaces, crack branching and deflection [4,9].

Based on the differently obtained crack lengths the J values were evaluated for each cantilever. Among one cantilever size the derived J values agree well over time, see Fig. 4. However, among the specimen sizes an increase of the J values is present. This is best seen by comparing the smallest cantilever data, Fig. 4c), with the other two in Fig. 4a) and b). The increasing J value can be attributed to a sample size effect, as the plastic zone extends over the whole initial ligament of the smallest cantilever. The R-curve of the largest specimen shows a slope change at larger crack extension, which is best seen at the mechanical data points, Fig. 5a). Therefore, the largest cantilever behaves similar to a macroscopic sample, although it just shows the beginning of the second stage of the R-curve. In the second stage the R-curve starts to flatten and the materials toughness increase is reduced. For the medium sized cantilever, the R-curve has a slightly increased slope and does not show any R-curve flattening, see Fig. 5b). This can be related to sample size changes, as the W/B ratio is slightly different to the lager specimen, and the plastic zone takes up a larger fraction of the ligament. However, by comparing the R-curve of the large and medium cantilever it is obvious that the J-values of the medium sized cantilever are all within J values of the first R-curve stage of the largest cantilever, although the R-curve slope is increased. In case of the smallest specimen the R-curve slope is strongly increased and shows a continuous increase, Fig. 5c). Similar to the increased J values this might also provide an indication for a sample size effect, or a crack extension dominated by crack tip blunting.

Evaluation of the J_{q} values was not possible for each specimen and method, as the shifted blunting line does not always intersect with the R-curve, as the blunting line slope is too low, Fig. 5. Further, from mechanical data no blunting line was constructed for the medium sized cantilever, because by excluding all negative crack extension values only one value

remained, making a linear fit impossible. Nonetheless, determined J_{q} values agree well among a cantilever size, see Table 1. Evaluated J_q values are sample size independent if the sample dimensions fulfill the condition $B, (W-a) > 10\frac{J_q}{\sigma_y}$. For the validation the yield strength σ_y was approximated from Vickers hardness measurements with the relationship $\sigma_y \approx 3.3\ HV$ [30,31], which resembles to $\sigma_y \approx 1600$ MPa. By assuming the worst case for each specimen using the highest determined J_{q} this results in validation values of 2.4 µm, 4 µm and 3.7 µm for the large, medium and small specimen, respectively. Hence, for the larger two specimens the J_{q} value can be assumed to be sample size independent and are valid J_{IC} values. Conversion of these J_{IC} values gives for the largest specimen a K_{IC} value of 9.5 ± 0.7 MPa$\sqrt{m}$ and 8 ± 0.4 MPa$\sqrt{m}$ for mechanical and manual data. The K_{IC} values of the medium sized cantilever are slightly increased, 12.6 ± 0.2 MPa$\sqrt{m}$ as well as 12 ± 1 MPa$\sqrt{m}$ for manually and algorithmic measured data, respectively. To put these values in context, literature states for polycrystalline textured tungsten at the macro scale with larger grains K_{IC} values of 14 MPa$\sqrt{m}$ and 9 MPa$\sqrt{m}$ for the direction normal to and along the grain texture [32], respectively. The reported K_{IC} values in the current work are in a comparable range, although pure tungsten was used in literature and the grain size is definitely larger compared to the investigated specimens. Magnetron sputtered tungsten, which has a more similar grain size as the investigated samples, shows a fracture toughness ranging from 1 to 2.5 MPa$\sqrt{m}$ [33]. However, these sputtered films again consist of pure tungsten, while in this work a W-Cu 20 wt.% was studied. Thus, the fracture toughness deviation can be largely attributed to the different composition, as the ductile copper phase is considered to improve the fracture toughness of tungsten.

4. Conclusion

In this work a semi-automated technique was proposed to extract the crack length from captured in-situ images at the micron scale. For verification stiffness based bending experiments were performed with differently sized cantilevers, which exhibited semi-brittle fracture behaviour. It was shown that the algorithmic determined crack lengths agree well with manual measurement and crack lengths calculated from unloading stiffness. Whereas the latter gives discrete values only, the algorithmic image evaluation provides a continuous crack length over the whole experiment, allowing to estimate fracture parameters quasi-continuously. Furthermore, the algorithmic procedure enables investigations of more complicated fracture processes, such as heterogeneous structures, for which mechanical evaluation is not feasible due to, *e.g.* layer wise different Young's moduli or other distributed inhomogeneities. Also materials exhibiting a higher blunting tendency will benefit from this analysis. Taken altogether, this will allow to gain more detailed insights into the fracture characteristics of complex high performance materials in future.

Extending the algorithm further to locate and extract both crack flanks as well as the specimen surface edges, it would be possible to obtain additional fracture characteristics, such as crack tip opening displacement, crack tip-opening angle and crack mouth opening displacement.

5. Methodology and Experimental

5.1 Experimental

The investigated samples in this study were fabricated from a rod with a diameter of 8 mm and the material composition W-Cu 20 wt.%. From this material, disks were cut with a thickness of 0.8 mm and subjected to high pressure torsion (HPT) up to an equivalent strain of 120. This resulted in a bi-modal microstructure with a nano-crystalline matrix with a mean grain size of about 10 ± 4 nm and some statistically distributed elongated W inhomogeneities. Corresponding micrographs are shown in the supplementary. Further, the HPT process reduced the sample thickness to about 0.5 mm. The HPT disks were cut in halves, which were manually ground and polished down to a thickness of approximately 50 µm to reduce FIB time.

Three differently sized cantilever beams were fabricated by combined femtosecond laser ablation [34] for coarse machining, and FIB milling for fine cutting, within a scanning electron microscope (SEM/FIB; Zeiss Auriga Laser platform, Carl Zeiss AG, Oberkochen, Germany). The FIB current was subsequently decreased from 10 nA for coarse milling to 500 pA for the final polishing step. The fabricated cantilever had cross-sections (W x B) of 34.3 x 31.8 µm^2, 14.2 x 13.8 µm^2 and 6.5 x 4.3 µm^2 as well as lengths of 150.6 µm, 82.9 µm, and 35.8 µm, respectively. For each cantilever, a notch was introduced in top-view by line milling with a current of 500 pA to depths of about 0.4 x W. The notch of the largest cantilever required a precutting from the side-view to reach the required depth and was afterward finalized in top-view, too.

Mechanical tests were performed with a micro indenter (UNAT_SEM 1, ASMEC GmbH, Dresden, Germany) which operates in a displacement controlled open-loop mode. In vacuum the indenter has an undampened force noise level of 50 µN. and was situated inside a scanning electron microscope (DSM 982, Carl Zeiss AG, Oberkochen, Germany) to record in-situ images at a rate of one image per second during the experiments. For the experiments, a constant displacement rate of 0.05 µm/s was used. Furthermore, for each cantilever 15 unloading steps were performed, which consist of a displacement drop of at least 10% of the current displacement, but at maximum 2 µm. For the largest, medium, and smallest cantilever the maximum displacement was set to 32 µm, 16 µm, and 8 µm, respectively. One

loading cycle consists of loading, unloading and a hold segment of about 10 s before the next loading cycle starts. For the smallest cantilever, the entire bending beam was imaged, while for the two larger cantilevers, the image area was limited to the crack tip vicinity. Images were captured using an in-lens secondary electron detector for all three samples.

5.2 Image-based crack length measurement

The image acquisition rate defines the time resolution during small-scale in-situ fracture experiments. Typically, these experiments are performed within a SEM, where image quality suffers from high image acquisition rates necessary to monitor crack growth.

Digital image analysis aims to extract information from an image by utilizing feature extraction, optical flow, image segmentation, or edge detection methods [14,35–38]. The former two did not apply to in-situ crack growth images captured by SEM, as the recorded images contain only a limited amount of properly recognisable features on each individual frame. Image segmentation simplifies an image by partitioning it into segments, e.g. background-sample, and does not rely on proper feature detection between frames. However, due to the low contrast in the crack tip vicinity, image segmentation is hardly applicable. Contrarily, edge detection extracts edges from the image by calculating the image gradient and thresholds the image gradient for edge extraction. This allows to detect edges on each frame and localize the crack flank.

5.2.1 Pre-processing

The proposed algorithm was implemented in Python 3.8 [39] utilizing Numpy 1.20.2 [40], Scipy 1.5.4 [41], and Scikit-Learn 0.24.1 [42]. Image processing was done via the python-based OpenCv community library 4.5.1.18 [43] as well as Scikit-Image 0.18.0 [44]. Captured images are typically noisy due to the high image acquisition rates when monitoring crack growth due to non-uniform illumination [14,45]. Hence, a few pre-processing steps were required: First a region of interest (ROI) was selected to reduce the computational burden, Fig. 7a). For this selection, it had to be ensured that the crack was within this ROI on all frames.

Noise was reduced by filtering, involving Non-local Means filter (NLM) [46] and, if necessary, Gaussian blurring. The former does a decent job of reducing speckle as well as salt and pepper noise, which are randomly distributed bright and dark pixels due to detector disturbance. NLM filtering consists of the parameters filter strength, which is directly related to noise removal, patch sizes, used to calculate weights, and search window size, defining the regions considered to compute the average pixel value, see Fig. 7b). However, to prevent NLM from edge blurring, the filter strength value has to be used in moderation. In this work, suitable

values were found in the range from 0 to 10. Gaussian blur does significantly reduce white noise at the cost of a blurred image, shown in Fig. 7c). For that, the Gaussian blur computes a normalized weighted average value to set the central pixel of the considered region. The filter process is adjusted by the kernel size, defining the considered region and standard deviation, from which weights are computed.

To enhance contrast and improve segmentation between sample and background, contrast limited adaptive histogram equalization (CLAHE) [47] was applied, which equally enhances bright and dark regions as seen in Fig. 7d). This is done after noise removal to avoid undesired noise enhancement. As filter parameters CLAHE takes the number of tiles used to split the image into equal spaced sub-regions and clip limit, defining the limiting count for each bin of the histogram. For each sub-region, the algorithm calculates a histogram and equally redistributes all values above the clip limit, which should be in the range from 1 to 5 for reasonable results and to avoid noise enhancement due to maximizing local contrast.

Image segmentation is realized using the Canny method [35], which is a well-established technique to extract edges from images. The Canny parameters are kernel size, defining the considered region for gradient calculation and two thresholds, which are used to locate edges on the intensity gradient image. Gradient values above both thresholds are considered as strong edges, while gradient values between them are weak edges and only contribute to an edge if they are connected to a strong edge. All gradients below both thresholds are rejected, leading to a binary segmented image. Finally, to extract the edge location, border following was applied [48].

5.2.2 Crack length measurement

According to ASTM E399 [49] crack length is the average crack front extension into the sample. However, images captured via SEM represent only the surface projection of the crack flank. Hence, for images, the crack length is the furthest crack extension into the sample material on the surface.

To measure crack lengths from images it was necessary to locate the crack tip on each frame from the extracted edges. Therefore, only minor position changes of the crack flank were assumed between consecutive frames near the crack tip (< 25 pixels). This allows to obtain a crack flank on the following frame by calculating the pair wise distance between the current crack flank pixels and all pixels of each extracted edge. For each contour line the minimal distance between each pixel and the current crack flank was calculated. These distances were then summed and divided by the length of the edge and current crack flank for normalization. This should ensure to prefer longer edges over small ones. The edge with the smallest resulting value from this procedure is selected as new crack flank. From these

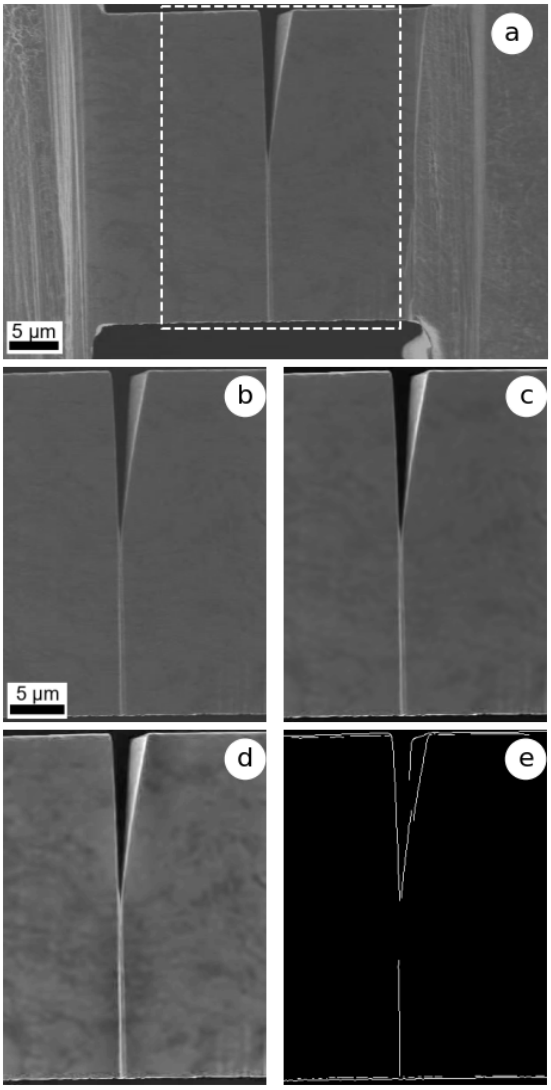

Figure 27: Subsequent pre-processing steps for crack length determination. a) Original SEM image with a dashed white rectangle for ROI selection, b) NLM filtering, c) Gaussian blur, d) Enhance contrast with CLAHE, e) Edge extraction with Canny algorithm.

newly selected crack flank, the crack tip is determined by assuming that the crack tip lies on the newly selected crack flank and that it is the point that extends furthers into the material, see Fig. 8. Thus, the point on the newly selected crack flank which is maximal in crack growth direction is selected as new crack tip.

However, this procedure does not ensure to detect the whole crack flank, because extracted edges are often detached from each other and may represent only a fragment of the crack flank. Multiple edges are combined to form a new crack flank. Hence, the crack length was calculated as the distance between a fixed point on the top surface of the cantilever and the determined crack tip. Further, algorithmically obtained crack lengths were median

filtered to remove outliners, which might occur due to fragmented crack flanks as well as low contrast and resolution around the crack tip.

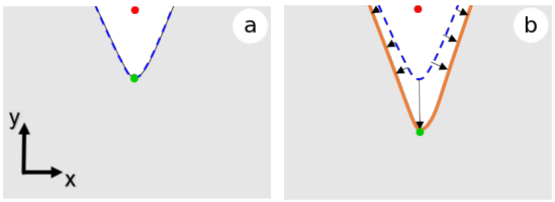

Figure 28: Schematic crack flank detection on consecutive frames: a) Previous frame with the located crack flank (dashed blue line). b) Following frame with the previously found crack flank (dashed blue line), a possible found contour line (orange solid line), representative distance measure between previous crack flank and contour line for all pixels on that contour line (black arrows), reference point for measurement (red dot) and the possible crack tip (green dot).

5.3 Crack length estimation from mechanical data

Mechanical data was used to estimate the average crack length over the cantilever cross-section. For that the recorded load and displacement data were smoothed by low pass filtering in a forward and backward manner [50] to reduce noise. Following the description in [20] crack lengths were calculated by relating stiffness changes to cross-section reduction at expense of crack growth. Stiffness changes were calculated by linear regression from the load-displacement curve during unloading as described in [15]. Form the first unloading stiffness and the corresponding crack length the initial stiffness was calculated, which was used as reference.

5.4 J-integral evaluation

Mechanical data and sample dimensions in conjunction with the differently obtained crack lengths were used to calculate the J-integral (J) for each specimen according to elastic plastic fracture mechanics by following the iterative procedure described in ASTM 1820 [19],

$$J(a) = J^{el}(a) + J^{pl}(a), \tag{4}$$

$$J_n^{el} = \frac{K_{q,n}^2(1-\nu^2)}{E}, \tag{5}$$

$$J_n^{pl} = \left(J_{n-1}^{pl} + \frac{\eta_{n-1}^{pl}}{W-a_{n-1}}\frac{A_n^{pl}-A_{n-1}^{pl}}{B}\right)\left(1-\gamma\frac{a_n-a_{n-1}}{W-a_{n-1}}\right), \tag{6}$$

with the iteration step number n, the elastic part J^{el} and the plastic part J^{pl} of the J-integral at a specific crack length a_n. As geometry independent pre-factors $\eta = 1.9$ and $\gamma = 0.9$ were used as stated by ASTM 1820 [19] for single edge notched bend specimen due to the loading similarities between this geometry and cantilever shaped beams. The Young's modulus was set to $E = 221$ GPa and the Poissons ratio was inserted with $\nu = 0.32$. The stress intensity factor K_q was calculated according to ASTM 399 [49],

$$K_n = \frac{F_n\, L}{B W^{\frac{3}{2}}}\, f\left(\frac{a_n}{W}\right), \tag{7}$$

with the load given as F and the geometry factor as $f(\frac{a}{W})$, where the function proposed by Riedl *et al.* [5] was used. The geometry dependent variables B, W and L were sample width, -thickness and length, respectively, as seen in Fig. 9. Further from the load-displacement curve the plastic work at each step is calculated according to [21],

$$A_n^{pl} = A_n^{tot} - A_n^{el} = \int_0^{u_n} F du - \frac{F_n^2}{2\, k_n}\,, \tag{8}$$

where u_n is the mechanical displacement, F_n the load at unloading and k_n the corresponding stiffness. Note that for the image-based evaluation methods the stiffness was estimated from the crack length by numerical evaluation of

$$k_n = k_0 \frac{1}{(1 + 18 * (1 - \nu^2)\, \frac{L^2}{L'^3} \int_0^a \frac{a}{W} f\left(\frac{a}{W}\right)^2}, \tag{9}$$

with k_0 as initial stiffness from the first unloading step and L as length between crack and loading point.

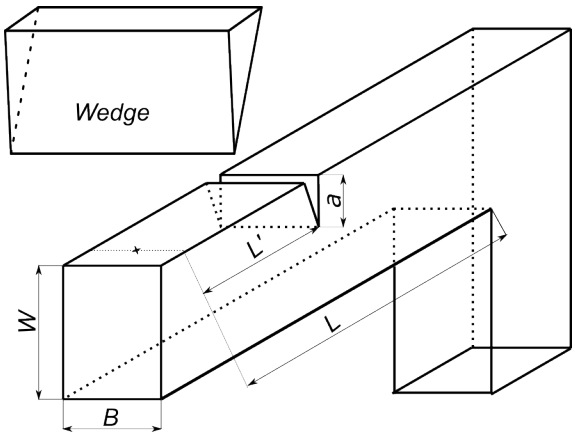

Figure 29: Cantilever geometry with thickness W, width B, notch depth a, length to the notch L, and the length to the base L'.

Acknowledgements

The authors thank Dr. Michael Burtscher for the TEM analysis.

Declarations

Funding

The authors acknowledge funding provided by the European Research Council under Grant number: 771146 (TOUGHIT).

Conflicts of Interest

The authors declare that they have no known competing financial interests or personal relationships that could have appeared to influence the work reported in this paper.

Data availability

The data sets generated during the current study are available from the corresponding author on a reasonable request.

Code availability

The data sets generated during the current study are available from the corresponding author on a reasonable request.

Author contribution

Conceptualization, D.K. and K.S.; methodology, M.A. and K.S.; software, K.S.; validation, K.S.; formal analysis, K.S. and M.A.; investigation, M.A. and K.S.; resources, D.K.; data curation, K.S.; writing—original draft preparation, K.S; writing—review and editing, K.S., M.A. and D.K.; supervision, D.K.; project administration, D.K.; funding acquisition, D.K. All authors have read and agreed to the published version of the manuscript.

References

[1] K.S. Ng, A.H.W. Ngan, Effects of trapping dislocations within small crystals on their deformation behavior, Acta Mater. 57 (2009) 4902–4910.

https://doi.org/10.1016/j.actamat.2009.06.053.

[2] J.A. El-Awady, S.I. Rao, C. Woodward, D.M. Dimiduk, M.D. Uchic, Trapping and escape of dislocations in micro-crystals with external and internal barriers, Int. J. Plast. 27 (2011) 372–387. https://doi.org/10.1016/j.ijplas.2010.06.006.

[3] J.R. Greer, J.T.M. De Hosson, Plasticity in small-sized metallic systems: Intrinsic versus extrinsic size effect, Prog. Mater. Sci. 56 (2011) 654–724. https://doi.org/10.1016/j.pmatsci.2011.01.005.

[4] R. Treml, D. Kozic, R. Schöngrundner, O. Kolednik, H.P. Gänser, R. Brunner, D. Kiener, Miniaturized fracture experiments to determine the toughness of individual films in a multilayer system, Extrem. Mech. Lett. 8 (2016) 235–244. https://doi.org/10.1016/j.eml.2016.01.004.

[5] A. Riedl, R. Daniel, M. Stefenelli, T. Schöberl, O. Kolednik, C. Mitterer, J. Keckes, A novel approach for determining fracture toughness of hard coatings on the micrometer scale, Scr. Mater. 67 (2012) 708–711. https://doi.org/10.1016/j.scriptamat.2012.06.034.

[6] D.E.J. Armstrong, M.E. Rogers, S.G. Roberts, Micromechanical testing of stress corrosion cracking of individual grain boundaries, Scr. Mater. 61 (2009) 741–743. https://doi.org/10.1016/j.scriptamat.2009.06.017.

[7] K. Matoy, T. Detzel, M. Müller, C. Motz, G. Dehm, Interface fracture properties of thin films studied by using the micro-cantilever deflection technique, Surf. Coatings Technol. 204 (2009) 878–881. https://doi.org/10.1016/j.surfcoat.2009.09.013.

[8] D.S. Gianola, A. Sedlmayr, R. Mnig, C.A. Volkert, R.C. Major, E. Cyrankowski, S.A.S. Asif, O.L. Warren, O. Kraft, In situ nanomechanical testing in focused ion beam and scanning electron microscopes, Rev. Sci. Instrum. 82 (2011) 1–12. https://doi.org/10.1063/1.3595423.

[9] J. Ast, M. Ghidelli, K. Durst, M. Göken, M. Sebastiani, A.M. Korsunsky, A review of experimental approaches to fracture toughness evaluation at the micro-scale, Mater. Des. 173 (2019) 107762. https://doi.org/10.1016/j.matdes.2019.107762.

[10] P. Hosemann, Small-scale mechanical testing on nuclear materials: bridging the experimental length-scale gap, Scr. Mater. 143 (2018) 161–168. https://doi.org/10.1016/j.scriptamat.2017.04.026.

[11] G. Dehm, B.N. Jaya, R. Raghavan, C. Kirchlechner, Overview on micro- and nanomechanical testing: New insights in interface plasticity and fracture at small length scales, Acta Mater. 142 (2018) 248–282. https://doi.org/10.1016/j.actamat.2017.06.019.

[12] J.C. Lindsay, in Situ Measurement of Fatigue Induced Crack Growth in Inconel 718 Using Direct Current Potential Drop Method, Statler College of Engineering and Mineral Resources, 2019. https://doi.org/https://doi.org/10.33915/etd.4050.

[13] C. Bohnert, N.J. Schmitt, S.M. Weygand, O. Kraft, R. Schwaiger, Fracture toughness characterization of single-crystalline tungsten using notched micro-cantilever specimens, Int. J. Plast. 81 (2016) 1–17. https://doi.org/10.1016/j.ijplas.2016.01.014.

[14] M. Sutton, J.-J. Orteu, H. Schreier, Image Correlation for Shape, Motion and Deformation Measurements, Springer Berlin Heidelberg, 2009. https://doi.org/10.1007/978-0-387-78747-3.

[15] S. Wurster, C. Motz, R. Pippan, Characterization of the fracture toughness of micro-sized tungsten single crystal notched specimens, Philos. Mag. 92 (2012) 1803–1825. https://doi.org/10.1080/14786435.2012.658449.

[16] J. Ast, B. Merle, K. Durst, M. Göken, Fracture toughness evaluation of NiAl single crystals by microcantilevers - A new continuous J-integral method, J. Mater. Res. 31 (2016) 3786–3794. https://doi.org/10.1557/jmr.2016.393.

[17] F. Iqbal, J. Ast, M. Göken, K. Durst, In situ micro-cantilever tests to study fracture properties of NiAl single crystals, Acta Mater. 60 (2012) 1193–1200. https://doi.org/10.1016/j.actamat.2011.10.060.

[18] J. Ast, T. Przybilla, V. Maier, K. Durst, M. Göken, Microcantilever bending experiments in NiAl - Evaluation, size effects, and crack tip plasticity, J. Mater. Res. 29 (2014) 2129–2140. https://doi.org/10.1557/jmr.2014.240.

[19] ASTM Standard E1820, Standard Test Method for Measurement of Fracture Toughness, ASTM B. Stand. (2013) 1–54. https://doi.org/10.1520/E1820-13.Copyright.

[20] M. Alfreider, S. Kolitsch, S. Wurster, D. Kiener, An analytical solution for the correct determination of crack lengths via cantilever stiffness, Mater. Des. 194 (2020) 3–7. https://doi.org/10.1016/j.matdes.2020.108914.

[21] M. Alfreider, D. Kozic, O. Kolednik, D. Kiener, In-situ elastic-plastic fracture mechanics on the microscale by means of continuous dynamical testing, Mater. Des. 148 (2018) 177–187. https://doi.org/10.1016/j.matdes.2018.03.051.

[22] R.M.N. Pelloux, Crack extension by alternating shear, Eng. Fract. Mech. 1 (1970) 697–700. https://doi.org/10.1016/0013-7944(70)90008-1.

[23] R.O. Ritchie, Mechanism of Fatigue-Crack Propagation in Ductile and Brittle Materials, Int. J. Fract. 100 (1998) 55–83.

[24] J.E. Hack, S.P. Chen, D.J. Srolovitz, A kinetic criterion for quasi-brittle fracture, Acta Metall. 37 (1989) 1957–1970. https://doi.org/10.1016/0001-6160(89)90080-1.

[25] R. Pippan, S. Wurster, D. Kiener, Fracture mechanics of micro samples: Fundamental considerations, Mater. Des. 159 (2018) 252–267. https://doi.org/10.1016/j.matdes.2018.09.004.

[26] M. Burtscher, M. Alfreider, K. Schmuck, H. Clemens, S. Mayer, D. Kiener, In situ fracture observations of distinct interface types within a fully lamellar intermetallic TiAl alloy, J. Mater. Res. 36 (2021) 2465–2478. https://doi.org/10.1557/jmr.2020.306.

[27] C.F. Shih, Relationship between the J-integral and the COD for stationary and extending cracks, J. Mech. Phys. Solids. 29 (1981) 305–326.

[28] W. Brocks, D. Klingbeil, J. Olschewski, Lösung der HRR-Feld-Gleichungen der elastisch-plastischen Bruchmechanik, Bremerhaven, 1990.

[29] A.K. Saxena, S. Brinckmann, B. Völker, G. Dehm, C. Kirchlechner, Experimental conditions affecting the measured fracture toughness at the microscale: Notch geometry and crack extension measurement, Mater. Des. 191 (2020) 1–11. https://doi.org/10.1016/j.matdes.2020.108582.

[30] P.G. Sanders, C.J. Youngdahl, J.R. Weertman, The strength of nanocrystalline metals with and without flaws, Mater. Sci. Eng. A. 234–236 (1997) 77–82. https://doi.org/10.1016/s0921-5093(97)00185-8.

[31] P. Zhang, S.X. Li, Z.F. Zhang, General relationship between strength and hardness, Mater. Sci. Eng. A. 529 (2011) 62–73. https://doi.org/10.1016/j.msea.2011.08.061.

[32] D. Rupp, S.M. Weygand, Experimental investigation of the fracture toughness of polycrystalline tungsten in the brittle and semi-brittle regime, J. Nucl. Mater. 386–388 (2009) 591–593. https://doi.org/10.1016/j.jnucmat.2008.12.184.

[33] E. Harry, A. Rouzaud, P. Juliet, Y. Pauleau, M. Ignat, Failure and adhesion characterization of tungsten-carbon single layers, multilayered and graded coatings, Surf. Coatings Technol. 116–119 (1999) 172–175. https://doi.org/10.1016/S0257-8972(99)00071-7.

[34] M.J. Pfeifenberger, M. Mangang, S. Wurster, J. Reiser, A. Hohenwarter, W. Pfleging, D. Kiener, R. Pippan, The use of femtosecond laser ablation as a novel tool for rapid micro-mechanical sample preparation, Mater. Des. 121 (2017) 109–118. https://doi.org/10.1016/j.matdes.2017.02.012.

[35] J. Canny, A Computational Approach to Edge Detection, IEEE Trans. Pattern Anal.

Mach. Intell. PAMI-8 (1986) 679–698. https://doi.org/10.1109/TPAMI.1986.4767851.

[36] D. Vikram Mutneja, Methods of Image Edge Detection: A Review, J. Electr. Electron. Syst. 04 (2015) 1–5. https://doi.org/10.4172/2332-0796.1000150.

[37] M. Vidal, M. Ostra, N. Imaz, E. García-Lecina, C. Ubide, Analysis of SEM digital images to quantify crack network pattern area in chromium electrodeposits, Surf. Coatings Technol. 285 (2016) 289–297. https://doi.org/10.1016/j.surfcoat.2015.11.049.

[38] C. Roux-Langlois, A. Gravouil, M.C. Baietto, J. Réthoré, F. Mathieu, F. Hild, S. Roux, DIC identification and X-FEM simulation of fatigue crack growth based on the Williams' series, Int. J. Solids Struct. 53 (2015) 38–47. https://doi.org/10.1016/j.ijsolstr.2014.10.026.

[39] G. Van Rossum, F.L. Drake, Python 3 Reference Manual, CreateSpace, Scotts Valley, CA, 2009. https://www.python.org/ (accessed August 9, 2021).

[40] C.R. Harris, K.J. Millman, S.J. van der Walt, R. Gommers, P. Virtanen, D. Cournapeau, E. Wieser, J. Taylor, S. Berg, N.J. Smith, R. Kern, M. Picus, S. Hoyer, M.H. van Kerkwijk, M. Brett, A. Haldane, J. Fernández del Río, M. Wiebe, P. Peterson, P. Gérard-Marchant, K. Sheppard, T. Reddy, W. Weckesser, H. Abbasi, C. Gohlke, T.E. Oliphant, Array programming with {NumPy}, Nature. 585 (2020) 357–362. https://doi.org/10.1038/s41586-020-2649-2.

[41] P. Virtanen, R. Gommers, T.E. Oliphant, M. Haberland, T. Reddy, D. Cournapeau, E. Burovski, P. Peterson, W. Weckesser, J. Bright, S.J. van der Walt, M. Brett, J. Wilson, K.J. Millman, N. Mayorov, A.R.J. Nelson, E. Jones, R. Kern, E. Larson, C.J. Carey, I. Polat, Y. Feng, E.W. Moore, J. VanderPlas, D. Laxalde, J. Perktold, R. Cimrman, I. Henriksen, E.A. Quintero, C.R. Harris, A.M. Archibald, A.H. Ribeiro, F. Pedregosa, P. van Mulbregt, SciPy 1.0: Fundamental Algorithms for Scientific Computing in Python, Nat. Methods. 17 (2020) 261–272. https://doi.org/10.1038/s41592-019-0686-2.

[42] F. Pedregosa, G. Varoquaux, A. Gramfort, V. Michel, B. Thirion, O. Grisel, M. Blondel, P. Prettenhofer, R. Weiss, V. Dubourg, J. Vanderplas, A. Passos, M. Cournapeau, David Brucher, M. Perrot, É. Duchesnay, Scikit-learn: Machine Learning in Python, J. Mach. Learn. Res. 12 (2011) 2825–2830. http://jmlr.org/papers/v12/pedregosa11a.html.

[43] G. Bradski, The OpenCV Library, Dr. Dobb's J. Softw. Tools. (2000). https://docs.opencv.org/4.3.0/ (accessed August 9, 2021).

[44] S. van der Walt, J.L. Schönberger, J. Nunez-Iglesias, F. Boulogne, J.D. Warner, N. Yager, E. Gouillart, T. Yu, scikit-image: image processing in Python, PeerJ. (2014). https://doi.org/https://doi.org/10.7717/peerj.453.

[45] A.D. Kammers, S. Daly, Digital Image Correlation under Scanning Electron Microscopy: Methodology and Validation, Exp. Mech. 53 (2013) 1743–1761. https://doi.org/10.1007/s11340-013-9782-x.

[46] A. Buades, B. Coll, J.-M. Morel, Non-Local Means Denoising, Image Process. Line. 1 (2011) 208–212. https://doi.org/10.5201/ipol.2011.bcm_nlm.

[47] S.M. Pizer, E.P. Amburn, J.D. Austin, R. Cromartie, A. Geselowitz, T. Greer, B. ter Haar Romeny, J.B. Zimmerman, K. Zuiderveld, Adaptive Histogram Equalization and Its Variations., Comput. Vision, Graph. Image Process. 39 (1987) 355–368. https://doi.org/10.1016/S0734-189X(87)80186-X.

[48] S. Suzuki, K. Abe, Topological structural analysis of digitized binary images by border following, Comput. Vision, Graph. Image Process. 30 (1985) 32–46. https://doi.org/10.1016/0734-189X(85)90016-7.

[49] ASTM-E399, (1997) 413–433.

[50] F. Gustafsson, Determining the initial states in forward-backward filtering, IEEE Trans. Signal Process. 44 (1996) 988–992. https://doi.org/10.1109/78.492552.

Supplementary material to:

Crack length estimations for small scale fracture experiments via image processing techniques

K. Schmuck[a4] M. Alfreider[a], D. Kiener[a]

[a] *Department of Materials Science, Chair of Materials Physics, Montanuniversität Leoben, Jahnstraße 12, Leoben, Austria*

The microstructure obtained after the high pressure torsion process consists of bi-modal grain size distribution, with larger inhomogenities which are statistical distributed and embedded in a nano-crystalline matrix, see Fig. S 1 and Fig. S 2. For the quantification of the nano-crystalline grain size from transmission electron microscopy several images were captured and evaluated.

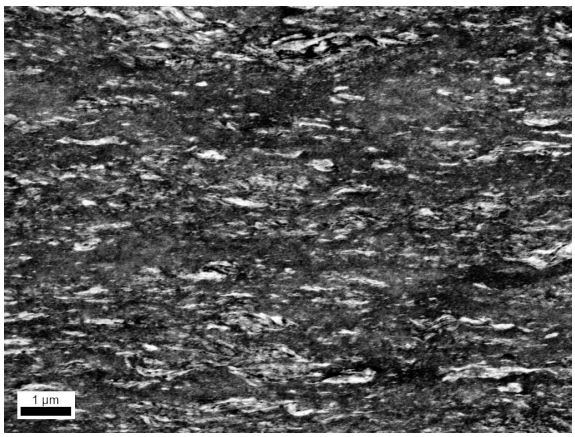

Figure 30: Obtained microstructure after the high pressure torsion process with elongated statistical distributed inhomogenities embedded in a nano-crystalline matrix. The image was acquired from backscatter electrons.

Smoothed load-displacement data is depicted in Fig. S 3, Fig. S 4 and Fig. S 5 for the largest, medium and smallest cantilever, respectively. Each diagram includes the fitted lines for unloading stiffness evaluation at every individual unloading step, drawn as dashed black lines. As can be seen in Fig. S 3, a load offset of about 2 mN occurred after the final unloading step for the largest cantilever. Thus, measured loads were corrected for this offset during all performed calculations. Measurement data of the smallest cantilever had a noticeable scatter, which is caused by the low measured forces. Thus, the measured data of the smallest cantilever was smoothed in two steps.

[4]Corresponding author at: Department of Materials Physics, Montanuniversität Leoben, Leoben, Austria.
E-Mail Address: klemens.schmuck@unileoben.ac.at (K. Schmuck)

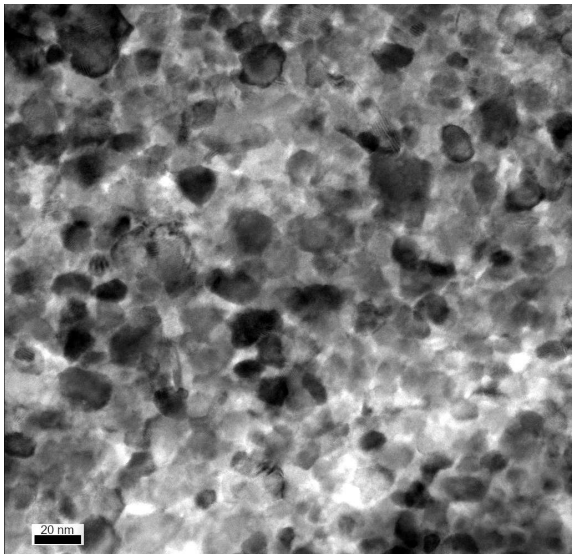

Figure 31: Embedding nano-crystalline matrix around statistical distributed inhomogenities, acquired by transmission electron microscopy.

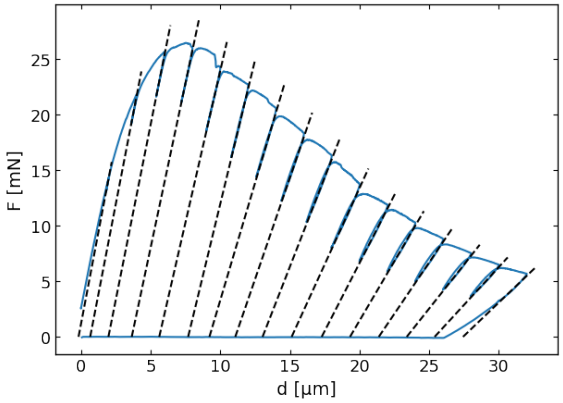

Figure 32: Load deflection data of the 34 x 31 µm^2 sized cantilever given by the blue solid line and the determined unloading stiffness as dashed black lines.

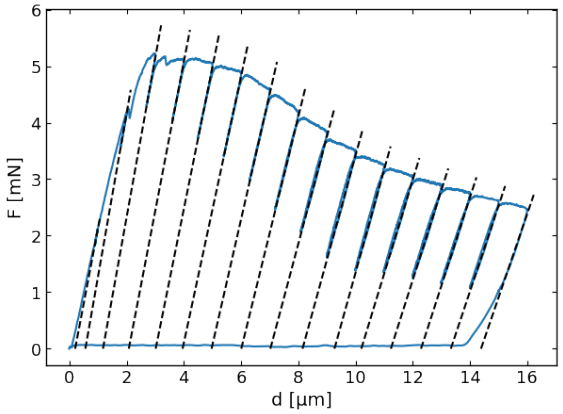

Figure 33: Load deflection data of the 14 x 13 µm^2 sized cantilever given by the blue solid line, and the determined unloading stiffness as dashed black lines.

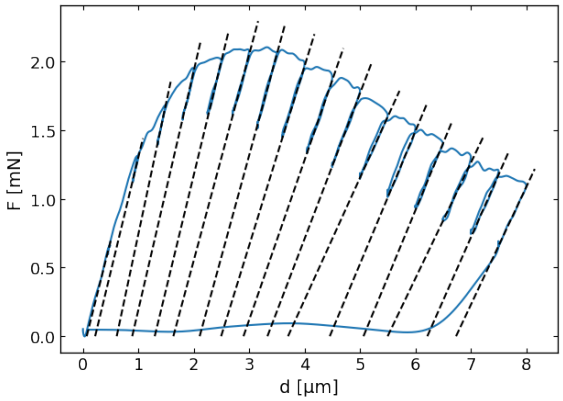

Figure 34: Load deflection data of the 6.5 x 4.3 μm^2 sized cantilever given by the blue solid line and the determined unloading stiffness as dashed black lines. Note that the load displacement curve is smoothed.

Publication D

Automatic and time-resolved determination of fracture characteristics from *in situ* experiments

Materials and Design 243, 113038, (**2024**)
doi: 10.1016/j.matdes.2024.113038

Automatic and time-resolved determination of fracture characteristics from *in situ* experiments

K. Schmuck[a5] M. Antenreiter[b], M. Alfreider[a], D. Kiener[a] [a] *Department of Materials Science, Chair of Materials Physics, Montanuniversität Leoben, Jahnstraße 12, Leoben, Austria* [b] *Montanuniversität Leoben, Department Mathematics and Information Technology, Chair of Information Technology, Erzherzog-Johann-Straße 3, Leoben, Austria*

Abstract

The characterization of materials in ever smaller dimensions is crucial for the growing demand for miniaturized devices. Hence, *in situ* fracture experiments are frequently performed at the micron to sub-micron scale. To evaluate fracture process of these experiments, knowledge of the crack length or the crack tip opening displacement is required. Acquired *in situ* frames provide a direct measurement of the crack length, crack tip opening displacement and -angle. An algorithm was developed to extract these parameters from the *in situ* frame sequences automatically. To verify the performance of the algorithm, fracture characteristics were measured manually for several frames of the available *in situ* experiments. The fracture behavior of these samples ranged from brittle over semi-brittle to ductile. The comparison between algorithmic results and manual measurements demonstrated the applicability of the algorithm to different fracture behaviors. Additionally, the fracture characteristics determined by the algorithm are in accordance with the fracture toughness data reported in literature. The crack tip opening displacement measurement gives thorough insight into the plastic deformation during fracture. The automatic extraction of the fracture characteristics allows a more detailed analysis of small-scale fracture processes and enables a reproducible, continuous evaluation of the fracture characteristics of all frames.

Keywords: In-situ microcantilever testing; Crack propagation; Image processing techniques; Small scale fracture experiments;

Introduction

The ongoing trend of device miniaturization and decreasing internal length scales requires testing of material properties, including fracture behavior, on increasingly smaller length scales, down to the micron and sub-micron regime [1,2]. To gain insights into the material-

[5]Corresponding author at: Department of Materials Physics, Montanuniversität Leoben, Leoben, Austria. *E-Mail Address:* klemens.schmuck@unileoben.ac.at (K. Schmuck)

and fracture behavior at this scale, *in situ* experiments are frequently conducted [1,3-5]. In these experiments, the plastic zone ahead of the crack tip extends over a considerable part of the ligament, which makes the application of elastic-plastic fracture mechanics (EPFM) necessary. The fracture evaluation in the framework of EPFM requires an accurate knowledge of the crack length. At the micron to sub-micron scale, crack length can be indirectly determined by measuring sample stiffness, which gives an average crack length over the crack front. Alternatively, crack length can be measured directly from acquired *in situ* frames [6-10]. Manual crack length measurement on all acquired frames is a tedious task and strongly depending on human individuality. Schmuck *et al.* [11] introduced an algorithm to extract the crack length from all frames semi-automatically by using image processing techniques. Their algorithm necessitates fine tuning of the evaluation parameters by the user.

Another characteristic parameter of fracture processes is the crack tip opening displacement (δ), which is a measure for crack tip blunting during the fracture process and is related to other fracture parameters through simplified models [8,12]. At the macro scale, it is possible to measure δ directly from a crack negative formed by filling the crack with a curing liquid, or indirectly via the hinge model, which relates the crack mouth opening displacement to δ via similar triangles [8,9,13-15]. The former is not applicable at the micron to sub-micron scale due to the small sample dimensions, though the hinge model is still applicable [8]. In addition, δ can be measured directly from *in situ* frames, which is frequently performed manually [16,17]. Manual measurements are a tedious and challenging task due to low resolution at the crack tip and image noise due to the high image acquisition rates necessary to capture crack growth. Often, as a result, only critical frames are evaluated manually.

In this work, the algorithm proposed by Schmuck *et al.* [11] is further enhanced to work automatically and extended to extract δ and crack tip opening angle (α) in addition to the crack length. These additional characteristics offer further insight into the ongoing fracture process and enhance data interpretation. To demonstrate the algorithms capabilities, it is applied to samples of different length scales, from micron to sub-micron scale, and varying fracture behavior ranging from brittle to ductile, substantiating the applicability of the algorithm to a wide range of problems.

Materials and Methods

The image-based evaluation of *in situ* fracture experiments faces various challenges, schematically illustrated in Figure 35. Mounting the sample is one of them, as a few degree tilt leads to a distorted view and visible side surfaces of the sample, depicted by Figure 35 a). Generally, the distortion is negligible due to low tilt angles. A few degrees tilt, however,

are sufficient to image side surfaces, leading to visible edges from the backside and possible material within the crack wake. Furthermore, the fracture process itself contributes to the challenges of image-based evaluation. Brittle fracture exhibits minor crack tip blunting before abruptly failing between two *in situ* images. Although the crack path is usually straight, the resulting thin crack is only a faint feature on the *in situ* images, shown in Figure 35 b). In case of ductile fracture, the crack exhibits extensive blunting, pore formation and tearing of the material between crack tip and pores, illustrated in Figure 35 c). The pores enlarge until they are in contact with the crack tip, resulting into crack propagation. This is again followed by crack tip blunting, more pore formation and tearing of the material, depicted by the increasing size of the pores closer to the crack tip in Figure 35 c). Semi-brittle failure combines the features occurring in brittle and ductile fracture and adds further fracture features, see Figure 35 d). Thereby, the crack at the crack tip is rather thin. Additionally, the tearing leads to material bridges during crack propagation, which, upon cracking, leaves behind material in the crack wake. During the propagation the crack might also deflect and bifurcate, displayed in Figure 35 d).

To summarize, thin crack paths resemble to be faint features on the *in situ* frame and crack deflection blurs the transition between blunting and crack flanks. Additionally, pore formation renders the crack tip position ambiguous due to residual material from tearing and bridging, while bifurcation causes an ill-defined crack tip due to multiple crack branches as reported in literature [18-20]. However, the transition between the different fracture types is smooth, hence, the features may combine or might be missing for individual experiments. All of these features complicate the extraction of the fracture characteristics.

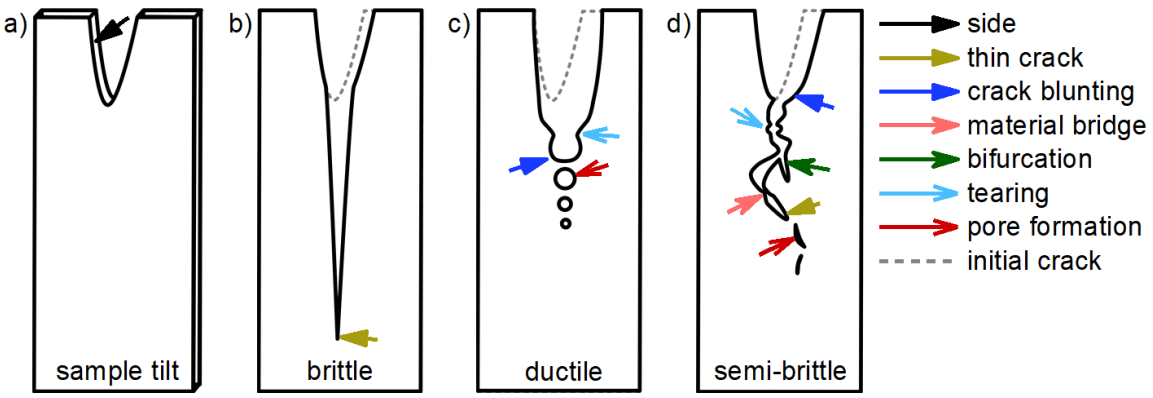

Figure 35: Schematic illustration of the challenges to detect the crack contour and extract thereof the fracture characteristics from *in situ* images. a) Slightly tilted sample, viewing material from the back in the crack wake. b)-d) Different fracture types with the corresponding prominent fracture features. To access the colored version of this graphic the reader is referred to the online version of the article.

Material

The algorithm was developed using *in situ* frames of tested single-edged notched cantilever bending beams. Figure 36 illustrates the standard geometry of these cantilevers. The fracture experiments were conducted in other publications and the cantilevers were fabricated from different materials, such as single crystalline tungsten, nano crystalline tungsten-copper composites and fully lamellar intermetallic titanium-alumina alloys [10,17,21]. Thereby, the cantilever size was situated in the micrometer regime. The cross-section of the cantilevers were approximately (3 x 3) µm^2 [10], (2.5 x 2.5) µm^2 [21] and from (5 x 5) µm^2 to (35 x 35) µm^2 [17]. To fabricate these cantilevers focused ion beam milling was employed. All fracture experiments were performed inside scanning electron microscopes (SEM; DSM 982, Carl Zeiss AG, Oberkochen, Germany; SEM/FIB, Leo 1540 XB, Carl Zeiss AG, Oberkochen, Germany) The *in situ* frames were acquired with the in-lens secondary electron detector at frame rates of either one [17], two [10] or six [21] frames per second. These frame rates provide a balance between image quality and ability to capture crack growth. Lower image acquisition rates benefit image quality, while higher are advantageous to capture crack growth. For cantilevers tested in [10, 17], the imaging area was limited to the crack vicinity to enhance image quality and resolution. All cantilevers tested in [17] were loaded displacement controlled by quasi-static loading at rate of 50 nm/s with an ASMEC indenter (UNAT SEM 1, ASMEC GmbH, Dresden, Germany), which has a noise level of 50 µN in vaccum. This loading involved 15 partial unloading steps, enabling stiffness measurements to be determined during post-processing from the load-displacement data at each unloading step [8]. The cantilevers tested in [10, 21] were tested in a force controlled scheme with a loading rate of 10 µN/s using a Hysitron Picoindenter PI 85 with a CSM module(Bruker Corporation, Billerica, USA). This indenter allows to perform dynamic loading and has a noise level of 1 µN. Thereby, the load signal is superimposed with a small sinusoidal signal, allowing the stiffness to be measured continuously [6]. The knowledge of stiffness in combination with the initial crack length allows the current crack length to be estimate from the mechanical data recorded [8, 10]. This, mechanical data includes the load and displacement signal, as well as the stiffness signal in dynamical testing. The tips used for loading were in all cases wedge shaped conductive diamonds (Synton MDP, Nidau, Switzerland). For further information to the respective experimental procedure applied the reader is referred to the respective publications [10, 17, 21]. The investigated cantilevers exhibited a fracture behavior ranging from brittle to semi-brittle failure to cover the variety of crack features described above.

To further verify generalization, the algorithm was tested with *in situ* frames recorded by a transmission electron microscope (TEM, JEOL JEM-2200FS microscope, JEOL Ltd., Japan). The tested cantilever was fabricated from a titanium-aluminum alloy by focused ion beam milling and had a cross-section of about (200 x 150) nm^2. *In situ* frames were acquired in

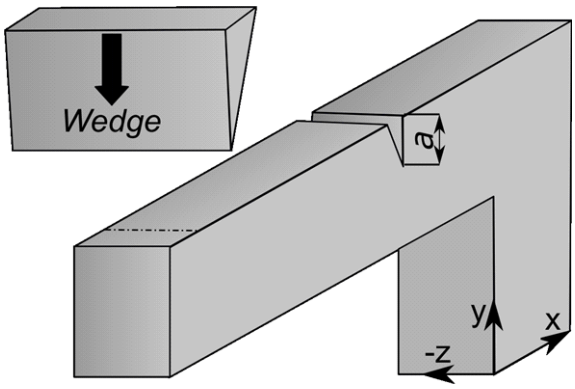

Figure 36: Micro cantilever bending beam geometry, with a the crack length and a coordinate system. The z-direction refers to the viewing direction during the experiment, while the x- and y-direction span the image area.

bright field mode at 1 frame per second. The sample exhibited additional distinct contrast changes over time due to dislocation movement. The cantilever was loaded displacement controlled by static loading with the Hysitron Picoindenter PI 85 and failed by extensive crack tip blunting.

Algorithm

The algorithm was written in Python 3.9 [22] using the image processing packages opencv (opencv-contrib-python-headless v4.6.0.66) [23] and sci-kit image (v0.19.2) [24] as well as the standard scientific packages numpy (v1.22.3) [25] and scipy (v1.8.0) [26]. To extract the fracture characteristics, the algorithm is split into preprocessing, pixel classification, crack flank contour retrieving and finally determination of the fracture characteristics from the extracted crack flanks, as detailed in the next chapters.

Image preprocessing

Depending on the experimental conditions, preprocessing is occasionally necessary. The algorithm assumes the following conditions: a top-down crack growth direction, consistent captured regions, and a consistent magnification across all frames. In cases of crack growth from bottom to top, the initial preprocessing involves a 180-degree rotation of all frames. Furthermore, the images sequences are split to include only images with a consistent magnification and region in case of different viewing areas or magnification during the experiment.

At small scale, thermal drift can significantly impact the result of the algorithm. Removing this drift from the frames is crucial to establish a consistently stable reference point across

all frames. Determining accurate fracture characteristics, like crack length, requires a stable reference point. The algorithm achieves this by aligning each frame with the previous frame using a registration technique known as phase cross-correlation [27], which provides the translative offset between two consecutive frames. To effectively align the frames, a region of interest (ROI) is selected to encompass the crack, ensuring that the crack remains within the ROI across all processed frames.

The algorithm is also sensitive to gray level changes between frames. Various recording devices might produce frames that are either darker or brighter by a constant factor. Shadowing or charging during the experiment can cause a change in gray scale distribution. Therefore, the algorithm compensates for constant gray level shifts between frames. In every frame, the median gray value in the ROI is calculated. The difference between two gray value medians is used to compensate for the variations in the recording process.

Pixel classification

After preprocessing, the objective is to classify each pixel in the image into two distinct classes. The first class, C_s, represents sample pixels, while the second class, C_b, denotes background pixels. The classification process relies on using the gray values of the pixels as a feature. To achieve this, the algorithm assigns each gray value v at position (x, y) within the range of $0 - 255$ to either the sample or background class based on a pre-calculated probability. The probability is determined by extracting gray values from user-defined regions in a reference frame. For the samples investigated, the initial frame was used as reference frame, as depicted in Figure 37 a). Here, the red rectangle defines the gray values for the corresponding background pixels, while the blue rectangle represents gray values for sample pixels. By employing these rectangles, a probability function for each gray value is derived, indicating whether it belongs to the sample or background class. To avoid mathematical issues arising from probabilities with a zero value, a consistent small probability for each gray value and class is added. This small value is determined automatically by dividing one with the pixel count of the selected regions. The resulting probability distribution is illustrated in Figure 37 b). The calculation of probabilities avoids a system with fixed absolute thresholds, because gray values can vary in each experiment, due to for example, differences in the interaction between the electron beam and sample, or the orientation of the scanned surface to the electron detector.

The gray values of the pixels are not always sufficient to assign a pixel to a class. Therefore, the algorithm incorporates edge information from crack contours by utilizing the Sobel operator [28] to extract additional information if a pixel belongs to an edge. This operator is designed to highlight rapid changes in the image intensity. Rapid changes can be edges

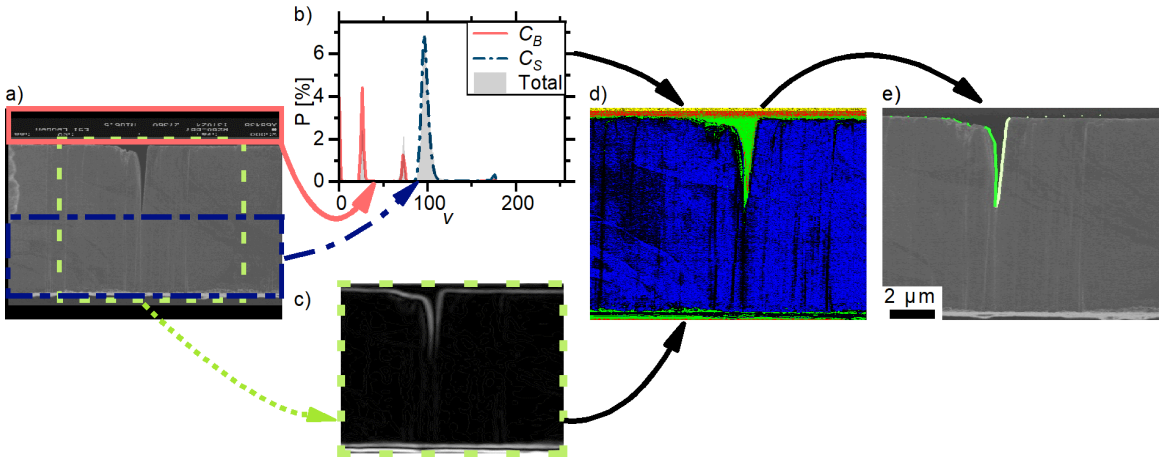

Figure 37: Segmentation and contour extraction process. a) Defining background (red rectangle), sample (blue rectangle) and a region of interest around the crack (green rectangle). b) Histogram of the region of interest with the probability curves of sample (C_s) and background (C_b). c) Illustrates the edge probabilities found by the Sobel operator. d) Depicts the probabilities of sample (blue, channel), background (red, channel) and $f(x, y)$ (green, channel), as RGB-image. e) Extracted crack contour from the probability image. There the contour is partitioned into a left (dark green) and right (light green) part, respectively. To access the colored version of this graphic the reader is referred to the online version of the article.

or noise from the image recording process. Therefore, usually a careful selected threshold has to be used at the end of an edge detection process. To avoid again the use of a fixed threshold, an automatic threshold adaption is implemented, described below in more detail.

The Sobel operator works by conducting a convolution of the image with a 3×3 kernel. The kernel emphasizes horizontal and vertical gradients in the image, enabling the identification of edges in both directions. The Sobel operator yields a low value if a pixel does not belong to an edge, but a high value if there are rapid changes in intensity, indicating a potential edge pixel. The Sobel operator, denoted as $S(x, y)$, does not provide probabilities. Therefore, the Sobel operator output cannot be combined with the probabilities from the gray values. To address this, the algorithm calculates S_{norm}, which falls within the range of 0.0 to 1.0, by normalizing it with the highest possible value of the Sobel operator.

After that, the values from grayscale and the edge information are combined by:

$$f(x, y) = 1 - P(v_{xy}|C_s) \cdot (1 - S_{\text{norm}}(x, y)) \,, \tag{1}$$

where v_{xy} is the gray value at position (x, y), $P(v_{xy}|C_s)$ is the likelihood that the gray value belongs to a sample pixel, and $S_{\text{norm}}(x, y)$ is a kind of likelihood that the pixel at (x, y) is an edge pixel. The range of $f(x, y)$ is between 0.0 and 1.0 and can be interpreted as follows: high values correspond to pixels from background or strongly visible edges and low values of $f(x, y)$ indicate the pixel is likely part of the sample. Figure 37 d) illustrates

the combination of the class probabilities with $f(x, y)$, as RGB image. Thereby, the color channels correspond to the individual classes. The color value represents the probability that is assigned by the algorithm to that pixel for the respective class. In the case of black pixels the algorithm is uncertain and assigns the basis probability described above, which is approximately 0.

To distinguish between background and sample, a threshold is automatically chosen for the function $f(x, y)$ from the probabilities of the two classes. Pixels are assigned to class C_s based on the condition $P(v_{xy}|C_s) > P(v_{xy}|C_b)$ and the corresponding $f(x, y)$ values are calculated from these pixels by employing the 95^{th} percentile $p^{0.95}_{sample}$. The second value of the threshold is calculated from the 5^{th} percentile $p^{0.05}_{background}$ of all $f(x, y)$ with the condition $P(v_{xy}|C_s) < P(v_{xy}|C_b)$. By utilizing these two values, the threshold th is determined, which distinguishes between sample and the background.

$$th = \frac{p^{0.95}_{sample} + p^{0.05}_{background}}{2} \tag{2}$$

This automatic threshold adjustment is calculated for each frame to achieve the best possible separation between background and sample pixels.

Contour extraction

All background pixels that satisfy the condition $f(x, y) > th$ are connected from the above analysis with a fill algorithm. This operation can be described as pouring a liquid into the crack. For this a modified flood fill algorithm was employed [29,30]. The algorithm searches along a line for points that belong to the background. To fill the crack, the algorithm iterates over points and analyses the neighboring pixels. If the neighboring pixel belongs to the background, it is added to the list of points. The iteration stops if no further points are found. The resulting points list represents the filled form. Contours can be computed from this filled form. The lowest point of the fill operation separates the crack into a left and right contour (see Figure 37 e).

The algorithm searches for crack-segments inside the sample by retrieving the outer sample contour and tests if regions with sufficient probability to be an edge are inside this contour. Crack segments are then connected by a shortest path search, which was proposed by Fredman *et al.* [31] and is implemented in in the sci-kit image package [24]. The resulting path is a continuous pixel-thin path between the crack segments. This path is then split into sections that connect the respective crack segments. Starting from the lowest crack segment, each segment is convoluted with the path section that connects the current crack segment with the segment above. For the convolution the segments and sections are extracted into binary

images, upon which the convolution is performed by discrete Fourier transformation of the binary images, multiplication in Fourier space and back transformation of the multiplication result. These are then added to the image with the filled crack to obtain the whole filled path, leading to a more natural crack shape. Segments with less than 4 px are neglected and assumed to be noise. This procedure allows the algorithm to overcome material bridges and barriers in the crack wake, which frequently occurs due to a possible sample tilt as well as generally during semi-brittle and ductile failure, as schematically illustrated in Figure 35 a), c) and d).

Fracture characteristics

Determination of the crack tip opening displacement δ and -angle α is adopted from the description given by Shih [12]. The procedure is schematically shown for a representative blunted crack in Figure 38 a) and b). The found contour lines are illustrated in Figure 38 a), while b) depicts a closer view of the crack and measurement procedure. Figure 38 c) shows the measurement for an ideally smooth crack. The angle α is measured by fitting both crack flanks linearly and measuring the angle between them, see the blue dotted lines in Figure 38. The δ determination requires additional steps, involving defining the center line between the two fitted lines and constructing a symmetric right-angled triangle at the crack tip, which is projected on the center line, depicted in Figure 38. In case of parallel lines, locating the center line is straightforward as it lies between the two fitted lines and is parallel to them. While otherwise two possibilities exist that are orthogonal. The line with the smaller orthogonal distance to the overall crack contour is used as center line, illustrated by the dashed violet line in Figure 38. Next, the crack tip is projected onto this center line, which acts as intersection point and rotation center for two lines that are rotated by $\pm\frac{\pi}{4}$, see orange lines in Figure 38. The intersection between these lines and the fitted crack flanks gives δ.

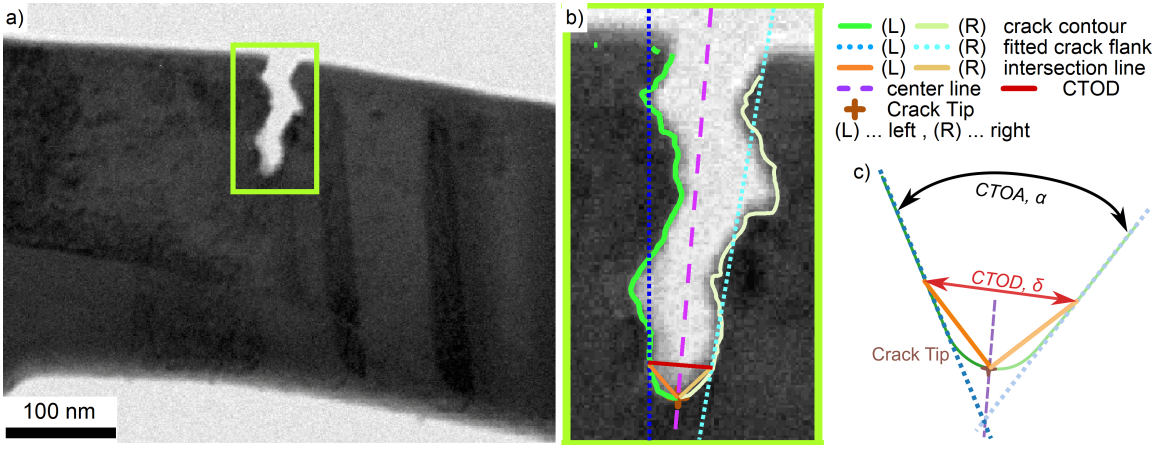

Figure 38: Extraction process of crack tip opening displacement δ and -angle α. a) Representative *in situ* frame with a blunted crack. b) Illustration of the crack region. c) illustration of the extraction for an ideal smooth crack. To access a colored version of this graphic the reader is referred to the online version of the article.

In general, the crack flanks are rather jagged, as illustrated by the representative crack in Figure 38. The crack contour shows a variety of different shapes depending on the material behavior, ranging from brittle to ductile fracture [12,14,18,20,32]. To only fit the crack flanks and avoid the possible blunt region, the algorithm selects the fitting region by calculating the sliding variance with a 1D-kernel of size 11 is applied to the x- and y-direction. By following the contour line, starting from the crack tip, the fit region begins where the y-variance is larger than the x-variance, as the blunted region would have an increased spread in x-direction. This requires a pronounced blunting region, which is only present in ductile and semi-brittle samples. Besides these measures the RANSAC algorithm [33,34] is employed to fit the crack flanks, since the algorithm is able to detect outliers and therefore neglects small blunting regions and portions of the jagged crack contour.

Fracture mechanics

To characterize fracture processes in EPFM the J-integral is used. The stress and strain fields in front of the crack tip can be modelled by the Hutchinson-Rice-Rosengren (HRR) theory [35,36]. As long as the fracture process is dominated by the HRR field [35,36], the fracture parameters δ and J are related according to:

$$\delta = d_n \frac{J_\delta}{\sigma_y}, \tag{3}$$

with σ_y as yield strength and d_n the Shih factor, which is 0.78 for a non-hardening material and plane strain-dominated fracture [12]. To compare the values with literature they can be

converted into stress intensity values, given the plane strain assumptions, by [9]:

$$K = \sqrt{\frac{EJ}{1-\nu^2}}, \tag{4}$$

with the Poisson ratio ν and the Young's modulus E. The material properties used in this work are tabulated in Table 4.

Table 4: Material properties at room temperature for the used materials with the yield strength (σ_y), the Young's modulus (E) and the Poisson ratio (ν).

Material	σ_y[MPa]	E [GPa]	ν
tungsten-copper (nc) [17]	2250	221	0.32
tungsten (sx) [10]	1750	410	0.28
titanium-aluminum [21,37]	660	189	0.23

Results

Fracture behavior challenges

Results of the algorithm, crack tip coordinates, δ and α, were directly compared to manual measurements, which were performed for each *in situ* experiment on an evenly distributed subset of the acquired frames. The manual measurement was performed at least 3 times to allow for an uncertainty estimate. The crack tip coordinates were converted into crack extension (Δa) by calculating the Euclidean distance between the initial crack tip coordinates and all subsequent crack tip coordinates. This provides a comparison to the Δa approximated by the mechanical data in literature, where available. All values determined by the algorithm were smoothed by low-pass filtering. For reference, the unsmoothed data was plotted into the corresponding graphs in a light green color.

For the tested cantilevers, the fracture behavior was either brittle, semi-brittle or ductile. The brittle cantilevers fractured unstable, with a straight crack flank and only faint initial crack growth. Figure 39 illustrates a brittle fracture cantilever, which was tested in [17]. Figure 39 c) depicts Δa over time, including data obtained from mechanical evaluation, d) shows δ and e) α determined by the algorithm and manually. The unstable fracture occurred between two consecutive frames, resulting into a narrow crack, depicted by the fractured *in situ* frame in Figure 39 b). Additionally, the processed frame is placed next to the acquired frame to illustrate the crack flanks found by the algorithm, highlighted by the green lines in Figure 39 a) and b). The dark and bright green lines represent the left and right flank, respectively.

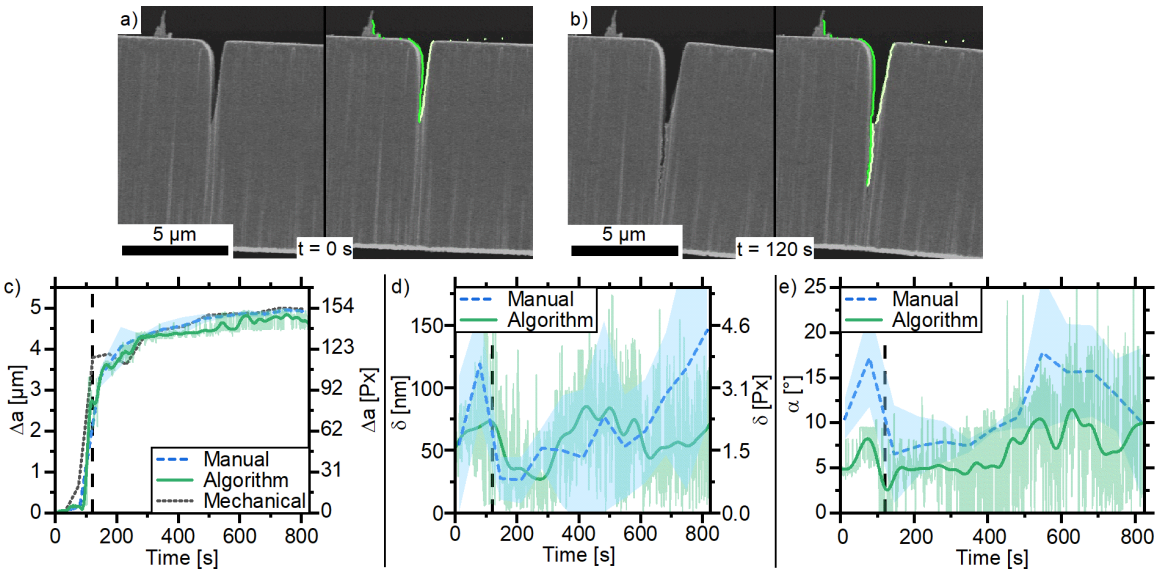

Figure 39: Fracture characteristics measured for representative unstable fracture. The recorded *in situ* frames are shown in a) and b). The left image illustrates the frame acquired and right image depicts the contour lines found by the algorithm. c) crack extension (Δa), d) crack tip opening displacement (δ) and e) -angle (α). The dashed lines in the graphs represent the *in situ* frames shown in subfigure a) and b). The cantilever was previously tested in [17].

A semi-brittle fractured cantilever tested in [17] is shown in Figure 40. Subfigure a) depicts the initial crack fabricated by FIB milling, while in Figure 40 b) the blunted crack before initiating crack growth can be seen. Figure 40 c) shows the crack evolving from material tearing, bridges, pores and a slight crack path deflection. The results obtained for Δa, δ and α are depicted in the subfigures d), e) and f), respectively. Figure 40 d) also includes the Δa determined from mechanical data for the respective fracture experiment. The blunting leads to an almost constant crack length and increasing δ and α, shown in Figure 40 d), e) and f). Additionally, contrast changes through out the experiment can be seen in the *in situ* frames.

The algorithm's generalization was examined by processing *in situ* frames acquired by TEM imaging and performed with a different measurement setup, illustrated in Figure 41. The initial crack is depicted by subfigure a) and the fully blunted evolved crack is illustrated in subfigure b). In Figure 41 b), the material at the crack tip starts to tear and a significant contrast change is visible, indicating crack initiation. Figure 41 c) depicts the crack contour detail of the *in situ* frame shown in Figure 41 b), highlighting possible blunting regimes in blue and red. The results determined from the acquired *in situ* frames are displaced for Δa, δ and α in subfigures d), e) and f), respectively.

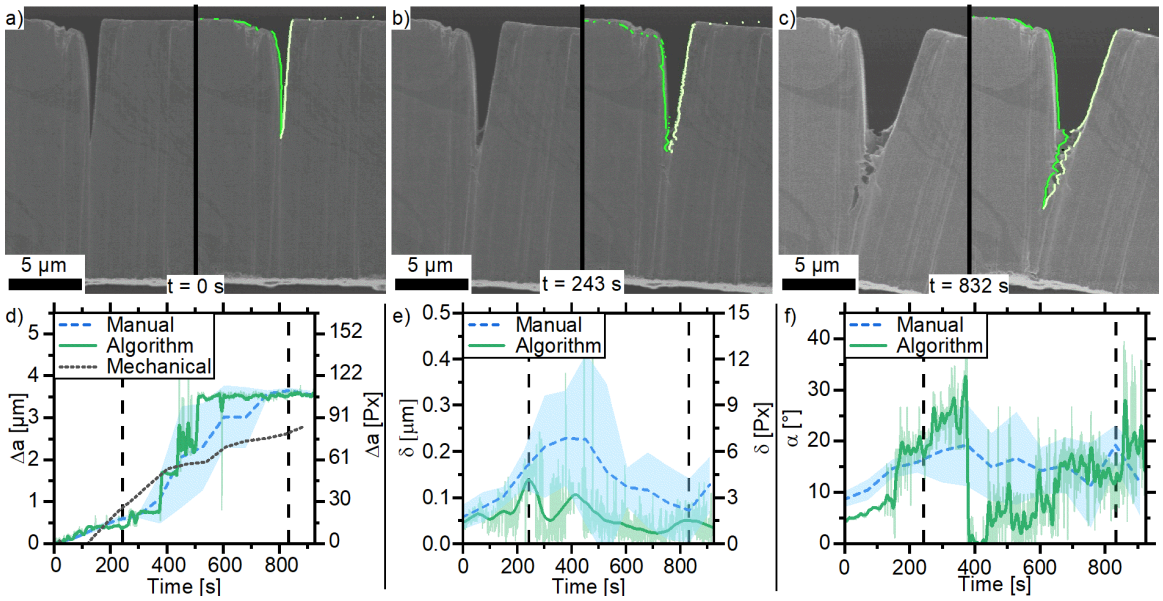

Figure 40: Comparison of the fracture characteristic measured for a semi-brittle fracture. a)-c) Illustrate the recorded *in situ* frames. The original frame to the left and the processed frame with the determined contours to the right, respectively. The diagrams depict, d) the crack extension (Δa), e) crack tip opening displacement (δ) and f) -angle (α). The *in situ* frames are indicated by the dashed lines. The cantilever was previously tested in [17].

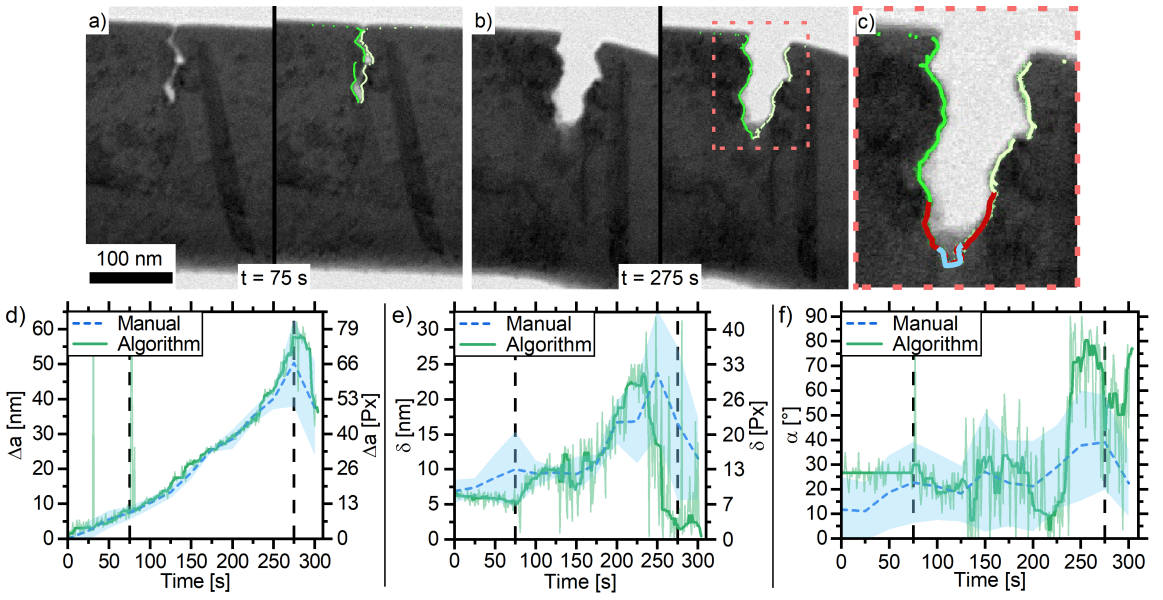

Figure 41: Fracture characteristics extraction for a sample tested inside a transmission electron microscope. a) and b) show the recorded *in situ* frames. To the left the recorded frame and to the right the processed frame with the crack contour lines found. c) Depicts the crack tip detail of subfigure b), highlighting different possible blunting regions in blue and red. The diagrams depict d) the crack extension (Δa), e) crack tip opening displacement (δ) and f) -angle (α). The dashed lines in the diagrams mark the *in situ* frame.

Algorithm vs. Human expert

In addition to the representative samples above, the algorithm was applied to several additional fracture experiments to validate its generalization capabilities and accuracy. Multiple manual measurements were performed on each sample, too. The mean and standard deviation for the manually measured crack tip coordinates (x, y), as well as δ and α, were calculated and the mean was used as ground truth estimate. To assess the manual measurement error, the mean (e_m) and standard deviation (std_m) were determined for each sample, using the variance of the individual frame to get a single value, comparable to the mean squared error, tabulated in Table 5. The standard deviation was calculated to emphasize the variability of manual measurement error. The error of the algorithm (e_a) was evaluated based on the Euclidean distance between the estimated ground truth and the algorithms output, which was obtained for each individual frame. There, $d_{x,y}$ and δ are given in pixels, while α is stated in degrees to enhance comparability, as the experiments were performed at different magnifications. The experiments in the Table 5 are grouped according to the fracture behavior, with samples B1-B3 representing brittle fracture, D1 indicating ductile failure, and all others samples, SB1-SB6, fractured semi-brittle.

Table 5: Accuracy assessment of the manual and algorithmic determined crack tip coordinates (x, y), crack tip opening displacement (δ) and -angle (α) for brittle (B1-B3) [17], ductile (D1, Figure 41) and semi-brittle (SB1-SB6) [10,17] fractured samples. For these values the mean squared error ($\overline{e}$) was evaluated. To asses the crack length error, the Euclidean distance ($d_{x,y}$) of (x, y) to the ground truth data was evaluated. The subscripts a and m refer to algorithmic and manual measured data, respectively. Additionally, for the manual measurement the standard deviations (std_m) was calculated to emphasize the manual measurement variability.

Sample	$d_{x,y}$ [pixel]			$\Delta\delta$ [pixel]			$\Delta\alpha$ [°]		
	$\overline{e}_a$	$\overline{e}_m$	std_m	$\overline{e}_a$	$\overline{e}_m$	std_m	$\overline{e}_a$	$\overline{e}_m$	std_m
B1	8.2	5.0	7.0	0.9	1.7	1.6	4.41	4.72	4.86
B2	22.2	7.4	8.9	1.1	1.1	1.1	6.32	2.44	1.92
B3	15.4	2.8	3.5	1.8	1.9	1.8	5.90	5.03	4.66
D1	3.3	9.4	12.3	5.3	6.7	8.0	13.66	16.86	11.80
SB1	9.6	17.9	22.5	2.6	2.5	1.7	6.95	5.07	2.64
SB2	119.9	6.9	10.0	5.8	2.8	2.8	16.11	2.85	2.79
SB3	10.8	4.8	6.0	2.6	2.9	3.4	6.79	5.67	5.20
SB4	7.8	6.2	7.4	1.3	2.4	2.5	10.77	10.85	11.96
SB5	30.2	38.5	5.9	2.9	3.5	1.7	6.28	9.33	3.50
SB6	17.9	7.9	9.7	5.1	3.0	3.7	7.45	4.94	4.41

Discussion

The evaluation of *in situ* frames enables direct investigation of fracture processes. The algorithm allows for a continuous and automatic evaluation in a short period of time, usually within minutes. Although the image-based evaluation faces various challenges, stemming from the sample mounting, the image formation process and the fracture process itself (Figure 35). How the algorithm deals with those challenges is discussed in the next section, followed by comparing the performance to human expert measurements and other possible approaches for retrieving data from images. The last section discusses the utilization of the algorithm to determine the local fracture behavior in detail and compares the results to literature data.

Fracture behavior challenges

Capturing continuous crack propagation necessitates high image acquisition rates, contradicting with high quality imaging in electron microscopy, e.g. a high quality SEM-image requires several seconds of acquisition. Thus, the acquisition rate is usually set to 1 frame/s, representing a good trade-off between following crack propagation and obtaining sufficient image quality. However, the frames retain some amount of noise and the feature resolution is limited by the pixel size. Faint features may perish and go undetected. Furthermore, the *in situ* frames capture only the surface section of the possibly jagged and curved crack front, meaning the crack front shape is a superposition of the local microstructure and stress state [11,20].

While only a narrow crack is evident in Figure 39 b), the image-based measurements both manual and calculated by the algorithm yielded a similar crack extension throughout the experiment (Figure 39 c)). However, the crack extension derived from mechanical data produced a higher crack extension of about 200 nm (∼6 pixel) directly after fracture. This difference stems from aforementioned limitations of resolving sub-pixel crack separation features. In the case of an ideal straight crack, the crack's feature thickness can be approximated by δ, which does not exceed ∼72 nm (2.2 pixels) in this example. By accounting for noise and possible pixel errors, the crack close to the crack tip resembles to be a thin undetected feature. In contrast to the crack extension, δ and α are sensitive to slight changes in the crack shape, due to the crack flank fitting procedure and the uncertainty of crack tip location, which leads to increased scatter. Outside of these understandable, minor deviations, the automatically determined values for δ and α are in good agreement with the manually measured fracture characteristics. Thereby, δ and α exhibit a drop after crack propagation initiation, which is obvious as the blunting regime ends ($t = 104$ s) and brittle failure occurs. Despite the brittle fracture, the crack stopped and the remaining ligament

(∼1 µm) fully plasticized, starting at $t = 300$ s. This lead to a constant Δa, while δ and α slightly increase until the end of the experiment, in accordance with the general yielding of the remaining ligament after crack extension, as shown in Figure 39 d) and e).

In the blunting regime of the semi-brittle sample, the algorithmic results closely match to the manual measurements and are in accordance with the results from mechanical data, outlined in Figure 40 d)-f), up to $t = 243$ s, where the crack initiates. During crack propagation, additional crack features form, such as pores, material tearing and -bridging, illustrated by the evolved crack in Figure 40 c). As a result, locating the crack tip and defining the crack contours during crack propagation is challenging. Therefore, the manual measurement displayed increased uncertainty, and the algorithm's results exhibited increased scatter, shown in Figure 40 d)-f). Nevertheless, for the algorithmic data at crack propagation initiation, a drop in δ and α is evident. During crack propagation, δ is constant and α raises, which is in accordance with the determined crack extension increase at $t = 243$ s, depicted in Figure 40 d). Despite the agreement of the data retrieved from the images, the mechanical evaluation resulted in a shorter crack extension of about 800 nm (∼24 pixels) for the last unloading step. This difference is possibly due to heterogeneous propagation of the crack front, stemming from semi-brittle fracture and the fact that mechanical evaluation averages over the whole crack front, while the images capture only the surface. In general, the crack length exhibits minor deviations exclusively over the crack front [20].

The sample tested inside the TEM underwent ductile fracture and exhibited extensive blunting, depicted by Figure 41 a) and b). These frames illustrate the enhanced contrast obtained between background and sample, improving the classification process compared to SEM recordings. Additional features are present inside the sample region, such as dislocation lines, shear bands, crystal orientation, atomic mass and thickness contrast, depicted by the *in situ* frames in Figure 41. These features originate in the TEM imaging process [28] and complicate crack tip localization. Teared material is visible in Figure 41 b) in the light gray region at the crack tip, which slightly blurs the surrounding material. Material tearing raised the manual measurement uncertainty for Δa and δ significantly, noted by blue shaded region in Figure 41 d) and e). This occurred due to the absence of sharp crack edges and made crack localization near the crack tip more challenging. The angle α seems unaffected by material tearing, but exhibits significant scatter throughout the experiment, masking any potential effect of material tearing. The scatter in α can be attributed to the curved shape of the crack, which complicates the crack flank fitting procedure. The algorithm encounters the same visual obstacles as the manual measurement. Prior to the material tearing regime, the algorithmically determined and manually measured data is in accordance (Figure 41 e)-f)). Up to $t = 225$ s, Δa and δ increase monotonically, while α remains constant, indicating crack blunting. After this frame, material tearing occurs and the algorithm defines the teared

material, shown by the light gray area in Figure 41 b), as cracked. As a result, the algorithm determined a slightly enhanced crack growth with decreasing δ, while α increased due to the blurred transition from blunted crack to crack flank. Several manual measurements revealed that the teared material is neglected as often as it is included in the crack shape measurements. This resulted in an increased uncertainty of the manual measurement after $t = 225$ s. At unloading, crack closure occurs due to the elastically stored energy, which induces a drop in Δa and δ.

The different fracture behaviors brittle, ductile and semi-brittle revealed a variety of topological crack features, which complicate crack detection. The features can be split into classification and evaluation related issues. For example, faint crack associated with brittle fracture makes it challenging to detect the crack completely and is related to the classification process. Contrarily, crack tip blunting in ductile fracture blurs the transition between blunt crack tip and the flanks. While this complicates the evaluation process, it simplifies classification due to an increased feature size. Material tearing and -bridging in ductile fracture increases the challenge of classifying the crack due to material left in the crack wake. Semi-brittle fracture can cause void formation, crack deflection and bifurcation, which makes distinct crack classification even more challenging. Due to these features, the crack flanks tend to be jagged and curved, complicating the fracture characteristic evaluation. In addition to these features, the cantilever alignment, with respect to the viewing direction, affects fracture characteristic evaluation, as the SEM views only a 2D plane of the 3D cantilever. Thus, cantilever mis-alignments, *e.g.* slight rotation around y-axis, see Figure 35 a), result in visible side surfaces, complicating crack contour detection.

Algorithm vs. Human expert

Manual measurements are frequently used to evaluate *in situ* images obtained from fracture experiments. Thus, the results determined by the algorithm were compared to manual measurements to asses the algorithms accuracy and its capability to localize the crack tip as well as extract δ and α. The results for the different fracture characteristics are listed in Table 5. Thereby, the overall error of the manual measurement illustrates the challenge of extracting fracture characteristics. In general, errors obtained by manual and algorithmic measurements are of the same order of magnitude, although, the algorithmic errors are slightly higher. For the semi-brittle fractures, SB2 and SB6, the algorithmic errors are higher by multiple orders of magnitude. For these samples, the algorithm failed to completely detect the crack flanks, due to background material visible from the onset of the measurement, noted by Figure 42 a) and b). Manual crack detection benefits from human extrapolation capabilities of the crack flanks, which leads to smaller variations. However, the crack flanks are blurred in SB6, depicted by Figure 42 b), which impairs human perception and increases

the manual measurement error and variability.

In the case of brittle fracture, the increased $d_{x,y}$ errors of the algorithm can be attributed to the thinness of the crack, see the thin crack extension in Figure 39 b) and Figure 42 c). The algorithmic errors of δ and α are in accordance with the manual measurement errors and within in the error variability of the manual measurement, despite the undetected portion of the crack. δ and α seem unaffected by the excluded faint crack due to a smaller crack opening, demonstrating the applicability of the algorithm for brittle failure.

The ductile fractured sample D1 evidenced a similar scatter of $d_{x,y}$ for the manual measurement, while δ and α exhibited an increased scatter, possibly stemming from crack tip blunting. Besides, crack tip blunting caused raised absolute values of δ. Thus, the increased scatter has a negligible affect on the δ measurement. Comparing the algorithm to the manual measurement, all errors are below the manual measurement errors, which can mainly be attributed to the enhanced image contrast and crack tip blunting, all of which benefit the classification process. This is supported by the measurement curves depicted in Figure 41 d)-f). Despite small deviations, the algorithm performs well for samples undergoing ductile fracture. Even though only a single ductile fractured sample was analyzed the repeating sequence of blunting, tearing and pore formation is characteristic of ductile failure, proofing the algorithm's capabilities.

Semi-brittle fracture complicates fracture characteristic evaluation due to the combination of features from brittle and ductile fracture, as well as the aforementioned additional fracture features. Thus, the manual measurement error exhibits an increased scatter for all fracture characteristics, compared to the brittle samples, due to additional features and the higher absolute values of δ and α. Despite the additional features, the error of the semi-brittle samples are reduced compared to the fully ductile sample, which may stem from the reduced absolute values of the individual characteristics and the differences in imaging conditions between SEM and TEM. The algorithmically determined fracture characteristics exhibited an increased error for $d_{x,y}$ and α, as a result of material in the crack wake and the curved crack flanks. However, the majority of the algorithmic errors are of the same order of magnitude as the manual measurement errors, pointing to the capabilities of the algorithm in analyzing semi-brittle failure. The algorithm successfully accounts for the additional complications, illustrated by Figure 35 d), that appear during semi-brittle fracture.

Besides the comparison of the resulting fracture characteristics, time constrains are an uprising issue. In general, manual measurements are time consuming, so only critical frames are evaluated, leading to sparse information about the fracture process. Manual measurement also includes a lot of scatter due to human individuality. The algorithm, on the other hand, allows all *in situ* images to be analyzed within minutes and offers increased data density.

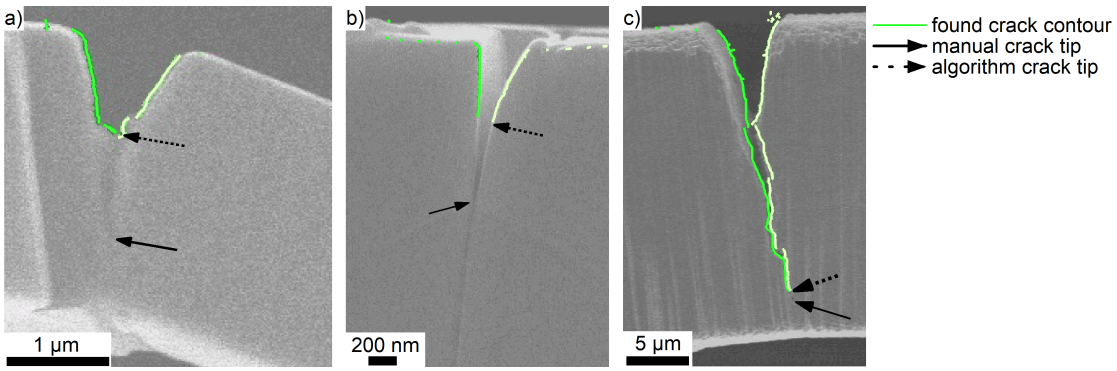

Figure 42: Respective *in situ* frames for possible detection challenges for automated crack detection. a) SB2 displaying material in the crack wake and contrast changes along the crack flanks, tested in [10]. b) SB6 illustrates a cantilever after semi-brittle fracture exhibiting material in the crack wake and blurred crack flanks, tested in [21]. c) Brittle fractured sample B3 exhibiting a faint crack extension, tested in [17].

Furthermore, the automatic procedure results in an independent evaluation, benefiting the reproducibility of the data.

Comparison to other techniques and possible enhancements

To evaluate *in situ* frames acquired from mechanical experiments, digital image correlation (DIC) is frequently conducted [5,39-47]. DIC tracks sample changes by correlating image-subsets of consecutive images [39,40]. The tracked sample changes can then be translated into sample deformations, allowing local strains to be determined [39,40,43-50]. These local strains are used to detect cracks and estimate the stress intensity factor [41,51,52]. The application to consecutive images facilitates tracking of crack propagation [42,53,54]. For macroscopic experiments Chen *et al.* [55] additionally determined δ and α by DIC. They achieved this by applying a wavelet transform to the displacement fields, enabling crack shape extraction. The δ was evaluated by using the crack shape as mask over the displacement field in x-direction, giving the crack flank displacement for each pixel. To obtain α the crack shape was quadratically fitted and the angle was measured at fixed distances from the crack tip. DIC is an advanced method, relying on the recognition of self-similar surfaces structures between consecutive images [5,39,40,48,50]. Thus, the sample surfaces are patterned to enhance surface structure recognition and suppress image noise [5,48]. To enable a high resolution imaging of the strain field, acquisition rates below 1 frame/minute are necessary [5,43,46,47]. This is unfeasible for the continuous crack growth monitoring during fracture experiments [5]. To enhance the image acquisition rate, Alfreider *et al.* [56] used a coarse grid pattern on the sample surface, at the cost of a lower strain field resolution. Due to the lower resolution, the crack shape can not be accurately determined from the *in situ* frames, leading to an imperfect crack shape. Furthermore, samples tested inside a TEM exhibit

changing image contrast in the sample region due to the imaging conditions. This renders classical DIC between frames infeasible. The presented algorithm in this work requires no self-similar structures on the sample surface and is capable of detecting the crack shape on an individual pixel basis, causing a flexible application to different testing setups inside SEMs and TEMs. Furthermore, the similar performance of the algorithm and manual measurements proved the applicability of the algorithm to different fracture behaviors. This allows the fracture characteristics (Δa, δ and α) to be automatically extracted from from noisy *in situ* frames.

Nevertheless, the capabilities of the algorithm would benefit from an enhanced classification process. This could be achieved by using a more sophisticated classifier, such as convolutional neural networks, *e.g.* U-net [57,58] or Segment Anything [59,60]. Although these classifiers might improve the overall performance of the algorithm, they require a lot of annotated input data for training, testing and validation. Another enhancement to the algorithm would be to include the time series information from subsequent images in the classification and evaluation process. This would make it possible to know the crack path before the classification and extraction of the crack contour, which would decrease the scatter of fracture characteristic data. Additionally, the crack flank fitting could be initialized by previously determined parameters. Besides, increasing the input image quality, through increased image resolution, contrast enhancement and decreased image noise would improve any image-based evaluation process. Lenthe *et al.* [61] found that during SEM imaging at high image acquisition rates, a pixel shift can occur due to the scanning process, resulting in image noise and blurred edges. To avoid this, they applied a correction function during the image formation process, leading to a decrease in pixel noise and sharper features.

Fracture mechanical implications

The fracture characteristics determined from *in situ* images allow a direct evaluation of the fracture process, based on the correlation of δ and α to the J-integral [8,62]. Additionally, recording the crack length enables the calculation of the J-integral without the necessity of quasi-static or dynamic loading to determine the cantilever stiffness throughout the experiment. However, the initial cantilever stiffness is required to convert the crack lengths measured by the algorithm into stiffness [10]. The initial cantilever stiffness can be obtained from a static pre-loading in the elastic regime or numerically estimated by Euler-Bernoulli beam theory [10]. This means that the fracture characteristics δ and α determined continuously by the algorithm allows the construction of crack-growth resistance curves (R-curves) without further parameter calculation. Compared to manual measurements and quasi-static loading, the automatic evaluation by the algorithm gives a higher data point density [5,11], making the transition from blunting to crack growth more obvious. For the representative

samples in Figure 39, Figure 40 and Figure 41, the resultant R-curves are depicted in Figure 43 a), b) and c), respectively. In the blunting regime, all R-curves are increasing. The end of the blunting regime is indicated by the dotted vertical line in Figure 43. This increase matches the typical R-curve behavior described in the ASTM1820 standard [9]. After crack initiation, the R-curve behavior starts to deviate. The brittle fractured sample (B1) exhibits a slight rise in δ and a decrease in α after crack initiation up to a crack extension of 2.5 µm, see Figure 43 a). Following the ASTM1820 standard, the maximum crack extension capacity (Δa_{max}) is 1/4 of the initial ligament length ($\Delta a_{max} = 0.25(W - a_0)$) [9,63], indicated by the gray shaded regions in Figure 43. In the case of sample B1, Δa_{max} is reached at a crack extension of 1.5 µm. This leads to the typical R-curve shape from $\Delta a = 0$ µm to $\Delta a_{max} = 1.5$ µm [9,63]. However, above Δa_{max} the R-curves of δ and α continue with the same trend until the remaining ligament fully plastifies at $\Delta a \approx 3$ µm. At this point, crack propagation is slowed due to reduced energy storing capabilities stemming from geometrical constrains, leading to purely plastic deformation. In conjunction, the manual measurements resulted in a similar R-curve as the algorithmic measurements. However, an increased scatter is observed for the manual measurements, which originates from a low number of measurement points.

In case of the semi-brittle (SB1) sample, δ decreases immediately at crack initiation, while α still increases. At the crack initiation ($\Delta a = 0.4$ µm) the crack sharpens, leading to an increase in α and Δa, while δ decreases, see Figure 43 b) and Figure 40 b). Also, at this time, pores form in front of the crack. The material bridges, between crack and pore, fracture later to connect them, leading to a decrease in α and enhanced crack growth rate at $\Delta a = 0.7$ µm, illustrated in Figure 43 b). The fractured material bridges are observable in Figure 40 c). Pore formation followed by crack advancement through material bridge failure continuous until the experiments end. This advancement of the crack leads to more challenging crack detection, as described in section 7.2, and, as a result, scatter increases. The manual measurements also exhibited an increased scatter, especially after crack initiation, leading to a rising R-curve until $\Delta a = 2$ µm. The algorithmically determined R-curve mostly resides within the increased scatter of the manual measurement.

The ductile sample (D1) exhibits a similar R-curve behavior to SB1. The crack sharpening after crack initiation is depicted by the *in situ* frames in Figure 41 b) and c). At $\Delta a \approx 50$ nm, α starts to decrease and the reduction of δ is damped, indicating continuous crack growth. Compared to the SB1 sample, no pore formation was observed, pointing to stable crack growth.

The correlation between *in situ* frames and the measured fracture characteristics by the algorithm can be best illustrated by a video. In the supplementary material, videos can be found for the representative samples discussed in this section. These illustrate the

measurement of δ and α correlated to the *in situ* frames, for brittle (B1, Supplementary video A), semi-brittle (SB1, Supplementary video B) and ductile (D1, Supplementary video C) fracture.

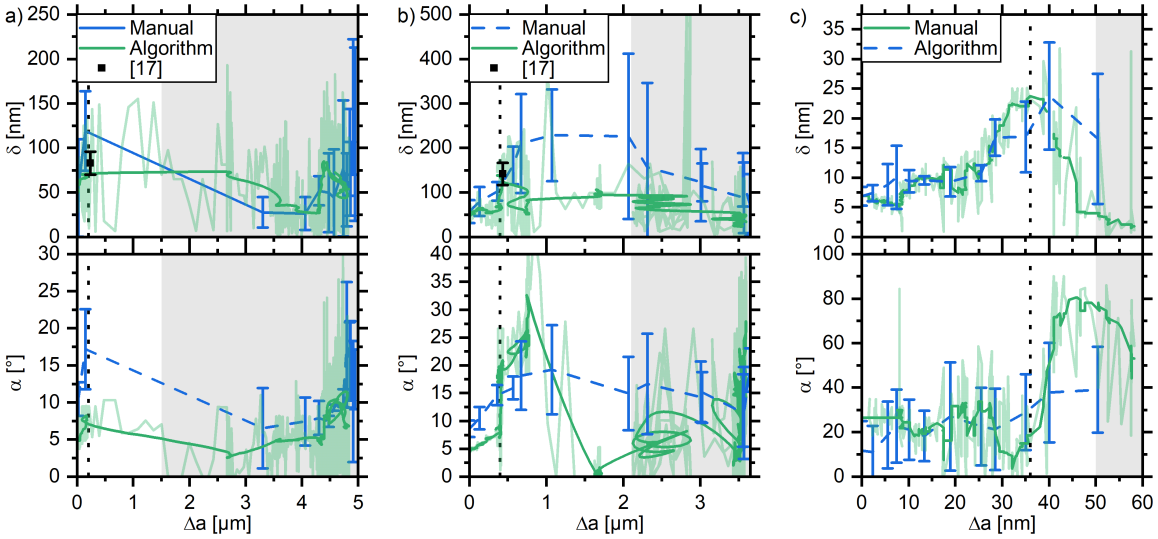

Figure 43: R-curves obtained for the crack tip opening displacement δ and -angle α for the representative samples B1, SB1 and D1, illustrated by the subfigures a), b) and c), respectively. The black data point in a) and b) was measured in [17].

Nevertheless, the decrease of δ after crack initiation and latter the α drop contradicts the typical R-curve [9,63]. This deviation occurs as the algorithm measures δ and α locally at the crack tip, while the ASTM1820 standard defines δ and α at the initial crack position [9], depicted by the red and green measurement marks in Figure 44, respectively. Therefore, the standard assumes homogeneous stress and strain fields, as well as isotropic material deformation throughout the fracture experiment [9,63]. Nevertheless up to crack initiation, the local measurement equals the measurement defined in the standard, noted the blunted crack to the left in Figure 44. The $J-$integral evaluation from mechanical data has similar constrains, as it expects a homogeneous stress and strain field [9,63]. To compare the obtained values with literature, only the crack initiation point is considered, which was determined by visual inspection of the *in situ* frames. For the B1, SB1 and D1 samples, the crack initiation occurred at $t = 97$ s, 248 s and 233 s, respectively. The δ results determined by the algorithm at the initiation points are translated into fracture toughness values utilizing Equation 3 and Equation 4. The results are summarized in Table 6.

The values determined for δ by the algorithm are in good agreement with manual measurement values from literature. Furthermore, the measurement errors are on the same order of magnitude, indicating a similar accuracy between the algorithm and manual measurements, outlined in Table 6. Moreover, conversion to the J-integral J_q and stress intensity K_q allows a direct comparison to the mechanically determined fracture characteristics reported in

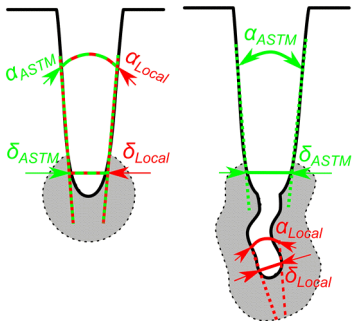

Figure 44: Different approaches to measure crack tip opening displacement (δ) and -angle (α) during crack tip blunting and crack growth. Green illustrates the measurement defined by the ASTM1820 standard. Red depicts the local measurement performed by the algorithm. The gray shaded region represents the plasticized region around the crack.

Table 6: Crack tip opening displacement δ determined by the algorithm at the crack initiation point for the exemplary shown cantilevers in Figure 39, Figure 40 and Figure 41. The δ values for B1 and SB1 are compared to manual measurements values found in literature [17], denoted by the subscript m. Additionally, for comparison with mechanical data, δ was transformed into the J-integral J_q and stress-intensity K_q according to Equation 3 and Equation 4.

sample	δ_a[nm]	$J_{\delta_a,q}[\frac{\mathrm{J}}{\mathrm{m}^2}]$	$K_{\delta_a,q}[\mathrm{MPa}\sqrt{\mathrm{m}}]$	δ_m[nm]	$J_{\delta_m,q}[\frac{\mathrm{J}}{\mathrm{m}^2}]$	$K_{\delta_m,q}[\mathrm{MPa}\sqrt{\mathrm{m}}]$	$J_q[\frac{\mathrm{J}}{\mathrm{m}^2}]$	$K_q[\mathrm{MPa}\sqrt{\mathrm{m}}]$
B1	72 ± 24	190 ± 64	6.8 ± 2.3	83 ± 14	219 ± 37	7.3 ± 0.6	180 ± 6	6.7 ± 0.1
SB1	135 ± 15	390 ± 43	9.8 ± 1.1	142 ± 25	400 ± 71	9.9 ± 0.9	398 ± 14	9.9 ± 0.2
D1	23 ± 5	37 ± 7	2.7 ± 0.5	21 ± 3	34 ± 5	2.6 ± 0.4	41 ± 3	2.8 ± 0.2

literature. The values obtained for J_q and K_q by the algorithm are in accordance with the mechanical literature data, though the errors of the algorithm are slightly increased. Nevertheless, the similarity of the respective fracture characteristics supports the potential of the algorithm to evaluate fracture experiments in the field of micromechanics. The algorithm is independent of the material properties and relies only on the 2D representation of the crack. Hence, as long as the material is reasonably isotropic, the crack on the surface would be related to the crack front inside the specimen and the evaluation is valid. Notably, elastic plastic fracture mechanics is based on the same assumption and assumes an isotropic homogeneous material [5,2063]. Thus, the algorithm necessitates similar material properties as commonly employed in fracture mechanics. Furthermore, the R-curves obtained from the *in situ* frames allow to deepen the knowledge of the fracture process occurring at the micron and sub-micron scale. Thus, the presented evaluation can be used in conjunction with mechanical calculations to characterize the fracture process and verify the validity of small-scale experiments [11,17,21]. Additionally, the fracture characteristics can directly be related to the micro structure using the available crack path information. This provides further insight into fracture processes with unexpected or unknown material behavior due to inhomogenities or local microstructural variations [64-66]. By extending the algorithms capabilities to account for multiple fracture paths, even more complex fracture processes

could be investigated.

Conclusion

An algorithm was developed that automatically adapts to the image input data of *in situ* experiments to provide deeper insight into the fracture process at the micron to sub-micron scale. This algorithm extracts the crack length and additional fracture characteristics such as crack tip opening displacement (δ) and -angle (α). The extraction process was split into a probabilistic classification, contour extraction, and evaluation of the fracture characteristics from the identified crack contours. For the development of the algorithm, samples exhibiting brittle, semi-brittle and ductile failure were used to cover the full range of fracture behavior and corresponding fracture features. For comparison, the crack length was also determined from mechanical stiffness data and manual measurements to access the accuracy of the image-based measurement. This comparison revealed an overall excellent agreement between the image and mechanical-based measurements. Several frames of each sample were manually evaluated multiple times to serve as ground truth data for the crack tip coordinates, crack tip opening displacement and -angle. This ground truth data was used to verify the performance of the algorithm, indicating comparable accuracy to manual measurements and proving the applicability of the algorithm on different fracture behaviors. This novel algorithm reproducibly evaluates all recorded *in situ* frames in minutes, compared to time intense manual process, requiring highly skilled experts. Analysis of crack tip opening displacement and -angle allows the verification of fracture toughness values calculated from mechanical data. The image-based evaluation allows fracture processes of more complex material structures to be evaluated, including materials with anisotropic properties and increased blunting tendency. In summary, this novel algorithm provides a powerful tool aid the understanding of complicated fracture processes and allow a more detailed understanding of the fundamental fracture processes of complex material structures at the micro- and nano scale.

Conflict of interest/Competing interests

The authors declare that they have no known competing financial interests or personal relationships that could have appeared to influence the work reported in this paper.

Availability of data and materials

The data generated during the current study are available from the corresponding author on a reasonable request.

Acknowledgments

This work was supported by European Research Council [Grant number: 771146 (TOUGHIT)]. This research was funded in part by the Austrian Science Fund (FWF) [Grant number: P 34840-N]. For the purpose of open access, the author has applied a CC BY public copyright license to any Author Accepted Manuscript version arising from this submission. We thank Michael Burtscher for the data of the *in situ* fracture experiment performed inside the transmission electron microscope.

CRediT authorship contribution statement

K. Schmuck: Writing – review & editing, Writing – original draft, Methodology, Data curation, Conceptualization. **M. Antenreiter:** Writing – review & editing, Writing – original draft, Methodology, Data curation, Conceptualization. **M. Alfreider:** Writing – review & editing, Methodology. **D. Kiener:** Writing – review & editing, Supervision, Resources, Project administration, Funding acquisition, Conceptualization

References

[1] G. Dehm, B.N. Jaya, R. Raghavan, C. Kirchlechner, Overview on micro- and nanomechanical testing: new insights in interface plasticity and fracture at small length scales, Acta Mater. 142 (2018) 248–282, https://doi.org/10.1016/j.actamat.2017.06.019.

[2] D.S. Gianola, A. Sedlmayr, R. Mnig, C.A. Volkert, R.C. Major, E. Cyrankowski, et al., In situ nanomechanical testing in focused ion beam and scanning electron microscopes, Rev. Sci. Instrum. 82 (6) (2011) 1–12.

[3] P. Hosemann, Small-scale mechanical testing on nuclear materials: bridging the experimental length-scale gap, Scr. Mater. 143 (2018) 161–168, https://doi.org/10.1016/j.scriptamat.2017.04.026.

[4] G. Sernicola, T. Giovannini, P. Patel, J.R. Kermode, D.S. Balint, T.B. Britton, et al., In situ stable crack growth at the micron scale, Nat. Commun. 8 (1) (2017), https://doi.org/10.1038/s41467-017-00139-w.

[5] D. Kiener, M. Wurmshuber, M. Alfreider, G.J.K. Schaffar, V. Maier-Kiener, Recent advances in nanomechanical and in situ testing techniques: towards extreme conditions, Curr. Opin. Solid State Mater. Sci. 27 (6) (2023) 101108, https://doi.org/10.1016/j.cossms.2023.101108.

[6] J. Ast, B. Merle, K. Durst, M. Göken, Fracture toughness evaluation of NiAl single

crystals by microcantilevers - a new continuous J-integral method, J. Mater. Res. 31 (23) (2016) 3786–3794.

[7] J. Ast, M. Ghidelli, K. Durst, M. Göken, M. Sebastiani, A.M. Korsunsky, A review of experimental approaches to fracture toughness evaluation at the micro-scale, Mater. Des. 173 (2019) 107762, https://doi.org/10.1016/j.matdes.2019.107762.

[8] S. Wurster, C. Motz, R. Pippan, Characterization of the fracture toughness of micro-sized tungsten single crystal notched specimens, Philos. Mag. 92 (14) (2012) 1803–1825.

[9] ASTM Standard, Standard Test Method for Measurement of Fracture Toughness, ASTM Book of Standards, 03.01 (January) 2013, pp. 1–54.

[10] M. Alfreider, D. Kozic, O. Kolednik, D. Kiener, In-situ elastic-plastic fracture mechanics on the microscale by means of continuous dynamical testing, Mater. Des. 148 (2018) 177–187, https://doi.org/10.1016/j.matdes.2018.03.051.

[11] K.S. Schmuck, M. Alfreider, D. Kiener, Crack length estimations for small - scale fracture experiments via image processing techniques, J. Mater. Res. 37 (17) (2022) 2848–2861, https://doi.org/10.1557/s43578-022-00681-4.

[12] C.F. Shih, Relationship between the J-integral and the COD for stationary and extending cracks, J. Mech. Phys. Solids 29 (4) (1981) 305–326.

[13] J. Heerens, M. Schödel, Characterization of stable crack extension in aluminium sheet material using the crack tip opening angle determined optically and by the $\delta 5$ clip gauge technique, Eng. Fract. Mech. 76 (1) (2009) 101–113, https://doi.org/10.1016/j.engfracmech.2008.04.009.

[14] U. Zerbst, M. Heinimann, C.D. Donne, D. Steglich, Fracture and damage mechanics modelling of thin-walled structures - an overview, Eng. Fract. Mech. 76 (1) (2009) 5–43, https://doi.org/10.1016/j.engfracmech.2007.10.005.

[15] British Standards Institution, Methods for Crack Opening Displacements (COD) Testing, DD 19:1972, 1972, p. 48.

[16] M. Wurmshuber, M. Alfreider, S. Wurster, R. Pippan, D. Kiener, Small-scale fracture mechanical investigations on grain boundary doped ultrafine-grained tungsten, Acta Mater. 250 (118878) (2023) 18, https://doi.org/10.1016/j.actamat.2023.118878.

[17] K. Schmuck, M. Burtscher, M. Alfreider, M. Wurmshuber, D. Kiener, Micromechanical fracture investigations on grain size tailored tungsten-copper nanocomposites, JOM (2024), https://doi.org/10.1007/s11837-023-06348-7.

[18] R. Pippan, S. Wurster, D. Kiener, Fracture mechanics of micro samples: fundamental considerations, Mater. Des. 159 (2018) 252–267, https://doi.org/10.1016/j.matdes.2018.09.004.

[19] B.N. Jaya, J.M. Wheeler, J. Wehrs, J.P. Best, R. Soler, J. Michler, et al., Microscale fracture behavior of single crystal silicon beams at elevated temperatures, Nano Lett. 16 (12) (2016) 7597–7603.

[20] A.K. Saxena, S. Brinckmann, B. Völker, G. Dehm, C. Kirchlechner, Experimental conditions affecting the measured fracture toughness at the microscale: notch geometry and crack extension measurement, Mater. Des. 191 (2020) 1–11.

[21] M. Burtscher, M. Alfreider, K. Schmuck, H. Clemens, S. Mayer, D. Kiener, In situ fracture observations of distinct interface types within a fully lamellar intermetallic TiAl alloy, J. Mater. Res. 36 (2021) 2465–2478.

[22] G. Van Rossum, F.L. Drake, Python 3 Reference Manual, CreateSpace, Scotts Valley, CA, 2009, Available from: https://www.python.org/.

[23] G. Bradski, The OpenCV library, Dr. Dobb's J. Softw. Tools (2000).

[24] S. van der Walt, J.L. Schönberger, J. Nunez-Iglesias, F. Boulogne, J.D. Warner, N. Yager, et al., scikit-image: image processing in Python, PeerJ (2014).

[25] C.R. Harris, K.J. Millman, S.J. van der Walt, R. Gommers, P. Virtanen, D. Cournapeau, et al., Array programming with NumPy, Nature 585 (2020) 357–362.

[26] P. Virtanen, R. Gommers, T.E. Oliphant, M. Haberland, T. Reddy, D. Cournapeau, et al., SciPy 1.0: fundamental algorithms for scientific computing in python, Nat. Methods 17 (2020) 261–272, Available from: https://rdcu.be/b08Wh.

[27] M. Guizar-sicairos, S.T. Thurman, J.R. Fienup, Efficient subpixel image registration algorithms manuel, Opt. Lett. 33 (2) (2008) 156–158.

[28] R.O. Duda, P.E. Hart, Pattern Classification and Scene Analysis, Wiley & Sons, New York, 1973.

[29] T. Pavlidis, Contour filling in raster graphics, Comput. Graph. 15 (3) (1981) 29–36.

[30] J.F. Hughes, A. Van Dam, M. McGuire, D.F. Sklar, J.D. Foley, S.K. Feiner, et al., Computer Graphics Principles and Practice, third edit ed., Addison-Wesley, Upper Saddle River, NJ, 2014.

[31] M.L. Fredman, R.E. Tarjan, Fibonacci heaps and their uses in improved network optimization algorithms, in: 25th Annual Symposium on Foundations of Computer

Science, 1984, Institute of Electrical and Electronics Engineers, 1984, pp. 338–346.

[32] R.O. Ritchie, Mechanism of fatigue-crack propagation in ductile and brittle materials, Int. J. Fract. 100 (1998) 55–83.

[33] M.A. Fischler, R.C. Bolles, Paradigm for model, Commun. ACM 24 (6) (1981) 381–395.

[34] R. Hartley, A. Zisserman, Multiple View Geometry, Cambridge University Press, 2004.

[35] J.R. Rice, G.F. Rosengren, Plane strain deformation near a crack tip in a power-law hardening material, J. Mech. Phys. Solids 16 (1) (1968) 1–12.

[36] J.W. Hutchinson, Singular behaviour at the end of a tensile crack in a hardening material, J. Mech. Phys. Solids 16 (1968) 13–31.

[37] M. Burtscher, T. Klein, J. Lindemann, O. Lehmann, H. Fellmann, V. Güther, et al., An advanced tial alloy for high-performance racing applications, Materials 13 (21) (2020) 1–14.

[38] C.B. Carter, D.B. Williams, Transmission Electron Microscopy: Diffraction, Imaging, and Spectrometry, Springer, 2016.

[39] M. Sutton, W. Wolters, W. Peters, W. Ranson, S. McNeill, Determination of displacements using an improved digital correlation method, Image Vis. Comput. 1 (3) (1983) 133–139.

[40] S.R. McNeill, W.H. Peters, M.A. Sutton, Estimation of stress intensity factor by digital image correlation, Eng. Fract. Mech. 28 (1) (1987 jan) 101–112, Available from: https://linkinghub.elsevier.com/retrieve/pii/001379448790124X.

[41] S. Roux, J. Réthoré, F. Hild, Digital image correlation and fracture: an advanced technique for estimating stress intensity factors of 2D and 3D cracks, J. Phys. D, Appl. Phys. 42 (21) (2009).

[42] T. Thäsler, J. Holtmannspötter, H.J. Gudladt, Monitoring the fatigue crack growth behavior of composite joints using in situ 2D-digital image correlation, J. Adhes. 95 (5–7) (2019) 595–613, https://doi.org/10.1080/00218464.2018.1562923.

[43] A.D. Kammers, S. Daly, Digital image correlation under scanning electron microscopy: methodology and validation, Exp. Mech. 53 (9) (2013) 1743–1761.

[44] F. Di Gioacchino, J. Quinta da Fonseca, Plastic strain mapping with sub-micron resolution using digital image correlation, Exp. Mech. 53 (5) (2013) 743–754.

[45] F. Di Gioacchino, W.J. Clegg, Mapping deformation in small-scale testing, Acta Mater.

78 (2014) 103–113, https://doi.org/10.1016/j.actamat.2014.06.033.

[46] T.E.J. Edwards, F. Di Gioacchino, R. Muñoz-Moreno, W.J. Clegg, Deformation of lamellar TiAl alloys by longitudinal twinning, Scr. Mater. 118 (2016) 46–50, https://doi.org/10.1016/j.scriptamat.2016.03.004.

[47] T.E.J. Edwards, X. Maeder, J. Ast, L. Berger, J. Michler, Mapping pure plastic strains against locally applied stress: revealing toughening plasticity, Sci. Adv. 8 (30) (2022) 1–11.

[48] M. Sutton, J.J. Orteu, H. Schreier, Image Correlation for Shape, Motion and Deformation Measurements, Springer, Berlin Heidelberg, 2009.

[49] J. Réthoré, S. Roux, F. Hild, An extended and integrated digital image correlation technique applied to the analysis of fractured samples: the equilibrium gap method as a mechanical filter, Eur. J. Comput. Mech. 18 (3–4) (2009) 285–306.

[50] K. Unterweger, O. Kolednik, The local deformation behaviour of MMCs -an experimental study, Z. Met.kd. (Materials Research and Advanced Techniques) 96 (9) (2005) 1063–1068.

[51] J. Réthoré, F. Hild, S. Roux, Extended digital image correlation with crack shape optimization, Int. J. Numer. Methods Eng. 73 (2) (2008) 248–272.

[52] M. Vidal, M. Ostra, N. Imaz, E. García-Lecina, C. Ubide, Analysis of SEM digital images to quantify crack network pattern area in chromium electrodeposits, Surf. Coat. Technol. 285 (2016) 289–297, https://doi.org/10.1016/j.surfcoat.2015.11.049.

[53] F. Mathieu, F.F. Hild, S. Roux, Identification of a crack propagation law by digital image correlation, Int. J. Fatigue 36 (1) (2012) 146–154, https://doi.org/10.1016/j.ijfatigue.2011.08.004.

[54] T. Strohmann, D. Starostin-Penner, E. Breitbarth, G. Requena, Automatic detection of fatigue crack paths using digital image correlation and convolutional neural networks, Fatigue Fract. Eng. Mater. Struct. 44 (5) (2021) 1336–1348.

[55] H. Chen, J. Shen, D. Scotson, X. Jin, H. Wu, T.J. Marrow, Fracture toughness evaluation of a nuclear graphite with non-linear elastic properties by 3D imaging and inverse finite element analysis, Eng. Fract. Mech. 293 ((October) 2023) 109719, https://doi.org/10.1016/j.engfracmech.2023.109719.

[56] M. Alfreider, M. Meindlhumer, V. Maier-Kiener, A. Hohenwarter, D. Kiener, Extracting information from noisy data: strain mapping during dynamic in situ SEM experiments, J. Mater. Res. 36 (11) (2021) 2291–2304, https://doi.org/10.1557/s43578-020-00041-0.

[57] R. Olaf, F. Philipp, B. Thomas, U-Net: convolutional networks for biomedical image segmentation, in: Medical Image Computing and Computer-Assisted Intervention – MICCAI 2015 MICCAI 2015, in: Lecture Notes in Computer Science, vol. 9351, 2015, pp. 234–241.

[58] N. Siddique, S. Paheding, C.P. Elkin, V. Devabhaktuni, U-net and its variants for medical image segmentation: a review of theory and applications, IEEE Access 9 (2021) 82031–82057.

[59] A. Kirillov, E. Mintun, N. Ravi, H. Mao, C. Rolland, L. Gustafson, et al., Segment anything, Computer Vision and Pattern Recognition, Available from: http://arxiv.org/abs/2304.02643, 2023.

[60] J.F. Keckes, A. Jelinek, D. Kiener, M. Alfreider, Neural network supported microscale in situ deformation tracking: a comparative study of testing geometries, JOM (2024), https://doi.org/10.1007/s11837-024-06437-1.

[61] W.C. Lenthe, J.C. Stinville, M.P. Echlin, Z. Chen, S. Daly, T.M. Pollock, Advanced detector signal acquisition and electron beam scanning for high resolution SEM imaging, Ultramicroscopy 195 (2018) 93–100, https://doi.org/10.1016/j.ultramic.2018.08.025.

[62] R.O. Ritchie, The conflicts between strength and toughness, Nat. Mater. 10 (11) (2011) 817–822, https://doi.org/10.1038/nmat3115.

[63] T.L. Anderson, Fracture Mechanics, 3rd ed., CRC Press, 2005.

[64] B.L. Boyce, S.L.B. Kramer, H.E. Fang, T.E. Cordova, M.K. Neilsen, K. Dion, et al., The sandia fracture challenge: blind round Robin predictions of ductile tearing, Int. J. Fract. 186 (1–2) (2014) 5–68.

[65] B.L. Boyce, S.L.B. Kramer, T.R. Bosiljevac, E. Corona, J.A. Moore, K. Elkhodary, et al., The second Sandia Fracture Challenge: predictions of ductile failure under quasistatic and moderate-rate dynamic loading, Int. J. Fract. 198 (1–2) (2016) 5–100.

[66] S.L.B. Kramer, A. Jones, A. Mostafa, B. Ravaji, T. Tancogne-Dejean, C.C. Roth, et al., The Third Sandia Fracture Challenge: Predictions of Ductile Fracture in Additively Manufactured Metal, vol. 218, Springer, Netherlands, 2019

.